Optical microsystems for genetically engineered biosensors. Case study: Glucose monitoring

Thèse N° 9609

Présentée le 2 décembre 2019

à la Faculté des sciences et techniques de l'ingénieur
Groupe SCI STI CD
Programme doctoral en microsystèmes et microélectronique

pour l'obtention du grade de Docteur ès Sciences

par

Bakul Jitendra VINCHHI

Acceptée sur proposition du jury

Dr J.-M. Sallese, président du jury
Prof. C. Dehollain, Dr. U. De Marchi, directeurs de thèse
Prof. M. M. Green, rapporteur
Dr S. Tanner, rapporteur
Prof. J.-M. Vesin, rapporteur

2019

ÉCOLE POLYTECHNIQUE
FÉDÉRALE DE LAUSANNE

”If everyone played it safe, we wouldn’t get anywhere.”
- Vinod Khosla

To the ebb and flow of life...

Acknowledgements

I would firstly like to thank my Professor Catherine Dehollain for giving me this opportunity to pursue my Ph.D. in her lab. She is a great role model for anyone who wants to learn to treat people with respect and treat human beings, like human beings. From the person cleaning the floor every evening, to bachelor and master students in courses, to her colleagues at work and even to the dean of electrical engineering, everyone respects her. I have seen her treating all of them with equal respect and dignity. Prof. Catherine Dehollain is also supportive of her students and this has allowed me to pursue and complete an executive management EPFL EMBA program in parallel with my Ph.D. work.

I would like to thank Dr. Christophe Boss and Dr. Umberto De Marchi, who were my Ph.D. co-directors from Nestlé Research, EPFL Innovation Park, Lausanne. Nicolas Bouche from the Nestlé Research in Lausanne for the collaboration. Thanks to Eric Meurville who participated in several brain storming sessions.

I would like to thank my thesis jury members, Dr. Jean-Michel Sallese (EPFL), Prof. Michael M. Green (University of California, Irvine), Dr. Steve Tanner (CTO, ecoRobotix, Switzerland) and Dr. Jean-Marc Vesin (EPFL) for reading my thesis and giving their valuable comments.

Life in EPFL was made easy and smooth, because of my colleagues, Isabelle Buzzi, Karin Jaymes and Raymond Sutter. Thanks to them for some really lively discussions and the coffee capsules. Special thanks to the EPFL official photographer Alain Herzog and webmaster John Maxwell.

At the RFIC group I would like to extend my gratitude to my colleagues Mehrdad Ghanad, Rosanne Santos, Kerim Ture and Mustafa Besirli.

The ELB floors had some special people around. I thank, Francois Gaugaz and Olivier Van Cutsem for the amazing times we had in Lausanne and California. Thanks to Guillaume Lanz and Ira Nagel for being good friends. Thanks to Georgios Lilis, Adil Koukab, Theodoros Kyriakidis, Chiara Rossi and Farzan Jazayeri for the interesting talks. Special thanks to Evi Voulgari and Aristea Grammoustianou for their support during my PhD writing.

Thanks to my good friends in EPFL, Ninad, Reza and Ali who helped me during my PhD. I met some really cool people at the campus and I would like to thank Insaf, John, Fiko, Kamilla, Novak and Gianmarco.

During my stay in Lausanne, the language center at EPFL was a place where I spend a lot of time. I would like to extend my gratitude to all my French and German language teachers. I have embarked on several entrepreneurial endeavors in Switzerland and met many like minded people who shared the same spirit, I would like to take this opportunity to thank Frederico Matteini and Tihomir Gvero for all our attempts to change the world.

Acknowledgements

Life in Lausanne was made interesting by pursuing several hobbies. I met Jeanne, Anouck, Cecile, Ana, Julia, Sophia and Dominic through Lindy Hop. Thanks to them for the amazing time, traveling to festivals in Europe, dancing and experiencing Jazz culture together. Special thanks to Alex Jewell and Celine Provins for their collaboration during my role as the President of EPFL Swing Kids.

I would like to thank my music Professors at the Ecole de Jazz et de Musique Actuelle (EJMA) in Lausanne. To my clarinet Professor Nicola Orioli, for being so patient and adeptly guiding me with the clarinet. To my singing Professor Anne-Florence Schneider, for encouraging me to use, and discover my voice.

Rowing has taught me a lot of things about teamwork, leadership and group dynamics. I would like to wholeheartedly thank my coaches and fellow rowers at the Rowing Club Lausanne for their amazing team-spirit.

Back in India, I would like to thank my friend Deepak Purushotham for all his encouragement and support. Thanks a lot to my family back home and special thanks to my mother, who despite having fought cancer during my PhD with a lot of courage, always spoke as if life was fine.

Lausanne, 11 August 2019 Bakul Vinchhi.

Abstract

Diabetes is a global epidemic with millions of people dying from it every year. Progress in microelectronics and machine learning has led to a huge number of FDA approvals of devices for continuous monitoring and treatment of diabetes with one product using light in its sensing principle. Invitro demonstrators were designed, build and tested successfully for monitoring the genetically engineered INS-1E F10 cell line that works on the FRET principle based on a ratio-metric principle. The advantage of the ratio-metric probe is that we directly see the relative changes in the glucose levels of the stimulated INS-1E F10 cells, the common effects are canceled out in the ratio to a great extent.

This first part of the work reports the design and testing of a bio-electronics system that measures cytosolic [Ca^{2+}] *in vitro* in the INS-1E pancreatic β-cells using a 430 nm excitation light with the excitation wavelength of the probe being at 435 nm. We inserted a plasmid in the cell that is responsible for the FRET based [Ca^{2+}] protein sensor complex, that emit light at both 485 nm and 535 nm. The system has a linear response upon characterization with flurosphere for various intensities of light. The system is sensitive for 2D cell cultures on normal petri dishes but suffers from poor SNR. Cell culturing to form 3D cell aggregates using a shaker in the incubator increases the number of cells and thus enhances the signal quality 35 times and 21 times for green and blue light counts respectively. The first system has been able to continuously monitor the fluorescence of a clone of INS-1E β-cells upon glucose stimulation, diazoxide injection and KCl injection, thus revealing insights in the cell response mechanisms.

The second *in vitro* system has been developed, tested and deployed. The angle independent absorption-based optical long pass filter MIDOPT LP470 improves the signal-to-noise ratio (SNR) by rejecting the reflections from the excitation source and auto-fluorescence components. A significant 480% improvement is witnessed in the SNR of the F10 cells after using the LP470 filter. The system has successfully monitored the genetically engineered INS-1E pancreatic β-cell line upon stimulation with 11 mM glucose in the cell culture medium and exchanging with KRBS solution with 0 mM glucose, which corresponds to a pulsating binary glucose stimulation. The system has been used to characterize the total number of cells in millions, cell growth and death, effect of temperature and periodic, continuous and binary glucose stimulation. Insights about the noise floor and saturation with respect to the LED bias current and integration times were obtained from both the electronics and biological perspectives. While too faint light intensity and short photo-detector integration times drives us down in the noise floor, the opposite on the contrary has a deleterious effect on the cells as it leads to a loss of fluorescence.

An analog front-end readout amplifier for monitoring glucose was designed and simulated with

UMC CMOS 180 nm technology. Detailed small signal analysis of the circuits were done and the design was tested with simulations using the cadence tool. The results were highly correlated and showed a promising step towards a low noise and low power analog front end circuit aimed at bio-medical applications.
Keywords: genetically engineered, pancreatic β-cell line, *in vitro*, automation, Continuous monitoring, glucose, optical filters, absorption based filters, 3D cell aggregates, bioelectronics system, analog front end amplifier, CMOS, negative resistance.

Résumé

Le diabète est une épidémie mondiale avec des millions de personnes qui meurent chaque année. Les progrès de la microélectronique et de l'apprentissage automatique ont conduit à un grand nombre d'approbations par la FDA d'appareils de surveillance et de traitement continus du diabète, un produit utilisant la lumière dans son principe de détection. Les démonstrateurs Invitro ont été conçus, construits et testés avec succès pour surveiller la lignée cellulaire INS-1E F10 génétiquement modifiée qui fonctionne sur le principe FRET basé sur le principe ratio-métrique. L'avantage de la sonde ratio-métrique est que nous voyons directement les changements relatifs dans les taux de glucose des cellules INS-1E F10 stimulées, les effets communs s'annulant dans une large mesure.

Cette première partie du travail décrit la conception et la mise à l'essai d'un système bioélectronique mesurant *in vitro* le [Ca^{2+}] cytosolique dans les cellules pancréatiques INS-1E à l'aide d'une lumière excitatrice à 430 nm, la longueur d'onde d'excitation de la sonde étant à 435 nm. Nous avons inséré dans la cellule un plasmide responsable du complexe capteur de protéine [Ca^{2+}] à base de FRET, émettant de la lumière à 485 nm et à 535 nm. Le système a une réponse linéaire lors de la caractérisation à la flurosphère pour diverses intensités de lumière. Le système est sensible aux cultures de cellules 2D sur des boîtes de Pétri normales mais souffre d'un SNR faible. La culture de cellules pour former des agrégats de cellules 3D en utilisant un agitateur dans l'incubateur augmente le nombre de cellules et améliore ainsi la qualité du signal 35 fois et 21 fois pour les comptages de lumière verte et bleue, respectivement. Le premier système a permis de surveiller en continu la fluorescence d'un clone de cellules INS-1E beta lors de la stimulation du glucose, de l'injection de diazoxide et de KCl, révélant ainsi des informations sur les mécanismes de réponse cellulaire.

Le second système in vitro a été développé, testé et déployé. L'angle indépendant le filtre optique long passe passe basé sur l'absorption MIDOPT LP470 améliore le rapport signal sur bruit (SNR) en rejetant les réflexions provenant de la source d'excitation et des composants auto-fluorescents. Une amélioration significative de 480% dans le SNR des cellules F10 après utilisation du filtre LP470. Le système a surveillé avec succès la lignée de cellules beta pancréatiques INS-1E génétiquement modifiée lors d'une stimulation avec du glucose 11 mM dans le milieu de culture cellulaire et d'un échange avec une solution de KRBS avec du glucose 0 mM, ce qui correspond à une stimulation pulsée du glucose binaire. Le système a été utilisé pour caractériser le nombre total de cellules en millions, la croissance et la mort cellulaires, l'effet de la température et la stimulation du glucose périodique, continue et binaire. Des informations sur le bruit de fond et la saturation en ce qui concerne le courant de polarisation de la LED et les temps d'intégration

ont été obtenues à la fois du point de vue électronique et biologique. Tandis qu'une intensité de lumière trop faible et des temps d'intégration de photodétecteurs courts nous font sombrer dans le bruit de fond, l'opposé a au contraire un effet néfaste sur les cellules car il entraîne une perte de fluorescence.
Un amplificateur de lecture frontal analogique pour la surveillance du glucose a été conçu et simulé avec la technologie UMC CMOS 180 nm. Une analyse détaillée du petit signal des circuits a été réalisée et la conception a été testée à l'aide de simulations à l'aide de l'outil de cadence. Les résultats étaient hautement corrélés et montraient une étape prometteuse vers un circuit frontal analogique à faible bruit et faible consommation aux applications bio-médicales.
Mots-clés : lignée génétiquement modifiée de lignée cellulaire beta de pancréas, *in vitro*, automatisation, surveillance continue, glucose, filtres optiques, filtres basés sur l'absorption, agrégats de cellules 3D, bioélectronique système, amplificateur frontal analogique, CMOS, résistance négative.

Acronyms

3D	**Three dimension**
AFE	**Analog Front End**
ANN	**Artificial Neural Network**
ATP	**Adenosine triphosphate**
B	**Blue**
BW	**Bandwidth**
CE	**Conformité Européenne**
CMOS	**Complementary metal-oxide-semiconductor**
CT scan	**Computed tomography scan**
EGA	**Error Grid Analysis**
FACS	**Fluorescence-activated cell sorting**
FDA	**Food and Drug Administration**
FRET	**Fluorescence Resonance Energy Transfer**
FPG	**Fasting Plasma Glucose**
G	**Green**
GBW	**Gain Bandwidth**
IR	**Infrared**
KCL	**Potassium chloride**
KRBH	**Krebs-Ringer bicarbonate-HEPES buffer**
LED	**Light Emitting Diode**
MARD	**Mean absolute relative difference**
mNIRS	**multi-wavelength near-infrared spectroscopy**
MRI	**Magnetic Resonance Imaging**
NIRS	**Near Infrared Spectroscopy**
nm	**nanometer**

NIRS	**Near Infrared Spectroscopy**
nm	**nanometer**
OD	**Optical Density**
OPAMP	**Operational Amplifier**
OTA	**Operational trans-conductance amplifier**
PCB	**Printed Circuit Board**
PD	**Photo-detector**
R	**Red**
SNR	**Signal to Noise Ratio**
TIA	**Trans-impedance amplifier**
UV	**Ultra Violet**

Contents

Acknowledgements v

Abstract (English/Français) vii

Acronyms xi

List of figures xv

List of tables xxii

1 Introduction 1
- 1.1 Diabetes: its prevalence, cost and trends on a global scale . . . 1
- 1.2 FDA approved glucose detection and monitoring devices . . . 4
  - 1.2.1 MiniMed 630G System with SmartGuard . . . 4
  - 1.2.2 Guardian Connect System . . . 5
  - 1.2.3 Freestyle Libre Flash Glucose Monitoring System . . . 6
  - 1.2.4 t:slim X2 Insulin Pump with Basal-IQ Technology - P180008 . . . 7
  - 1.2.5 MiniMed 670G System - P160017/S031 . . . 9
  - 1.2.6 Eversense Continuous Glucose Monitoring System - P160048 . . . 10
- 1.3 Cell Encapsulation Technology . . . 12
- 1.4 Fluorescence resonance energy transfer FRET . . . 14
- 1.5 Outline and challenges of this work . . . 14

2 *In vitro* demonstrators concept, design, implementation and testing 17
- 2.1 Introduction . . . 17
- 2.2 System Level Principle . . . 18
  - 2.2.1 Protein structure homology modelling . . . 19
- 2.3 Photodetector Selection . . . 20
- 2.4 Optical Filter Selection . . . 22
- 2.5 Electronic System Configuration . . . 23
- 2.6 Results and Discussion . . . 26
  - 2.6.1 Fluorescence characterization of the system . . . 26
  - 2.6.2 Reference characterization of the F10 INS-1E pancreatic β-cells using the CCS100/m spectrometer. . . . 26

2.6.3 Characterization of 2D and 3D cell cultures of INS-1E pancreatic β-cells with the FRET probe and control . . . 28
2.6.4 Continuous monitoring of the F10 INS-1E pancreatic 3D β-cell aggregates 31
2.7 Conclusion - *In vitro* Demonstrator 1 . . . 32
2.8 *In vitro* Demonstrator 2 . . . 33
2.8.1 Brief Motivation and Innovation . . . 33
2.8.2 Summary of the Methods . . . 35
2.8.3 Key Results . . . 37
2.8.4 Conclusions . . . 38

3 Optical Filters Characterization 39
3.1 Motivation for characterizing and selecting optical filters . . . 39
3.2 Experimental methods adopted for characterization of the optical filters . . . 40
3.3 Absorption based glass filters . . . 40
3.3.1 MIDOPT BP505 Cyan Bandpass Filter . . . 41
3.3.2 MIDOPT LP470 Light Yellow Longpass Filter . . . 48
3.3.3 Fuji Angle Independent Tri Acetyl Cellulose Filter: SC 46 . . . 55
3.3.4 Fuji Angle Independent Tri Acetyl Cellulose Filter: SC 48 . . . 65
3.3.5 Kodak gelatin based filters: Wratten 2 Filter 3 . . . 71
3.4 Dichroic principle angle dependent glass filters . . . 78
3.4.1 Laser Components (LC) dichroic glass based filter: LC-HBP40 10-586 Dual Band . . . 79
3.5 Filter of choice . . . 85
3.6 Filter of choice with offset correction . . . 85
3.7 LED bias current and integration time: design point . . . 86
3.8 Excitation LED center wavelength: effect on the SNR . . . 88
3.9 Conclusion on filter characterization . . . 89

4 *In vitro* measurements with INS-1E pancreatic β-cell based biosensor 91
4.1 INS-1E YC3.6$_{cyto}$ cell line generation and cell culturing . . . 91
4.2 Number of Cells . . . 92
4.3 Cell growth death trend characterization . . . 93
4.4 Temperature response of the FRET cell line . . . 94
4.4.1 Polynomial fit of the evolution of temperature, blue, green counts and the ratio with respect to time . . . 95
4.5 Fluorescence as function of light intensity and exposure time . . . 100
4.6 Response of the cells in KRBH solution and cell culture medium . . . 103
4.7 Oxygenation of the cells: stimulation using glucose and KCL . . . 104
4.8 Continuous automated glucose monitoring for 18 hours . . . 107
4.9 Periodic glucose stimulation . . . 108
4.10 Glucose binary pulse stimulation . . . 110
4.11 Conclusion of *in vitro* biological experiments and glucose monitoring . . . 112

5 Analog Front End Circuit in 0.18 µm CMOS for optical glucose detection 113
5.1 Metrics for classifying accuracy and precision of sensors used for glucose monitoring . . . 113
5.2 CMOS Analog Front-End (AFE) amplifiers for optical biosensor applications with pertinence to glucose sensing. . . . 115
5.3 Multimodal spectroscopy for non-invasive highly accurate estimation of blood glucose levels non-invasively . . . 116
5.3.1 Principle of Blood Glucose Estimation . . . 116
5.3.2 CMOS System Architecture for blood glucose measurement . . . 117
5.4 An innovative 3-stage Miller compensated, cross-coupled load, based photodiode front end readout is designed for glucose monitoring . . . 120
5.4.1 Introduction . . . 121
5.4.2 Glucose Readout System Architecture and system specifications . . . 121
5.4.3 Light Penetration Depth . . . 122
5.4.4 Wavelength and its specifications . . . 122
5.4.5 Sensor System Architecture . . . 122
5.4.6 Photodiode Sensor Model and and its specifications . . . 123
5.4.7 Circuit Architecture, Analysis and Design . . . 124
5.4.8 Amplifier Circuit . . . 124
5.4.9 Differential Pair with Cross-Coupled Load . . . 124
5.4.10 Circuit Architecture for the Glucose Sensor Front End Readout . . . 128
5.4.11 Results and Conclusion . . . 131
5.5 Short term outlook and long term vision for wearable glucose monitoring devices 132
5.5.1 Apple iWatch4 . . . 132

6 Conclusion and future scope 137

Bibliography 145

Curriculum Vitae 147

List of Figures

1.1 Global Diabetes Atlas - International Diabetes Federation. Source [1] 1
1.2 The top 10 countries for number of adults with diabetes account for 60% of people with diabetes and 69% of global healthcare expenditure on diabetes. Source [1] 2
1.3 4 out of 5 people with diabetes live in low- and middle-income countries. Source [1] 3
1.4 Undiagnosed percentage and undiagnosed cases of diabetes (20-79 years) by region. Legend (AFR: Africa, EUR: Europe, MENA: Middle East and North Africa, NACA: North America and Caribbean, SACA: South and Central America, SEA: South East Asia, WP: Western Pacific). Source [1] 4
1.5 MiniMed 630G System with SmartGuard. Source [2] 5
1.6 Medtronic Guardian Connect System P160007 6
1.7 Freestyle Libre Flash Glucose Monitoring System - P160030/S017. Source [3] [4] 7
1.8 Sensor working principle. Source [5] [4] 7
1.9 t:slim X2™ Insulin Pump Predicts and helps prevent lows with Basal-IQ™ Technology [6] 8
1.10 Basal-IQ Technology Working Principle [6] 8
1.11 Minimed 670G System. Source [7] 9
1.12 The change in the daily life of a patient after using the SmartGuard Technology. Source [7] 10
1.13 Eversense Continuous Glucose Monitoring SystemSource [8] 11
1.14 Eversense Sensor and System Working Principle. Source [9] 11
1.15 Smart Transmitter. Source [9] 12
1.16 Eversense App which allows users to set target glucose alert levels. Source [9] . 12
1.17 Principle of cell encapsulation technology. Source [10] 13
1.18 Principle of cell encapsulation technology. Source [11] 14
1.19 Principle of FRET. Source [12] 15

2.1 Electronic System configuration with the photodiode and photodetector with the cells in the Petri dish for *in vitro* monitoring of glucose stimulation based on FRET. 18
2.2 The working principle of the biological probe when excited with light of wavelength 430 nm emitting light respectively at 485 nm and 535 nm without and with glucose stimulation. 19

2.3 Homology modelling of the FRET probe in closed confirmation. 20
2.4 Key parameters for the selection of the photodetector. 21
2.5 Design choices for the selection of the photodetector. 22
2.6 S11059-01WT color sensor, Count value vs. illuminance (typical example). . . 23
2.7 Emission Filter used with the design employing a narrow band excitation LED, thus avoiding an excitation filter. 23
2.8 Typical peak wavelength vs. forward current. The typical spectral half-bandwidth is 14 nm. 24
2.9 The electronic components of the system with the photodiode (top) and photodetector (bottom). 24
2.10 *in vitro* demonstrator and its constituent components. 25
2.11 Petri dish with the glued cyclinder in the center hosting the cell culture medium and the INS-1E cells 25
2.12 Spectrometer with signatures of the excitation wavelength at 434 nm, emission wavelengths, buried at 485 nm and visible at 535 nm. 26
2.13 Fluorescence characterization with Fluospheres Polystyrene Microspheres. . . . 27
2.14 Spectrum showing the relative intensity levels of the excitation LED at 430 nm and the response of the F10 β-cells at 535 nm. 27
2.15 The INS1E cells fluoresence with the Edmond Optics bandpass filter atop. . . . 28
2.16 Stereomicroscopic (top, bottom) and fluorescent microscope view of F10 INS-1E pancreatic β-cell 2D culture 29
2.17 Stereomicroscopic (top, bottom) and fluorescent microscope view of F10 INS-1E pancreatic β-cell 3D culture 30
2.18 Photodetector counts of green and blue colors of 2D and 3D cell cultures for the F10 INS-1E β-cells and INS-1E β-cells control. 31
2.19 Green and blue photodetector counts vs time and ratio vs time. 32
2.20 Design Issues addressed from demonstrator one 33
2.21 *in vitro* platform with the Hamamatsu SW-00159 photodetector (PD), MIDOPT LP 470 optical filter, LUXEON 430 nm excitation LED, automated with National Instruments (NI) myRIO real time (RT) using LabView RT (real-time) (communication is performed using the I2C protocol), NI PXIe-1082e with the PXIe 4143 source measure unit (SMU) and PXIe 6361 DAQ. The hardware software co-designed system is fully autonomous. A photo-detector integration time of 493 ms was used per channel (R/G/B/IR). The excitation LED with a center wavelength of 430 nm with a FWHM of 20 nm was used. PD and LED: components of the *in vitro* demonstrator in a black printed circuit board to reduce the noise rising from auto-fluorescence. 34
2.22 Black PCB to reduce the auto fluorescence. 35
2.23 Green, blue counts for the continuous glucose monitoring experiment. 36
2.24 Ratio (Green counts /blue counts) for the continuous glucose monitoring experiment. 36

2.25 The relative percentage (%) change in the ratio (green/blue) for the F10 vs. INS-1E cells (black) , INS-1E cells without and with the LP470 filter (red), and F10 cells without and with the LP470 filter (blue): a 480% improvement in the ratio is observed for the F10 cells demonstrating the efficacy of the filter in mitigating the out-of-band noise and making the system selectively sensitive to the probe. 37

3.1 Spectromter showing the excitation LED spectrum alongside the emission wavelength at 535 nm and the 485 nm emission wavelength signal buried in the noise. 39
3.2 The Absorption Filter - Working Principle 41
3.3 BP505 Cyan Bandpass Filter. Source [13] 42
3.4 MIDOPT BP505 INS 1E Cells Blue and Green. 43
3.5 MIDOPT BP505 F10 Cells Blue and Green. 44
3.6 MIDOPT BP505 (F10 - INS1E) Counts for Blue and Green. 45
3.7 MIDOPT BP505 (Green - Blue) for both INS1E and F10 Cells. 46
3.8 MIDOPT BP505 (Green/Blue) Ratio for both INS1E and F10 Cells. 47
3.9 MIDOPT BP505 change in ratio with the filter for both INS1E and F10 cells. . 48
3.10 LP470 Light Yellow Longpass Filter. Source [14] 49
3.11 MIDOPT LP470 INS 1E Cells Blue and Green. 50
3.12 MIDOPT LP470 F10 Cells Blue and Green. 51
3.13 MIDOPT LP470 (F10 - INS1E) Counts for Blue and Green. 52
3.14 MIDOPT LP470 (Green - Blue) for both INS1E and F10 Cells. 53
3.15 MIDOPT LP470 (Green/Blue) Ratio for both INS1E and F10 Cells. 54
3.16 MIDOPT LP470 change in ratio with the filter for both INS1E and F10 cells. . 55
3.17 Fuji Angle Independent Tri Acetyl Cellulose Filter: Sharp Cut SC 46. Source [15] 56
3.18 Fuji Angle Independent Tri Acetyl Cellulose Sharp Cut SC 46 Filter pieces after detaching the masked out material. Source [15] 57
3.19 Fuji SC 46 INS 1E Cells Blue and Green. 58
3.20 Fuji SC 46 F10 Cells Blue and Green. 59
3.21 Fuji SC 46 (F10 - INS1E) Counts for Blue and Green. 60
3.22 Fuji SC 46 (Green - Blue) for both INS1E and F10 Cells. 61
3.23 Fuji SC 46 (Green/Blue) Ratio for both INS1E and F10 Cells. 62
3.24 Fuji SC 46 change in ratio with the filter for both INS1E and F10 cells. 63
3.25 Surface imperfections and mechanical stress causing non-linear material expansion around the edges of the filter. Source [15] 64
3.26 Fuji Angle Independent Tri Acetyl Cellulose Filter: Sharp Cut SC 48. Source [15] 65
3.27 Fuji SC 48 INS 1E Cells Blue and Green. 66
3.28 Fuji SC 48 F10 Cells Blue and Green. 67
3.29 Fuji SC 48 (F10 - INS1E) Counts for Blue and Green. 68
3.30 Fuji SC 48 (Green - Blue) for both INS1E and F10 Cells. 69
3.31 Fuji SC 48 (Green/Blue) Ratio for both INS1E and F10 Cells. 70
3.32 Fuji SC 48 change in ratio with the filter for both INS1E and F10 cells. 71

3.33 Kodak Wratten 2 Filter 72
3.34 Kodak Wratten 2 Filter: INS 1E Cells Blue and Green. 73
3.35 Kodak Wratten 2 Filter: F10 Cells Blue and Green. 74
3.36 Kodak Wratten 2 Filter: (F10 - INS1E) Counts for Blue and Green. 75
3.37 Kodak Wratten 2 Filter: (Green - Blue) for both INS1E and F10 Cells. 76
3.38 Kodak Wratten 2 Filter: (Green/Blue) Ratio for both INS1E and F10 Cells. . . 76
3.39 Kodak Wratten 2 Filter: change in ratio with the filter for both INS1E and F10 cells. 77
3.40 The Dichoric Filter - Working Principle 78
3.41 Laser Components Triband Dichoric Filter 78
3.42 Laser BP Filter: INS 1E Cells Blue and Green. 79
3.43 Laser BP Filter: F10 Cells Blue and Green. 80
3.44 Laser BP Filter: (F10 - INS1E) Counts for Blue and Green. 81
3.45 Laser BP Filter: (Green - Blue) for both INS1E and F10 Cells. 82
3.46 Laser BP Filter: (Green/Blue) Ratio for both INS1E and F10 Cells. 83
3.47 Laser BP Filter: change in ratio with the filter for both INS1E and F10 cells. . . 84
3.48 Comparison results of the optical filter characterization. 85
3.49 Final selected filter LP 470 with the offset correction. 86
3.50 Optimal operating point for the design. 87
3.51 Excitation LED Effect on the SNR of the G/B ratio. 88

4.1 F10 Cell Count Characterization. 92
4.2 F10 Cell Growth/Death Characterization. 93
4.3 Cell counts as a function of time with change in temperature. 94
4.4 Polynomial fit (red) of the temperature, blue, green counts and ratio. It can be seen the model fairy accurately traces the locus of the evolution of the counts,ratio and temperature with the change in the time. 95
4.5 Temperature profile - Residual Plot. 97
4.6 Blue Counts F10 cells - Residual Plot. 98
4.7 Green Counts F10 cells - Residual Plot. 99
4.8 Ratio Green/Blue Counts - Residual Plot. 99
4.9 Loss of fluorescence at high light intensities and exposure times. 100
4.10 Loss of fluorescence at high light intensities and long exposure times. 101
4.11 Loss of fluorescence for the same measurement conditions after exposure to high intensity light for long duration. 102
4.12 Distinguishing cell response for KRBH solution vs Cell Culture Medium. . . . 103
4.13 Green Counts: Oxygenation with a stirring magnet for Glucose and KCL stimulation. 104
4.14 Blue Counts: Oxygenation with a stirring magnet for Glucose and KCL stimulation. 105
4.15 Ratio (Green/Blue): Oxygenation with a stirring magnet for Glucose and KCL stimulation. 106
4.16 Continuous Glucose Monitoring for 18 hours. 107

4.17 Continuous Glucose Monitoring: Observe the average response of the F10 cells for every glucose stimulation. 108
4.18 Continuous Glucose Monitoring: Observe the average response of the F10 cells for every glucose stimulation. 109
4.19 Glucose Pulse Stimulation alternating between 11 mM Glucose of the cell culture medium and KRBH with 0 mM Glucose. Green and Blue Counts. 110
4.20 Glucose Pulse Stimulation alternating between 11 mM Glucose of the cell culture medium and KRBH with 0 mM Glucose. Cytosolic Ca2+ Ratio Green/Blue. . . 111

5.1 The Clarke Error Grid. Source [16] 114
5.2 Transimpedance Amplifiers (TIAs) Architectures. Source [17] 116
5.3 Cartoon Illustration of non-invasive glucose detection and monitoring (a) Image depicts the electrical impedance change that is used for the sensing principle for impedance spectroscopy (IMPS), (b) Image graphically shows the excitation of the glucose molecules inside the body and the reflected light being collected by the photo-detector. Source [18] 117
5.4 System Architecture with the Impedance and Multi-Wavelength NIRS detection blocks. Source [18] 118
5.5 Measurement setup and scenario for Glucose estimation using both IMPS and mNIRS. Source [18] 119
5.6 Artificial Neural Network (ANN) Data Combing Method . Source [18] 119
5.7 Results of the Glucose Estimation with the proposed system with 50 samples from one human volunteer (a) Prior to the ANN method (b) Results after 2 input ANN combination (c) Results after 4 input ANN combination. Source [18] . . 120
5.8 FPG and 2h-Glucose Range of modern CGM (Continuous Glucose Monitoring) devices with clinical interpretation 122
5.9 Architecture of the Trans-impedance Amplifier Based Glucose Readout System 123
5.10 Equivalent Circuit for a Photodiode 124
5.11 Complete OTA Circuit with the Output Stage 125
5.12 Differential Pair with Cross-Coupled Load 126
5.13 Small Signal Equivalence Circuit for the Differential Pair with Load 127
5.14 Small Signal Equivalence Circuit for the second stage of the Amplifier 127
5.15 Small Signal Equivalent Circuit for the output stage 128
5.16 Bode plot of the designed amplifier in open loop 129
5.17 Schematic of the photo-diode Amplifier with additional C_f for stability 129
5.18 Bode Plot for the closed loop Photodiode Amplifier 130
5.19 Noise Function of the closed loop Photo-diode Amplifier 131
5.20 Apple iWatch 4 with its optical based sensor for heart BPM monitoring. Source [19] 132
5.21 Apple Patent System Diagram. Source [20] 133
5.22 Apple Patent: Logical sequence of operations. Source [20] 134
5.23 Measurement phases: calibration phrase and the measurement phase. Source [20] 135

5.24 Drifting of the zero level due to long measurement phases. Source [20] 135
5.25 System diagram with the different components. Source [20] 136

List of Tables

4.1 Coefficients for the polynomial fit of the temperature and ratio. 96
4.2 Coefficients for the polynomial fit of the green and blue counts with respect to change in temperature over time. 96

5.1 Relevant values for the different glucose tests [5] [8] 121
5.2 Performance of the Photodiode Amplifier 131

1 Introduction

1.1 Diabetes: its prevalence, cost and trends on a global scale

There is a plethora of research dedicated to the detection and monitoring glucose in the body. Glucose detection, modulation and treatment of maladies such as diabetes are all still the holy grail both in research and the industry with a record number of products being approved by the FDA , CE, Swiss Medic approved products on the market. Diabetes remains a stubborn problem in the developed world and is a growing problem with the rise of middle class across geographies as shown in Figure 1.1.

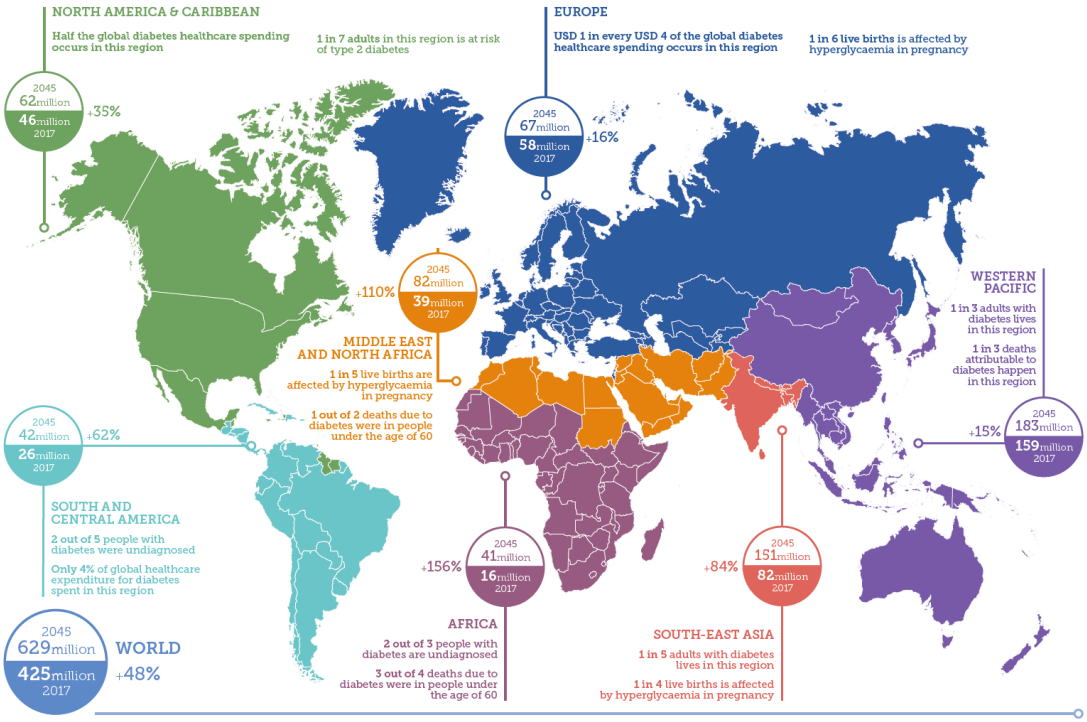

Figure 1.1 – Global Diabetes Atlas International Diabetes Federation. Source [1]

Given the propensity of obesity, health complications coupled with high diagnosis, as shown in Figure 1.1 half of the global spending of diabetes is in North America. In the European and Russian continents the spending on diabetes healthcare is comparable to that in North America. An increase in the access to wealth and a rising middle class has led to an increase in the consumption of fast food [1] as a huge population of people have access to a lot of wealth with spending power for the first time.

On the flip-side in the developed world, coupled by stagnant sedentary lifestyles the diabetes problem is aggrandized [1]. This combined effect can be seen in the spending on diabetes care with developing world accounting for 7 out of 10 countries in the global top 10 spenders as depicted by the Figure 1.2

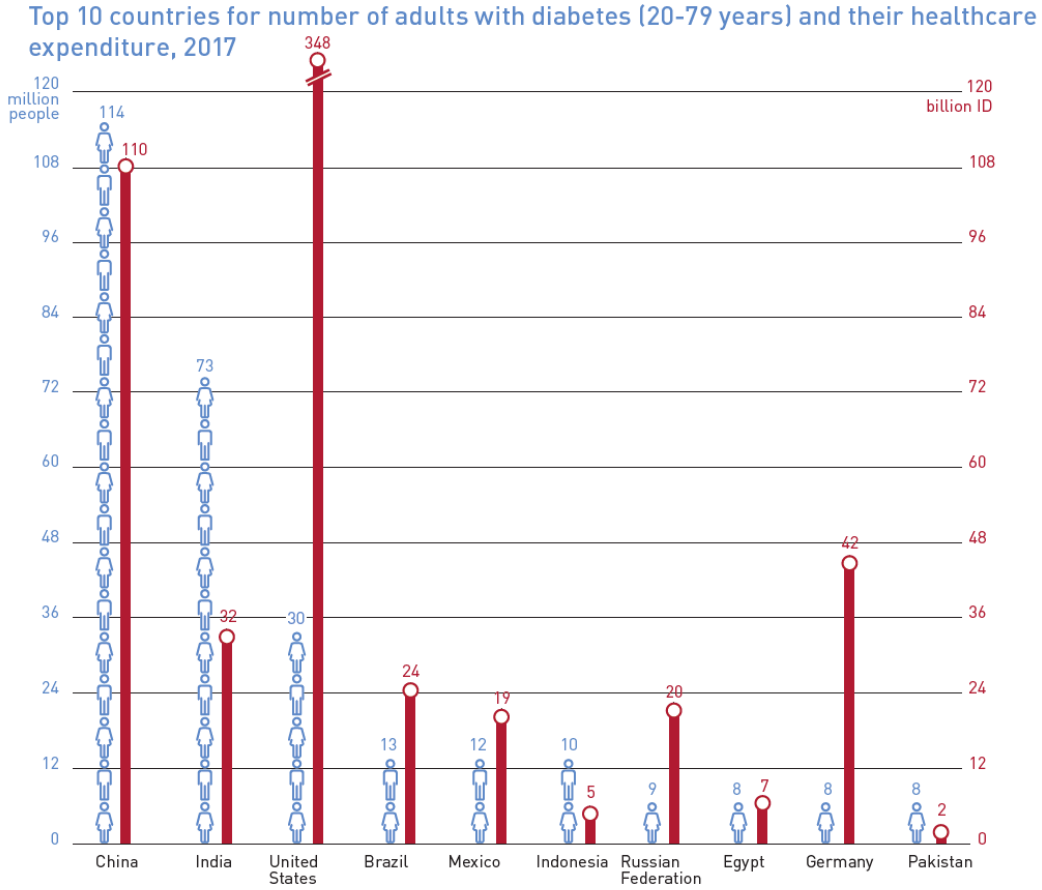

Figure 1.2 – The top 10 countries for number of adults with diabetes account for 60% of people with diabetes and 69% of global healthcare expenditure on diabetes. Source [1]

It can be seen in Figure 1.1 that 2 out of 5 people in South America live with diabetes undiagnosed and this number is gloomier in Africa with 2 out of 3 people undiagnosed, leading to a startling 3 out of 4 deaths due to diabetes in people under the age of 60. In the developing world 20% of the population of India lives with diabetes (approximately 260 Million people) and about 30% of adults in China, Japan and Australia live with diabetes [1]. In-fact 4 out 5 people with diabetes in

the world between ages 20 and 79 years live in low- and middle-income countries as shown in Figure 1.3.

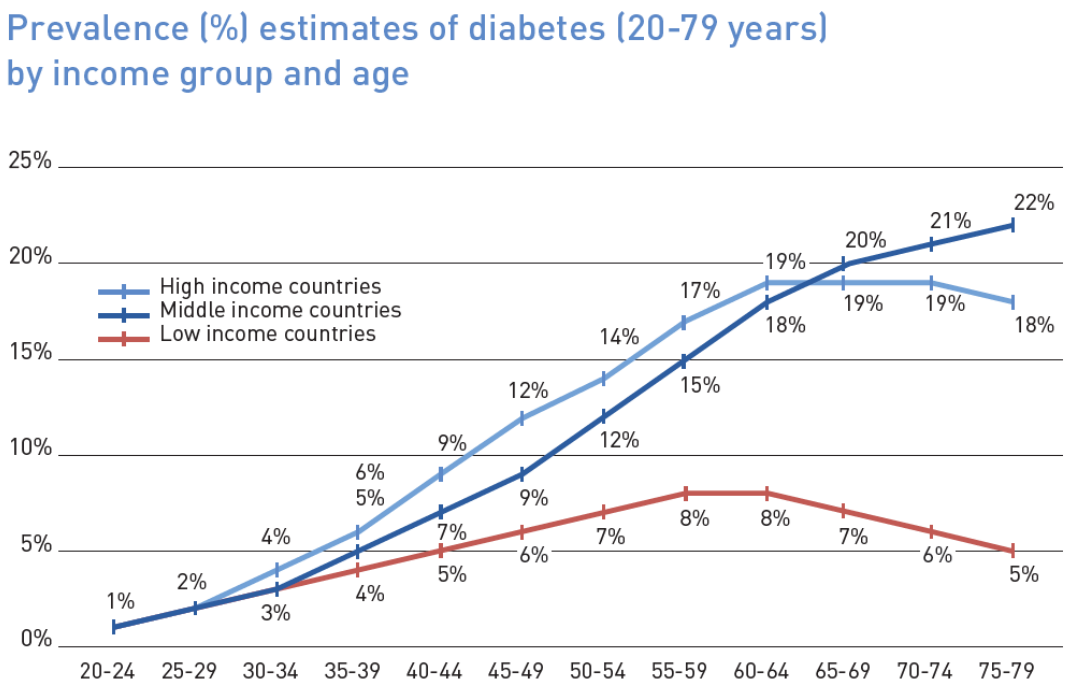

Figure 1.3 – 4 out of 5 people with diabetes live in low- and middle-income countries. Source [1]

This calls for scalable technological solutions for prevention of diabetes and for early pre-screening and diagnosis of diabetes in the developing and low income global South. The pre-screening technologies along with technologies to alleviate the lifestyle and make patient and general populations more aware of lifestyle choices in North America and Europe.

As shown in the startling numbers in Figure 1.4 more than half the people in the world with diabetes do not know that they have the disease. Microelectronic system coupled with glucose sensors and the rise of artificial intelligence (AI) based on portable and low-cost wearable devices indeed offer a hope. This part of the work in this thesis addresses a crucial electronic building block in this direction.

There are a number of startups around the globe and several research labs trying to find innovative solutions for diabetes. However, there are very few products that have been approved by FDA to be medically safe in the last 40 years [21]. Looking at the state of the art from the last 3 years, we see a spike in approval of glucose detection, sampled and continuous monitoring devices and system in the year 2018.

There are also closed-loop systems with insulin injection pump systems, automated with smart algorithms to predict glucose lows. These devices allow patients who suffer from diabetes to set their minds free and let them carry their day-to-day tasks with ease as they are predictably alerted

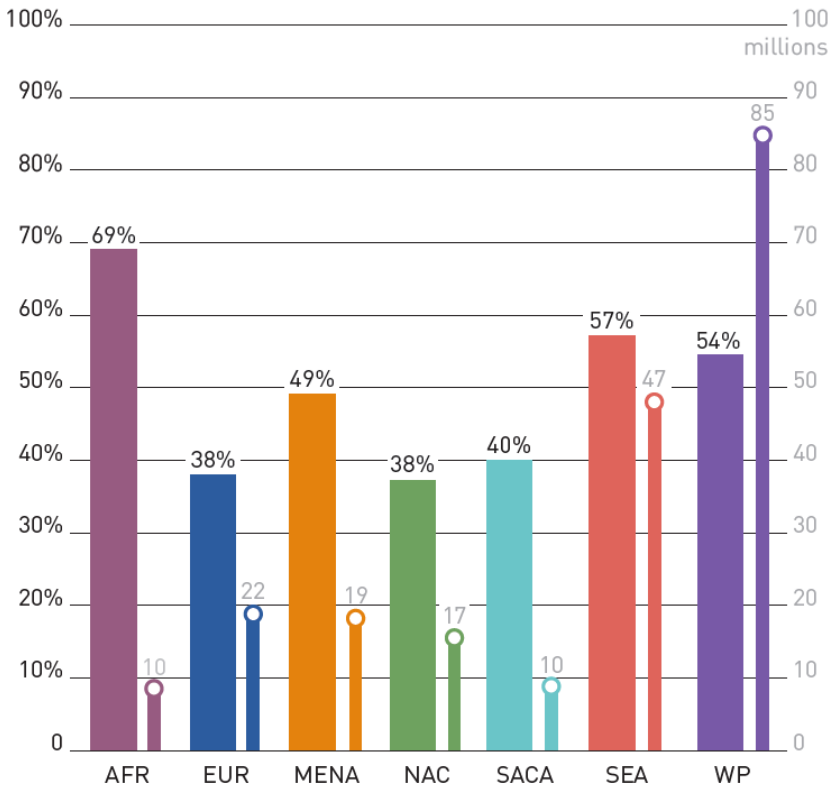

Figure 1.4 – Undiagnosed percentage and undiagnosed cases of diabetes (20-79 years) by region. Legend (AFR: Africa, EUR: Europe, MENA: Middle East and North Africa, NACA: North America and Caribbean, SACA: South and Central America, SEA: South East Asia, WP: Western Pacific). Source [1]

of a glucose low. These are summarized below to set the broad stage for different methods of glucose detection and monitoring.

1.2 FDA approved glucose detection and monitoring devices

1.2.1 MiniMed 630G System with SmartGuard

The Medtronic MiniMed 630G system was approved by the FDA as a new indication to allow the insertion of the sensor into the upper arm of the patient [2]. Together with the SmartGuard the MiniMed 630G functions as a closed-loop system for monitoring the glucose level and automatically adjusting the delivery of the basal insulin level pertinent to the glucose reading levels. It has the capability to continuously measure the glucose of the patient and automatically adjust the insulin delivery for 7 days with the aid of a glucose meter for calibration. The device is capable of adjusting the insulin boluses with the insulin pump up when the glucose level goes

high, and can either lower or stop insulin delivery when the glucose levels go low [2].

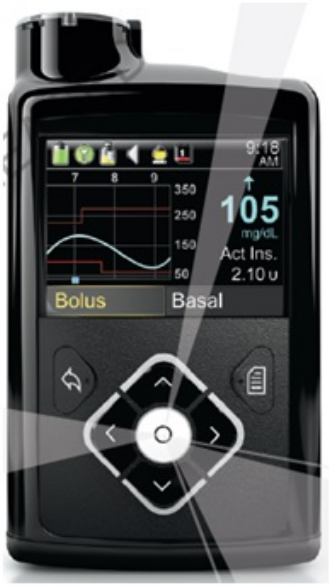

Figure 1.5 – MiniMed 630G System with SmartGuard P150001/S021. Source [2]

1.2.2 Guardian Connect System

The Medtronic Guardian Connect System was approved by the FDA in March 2018 [22]. This is essentially a continuous glucose monitoring system (CGM) comprising of three parts that measure and display the sugar (i.e. glucose) level periodically every 5 minutes with its Guardian sensor, transmits this information via the wireless transmitter called the Guardian Connect Transmitter to its app, the Guardian Connect app, on a smart phone and displays the glucose levels. The three components are shown below in the figure 1.6. Shown on the left in Figure 1.6a is the guardian connect system with the sensor that is inserted through the skin and measures the blood glucose levels in the tissue fluid [23]. It is recommended to be inserted either in the arm or the abdomen [22].

The device can be used by Type I and Type II diabetes patients and its main aim is not to replace the finger prick test method but rather monitor blood sugar patterns in order to know when to perform the finger prick test. The device manufacturer does not claim to use this sensor data for therapy. Since the system displays information on the mobile phone, it is intended for people who are able to hear and see the notifications and alerts set out by the Guardian Connect app [22]. Since the sensor is implanted, it is not recommended to expose it to Magnetic Resonance Imaging (MRI), diathermy services, equipment or devices that generate a strong magnetic field such as x-ray, CT (computed tomography) scan or any similar device as this may cause a device transmitter malfunction.

The artifact from common medicines such as paracetamol, Tylenol that reduce cold and fever

respectively is a false indication of raise in the blood glucose level. The inaccuracy level, dependent on the quantity of acetaminophen or paracetamol active in the body is different for various individuals. This can thus be seen as a disadvantage of this system as these chemicals react with the implanted sensor and give a false alarm [22] [23].

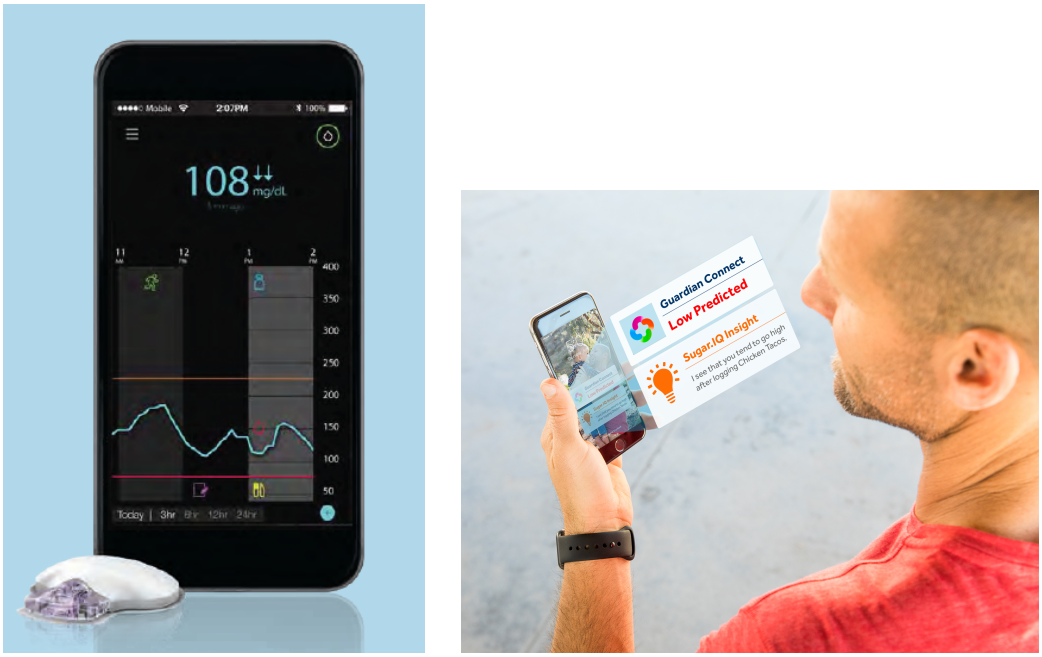

(a) Guardian Connect sensor and app

(b) Guardian Connect app

Figure 1.6 – Medtronic Guardian Connect System P160007. Source [22] [23]

1.2.3 Freestyle Libre Flash Glucose Monitoring System

In the middle of 2018 on July 23, the FDA approved Abbott Diabetes Care Incs 'Freestyle Libre Flash Glucose Monitoring System' shown in Figure 1.7 [4] [5]. This system is meant to be a replacement for the glucose prick test and here the onus of making the glucose test is totally on the patient [5]. The patient triggers the onset of a test every-time and there is no automated test done by the device nor is there any automated logging of data or any kind of indication such as a message or alarm based on the glucose level [4]. As shown in Figure 1.7a, the sensor is meant to be used only for 14 days, and its different components namely the sensor applicator, sensor pack, sensor and the reader are shown in Figure 1.7.

The sensor is worn by the patient in the upper arm for example and a small needle style wire goes through the skin (Figure 1.8) and measures the interstitial glucose level as a function of an electrical stimulus to it [3]. This electronic signal is converted into a digital value which corresponds to a certain level of glucose, and then transmitted to a mobile device that acts as the reader, which can readout signals when placed at a short distance above the sensor [5]. These glucose readings can be used to classify the types of foods that have to be consumed and track

(a) 14 days use system package (b) System components of the FreeStyle Libre System

Figure 1.7 – Freestyle Libre Flash Glucose Monitoring System - P160030/S017. Source [3] [4]

lifestyle habits that lead to hypoglycemia (low glucose) and hyperglycemia (high glucose). It can of course, be used as an indicator to administer insulin [4]. However, the device can only be used by a prescription from a doctor [4].

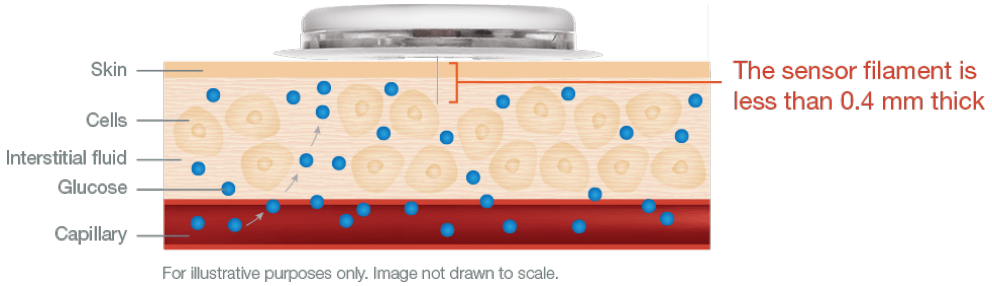

Figure 1.8 – Sensor working principle, showing the trans-cutaneous sensor filament implant though the skin. Source [5][4]

1.2.4 t:slim X2 Insulin Pump with Basal-IQ Technology - P180008

The Insulin Pump with Basal-IQ Technology P18008 was approved in the year 2018. It is an insulin bolus delivery pump based on Basal-IQ technology [24]. Its user interface is extremely easy to use and setting insulin delivery number is seamless. It is a small durable insulin pump with a sleek slim design that makes it robust and also durable as its body is made out of aluminum as shown in Figure 1.9. The user can easily conceal this device and its also available in multiple design templates. The bright color display shows the blood glucose levels, which adjusts the insulin level automatically using algorithms. This allows the body to maintain the glucose within predefined ranges.

The user is well informed as there is a complete display of glucose levels, ongoing trends, alterations on the device, alarms and also information on the infusion pump. The CGM system measures the glucose in the body every 5 minutes with the help of the Basal-IQ technology and proactively predicts if the glucose level will fall too low within the next 30 minutes or if the current glucose levels is already too low as shown in Figure 1.10 [6]. Therefore, the t:Slim X2 Insulin Pump with Basal Technology works by measuring the glucose levels and automatically either

Figure 1.9 – t:slim X2™ Insulin Pump Predicts and helps prevent lows with Basal-IQ™ Technology [6]

temporarily suspends the administration of insulin or administers the necessary bolus [24][6].

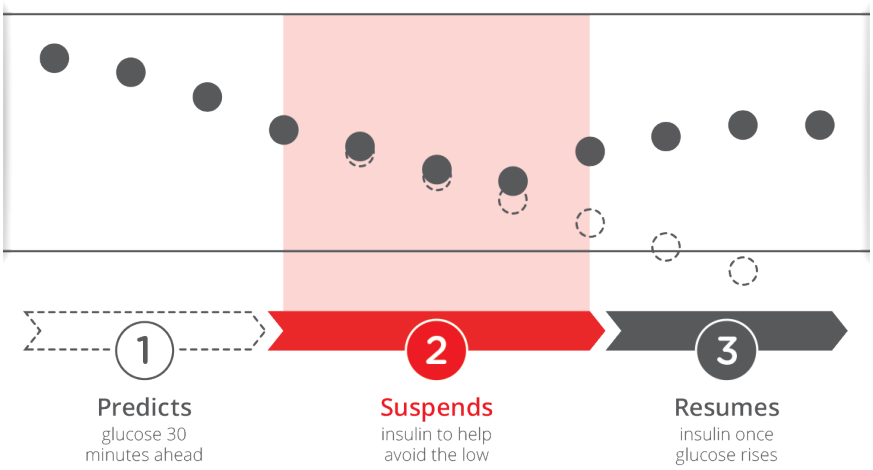

Figure 1.10 – Basal-IQ Technology Working Principle [6]

The t:Slim X2 Insulin Pump with Basal-IQ Technology system [24][6] is intended for people who are six years old or more, suffering from diabetes to continuously deliver basal insulin at user set rates and configurable insulin bolus amounts. It can also be used concomitantly with insulin pumps other than the Dexcom G5 Mobile CGM. The use of this system necessitates a doctor's prescription and is valid for use only with NovoLog or Humalog U-100 insulin. The onus of this system is that its not recommended for patients whom visual or hearing senses hinder the recognition of System alerts. It is also not recommended (Reference: [6]) for patients who are either unable to or unwilling to:

(a) Self test their glucose levels at a periodicity set by the physician

(b) Preferably show that they have adequate carbohydrate counting skills

(c) Hold minimum self-care skills for diabetes

(d) Consult with their health-care professional on a regular basis

1.2.5 MiniMed 670G System - P160017/S031

In June 2018 Medtronic Inc had another FDA approval for their MiniMed 670G System [25], which is vouched to be the first hybrid closed-loop system capable of monitoring glucose and automatically adjusting the delivery of insulin through the insulin pump. The unique update in the design and approval of this device is that it is suitable for users 7 years old and more [25], which is an update from a similar approval granted by the FDA in the year 2016 for the P160017 which was suitable for users of age 14 years and older. The Medtronic MiniMed 670G system consists of three parts, the continuous glucose monitor (CGM) for measuring glucose for up to seven days, an insulin pump for delivering boluses of insulin to the user and a glucose meter used for calibrating the CGM system as shown in Figure 1.11.

Figure 1.11 – Minimed 670G System. Source [7]

The MiniMed 670G system is capable of automatically injecting insulin if it senses that the glucose level is very high and on the contrary also capable of stopping insulin delivery if it detects a low glucose level [7]. The advantage of this is that it is totally autonomous freeing the user from the onus of worrying about constantly monitoring and adjusting their insulin pump. This system also relies on an invasive method and consists of a wire that is inserted through the skin to measure the blood glucose levels from the tissue fluids. The measured glucose levels are

transmitted via a wireless signal to the insulin pump and the information is also displayed on the device screen with the alerts, trends and alarms.

The system has two modes namely Manual Mode and Auto Mode. In Manual Mode the system can be programmed by the user to administer a basal insulin level while in the Auto Mode the system automatically adjusts or suspends the basal insulin delivery [7]. An use case of the improvement in the glucose trends of a user of this system is shown in Figure 1.12. As seen in the figure the glucose is 70% of the time in range as opposed to 52% before using the system [7].

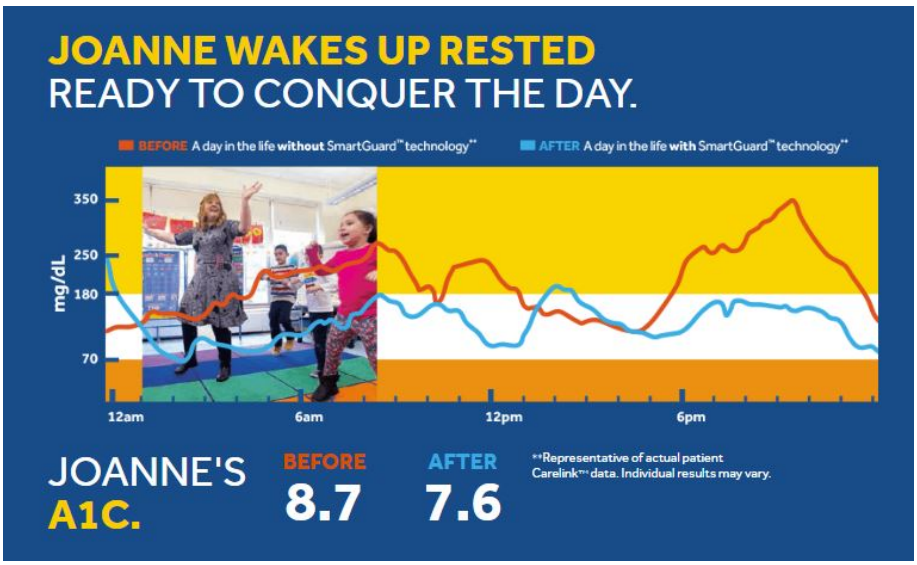

Figure 1.12 – The change in the daily life of a patient after using the SmartGuard Technology. Source [7]

Like many systems this FDA-approved closed-loop system claims not to replace direct insulin delivery therapy systems but only provides an indicator for when the glucose measurements ought to be made [25]. The clinical trial done for the FDA approval of this device consisted of a batch of 123 people who were medically diagnosed with Type 1 diabetes. The protocol for the clinical trial entailed that Medtronic MiniMed 670G System not be used in the first two weeks of the trail followed by a three-month duration during which the system with its complete hybrid loop was used by the cohort as frequently as possible. The outcome was that it was deemed safe for patients with age 7 and above suffering from Type 1 diabetes.

1.2.6 Eversense Continuous Glucose Monitoring System - P160048

In June 2018, the FDA approved Senseonics, Incs Eversense Continuous Glucose Monitoring System - P160048 [8]. The system can be used after a prescription is issued by a medical doctor and can monitor the glucose at a periodicity of 5 minutes in real-time for a duration of up to 90 days [8]. The system consists of three parts as shown in Figure 1.13 [8]. These are the implanted sensor, transmitter and the mobile application (app) for displaying the information.

Figure 1.13 – Eversense Continuous Glucose Montioring System. Source [8]

This is an implantable system that works based on florescence light signal that is generated when glucose binds to the chemically coated surface [9]. The light is mapped to an apposite level of glucose and transmitted using a built in wireless system as shown in Figure 1.14a [9].

(a) Sensor (b) Operating Principle based on Optical Detection

Figure 1.14 – Eversense Sensor and System Working Principle. Source [9]

The Eversense sensor is implanted by a licensed physician below the skin of the user as shown in Figure 1.15 [9]. The sensed glucose is transmitted to the transmitter patch attached outside the skin of the user and then via Bluetooth to a smartphone or smart watch as shown in Figure 1.13 [9].

The mobile Eversense app is capable of predicting and altering the user of both hypoglycemia and hyperglycemia events [9]. The settings in the Eversense mobile app can be programmed by the user to set these custom user specific levels for highs and lows as shown in Figure 1.16. The app also allows addition of information such as meals, insulin dosages, exercises and times when blood glucose measurements were performed. The data log from this device can aid physicians to adjust the therapy.

However, this device is not intended to replace a standard blood glucose test, such as a finger prick method for instance.

The Eversense sensor is essentially comprised of 4 main parts, the chemically coated surface for glucose binding, an LED to excite the fluorescence bound glucose sensing membrane, a photo readout detector and a wireless antenna system [9]. This system is one of the only devices

Figure 1.15 – Smart Transmitter. Source [9]

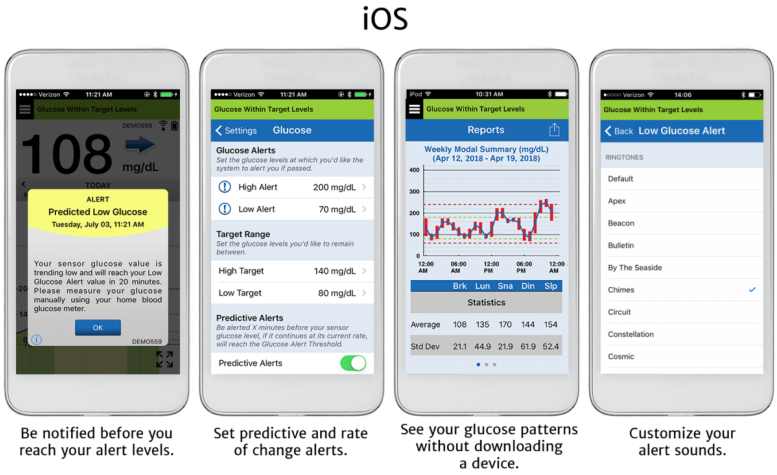

Figure 1.16 – Eversense App which allows users to set target glucose alert levels. Source [9]

approved by the FDA recently that uses light as a part of its sensing mechanism. Regarding the other approved devices, all of them measure glucose with the aid of an electrode through electro-chemical reactions. In the scope of this thesis, this system is the closest in terms of its relevance from the design point of view.

1.3 Cell Encapsulation Technology

Cell encapsulation is a technology that exists since early second half of the 20 th century, obviating drugs and medicines, toning down the human body immune system assault when a transplanted organ is surgically implanted. The underlying principle is to encapsulate the cells all around with a semi-permeable membrane that facilitates the exchange the nutrients that have a size less than the holes of the porous membrane. It also allows oxygenation of the cells which is quintessential

for the functioning of the cells as it prevents cell mortality.

Most importantly it provides a defensive barrier for all the harmful molecules that can be unleashed by the immune system when foreign cells are implanted in the body. The aforementioned features are all depicted in Figure 1.17. The size, material and texture of the pore are therefore key parameters.

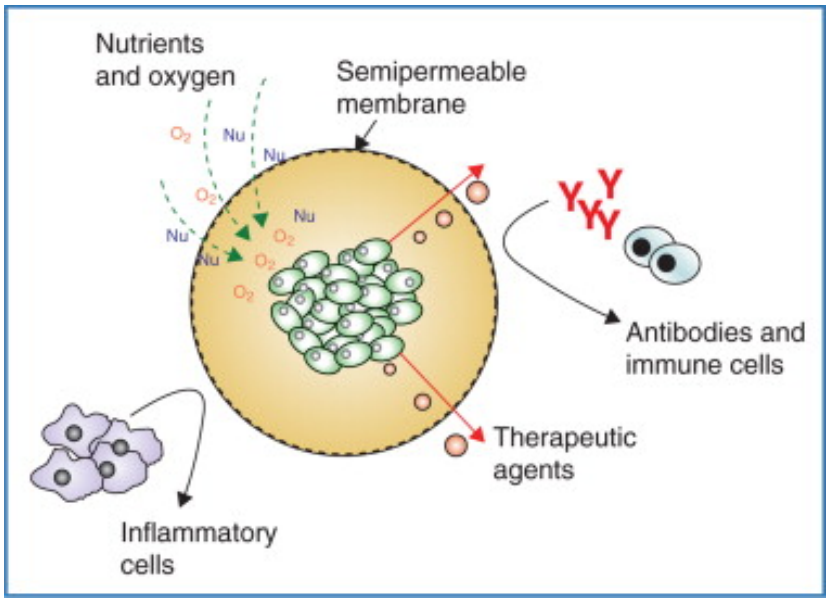

Figure 1.17 – Principle of cell encapsulation technology. Source [10]

Cell encapsulation holds a great promise for the detection, monitoring and treatment of diseases such as diabetes [26] [27] [28] [29]. Several examples of pancreatic beta cell encapsulation that were successful have proven this even more and this indeed open up a slew of possibilities for both research and going towards the development of artificial pancreas [11] [30] [31]. There are several microfluidic, microgel and microneedles platforms designed and tested that show the promise of cell encapsulation technology [32] [33] [34] [35].

Shown in Figure 1.18 is an example of the Encaptra drug delivery system in which the pancreatic beta-cell islets are concealed in a semi-permeable barrier based membrane. This membrane guards the cells from the immune cells, allows glucose, oxygen and other nutrients to enter the capsule and allows the production of the insulin and gamut of necessary hormones to treat diabetes.

This open up the space for using the cells as both a biosensor and closed loop remedy agents. Coupled with techniques like fluorescence resonance energy transfer (FRET) we can make an optical cell-based biosensor that can be used for several biological applications related to diabetes.

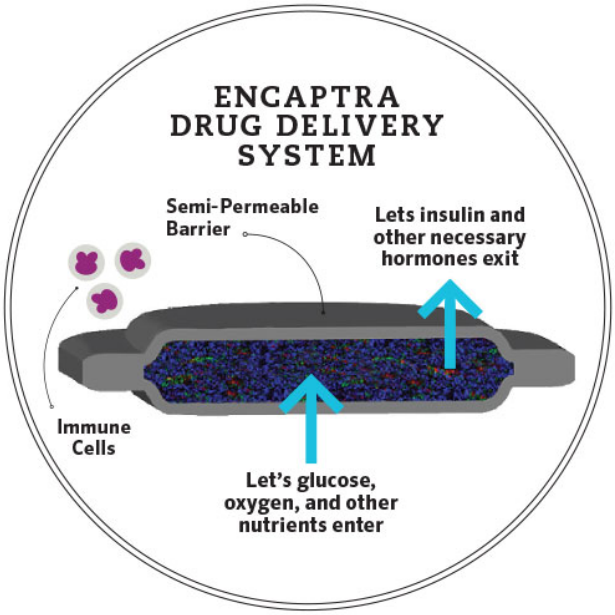

Figure 1.18 – Principle of cell encapsulation technology. Source [11]

1.4 Fluorescence resonance energy transfer FRET

FRET is based on the non-radiation based energy transfer between two molecules [36] which are proximal in distances about (10 – 100) A°. Upon specific optical wavelength excitation of the donor molecule in the presence of an acceptor molecule in a proximal spatial distance [37], the acceptor absorbs the energy from the donor and emits light at another wavelength. The efficiency of the FRET emission is inversely proportional to the 6^{th} power of the distance between the donor and acceptor molecules as illustrated in Figure 1.19.
Several biosensors and biological methods to detect cell activity using FRET have been reported in literature [38] [39] [40] [41]. A lot of nano-particle and nano-sensing bio-sensing platforms have shown promising results using the FRET mechanism [42] [41] [43]. Glucose sensing and pancreatic beta cell based FRET probes have been reported with varying degrees of glucose quantification [44] [45] [46] [47] [48] [49].

We use the FRET mechanism within the scope of our project and describe its role in the next section.

1.5 Outline and challenges of this work

The next chapters are organized into the design, implementation and testing of the in-vitro demonstrators. The selection of the electronic and optical parts are outlined in Chapter 2. Cell culturing is performed both in both 2D and 3D techniques are described in Chapter 2. The challenges for obtaining a good signal-to-noise (SNR) ratio whilst keeping a low power

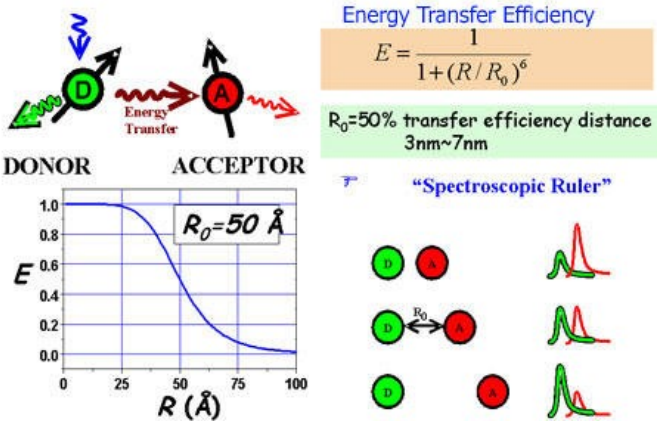

Figure 1.19 – Principle of Fluorescence resonance energy transfer (FRET). Source [12]

are outlined. These challenges are addressed at the system level through the optical sensor performance characteristic that is most conducive for this system in Chapter 3. Various optical filters were tested and characterized in great detail as described in Chapter 3. This is the major bulk of the work. The biological experiments that were carried out using the chosen filter are described in great detail in Chapter 4. The panoply of biological measurements done with the built system using the pancreatic beta cells as the biosensor directly are explained in detail in Chapter 4. Finally an analog front-end amplifier design that was designed to achieve high-gain, simultaneously keeping the power low, is described with its small signal model and simulation results in Chapter 5.

2 *In vitro* demonstrators concept, design, implementation and testing

This work reports a compact bioelectronics system for sensing cytosolic Ca^{2+} influx *in vitro* for INS-1E pancreatic β-cells using a 430 nm excitation light. The cells emit light based on a genetic probe using a FRET mechanism. The system has a linear response and has been characterized for fluorescence for various intensities of light.

The system is sensitive for 2D cell cultures on normal Petri dishes. Forming cell aggregates using 3D cell culturing techniques increases the number of cells and thus enhances the signal quality 35x and 21x for green and blue lights, respectively.

The system has been able to continuously monitor the F10 INS-1E β-cells upon glucose stimulation, diazoxide injection and KCl injection, thus revealing insights on the cell response mechanisms. The system was subsequently improved, firstly in terms of performance, and secondly by making it totally automated for the measurement of glucose as described in the second part of this chapter.

2.1 Introduction

Biosensing platforms today face huge challenges in terms of their usability with respect to their life-time which is typically a couple of hours only [50]. Moreover, these biosensing platforms are invasive and spatially restrictive. In this thesis we address a pertinent challenge directed towards a Ca^{2+} imaging biosensor platform based on the Fluorescence Resonance Energy Transfer (FRET) imaging technique. FRET is a non-radiative method of energy transfer between a donor and acceptor which are in a close conformation spatially and have overlapping absorption and emission spectra [36].

A pancreatic β-cell line with an engineered FRET probe is used. The designed electronic system is used to excite the cells with a sharp bandpass blue light centered at a wavelength of 430 nm. In the absence of Ca^{2+} ions, the β-cells emit light at a wavelength centered at 485 nm as there is no energy transfer through FRET [51] [52]. Conversely, the presence of Ca^{2+} ions causes the

β-cells to emit light at a wavelength centered at 535 nm. The FRET probe relies on a ratio-metric principle, thus elucidating the trend of the Ca^{2+} ions uptake in the cells. This emitted light at the two wavelengths of 485 nm and 535 nm is captured by an ultra-low power RGB color sensor from Hamamatsu. Excitation light filtering is a major concern in optical light based biosensors, and also impairs our system performance due to the overlap of the spectra in the blue wavelength. In order to mitigate this effect we have used custom diced emission filters from Edmund Optics in our design.

2.2 System Level Principle

To continuously follow INS-1E beta-cells function *in vitro*, intracellular Ca^{2+} is a good indicator since it is closely linked to glucose stimulation and insulin secretion. Upon glucose stimulation, cytosolic Ca^{2+} rises, which causes insulin secretion. To monitor cytosolic Ca^{2+}, a genetic FRET probe is used, featuring an excitation wavelength at 430 nm and two emission wavelengths at 480 nm and 535 nm. The miniature fluorescence sensor based on a LED and a RGB photodiode is placed under the cell culture as shown in Figure 2.1.

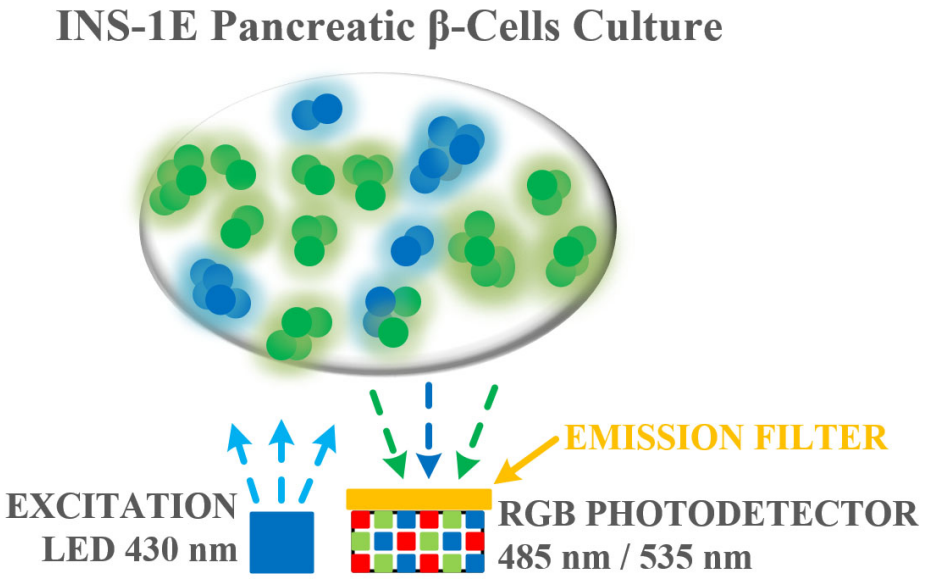

Figure 2.1 – Electronic System configuration with the photodiode and photodetector with the cells in the Petri dish for *in vitro* monitoring of glucose stimulation based on FRET.

As illustrated in Figure 2.2, the absence of glucose inhibits any rise in the Ca^{2+} ions in the cells. A depletion of Ca^{2+} ions in the cells prevents the ECFP (Cyan Fluorescent Protein) and cpV (Yellow Fluorescent Protein) molecules from transferring energy through FRET. Upon stimulating the cells with glucose the ECFP and cpV complexes are spatially conformed in a distance less than 10 nm. With the excitation of this Ca^{2+} bound complex at 430 nm there is a FRET transfer from the ECFP to cpV leading to the emission of light around a wavelength of 535 nm [51].

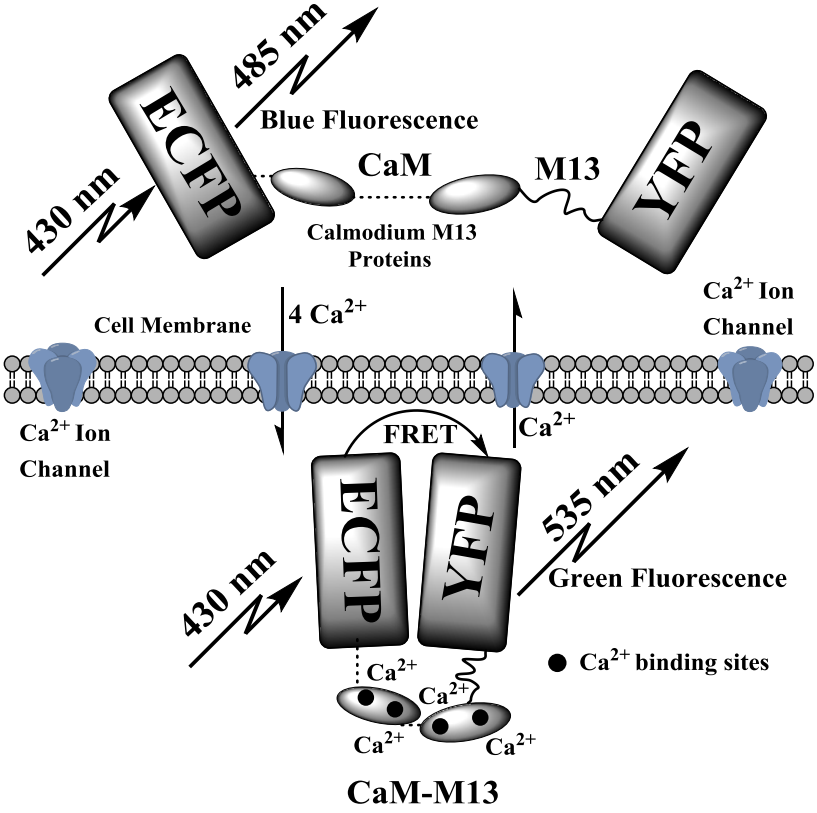

Figure 2.2 – The working principle of the biological probe when excited with light of wavelength 430 nm emitting light respectively at 485 nm and 535 nm without and with glucose stimulation.

2.2.1 Protein structure homology modelling

Four [Ca^{2+}] ions bind to the Calmodium protein at the four distinct binding sites as shown in Figure 2.3. The bound [Ca^{2+}] induce a conformational change of the fusion protein complex by wrapping the Calmodium around the M13 domain. This brings ECFP and YFP proteins in proximity of less than 10 increasing the FRET efficiency.

The 3D protein model was built by using the structural information of the CaM-M13-YFP calcium sensor protein data bank ID (PDBID) 3078 and structural information of enhanced cyan fluorescent protein physiological pH, PDBID 2WSN [53].

The structures were connected through a peptide linker sequence (GTGGSGGGTGGSGGGT) [52]. The model for FRET sensor in [Ca^{2+}] bound conformation was generated by Protein structure homology modelling using the SWISS-MODEL server.

The wavelengths of interest are in the blue-green regime of the light spectrum. The development of a compact electronic system for detecting the level of light in the cells entails the need of such a RGB photodetector. To control such a photodetector in a flexible way, a microcontroller must be implemented.

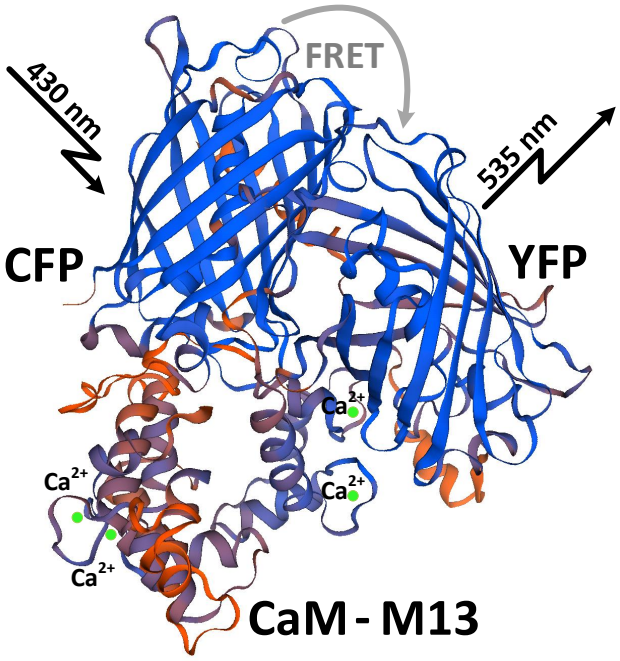

Figure 2.3 – Homology modelling of the FRET probe in closed confirmation.

2.3 Photodetector Selection

Within the scope of this thesis, our objective was to build an electronic system in order to validate the proof-of-concept of the cell based biosensor. The priority therefore was not to build a full custom analog front end read out, along with the analog-to-digital converter, on board memory and mixed signal blocks such as the SPI or I2C interfaces. Our goal was to select the best available integrated circuit that matched a majority of our application requirements. The key parameters for the selection of the photodetector as shown in Figure 2.4 are:

- Interface: Photodetectors can either be fully analog with a voltage or current output or be smart sensors with a built in digital interface protocols such as SPI or I2C. From the perspective of saving design time and complexity a fully digital smart photodetector is preferable.
- Area: The area of the photodetector is directly proportional to its sensitivity. A larger area can integrate more photons, while a smaller area is less sensitive as it can sense fewer photons. Larger areas are a constraint in-lieu of implantable system as they can easily run into several centimeters (cm) which makes them impractical. Also most large area photodetectors have an analog output making the system design complicated with the need to integrate extra analog processing circuitry. Digital RGB pixel based photodetectors are usually compact and more suitable for their area and simplicity.
- Sensitivity: The sensitivity of the photodetector is directly related to the area and its ability

Figure 2.4 – Key parameters for the selection of the photodetector.

to detect photons in the wavelengths of interest for our application. The sensitivity is also related to the amount of amount of excitation power needed from the excitation LED in-order to have the blue and green wavelength components successfully distinguished and detected with the least power.

- Weight: The weight of the photodetector is a flexible requirement for *in vitro* applications, however, for bio-implantable systems the weight plays an important role in the selection of the photodetector as the overall weight of implants should be within ten percent of the weight of the mice.

Based on the above four design parameters, several smart photodetector ICs were identified. Most of these ICs did not fit with the specifications of the cell based biosensors wavelength of interest.

The photodetectors of Hamamatsu were good candidates and they have been compared in detail in Figure 2.5.

The analog S9032-02, S9702, S10917-35GT and S10942-01CT photodetectors were not preferred as they would add additional complexity with respect to the area and weight that would come be needed with the interfacing electronics.

Among the digital photo ICs, S9706, S11012-01CR, S11059-02DT/-03DS and S11059-01WT, the former two ICs offered a larger sensitivity were rejected owing to their big areas. The latter two ICs namely S11059-02DT/-03DS and S11059-01WT had smaller areas.

The S11059-02DT/-03DS was rejected as its plastic package increased the area and the weight of the overall system. The S11059-01WT, though having slightly lower sensitivity than S11059-02DT/-03DS, was selected owing to its compact size and ease of placing the optical filter directly

atop the photodetector.

Thus area, weight and digital interface were traded for sensitivity in this design.

Type no.	Type	Photosensitive area size (mm)	Package (mm)	Peak sensitivity wavelength (nm)	Photosensitivity						Photo
S9032-02	Photodiode	ϕ2.0	4 × 4.8 × 1.8^t 6-pin (filter 0.75^t)	B 460 G 540 R 620	B G R	0.18 (A/W) [λ=460 nm] 0.23 (A/W) [λ=540 nm] 0.16 (A/W) [λ=620 nm]					
S9702	Photodiode	1.0 × 1.0	3 × 4 × 1.3^t 4-pin (filter 0.75^t)	B 460 G 540 R 620	B G R	0.18 (A/W) [λ=460 nm] 0.23 (A/W) [λ=540 nm] 0.16 (A/W) [λ=620 nm]					
S10917-35GT	Photodiode	1.0 × 1.0	3 × 1.6 × 1.0^t COB (on-chip filter)	B 460 G 540 R 620	B G R	0.2 (A/W) [λ=460 nm] 0.23 (A/W) [λ=540 nm] 0.17 (A/W) [λ=620 nm]					
S10942-01CT	Photodiode	1.0 × 1.0	3 × 1.6 × 1.0^t COB (on-chip filter)	*	B G R	0.21 (A/W) [λ=460 nm] 0.25 (A/W) [λ=540 nm] 0.45 (A/W) [λ=640 nm]					
S9706	Digital photo IC	1.2 × 1.2	4 × 4.8 × 1.8^t 6-pin (filter 0.75^t)	B 465 G 540 R 615	Low B 0.21 (LSB/lx) G 0.45 (LSB/lx) R 0.64 (LSB/lx)			High B 1.9 (LSB/lx) G 4.1 (LSB/lx) R 5.8 (LSB/lx)			
S11012-01CR	Digital photo IC	1.2 × 1.2	3.43 × 3.8 × 1.6^t COB (on-chip filter)	*	Low B 0.3 (LSB/lx) G 0.6 (LSB/lx) R 1.4 (LSB/lx)			High B 2.6 (LSB/lx) G 5.3 (LSB/lx) R 12.9 (LSB/lx)			
S11059-02DT /-03DS	I^{2}C compatible color sensor	0.56 × 1.22	3 × 4.2 × 1.3^t 10-pin (on-chip filter)	B 460 G 530 R 615 IR 855	Low B 4.4 (count/lx) G 8.3 (count/lx) R 11.2 (count/lx) IR 3.0 (count/lx)			High B 44.8 (count/lx) G 85.0 (count/lx) R 117.0 (count/lx) IR 30.0 (count/lx)			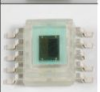
S11059-01WT	I^{2}C interface-compatible color sensor	1.22 × 0.56	1.68 × 1.18 × 0.58^t WL-CSP (on-chip filter)	B 460 G 530 R 615 IR 855	Low B 3.35 (count/lx) G 7.61 (count/lx) R 9.48 (count/lx) IR 1.66 (count/lx)			High B 31.7 (count/lx) G 76.2 (count/lx) R 94.5 (count/lx) IR 15.3 (count/lx)			

Figure 2.5 – Design choices for the selection of the photodetector. Source [54]

Figure 2.6 shows the counts versus the illuminance times. The counts can go from 0 to 65535 as its a 16-bit resolution. The illuminance is the amount of ambient brightness that is perceived. The unit of illuminance is lux. As it can be seen every pixel has a slightly different sensitivity with 4.4 counts/lx for the blue pixel and 8.35 counts/lx for the green pixel of the photodetector. This can be mathematically correction after measurement.

2.4 Optical Filter Selection

Since the excitation wavelength (435 nm) and emission wavelengths (485 nm and 535 nm) were close, it was necessary to have optical filters in the system to eliminate the out-of-band noise. As shown in Figure 2.7 the three possibilities were to, have a filter on both the excitation source and emission detector or have a filter on either one of them only. We chose to go with a design principle of having a filter on the emission photodetector to reject the reflected noise from the excitation source and its auto-fluorescence from the 3D printed mechanical structure. For the excitation source we chose an LED with a stable center wavelength and a narrow bandwidth of 14 nm as shown in Figure 2.8.

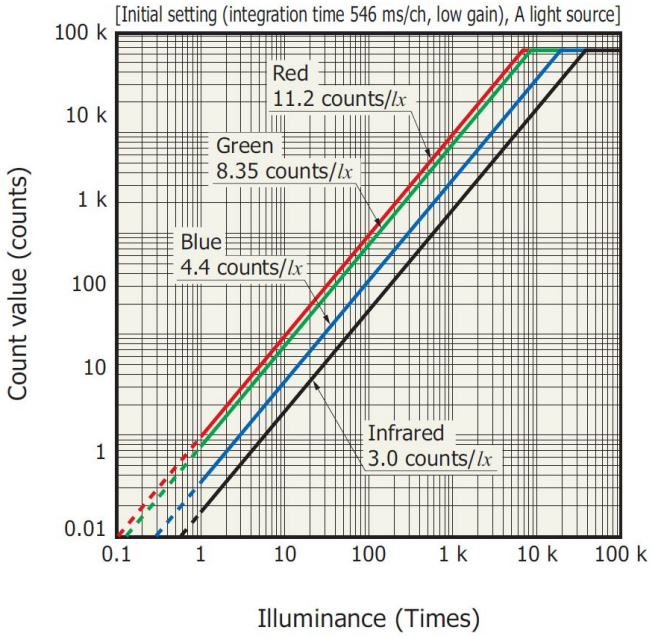

Figure 2.6 – S11059-01WT color sensor, Count value vs. illuminance (typical example). Source [54]

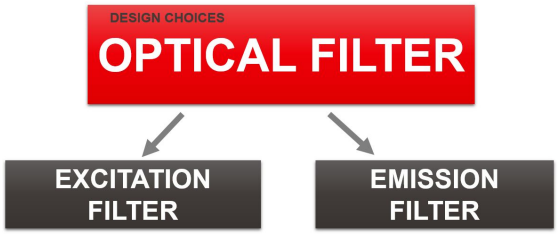

Figure 2.7 – Emission Filter used with the design employing a narrow band excitation LED, thus avoiding an excitation filter.

2.5 Electronic System Configuration

The system setup board with the Hamamatsu S11059-01WT color sensor and the Philips LUXEON UV LED is shown in Figure 3. The Philips LUXEON UV LED having a center wavelength of 430 nm, with a sharp bandwidth of 25 nm around it is used to excite the cells. LED has an iso-radiometric light intensity distribution of 120°.The LED and the PD are placed adjacent to one another as shown in Figure 2.9.

The Hamamatsu S11059-01WT color sensor with a total area of 1.7 x 1.2 x 0.7 mm^3, comprising an active photosensitive area of 1.1 mm x 0.54 mm, that is sensitive to RGB wavelengths using an I^2C interface, is selected. The photodetector (PD) operates at a voltage of 3V consuming a current of 75 μA. The integration time for the light can be tuned and the PD has a 16 bit digital resolution.

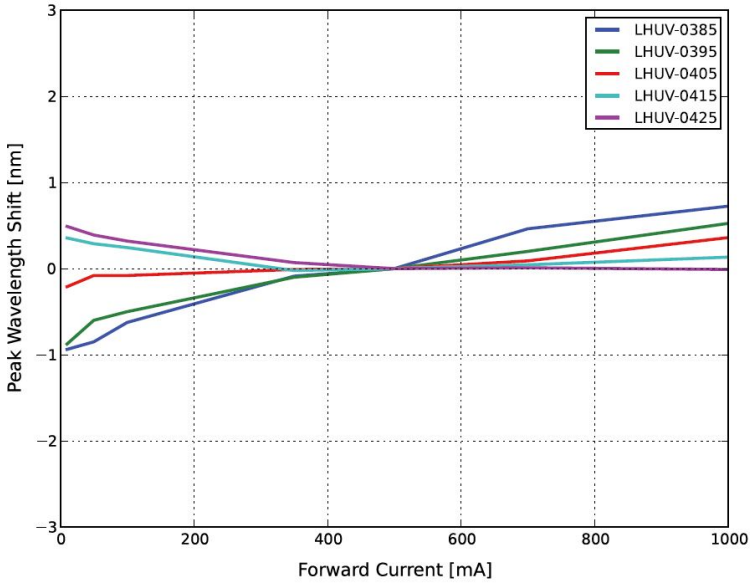

Figure 2.8 – Typical peak wavelength vs. forward current. Stable wavelength with a relative change of less than 1 nm. The typical spectral half-bandwidth is 14 nm. Source [55]

The entire system with the photodiode and the LED is placed inside a scaffold which is designed using Solidworks® and printed with a 3D printer as shown in Figure 2.10.

A diced optical filter is placed atop the PD to prevent the blue wavelength of light from the 430 nm to interfere with the 485 nm light wavelength. We have used a diced 2 mm^2 Edmond Optics bandpass filter (No. 84-097). The filter has a center wavelength at 510 nm and a bandwidth of 84 nm.

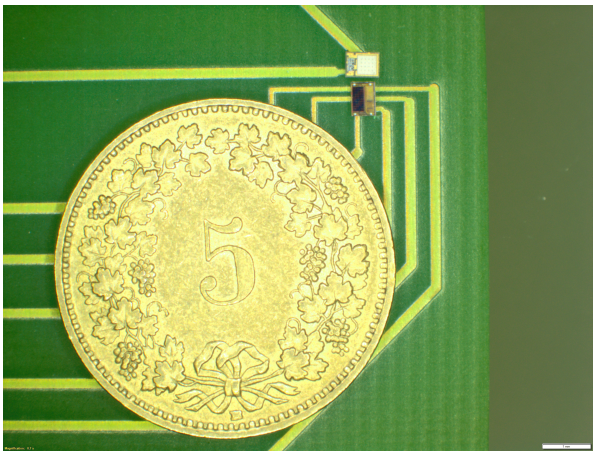

Figure 2.9 – The electronic components of the system with the photodiode (top) and photodetector (bottom).

The entire experiment is performed inside a dark chamber to prevent external light interference. The entire electronic system is hosted in the 3D printed assembly structure that has been designed using Solidworks®.

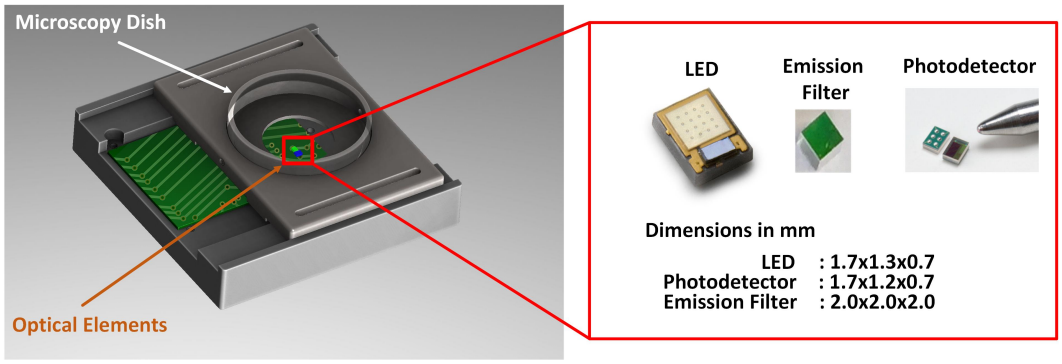

Figure 2.10 – *in vitro* demonstrator and its constituent components.

Filtering is an important aspect of optical systems [56] to eliminate unwanted light components such as excitation light and auto-fluorescence of the system.

This is evident from the spectrometer result in Figure 2.12 in which the 485 nm component of light is buried in noise. In our system it is used to mitigate the reflections of the incident 430 nm light and the associated auto-fluorescence it causes from the Petri dish and the 3D printed parts.

The scaffold also has a circular sliding holder for the Petri dish. The Petri dish has a cylinder glued to its center for localizing the cells as shown in Figure 2.11. The communication with the photodiode is done using the I^2C protocol and the data is logged using the National Instruments myRIO card controlled through a Labview interface. The hexadecimal ASCII format of data in 16 bits for each color is used over the I^2C interface.

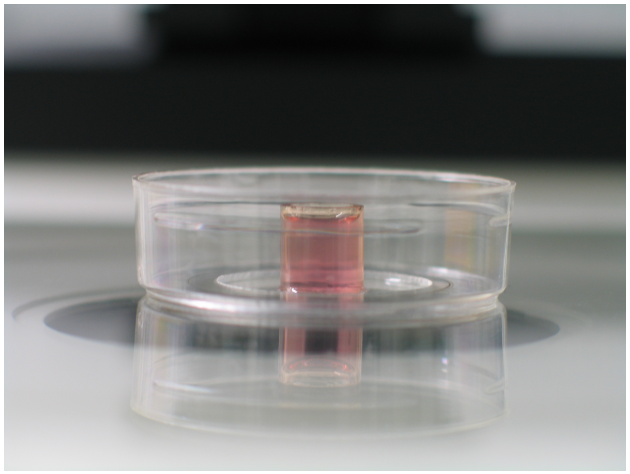

Figure 2.11 – Petri dish with the glued cyclinder in the center hosting the cell culture medium and the INS-1E cells.

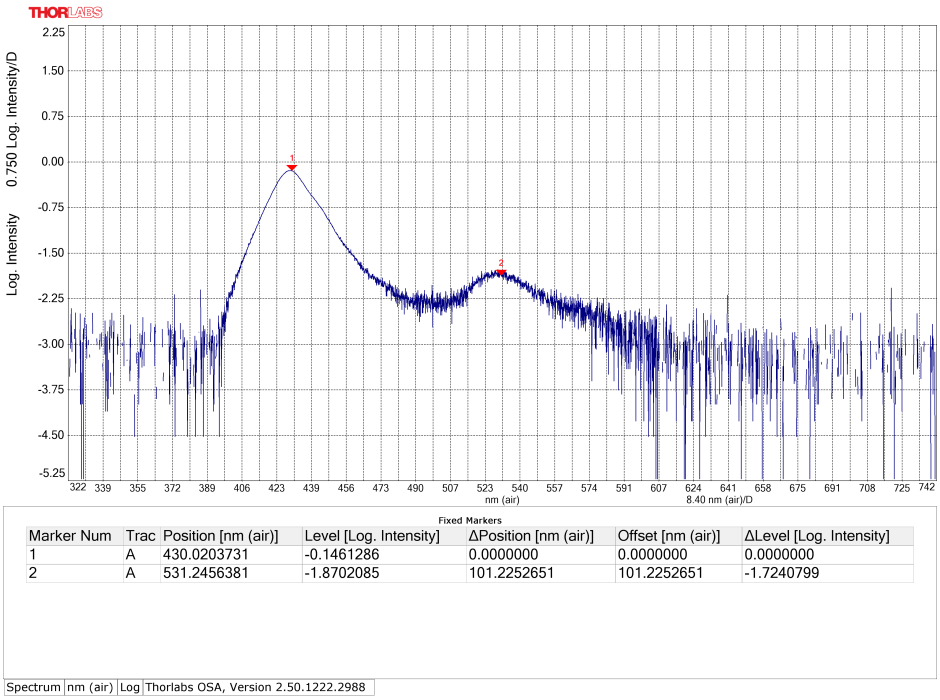

Figure 2.12 – Spectrometer with signatures of the excitation wavelength at 434 nm, emission wavelengths, buried at 485 nm and visible at 535 nm.

2.6 Results and Discussion

2.6.1 Fluorescence characterization of the system

The Figure 2.13 shows the fluorescence characterization of the system with the Fluospheres Polystyrene Microspheres using the Philips LUXEON LED emitting light at 430 nm.

The intensities of the light were varied by changing the bias current of the LUXEON LED by factor of 10 every time, that is 100 mA, 10 mA and 1 mA respectively. The Fluospheres Polystyrene Microspheres (3 ml original concentration) were diluted with water. The measurements of Figure 2.13 correspond to the blue and green output counts of the PD.

2.6.2 Reference characterization of the F10 INS-1E pancreatic β-cells using the CCS100/m spectrometer.

The F10 β-cells were excited with a 430 nm LED light with a LED bias current of 100 mA. The light was collected with an optical fiber connected to an UV-Visible spectrometer (CCS100 Thorlabs). As shown in Figure 2.14, the Y axis represents the relative intensity of light and the X axis represents the wavelength of light. The light was collected without any filter.

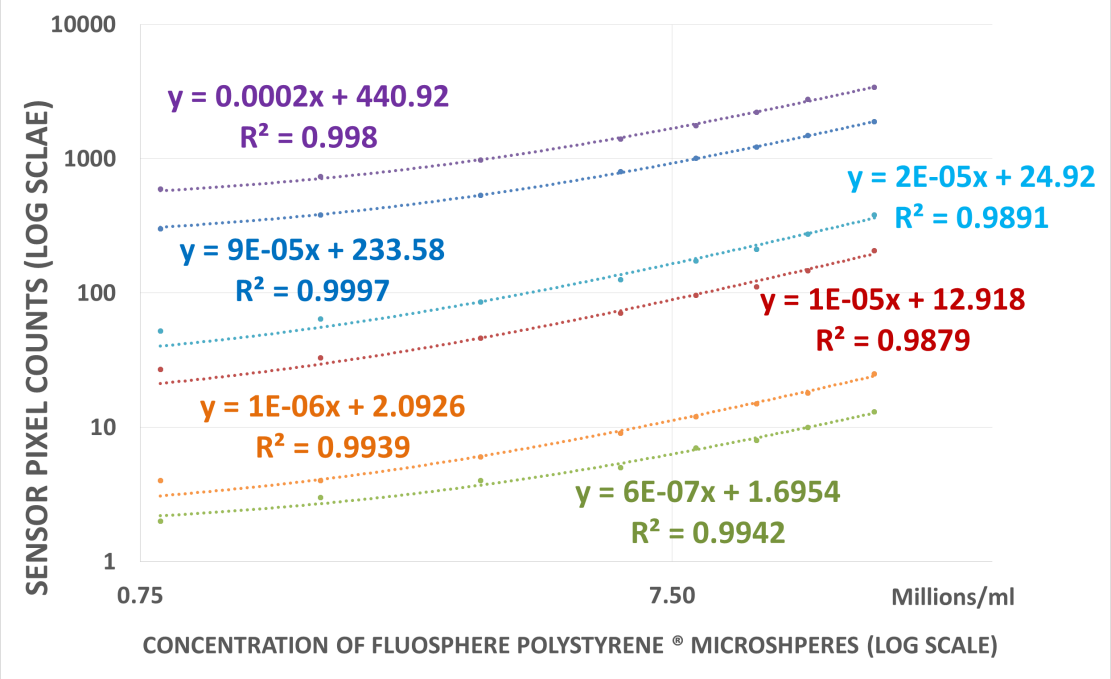

Figure 2.13 – Fluorescence characterization with Fluospheres Polystyrene Microspheres.

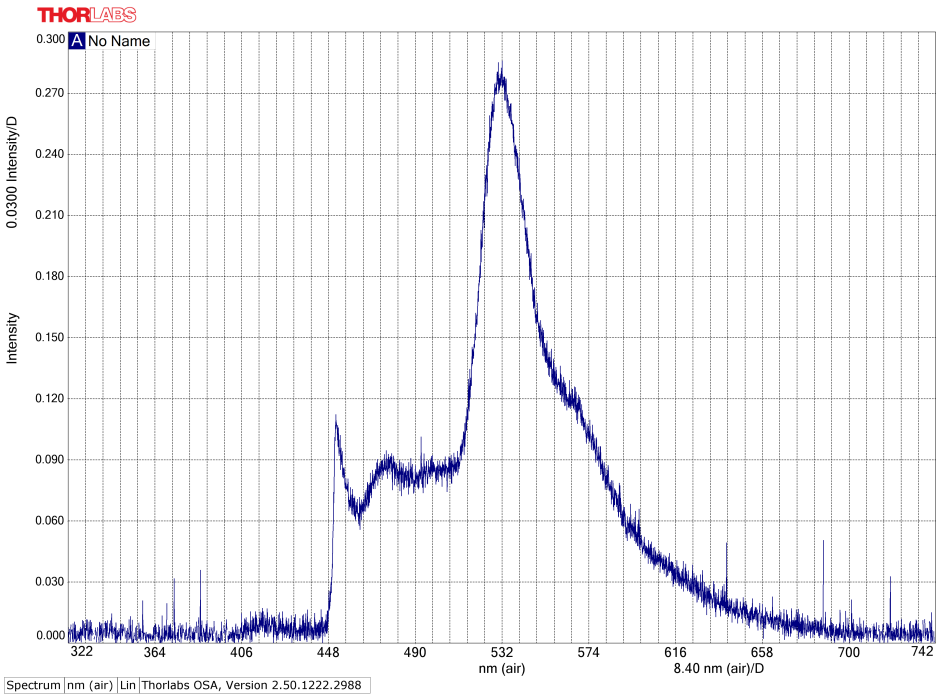

Figure 2.14 – Spectrum showing the relative intensity levels of the excitation LED at 430 nm and the response of the F10 β-cells at 535 nm.

It can be seen that there are three distinct peaks at 430 nm (LED excitation), 485 nm (Probe response: blue) 535 nm (Probe response: green).

2.6.3 Characterization of 2D and 3D cell cultures of INS-1E pancreatic β-cells with the FRET probe and control

Two types of cells (Figure 2.16 Figure 2.17) have been studied to assess the capability of the system to measure the fluorescence emitted by the Ca^{2+} probe as shown in Figure 2.16. A stable clone of INS-1E cells expressing the Ca^{2+} probe (F10 INS-1E) was compared to unmodified INS-1E cells used as control (control INS-1E). The Figure 2.18 shows the difference of the mean values of green and blue color counts of 2D and 3D cell cultures ((Figure 2.16 Figure 2.17)).

The Philips LUXEON 430 nm LED at 100 mA bias current was used as the excitation source. The PD was configured for an integration time of 1.4 ms. Only a small difference was observed between the F10 clone (μ_{green}: 169(σ=1.95%), μ_{blue}: 531 (σ=0.84%)) and the control (μ_{green}:157(σ=0.61%), μ_{blue}: 517 (σ=1.16%)) in 2D cell culture, in which noise coming from incomplete excitation light filtering was dominant.

A much significant difference between the F10 INS-1E (μ_{green}: 599 (σ=3.59%), μ_{blue}: 935 (σ=4.37%)) and the control (μ_{green}: 142 (σ=2.15%), μ_{blue}: 639 (σ=2.78%)) was observed in a 3D cell culture, which is mainly due to an increased number of cells thus producing a stronger fluorescence signal.

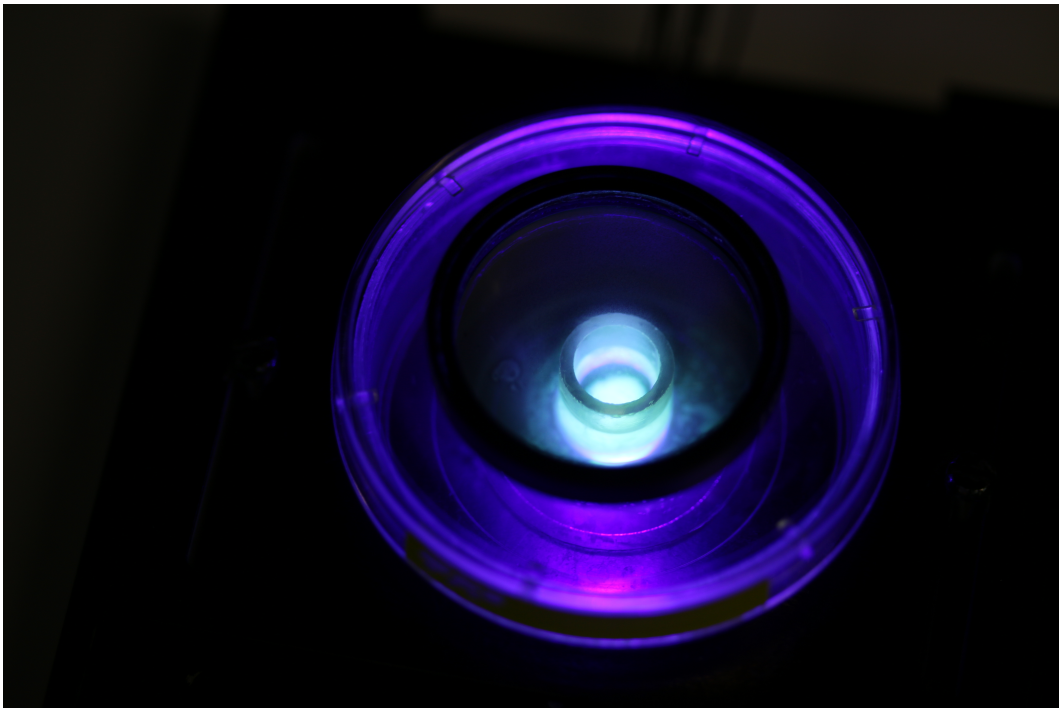

Figure 2.15 – The INS1E cells fluoresence with the Edmond Optics bandpass filter atop.

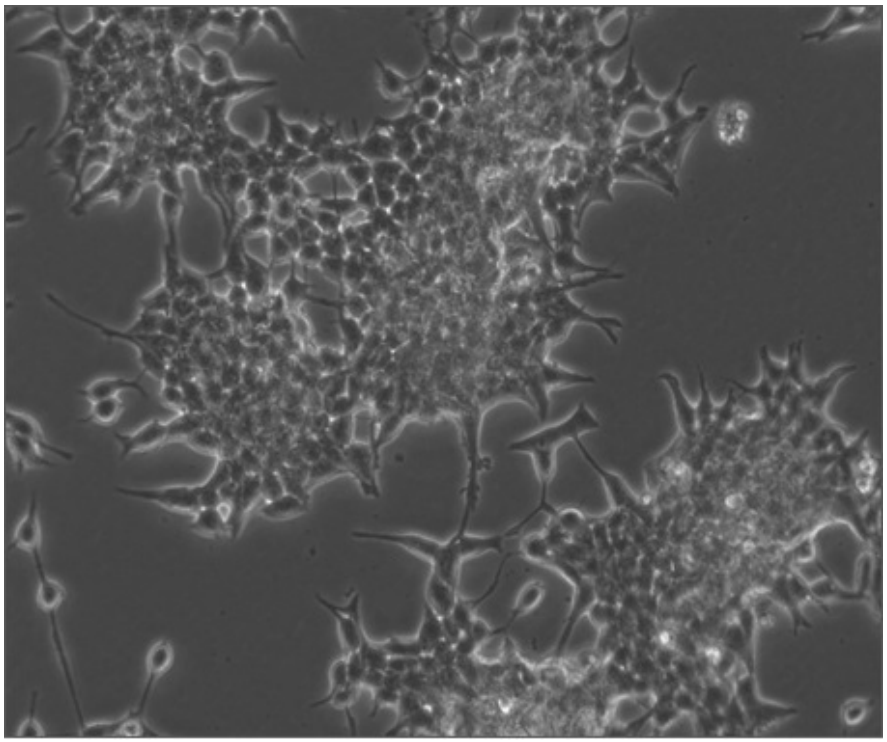

(a) Stereomicroscopic microscope view of F10 INS-1E pancreatic β-cell 2D culture

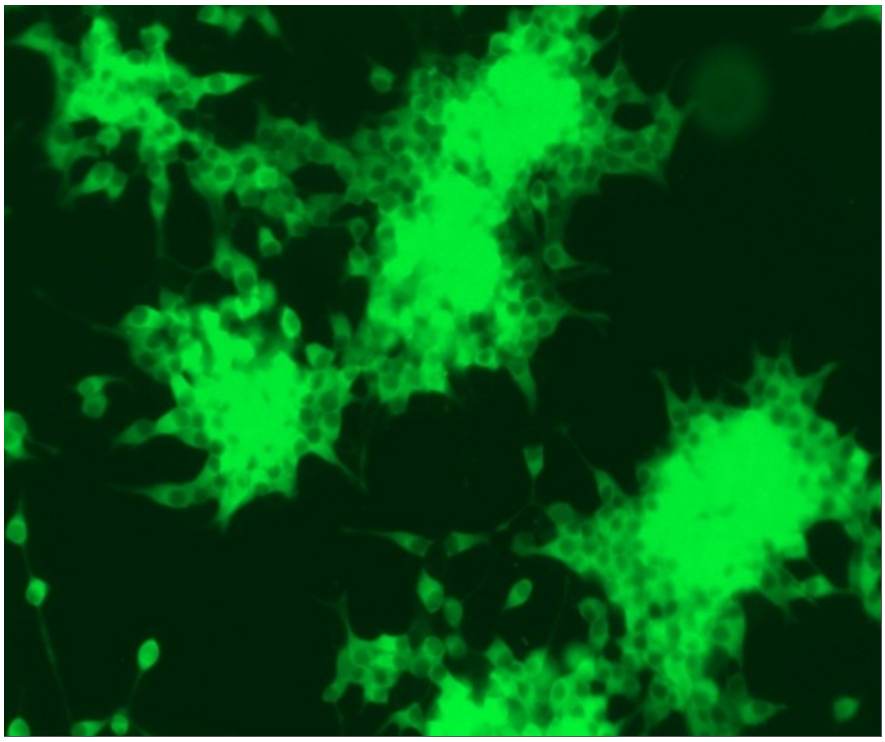

(b) Fluorescent microscope view of F10 INS-1E pancreatic β-cell 2D culture

Figure 2.16 – Stereomicroscopic (top, bottom) and fluorescent microscope view of F10 INS-1E pancreatic β-cell 2D culture.

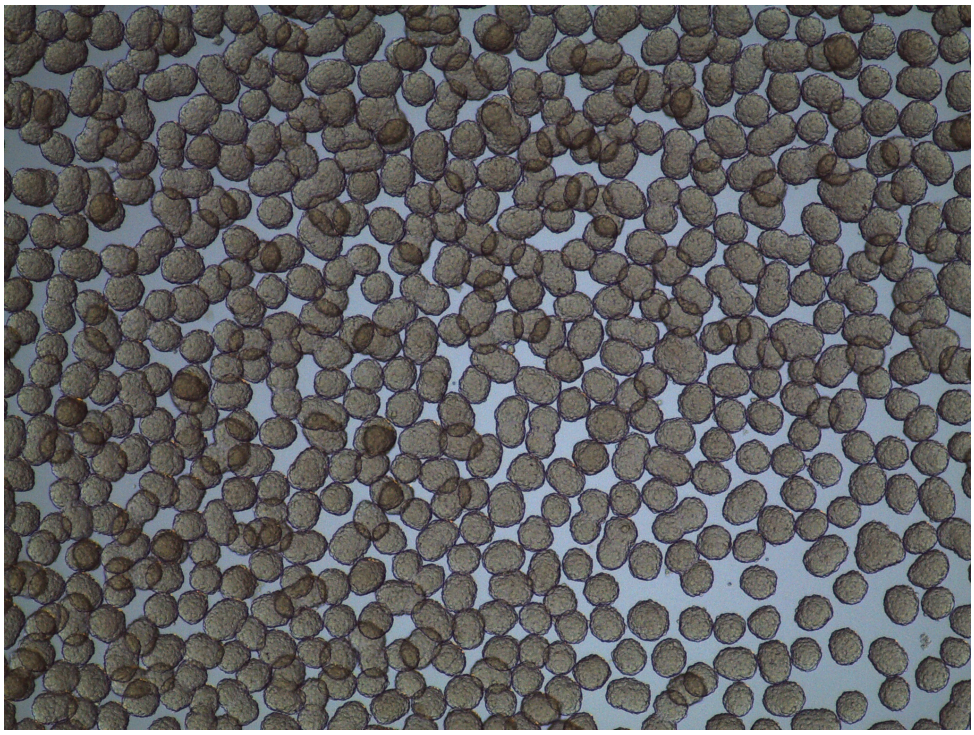

(a) Stereomicroscopic microscope view of F10 INS-1E pancreatic β-cell 3D culture

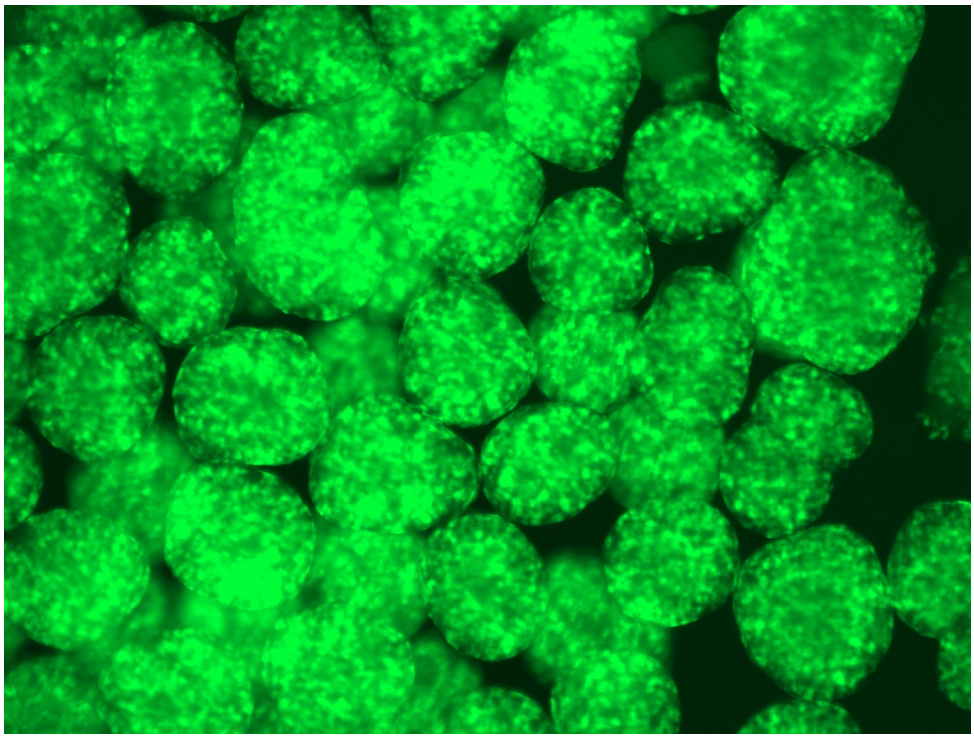

(b) Fluorescent microscope view of F10 INS-1E pancreatic β-cell 3D culture

Figure 2.17 – Stereomicroscopic (top, bottom) and fluorescent microscope view of F10 INS-1E pancreatic β-cell 3D culture.

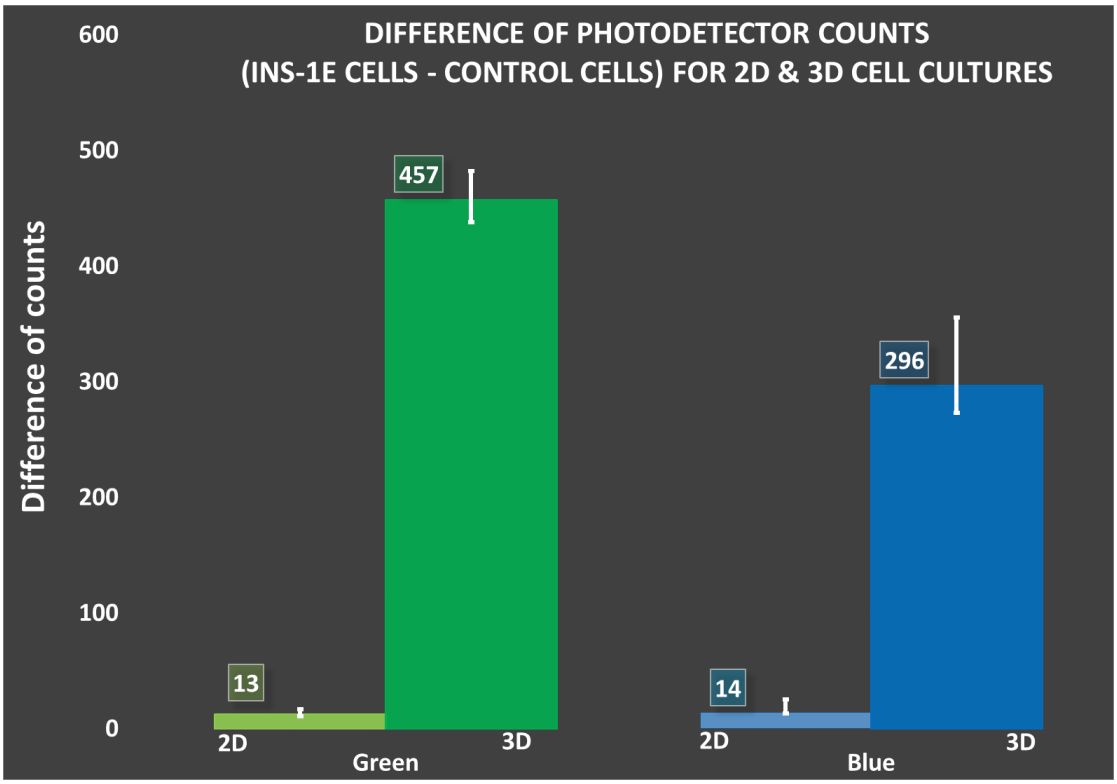

Figure 2.18 – Photodetector counts of green and blue colors of 2D and 3D cell cultures for the F10 INS-1E β-cells and INS-1E β-cell control.

35-fold and 21-fold improvements were observed in the absolute difference of the means of the green and blue counts for 3D cell cultures compared to the 2D cell cultures. These results demonstrate that the system has enough sensitivity to measure fluorescence from a 3D cell culture. Better light filtering would still be required to improve the system performance, especially in the blue where the excitation and emission wavelength are very close.

2.6.4 Continuous monitoring of the F10 INS-1E pancreatic 3D β-cell aggregates

In Figure 2.19a green and blue PD counts show continuous monitoring of the 3D cell aggregates of F10 INS-1E pancreatic β-cells under different stimuli. For all recorded values the Philips LUXEON LED (430 nm) was biased with 100 mA current. The PD was used with an integration time of 716.8 ms for each green and blue colors. At the starting time of the experiment (t = 0 s) F10 INS-1E aggregates were loaded from the incubator to the Petri dish in Krebs–Ringer bicarbonate buffer (KRBH) for continuously monitoring in a controlled temperature black box preheated at 37 °C. The cells were allowed to stabilize for the first 21 minutes and readings were taken every minute. At 21 minutes 16.7 mM glucose was injected in the cell culture. Green color counts showed a slightly rising trend upon glucose injection, whereas a steady decrease in the blue color count was observed until the 48^{th} minute. This trend is consistent with the theoretical working principle of the biological probe. At the 48^{th} minute 100 μM diazoxide cell inhibitor

was injected in the Petri dish with the cells, causing a sharp fall in both the blue and green counts. Finally, 30 mM KCl was injected in the system and there was a significantly sharper and larger spike in the green color counts in lieu of the huge Ca^{2+} influx. Figure 2.19b shows the ratio of the green and blue photodetector counts, which indicates the trend of the cytosolic Ca^{2+} in the F10 INS-1E pancreatic β-cells. It can be observed that the cells take about 10 minutes to settle between an average of 0.415 and 0.42. Upon glucose stimulation at the 21^{st} minute, the ratio shows an overall upward trend until the 48^{th} minute. Next, the ratio drops when diazoxide is injected in the system and suddenly increases upon stimulating the cells with KCl solution. This is due to the fact that KCl opens up the cells channels enabling a huge influx of Ca^{2+} ions. The system was clearly able to monitor Ca^{2+} changes due to diazoxide inhibitor blocking Ca^{2+} influx and KCl depolarization, which demonstrates that the system is sensitive enough to monitor Ca^{2+} levels. The experimental results show a 1.2% average rise in the ratio between the glucose stimulation and diazoxide injection which is in agreement with the expected trend [51]. We can infer from the measurements that the cell environment is important for the cells to respond with high efficiency upon glucose stimulation.

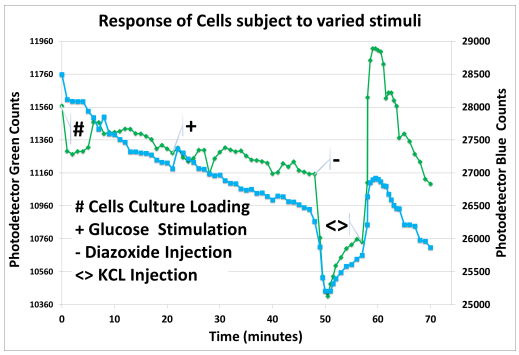

(a) Green and blue photodetector counts vs time (legend: green: green color; blue: blue color).

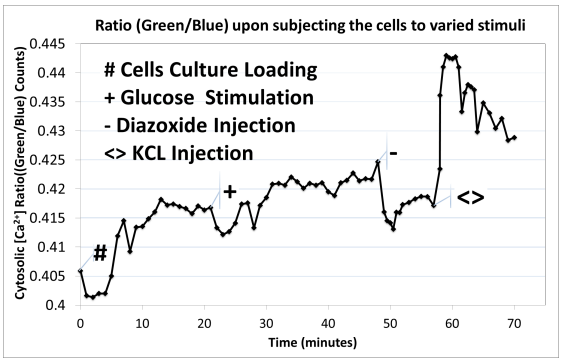

(b) Ratio (Green/Blue counts of the PD) indicating the flux of the cystolic Ca^{2+} ions.

Figure 2.19 – Green and blue photodetector counts vs time and ratio vs time.

2.7 Conclusion - *In vitro* Demonstrator 1

This work has presented the design of an electronic system using extremely small dimension components. Optical filters have been shown to be effective in eliminating a major component of the reflected blue light and light from the auto-fluorescence of the 3D printed parts.

The system response is linear and has been characterized by diluting the Fluospheres polystyrene Microspheres and measuring linear fluorescence levels at three different intensities of light for each diluted concentration. The system has successfully distinguished two separate cell types, one with a FRET probe and one without and is shown to be sensitive to both 2D and 3D cell cultures.

It has been proven through this system that 3D cell culturing methods, to make cell aggregates, increases the number of cells and thus enhances the quality of signal detected by the photodetector. The system has successfully monitored the cytosolic ratio of Ca^{2+} ions in the F10 INS-1E pancreatic β-cells. An improvement of the sensitivity of the system will be the next goal in order to monitor continuously glucose stimulation with higher sensitivity.

2.8 *In vitro* Demonstrator 2

2.8.1 Brief Motivation and Innovation

As shown in Figure 2.20, a number of design challenges were faced in the initial design of the *in vitro* demonstrator. Glucose sensitivity, oxygenation and the SNR of the optical filter were the top three challenges among them.

Figure 2.20 – Key design issues that were addressed in demonstrator 2 are shown in this picture.

This part of the thesis reports a continuous, cytosolic Ca^{2+} ions monitoring system, upon glucose stimulation using a fully automated compact bio-electronics system as shown in Figure 2.21 [57].

An ultra-small fluorescence system based on microelectronic and optical components, was designed to detect light emitted by the FRET-based genetic probe cameleon YC3.6 expressed in INS-1E pancreatic β-cells.

The probe works on a ratio-metric principle emitting light at 480 nm (blue) and 535 nm (green) for 430 nm excitation, based on the glucose levels which trigger the Ca^{2+} ions influx as seen in Figure 2.2 [51] [52]. This automated electronic system allows continuous monitoring of the changes of glucose stimulation without perturbing the temperature, humidity and oxygenation of the cells in the *in vitro* system.

in vitro platform with the Hamamatsu SW-00159 photodetector (PD), MIDOPT LP 470 optical filter, LUXEON 430 nm excitation LED is shown in Figure 2.21. Automated with National Instruments (NI) myRIO real time (RT) using LabView RT (real-time) (communication is performed using the I2C protocol), NI PXIe-1082e with the PXIe 4143 source measure unit (SMU) and PXIe 6361 DAQ. The hardware software co-designed system is fully autonomous. A photo-detector integration time of 493 ms was used per channel (R/G/B/IR). The excitation LED with a center wavelength of 430 nm with a FWHM of 20 nm was used. PD and LED: components of the *in vitro* demonstrator in a black printed circuit board to reduce the noise rising from auto-fluorescence.

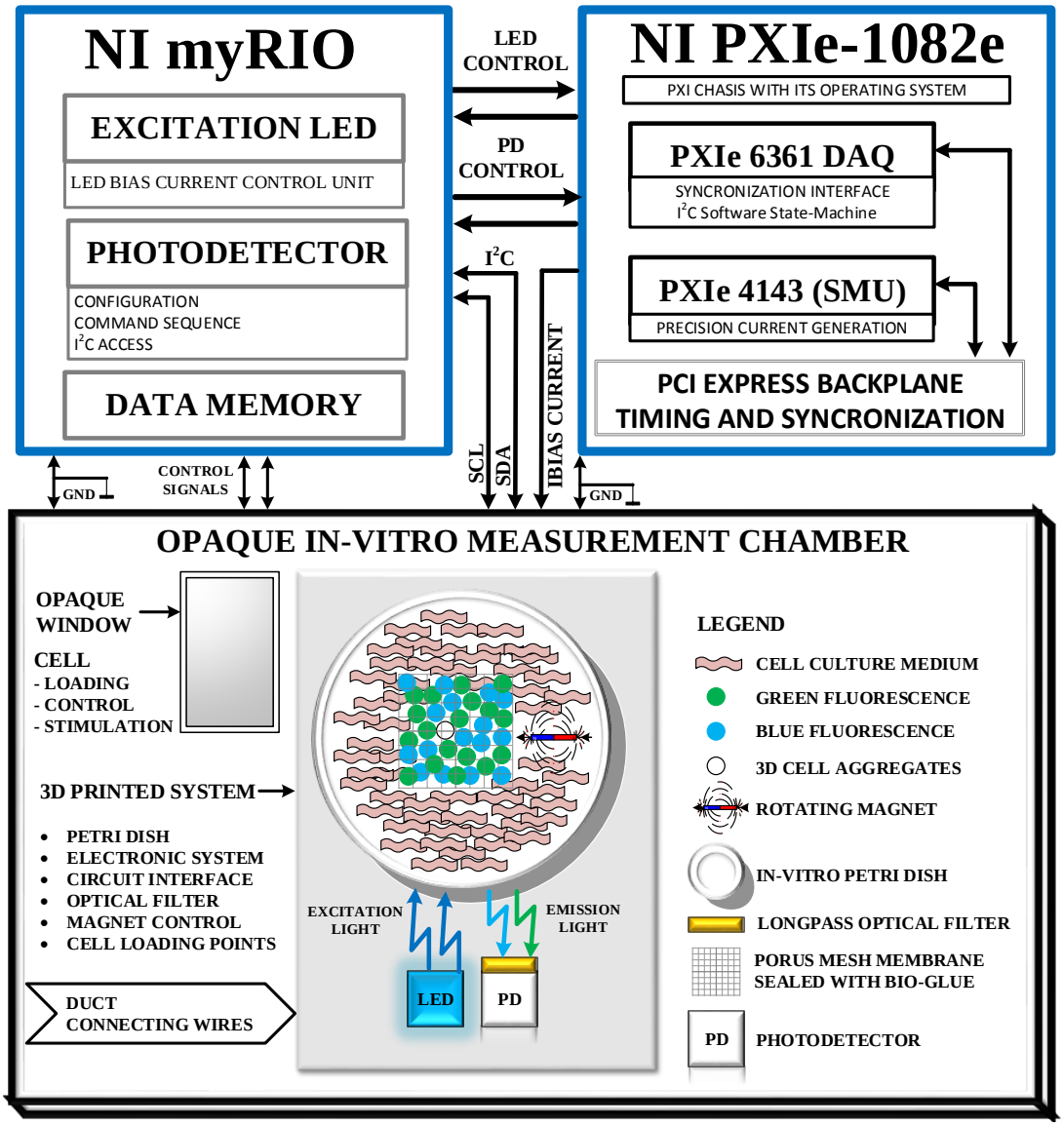

Figure 2.21 – *in vitro* demonstrator 2 system diagram. The measurements are all done in the temperature chamber that is pre-heated at 37 °C. The opaque window is used for loading the cells, adding the stimulants such as glucose an allows as it allows easy access to the petri dish.

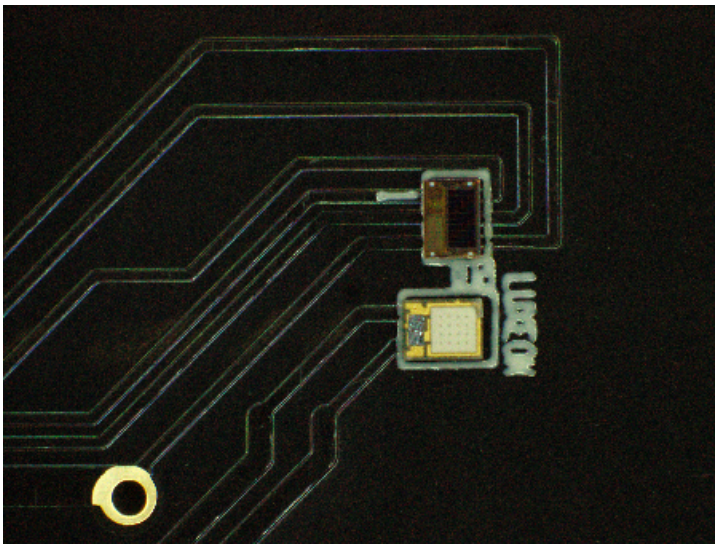

Figure 2.22 – Black PCB to reduce the auto fluorescence.

2.8.2 Summary of the Methods

Optical filter characterization:

Native INS-1E cells and a stable clone of INS-1E cells expressing the Ca^{2+} sensor YC3.6 (F10 cells) were optically characterized. The signal measured from F10 cells was compared to INS-1E cells which act as control as they do not emit fluorescence.

Continuous monitoring:

To form aggregates, cell suspensions were placed in ultra-low attachment 6-well culture plates on an orbital shaker for 24 hours. These 3D cell aggregates were used for monitoring the effect of glucose when changing from KRBH (Krebs–Ringer bicarbonate HEPES buffer) 0 mM glucose to culture medium (RPMI 1640 medium from invitrogen containing 11 mM glucose).

The cells were allowed to stabilize for 30 minutes before starting the experiment, which was performed in a temperature chamber pre-heated at 37 °C owing to the high sensitivity of cytosolic Ca^{2+} to temperature changes [58] [59] [60].

Green, blue counts of the F10 cells for alternating cell media from KRBH medium with 0 mM glucose to cell culture medium with 11 mM glucose concentration. The cells were pre-conditioned in the temperature chamber for 30 minutes initially.

An automatic continuous measurement was carried out and the data was stored once every 10 seconds. Initially KRBH medium with 0 mM glucose was used, followed alternately by cell culture medium exchange with 11 mM glucose (minutes: 7, 23 and 40) and KRBH medium with 0 mM glucose (minutes: 0, 15, 32 and 49).

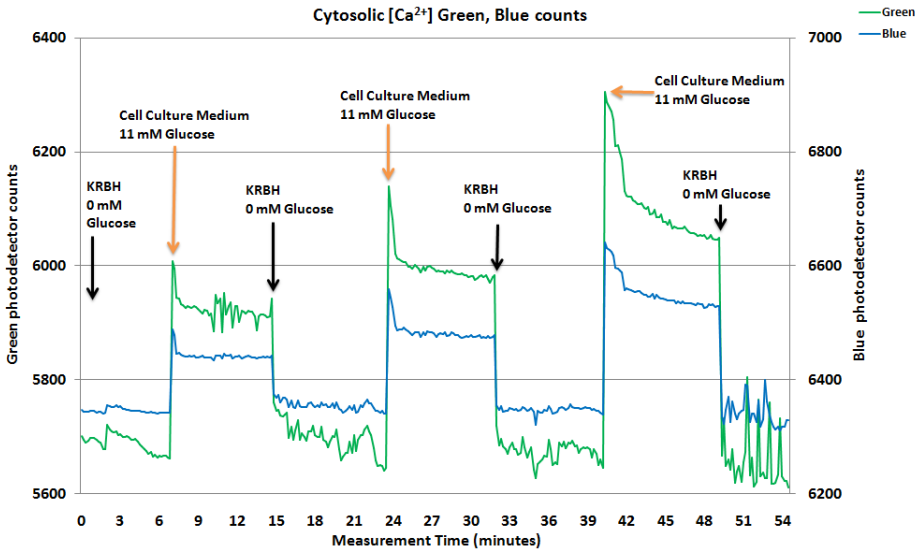

Figure 2.23 – Green, blue counts for the continuous glucose monitoring experiment.

Cytosolic [Ca^{2+}] (Green/Blue) ratio of the F10 cells for alternating cell media from KRBH medium with 0 mM glucose to cell culture medium with 11 mM glucose concentration. The cells were pre-conditioned in the temperature chamber for 30 minutes initially. An automatic continuous measurement was carried out and the data was stored once every 10 seconds. Initially KRBH medium with 0 mM glucose was used, followed alternately by cell culture medium exchange with 11 mM glucose (minutes: 7, 23 and 40) and KRBH medium with 0 mM glucose (minutes: 0, 15, 32 and 49).

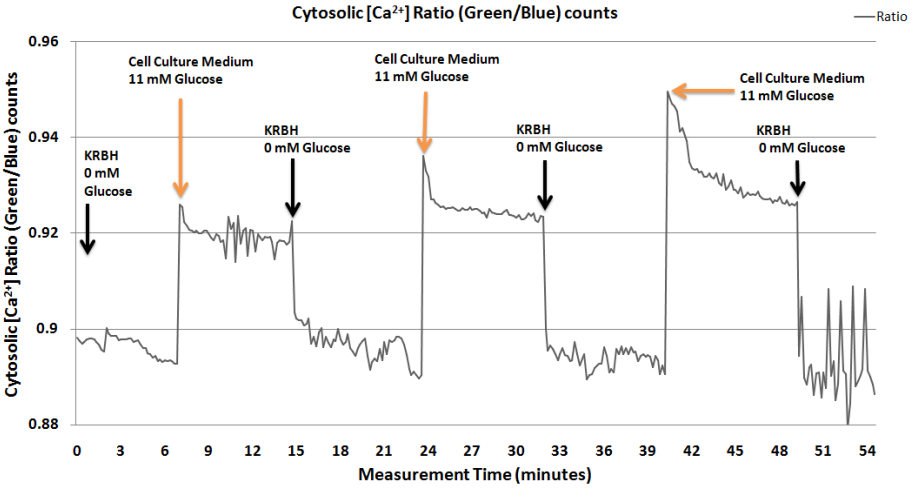

Figure 2.24 – Ratio (Green counts /blue counts) for the continuous glucose monitoring experiment.

2.8.3 Key Results

The *in vitro* system has been developed, tested and deployed. The angle-independent absorption-based optical filter MIDOPT LP470 improves the signal-to-noise ratio (SNR) of the emitted optical signal as shown in Figure 2.25. A 480% improvement in the SNR of the F10 cells is achieved with the LP470 filter. The system has successfully monitored the genetically engineered INS-1E pancreatic β-cell line upon stimulation with 11 mM glucose in the cell culture medium and exchanging with KRBS solution with 0 mM glucose as seen in Figure 2.24.

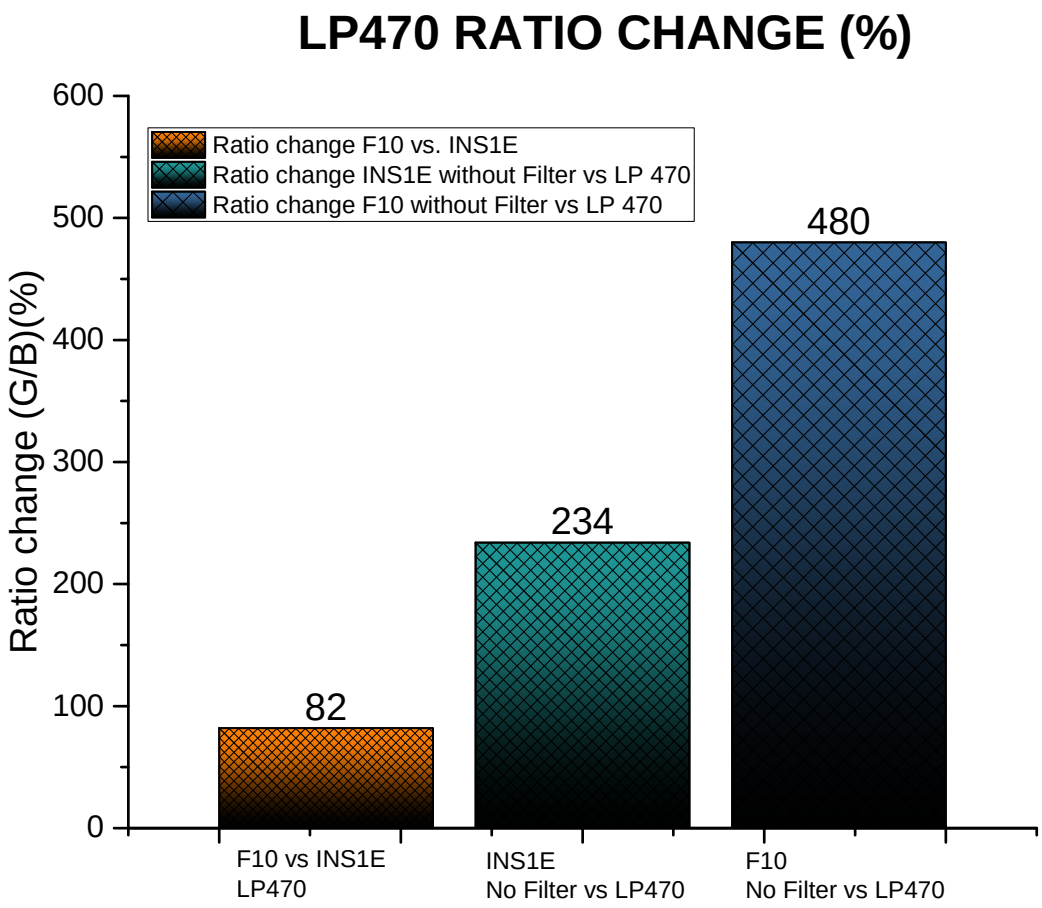

Figure 2.25 – The relative percentage (%) change in the ratio (green/blue) for the F10 vs. INS-1E cells (black) , INS-1E cells without and with the LP470 filter (red), and F10 cells without and with the LP470 filter (blue): a 480% improvement in the ratio is observed for the F10 cells demonstrating the efficacy of the filter in mitigating the out-of-band noise and making the system selectively sensitive to the probe.

2.8.4 Conclusions

A fully automated compact microelectronics-based system has been developed to monitor the response of a genetically encoded Ca^{2+} probe expressed in INS-1E pancreatic β-cells. The *in vitro* system confirms that the FRET-based probe triggered by cytosolic Ca^{2+} influx can be used to monitor the effect of glucose stimulation.

The optical filter described in this chapter was a result of a huge body of work on optical filters that is dealt with in detail in the next chapter.

3 Optical Filters Characterization

3.1 Motivation for characterizing and selecting optical filters

In the scope of this application we have three wavelengths very close to one another. The excitation wavelength is at 435 nm (we use an LED centered with its center wavelength for its peak transmission power at 430 nm). The emission wavelengths are at 535 nm for the green component of the FRET probe and 485 nm (buried in the noise) for the blue component of the FRET probe as seen in Figure 3.1.

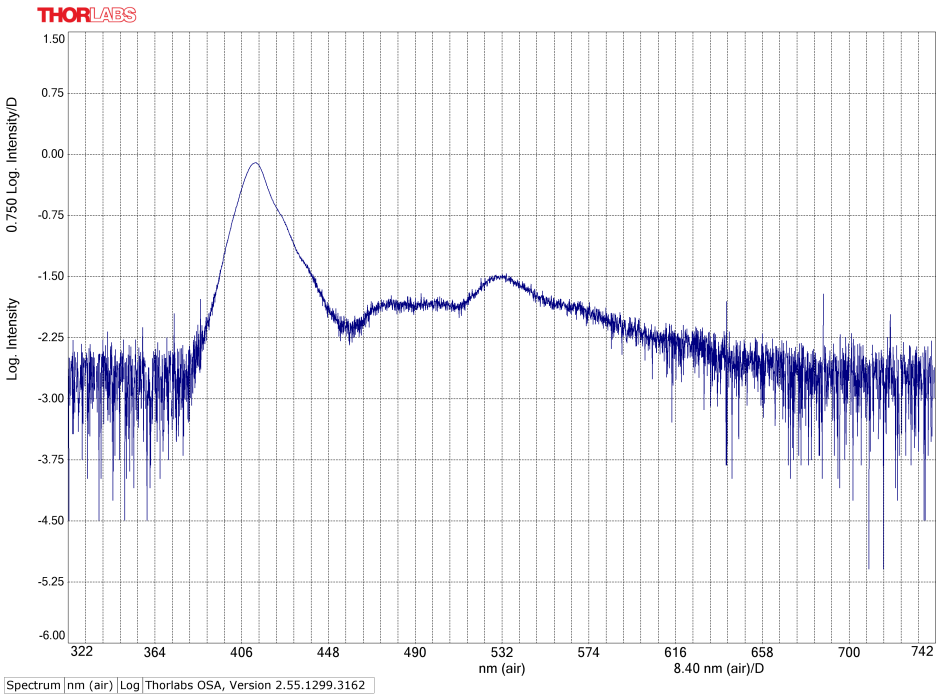

Figure 3.1 – Spectrometer showing the excitation LED spectrum alongside the emission wavelength at 535 nm and the 485 nm emission wavelength signal buried in the noise.

Figure 3.1 the 485 nm blue component of light is buried under the noise arising from the reflections of the petri dish having the cell culture media with the cells and the auto-fluorescence of the system components. This deteriorates the SNR of the final ratio that is measured. In order to mitigate this noise it is necessary to use an optical filter that suits the bandwidth requirements of this application. The two choices that can be made are between dichoric filters and absorption based filters. The material of each of these filters and their design integration ease are also important parameters to consider. Another important distinction between absorption and dichoric filters is that, the former are angle independent while the latter are angle dependent.

Various filters from both families of filters were tested and characterized with several thousand automated measurements in order to determine the best candidate. In this chapter we first describe the results of absorption based filters, followed by the results of the dichoric filters.

3.2 Experimental methods adopted for characterization of the optical filters

The culture of the INS-1E and F10 cells aggregates that were incubated in the clean room were first loaded into a small incubator in the lab. The cells were temporarily stored in petri dishes at 37.2°C with the same humidity and CO_2 levels as in the clean room incubator.
A total number of 5 measurements were made for each data point, n= 5. The LED excitation wavelength of 425 nm with a LED Bias Current of 100 mA were used. The photodetector integration time (ms) of 22.400 ms was used per channel (green, blue). 10 ms was set as the measurement gap between the data points.

3.3 Absorption based glass filters

Absorption based filters transmit the pertinent wavelength of light and block the other out-of-band wavelengths by absorbing them in the material of the filter. The working principle of these filters is shown in Figure 3.2

The various classes of filters are short-pass, long-pass, band-pass, band-reject and multiple band-pass and band-reject filters. The characteristics of the filter are classified based on center wavelength, cut-off wavelength, full width half maximum (FWHM) range, optical density (OD), transmission percentage and out-of-band rejection strength.

The central wavelength is where the filter transmits most of the filtered signal after absorbing the input light signal in on the opposite side of the filter face. It is also the center of the filter spectrum. The FWHM or the bandwidth of the filter can be visualized for the bandpass filter as the difference in the wavelength, taking the 50% peak rising transmission power point from the rising slope of the filter to the 50% peak transmission falling power point of the filter.

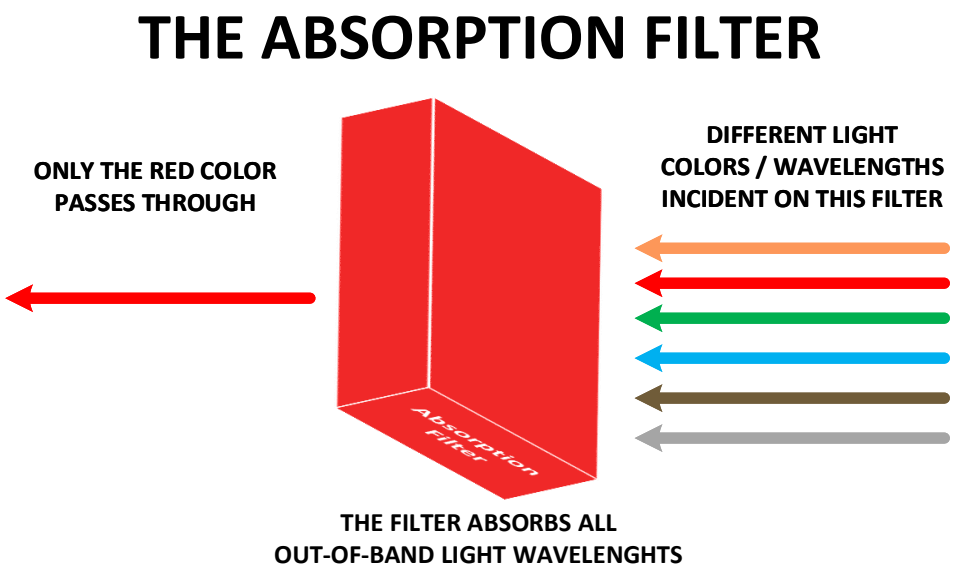

Figure 3.2 – The Absorption Filter - Working Principle

Another important parameter is the optical density (OD) of the filter. The higher the OD, more the filter absorbs and lower the OD lower the energy, that the filter absorbs.

The cut off wavelength is the point where the transmission power reaches 50%. The advantage of these filters is that they are angle independent, which makes them viable for applications in which the emitted light ought to be collected from a sample with a huge surface area w.r.t the photodetector.

The biggest disadvantage of these filters is the rise in the temperature of the filter owing to the energy that is absorbed. For bio-implantable applications the weight of the glass filter could be a design trade-off parameter as there are strict regulations for the weight of an implantable system in comparison to the weight of an animal for lab testing.

3.3.1 MIDOPT BP505 Cyan Bandpass Filter

The MIDOPT BP505 Cyan Bandpass filter is shown in Figure 3.3. It is an absorption-based angle independent filter that is cut into the dimensions of the photo detector to be placed atop for emission filtering of the light. This filter was tested with the F10 cell probe as the emissions of the probe were at 485 nm and 535 nm.

The main goal was to reject as much reflection and exponential residue of the light from the 435 nm excitation LED. The transmission of wavelengths $\leq$ 450 nm was 0.01% Source [13]. This made it an excellent choice for noise rejection. At the same time the transmission around the 485 nm was around 75% and that around 535 nm was around 91% [13].

The filter was diced in the Center of micro-nanotechnology at EPFL, namely the CMi.

The optical characteristics of this filter are listed below:

- Useful Range: 485-550 nm
- FWHM: 90 nm
- Tolerance : +/- 10 nm
- Peak Transmission : $\geq$90 %
- Surface Quality : 40/20

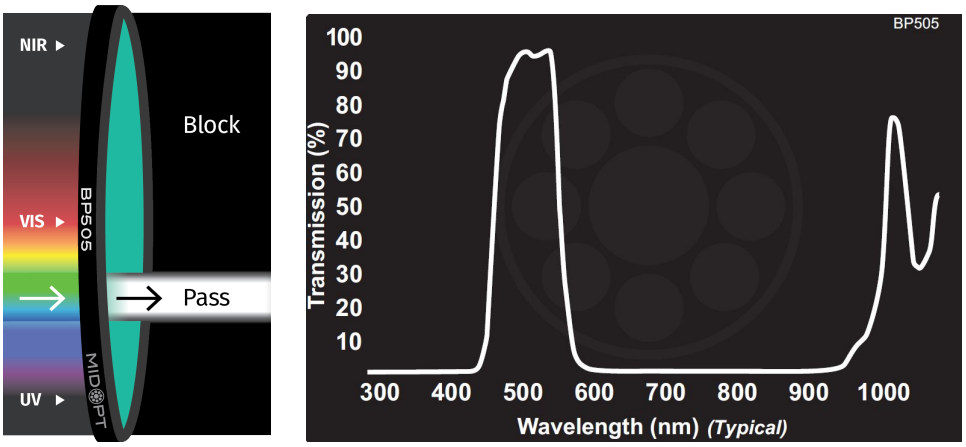

(a) BP505 Cyan Bandpass Filter

(b) BP505 Transmission Data (Typical)

Figure 3.3 – BP505 Cyan Bandpass Filter. Working principle and transmission data. Source [13]

The filter was systematically characterized for several optical parameters with the INS1E and F10 cells with the genetic FRET probe.

The ratios of the green/blue counts were analyzed and discussed, along with probing insights into the absolute value of the photodetector counts and their differences for each cell type and between the cell types.

MIDOPT BP505 INS1E Cells

It can be seen from Figure 3.4 that the INS1E green counts, over a sample of five data points, were 582.4 and the blue counts were 1101. The standard deviation was negligible in both cases.

The counts are very well marked with two distinct levels and these separate non-overlapping signatures add a degree of clarity into distinguishing these cells.

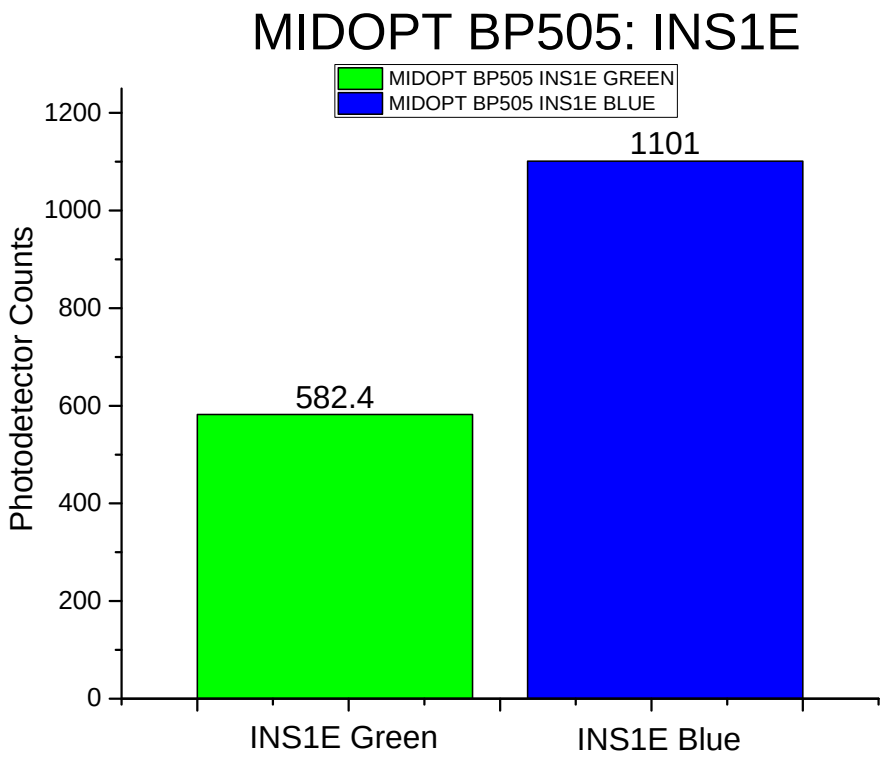

Figure 3.4 – MIDOPT BP505 INS 1E Cells Blue and Green. The standard deviation for the Blue count was 1.67 counts or 0.28 %. The standard deviation for the Green count was 1.5 counts or 0.14%.

The values also clearly demonstrate that the blue counts are higher than the green ones, hence, verifying that the probe is non-existent. These distinct count levels enable offset calibration when used in relation to the F10 cells that have the probe. The offset correction is necessary as the reflections arise from various sources including the petri dish, the mechanical 3D printed part creating auto-fluorescence and the cell culture medium that reflects off right owing to its light red color.

MIDOPT BP505 F10 Cells

It can be seen from Figure 3.5 that the F10 green counts, over a sample of five data points, were 1298 and the blue counts were 1105. The standard deviation was negligible in both cases.

The counts are very well marked with two distinct levels and these separate non overlapping signatures add a degree of clarity into distinguishing these cells. The values also clearly demonstrate that the green counts are higher than the green counts of the INS1E cells, hence, verifying that the probe is existent in the F10 cells.

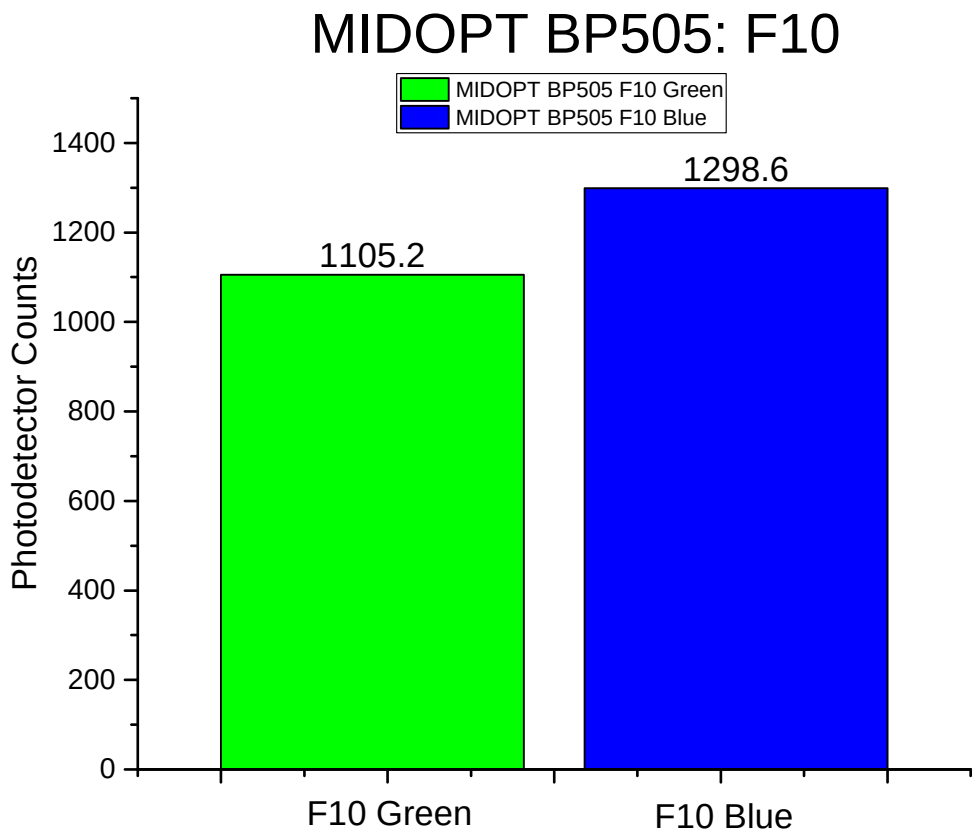

Figure 3.5 – MIDOPT BP505 F10 Cells Blue and Green.The standard deviation for the Blue count was 1.94 counts or 0.15 %. The standard deviation for the Green count was 3.27 counts or 0.29%.

The effect of the fluorescence of the cells depends on the number, size and health of the 3D cell aggregates that were cultured. It should be noted that the same number of cells were used for both INS1E and F10 cells.

MIDOPT BP505 (F10 - INS1E) Cells for Green Fluorescence and Blue Fluorescence Components

Figure 3.6 shows the result after removing the INS1E component of the Green and Blue counts from F10 cell counts. As alluded in the previous sections this helped us with offset compensation. The system used for the measurement is ditto for both the Blue and Green counts. This means that all external artifacts and noise sources are identical in both measurements. The beauty of using this is that when we subtract the two measurements we mitigate by far the effects of most of these common artifacts. Since these are two independent data sets we first find the variance for each

data set and then use that to get the Gaussian error of propagation as we cannot directly subtract the standard deviations directly. The excitation wavelength needed for the FRET probe was 435 nm, we used an LED of 425 nm, which is quite close to this, as the 435 nm is near the peak transmission power of the LED. However, even though the LED has a sharp bandwidth there is an exponential decay when observed on the log-log scale with a photo-spectrometer. This decay has an overlap not only with the filter cut-off wavelength but also the bandwidth over which the photo-detector integrates the photon counts. At first sight, it might appear that these components just cancel each other when the counts are subtracted. However, the important issue that obviates this, is that the photo conversion efficiency of the photo-detector is not exactly the same over the working bandwidth for both the blue and green pixels. This is because, ideally, we would need a measuring device, with the photo-detector and/or a sharp bandpass filter to collect light only over 485nm and 535 nm and calculate the counts with the same transmission efficiency characteristics as the used RGB photodetector. Given this limitation, we can interpret the difference of the two counts as being qualitatively close to the Blue and Green emission components of F10 cells FRET probe. It is however clear that the Green component of the fluorescence is much higher than the Blue component of the fluorescence which validates the qualitative working principle of the FRET probe as the Green wavelength is indeed strongly expressed by the FRET probe as opposed to the Blue wavelength. This rationale is applicable for all the filters tested in the scope of this thesis.

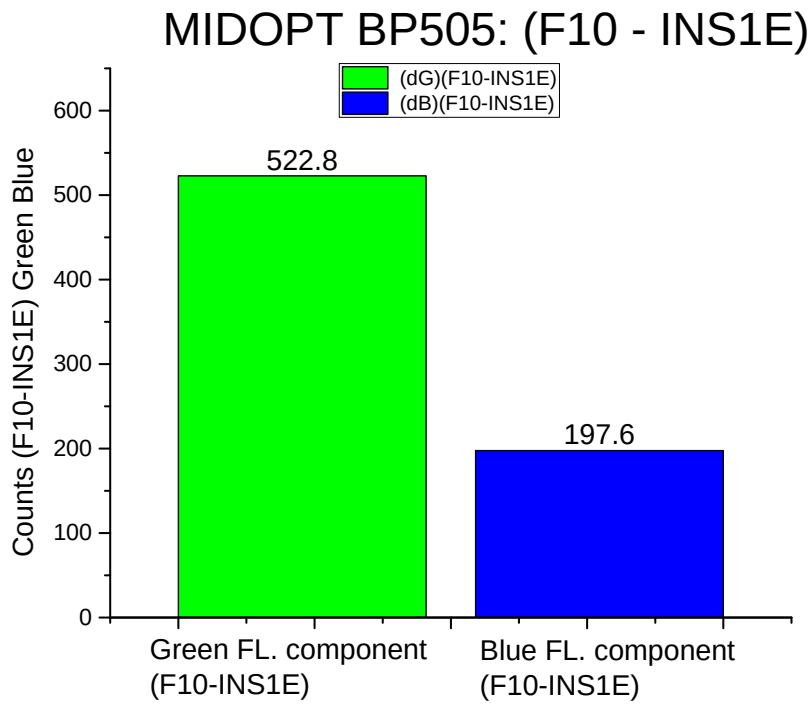

Figure 3.6 – MIDOPT BP505 (F10 - INS1E) Counts for Blue and Green. The Gaussian error of propagation for the Blue count is 2.55 counts and Green Count is 3.59 counts.

MIDOPT BP505 (Green - Blue) for INS1E and F10 Cells.

Figure 3.7 shows the result of subtracting the Green and Blue components of light to demonstrate the efficacy of the filter for both INS1E and F10 cell counts.

It is clear that in both cases there is a higher component of the Blue counts on both the photo-detector pixels indicating a higher amount noise and artifacts. The Green-Blue for the INS1E cells was -518.6 while that for the F10 cells was -193.4. The lower difference of -193.4 in the F10 cells is indicative of the FRET probe and the fluorescence effect.

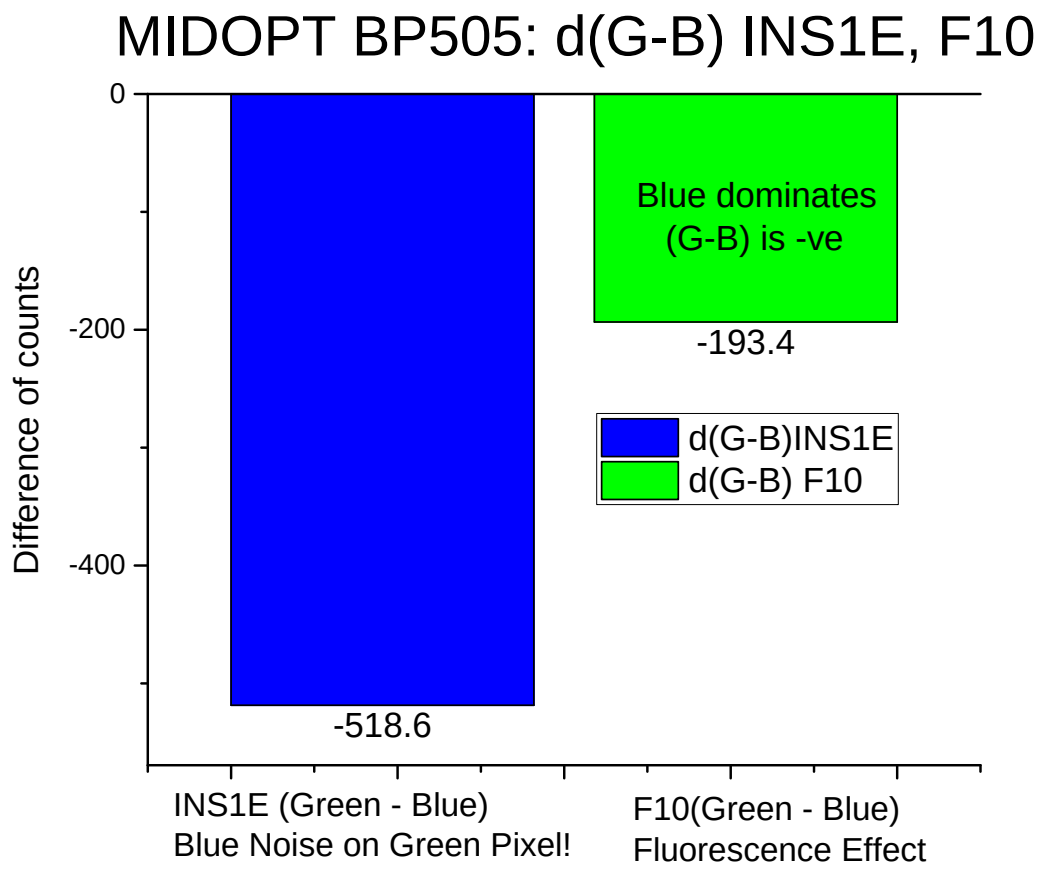

Figure 3.7 – MIDOPT BP505 (Green - Blue) for both INS1E and F10 Cells. This graph shows if strength of the Green vs Blue components of the light as a function of the filtering efficacy of the filter and also elucidates the effect of the overlapping wavelength range among the Green and Blue pixels of the PD and the leakage from spectrum of the excitation LED's FWHM range.

MIDOPT BP505 (green/blue) ratio for INS1E and F10 Cells.

Figure 3.8 shows the ratio of the green/blue counts for both INS1E and F10 cells. Since we use a Ca^{2+} signalling FRET probe that works on a ratio metric principle, this is one of the most

important measurements to be analyzed.

The ratio for the INS1E cells was 0.52 while that for the F10 cells was 0.85. This clearly shows the signature of the FRET probe producing the florescence in the cell culture medium, when excited with the 435 nm light, was the YFP and CFP molecules come closer than 10 nm in distance and thus create a sub-conduction band tunneling and emit, a light at a lower energy or a higher wavelength of 535 nm.

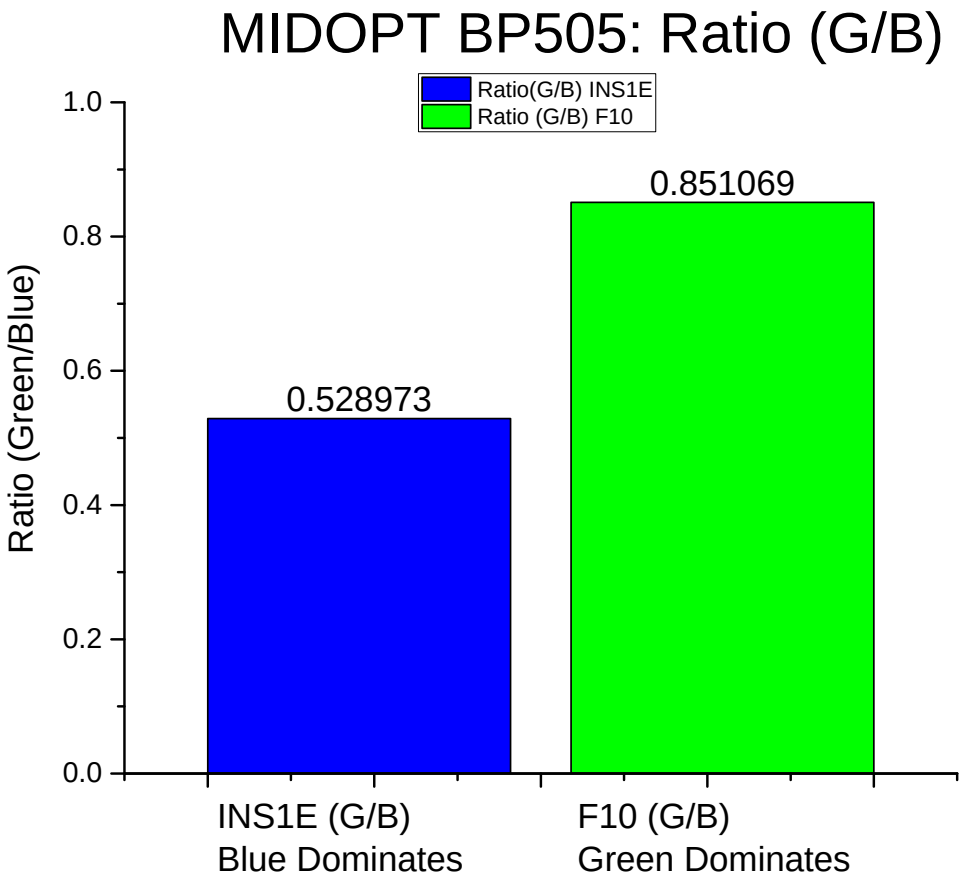

Figure 3.8 – MIDOPT BP505 (Green/Blue) Ratio for both INS1E and F10 Cells. The standard deviation of the ratio for the INS1E cells was 0.5209 or 0.15%. The standard deviation of the ratio for the F10 cells was 0.85 or 0.15%.

MIDOPT BP505 efficacy on the overall change Signal to Noise (SNR) ratios

Figure 3.9 shows the ratio of the green/blue counts for both INS1E and F10 cells.

There is 60.98% improvement in the ratio between the F10 and INS1E cells. Measurements were made without the filter, with just the bare photodiode in the electronic system and the relative change measured w.r.t the case when the optical absorption filter was used. We observe 162.8%

improvement in the ratio for the INS1E cells and a significant 301.79% change in the ratio in the case of the F10 cells. Overall, the performance using this filter was definitely among the better ones. However, these results were not the best in terms of the overall performance of the system.

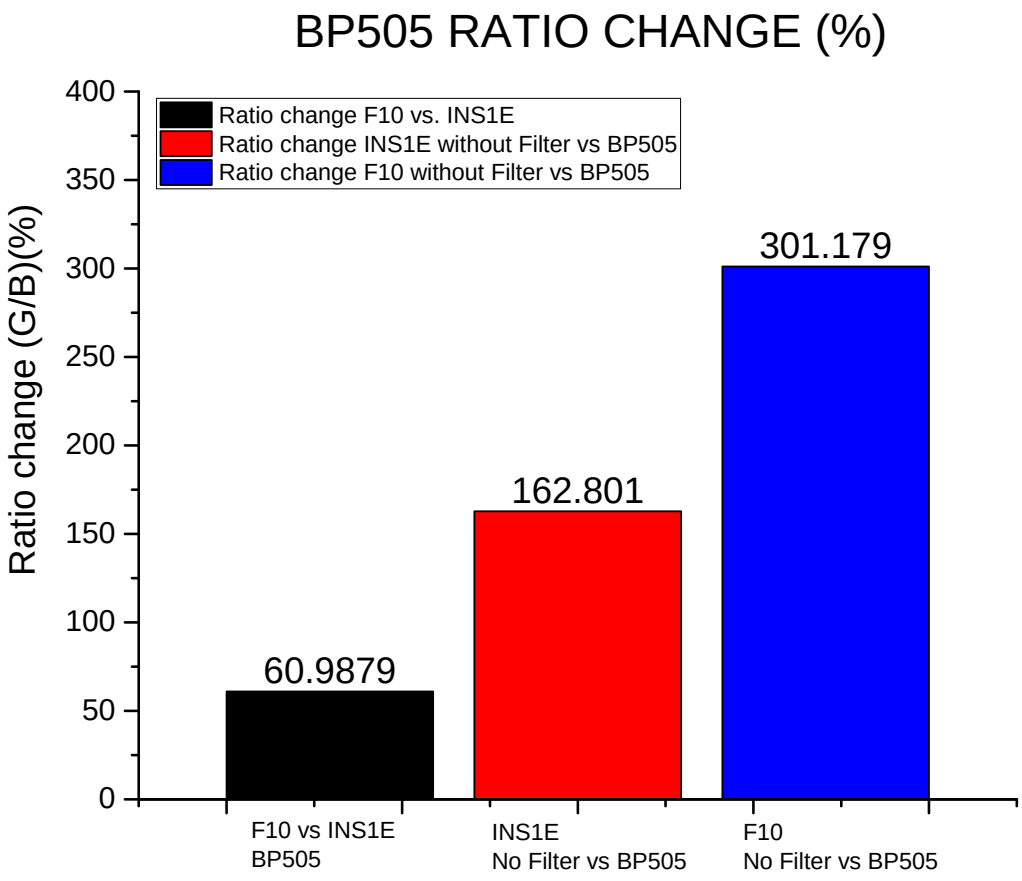

Figure 3.9 – MIDOPT BP505 change in ratio with the filter for both INS1E and F10 cells. This graph shows a high level picture of the impact of the optical filter as it helps improve the SNR significantly. The F10 cells ratio is significantly higher than that of the INS1E cells as it has the FRET probe and in both cases there is 162.8% and 301.79% improvement in the SNR as opposed to without a filter.

3.3.2 MIDOPT LP470 Light Yellow Longpass Filter

The MIDOPT LP470 Cyan Bandpass filter is shown in Figure 3.10. It is an absorption based angle independent filter that is cut into the dimensions of the photo detector to be placed atop for emission filtering of the light. This filter was tested with the F10 cell probe as the emissions of the probe were at 485 nm and 535 nm. The main goal was to reject as much reflection and exponential residue of the light from the 435 nm excitation LED. The transmission of wavelengths

$\leq$ 450 nm was 0.02% [14]. At the same time the transmission around the 485 nm was around 87% and that around 535 nm was around 98.3% [14]. This made it an excellent choice for the noise rejection but was also very interesting owing to the high transmission ranges at the two wavelengths of interest. The filter was diced in Center of micro-nanotechnology at EPFL, namely the CMi.

The optical characteristics of this filter are listed below:

- Useful Range : 480-1100 nm
- Cut-on Wavelength 50 % T : 470 nm
- Tolerance : +/- 10nm
- Peak Transmission : $\geq$ 90 %
- Surface Quality : 40/20

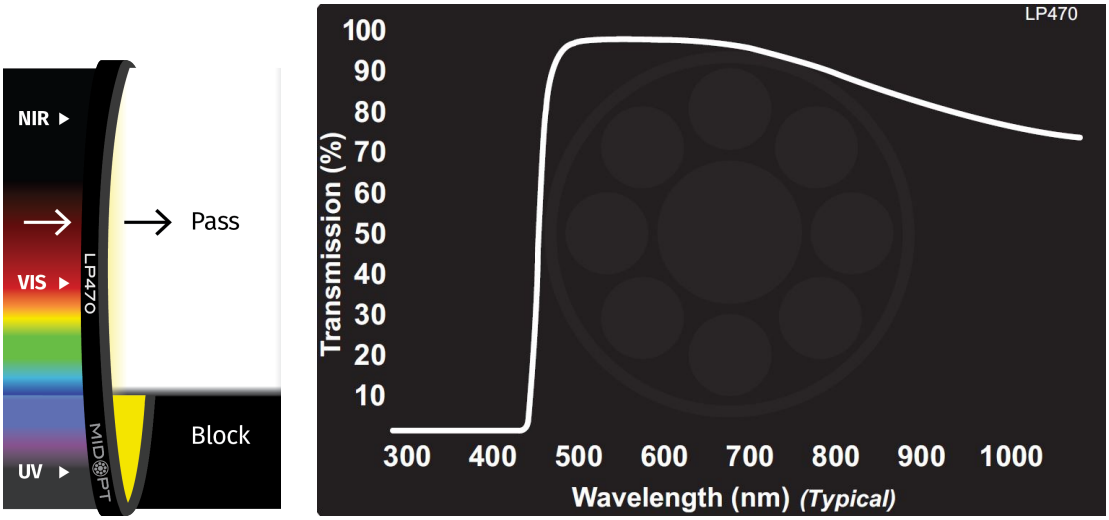

(a) LP470 Light Yellow Long-pass Filter

(b) LP470 Transmission Data (Typical)

Figure 3.10 – LP470 Cyan Bandpass Filter. Working principle and transmission data. Source [14]

The filter was systematically characterized for several optical parameters with the INS1E and F10 cells with the genetic FRET probe. The ratios of the green/blue counts were analyzed and discussed, along with probing insights into the absolute value of the photodetector counts and their differences for each cell type and between the cell types.

In the parlance of optics a long pass filter passes the higher wavelengths of light and rejects the ones below. The following section below elucidates each in detail.

MIDOPT LP470 INS 1E Cells

The characterization of the INS 1E cells with the MIDOPT LP 470 is described in this section. It can be seen from Figure 3.11 that the INS1E green counts, over a sample of five data points, that the green counts were 777.6 and the blue counts were 1153.6. The standard deviation was negligible in both cases.

The key insights here are that the filter is first even at 100 mA LED bias current and 22.4 ms integration time able to keep the absolute value of the counts well within the dynamic range of the 16 bit photo-detector, thus giving us room to add more cell aggregates and most importantly not saturating the photodetector.

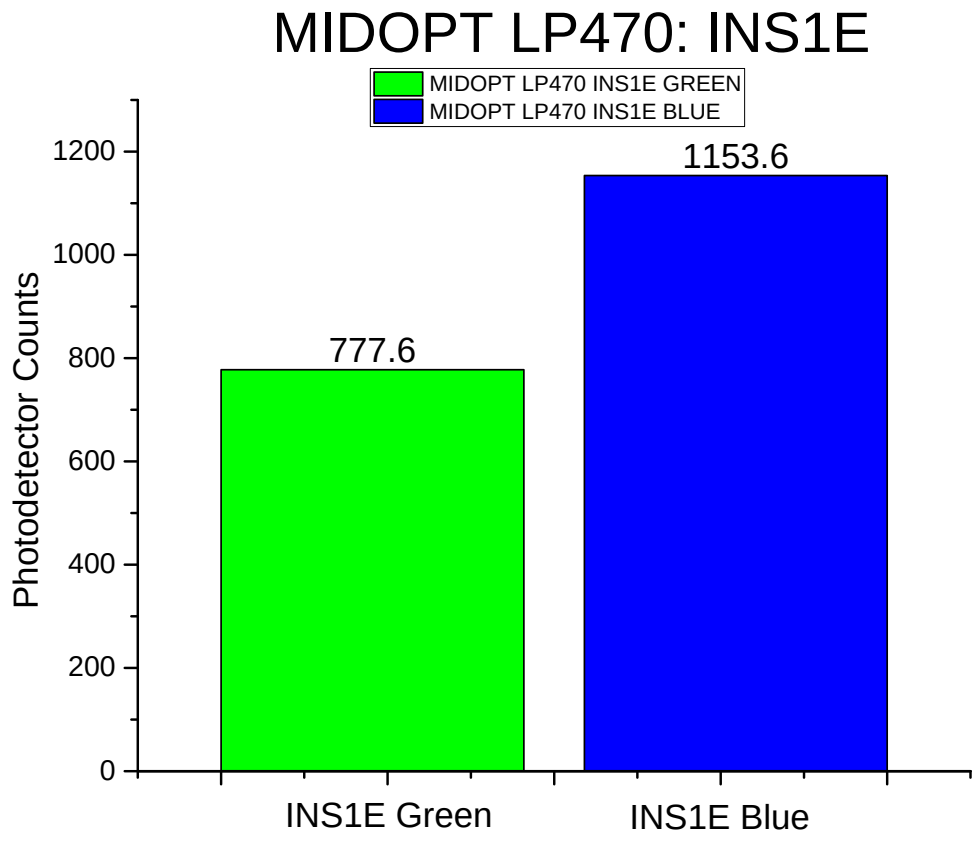

Figure 3.11 – MIDOPT LP470 INS 1E Cells Blue and Green. The standard deviation for the Blue count was 2.07 counts or 0.18 %. The standard deviation for the Green count was 2.4 counts or 0.3%.

MIDOPT LP470 F10 Cells

Figure 3.12 shows the green and blue counts of the F10 cells, over a sample of five data points, the green counts were 1847.6 counts and the blue counts were 1501.4.

The counts are very well marked with two distinct levels. These separate non-overlapping signatures add a degree of clarity into distinguishing these cells. The values also clearly demonstrate that the blue counts are higher than the green ones, hence, verifying that the probe is non-existent. These distinct count levels enable offset calibration when used in relation to the F10 cells that have the probe. The offset correction was necessary as the reflections arise from various sources including the petri dish, the mechanical 3D printed part creating auto-fluorescence and the cell culture medium that reflects off right owing to its light red color. Given this limitation, we can interpret the difference of the two counts as being qualitatively close to the Blue and Green emission components of the F10 cells FRET probe.

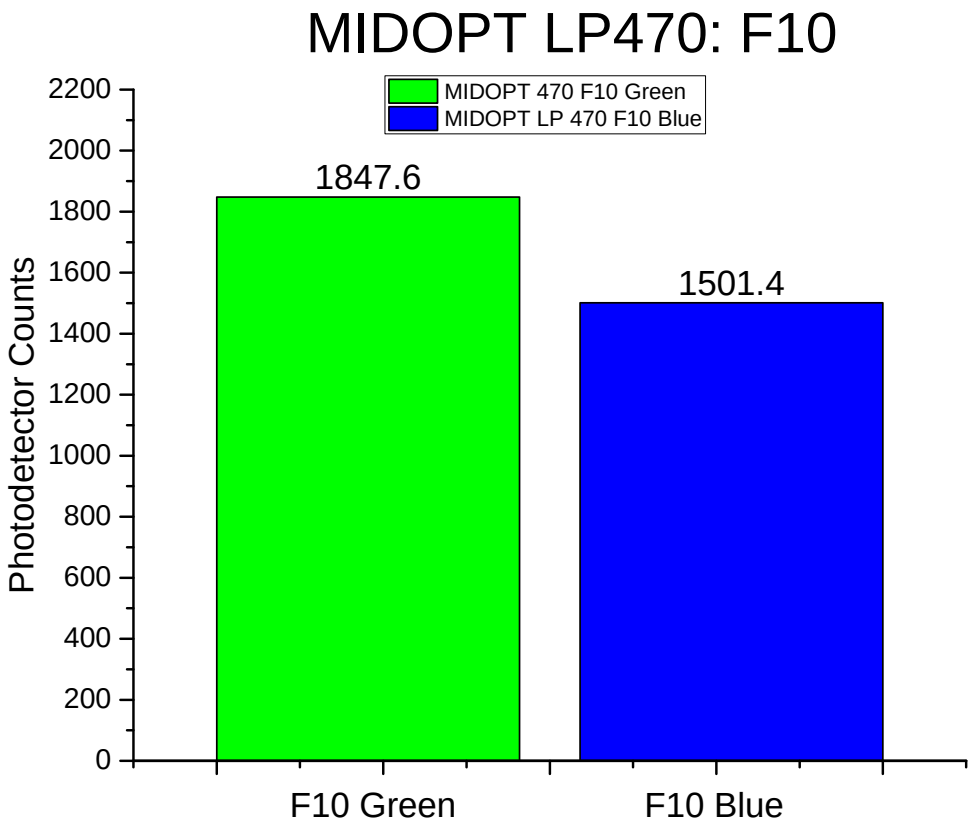

Figure 3.12 – MIDOPT LP470 F10 Cells Blue and Green.The standard deviation for the Blue count was 0.89 counts or 0.05 %. The standard deviation for the Green count was 5.54 counts or 0.3%.

MIDOPT LP 470 (F10 - INS1E) Cells for Green Fluorescence and Blue Fluorescence Components

Figure 3.13 shows the result after removing the INS1E component of the Green and Blue counts from the F10 cell counts.

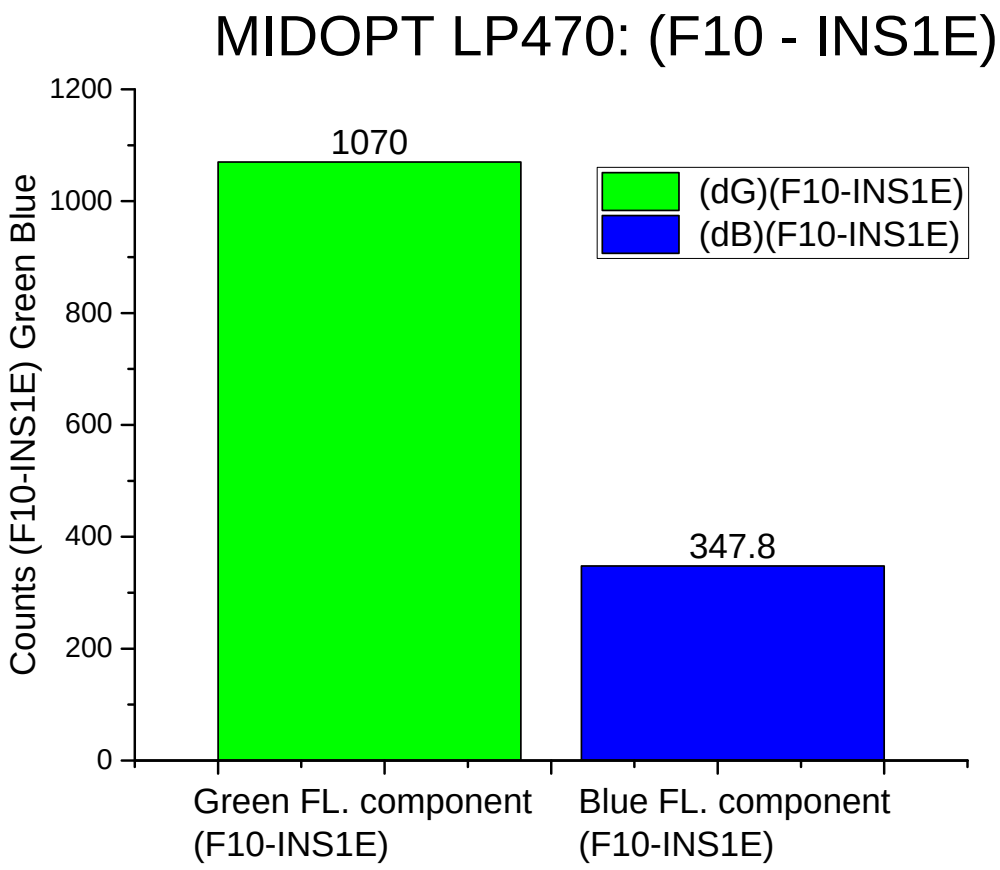

Figure 3.13 – MIDOPT LP470 (F10 - INS1E) Counts for Blue and Green. The Gaussian error of propagation for the Blue count is 2.25 counts and Green Count is 6.03 counts.

The efficacy of the filter is really evident here as opposed to the MIDOPT BP 505 bandpass filter with the green fluorescence component being 1070 counts and the blue being 347.8 counts.

MIDOPT LP470 (Green - Blue) for INS1E and F10 Cells.

It is clear that in both cases there is a higher component of the Blue counts on both the photo-detector pixels indicating a higher amount noise and artifacts. The Green-Blue for the INS1E cells was -376 while that for the F10 cells was +346.2. There is almost a two fold increase in the dynamic range of the counts with the MIDOPT LP470 filter vs the MIDOPT BP 505 with respect

to the difference in the INS1E and F10 cells. There is significant improvement in performance for this application in comparison to the MIDOPT BP 505 bandpass filter.

Figure 3.14 shows the result of subtracting the Green and Blue components of light to observe the efficacy of the filter for both INS1E and F10 cell counts. A higher and more positive value of this difference is clearly an indicator of higher fluorescence from the green component of the light. A lower value is indicative not only of a lower fluorescence but also for lack of a specific filters performance in its ability to reject the blue reflections arising from the auto-fluorescence of its mechanical components and the direct reflections from the petri dish with the cell culture medium, all of which is integrated over the PD pixels.

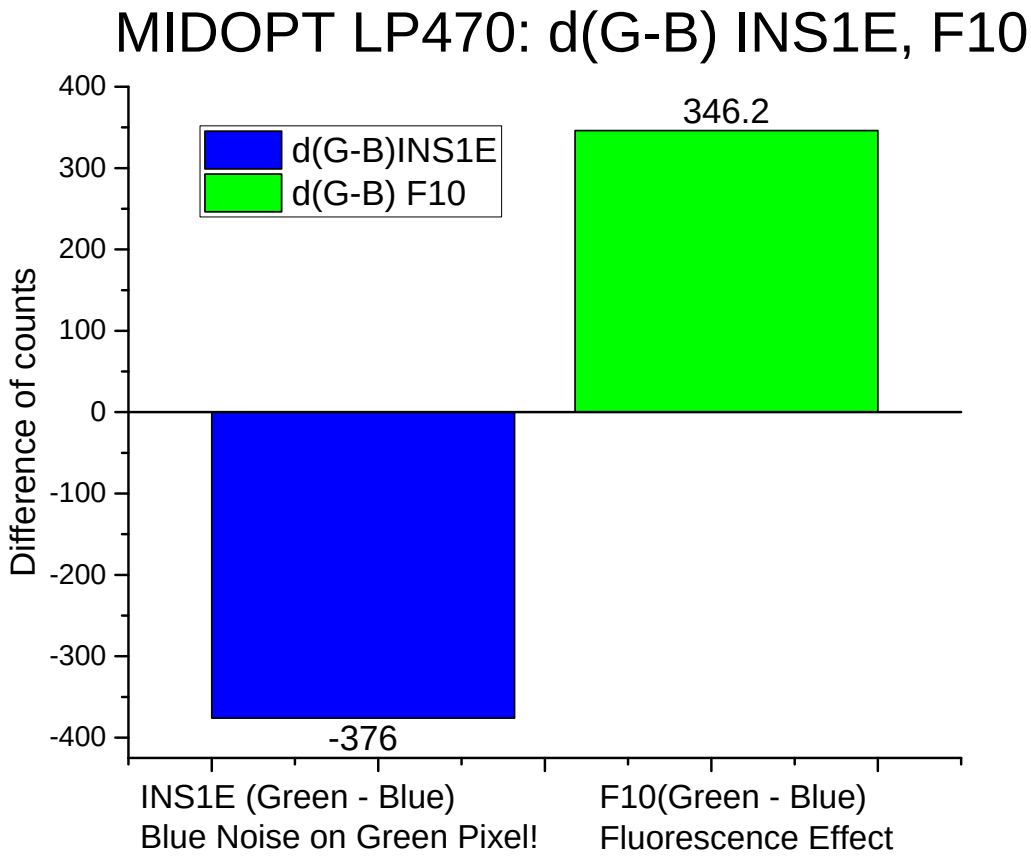

Figure 3.14 – MIDOPT LP470 (Green - Blue) for both INS1E and F10 Cells. This graph shows if strength of the Green vs Blue components of the light as a function of the filtering efficacy of the filter and also elucidates the effect of the overlapping wavelength range among the Green and Blue pixels of the PD and the leakage from spectrum of the excitation LED's FWHM range. In this case a clear fluorescent signal is seen in the F10 cells.

MIDOPT LP 470 (green/blue) ratio for INS1E and F10 Cells.

Figure 3.15 shows the ratio of the green/blue counts for both INS1E and F10 cells. Since we use a Ca^2 signaling FRET probe that works on a ratio metric principle, this is one of the most important measurements to be analyzed. The measurement configuration parameters are described in the caption in Figure 3.15. The ratio for the INS1E cells was 0.67 while that for the F10 cells was 1.23. This clearly shows the signature of the FRET probe producing the florescence in the cell culture medium when excited with the 435 nm light was the YFP and CFP molecules come closer than 10 nm in distance and thus create a sub-conduction band tunneling and emit a light at a lower energy or a higher wavelength of 535 nm. This is a significant improvement in the ratio in comparison to the MIDOPT BP505 filter.

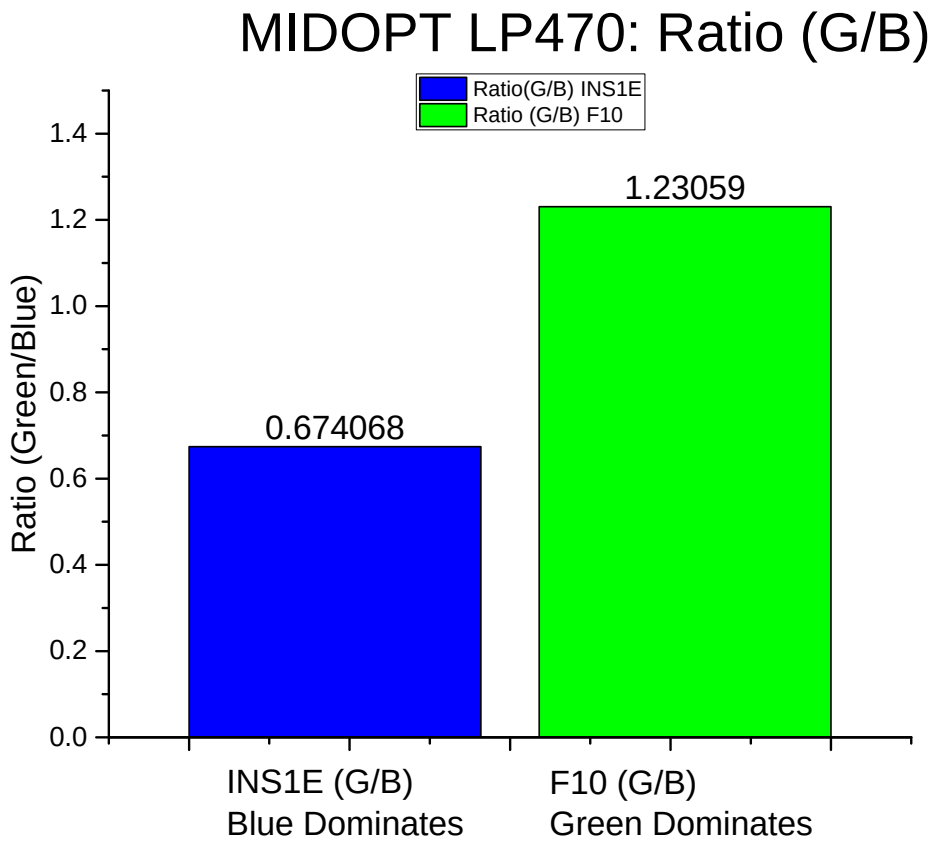

Figure 3.15 – MIDOPT LP470 (Green/Blue) Ratio for both INS1E and F10 Cells. The standard deviation of the ratio for the INS1E cells was 0.0032 or 0.48%. The standard deviation of the ratio for the F10 cells was 0.0043 or 0.34%.

MIDOPT LP 470 efficacy on the overall change Signal to Noise (SNR) ratios

Figure 3.16 shows the ratio of the green/blue counts for both INS1E and F10 cells.

There is 82% improvement in the ratio between the F10 and INS1E cells. Measurements were made without the filter, with just the bare photodiode in the electronic system and the relative change was measured w.r.t the case when the optical absorption filter was used. We see 234% improvement in the ratio for the INS1E cells and a significant 480% change in the ratio in the case of the F10 cells.

Overall, the performance with this filter definitely better than MIDOPT BP 505.

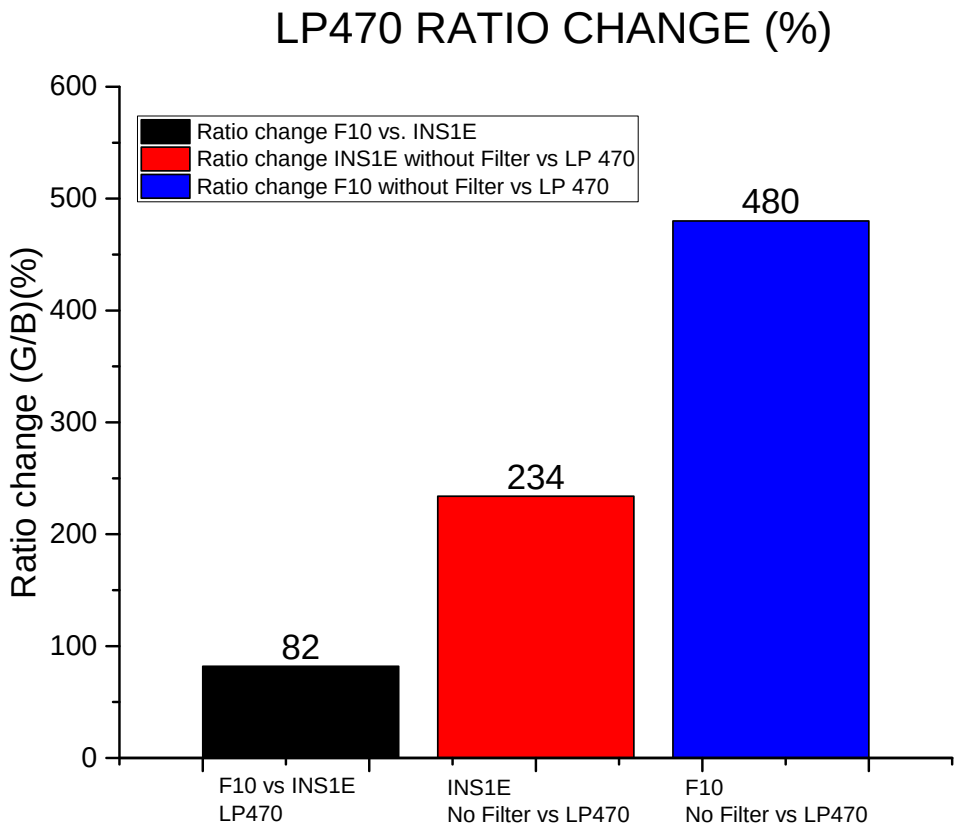

Figure 3.16 – MIDOPT LP470 change in ratio with the filter for both INS1E and F10 cells. This graph shows improvement of the SNR. The F10 cells ratio is significantly higher than that of the INS1E cells as it has the FRET probe and in both cases there is 234% and 480% improvement in the SNR as opposed to without a filter.

3.3.3 Fuji Angle Independent Tri Acetyl Cellulose Filter: SC 46

Figure 3.17 shows the picture of the Fiji sharp cut (SC) Tri Acetyl Cellulose Filter and its transmission characteristic. As seen this is a thin sheet of filter that looks yellowish in color and is very pertinent based on its transmission characteristics.

(a) Fuji Tri Acetyl Cellulose Filter SC 46

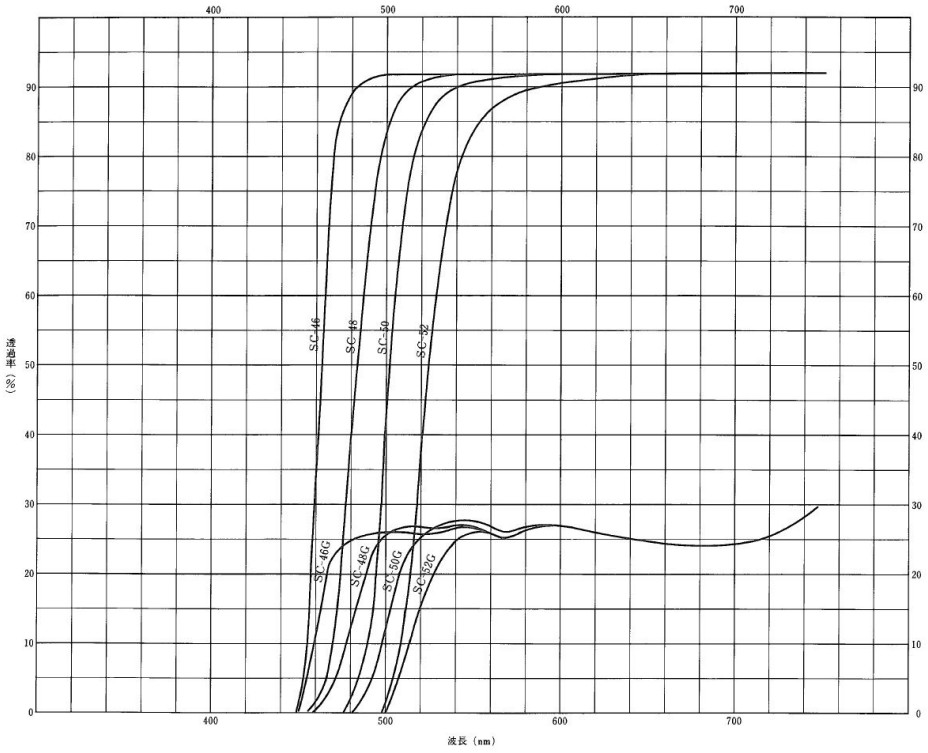

(b) Fuji SC 46 Transmission Data (Typical) X axis-Wavelength, Y-axis: Transmission Percentage

Figure 3.17 – Fuji Angle Independent Tri Acetyl Cellulose Filter: Sharp Cut SC 46. SC 46 transmission data. Source [15]

The filter has a flat transmission percentage of more than 90% and it takes about 25 nm from total cut off to maximum transmission.

The real conundrum for this filter is that the FC 46 filter, has the FWHM is just 20 nm shifted affecting the noise and the fluorescent components.

A thin-film of the filter was taken and then cut with a sharp automated cutting machine in the CMi at EPFL.

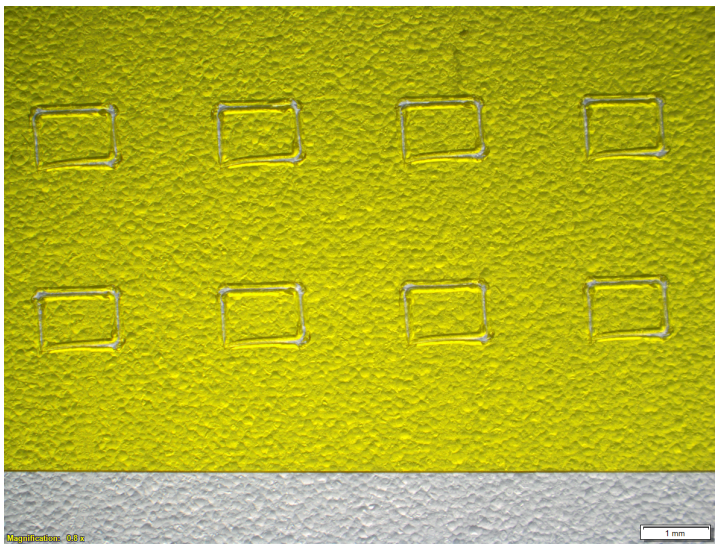

(a) Fuji Tri Acetyl Cellulose Filter SC 46 Substrate Adherence and Cutting

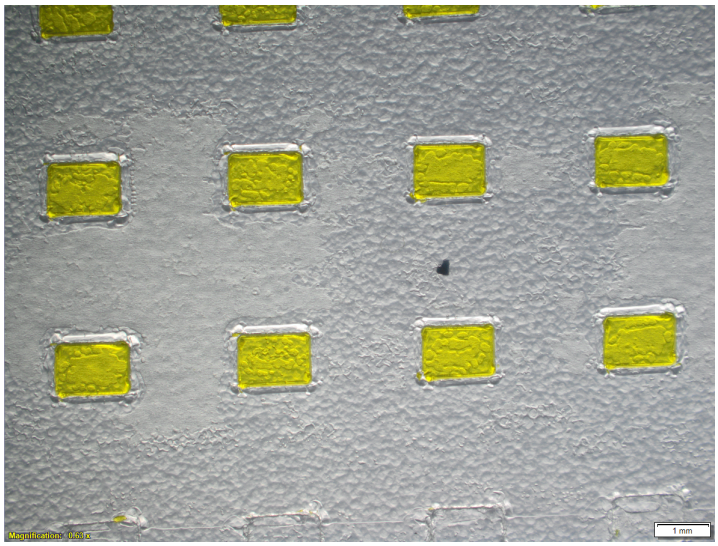

(b) Fuji SC 46 Filter adhered on a substrate and then cut with an automated cutter

Figure 3.18 – Fuji Angle Independent Tri Acetyl Cellulose Sharp Cut SC 46 Filter pieces after detaching the masked out material. Source [15]

Fuji SC 46 INS1E Cells

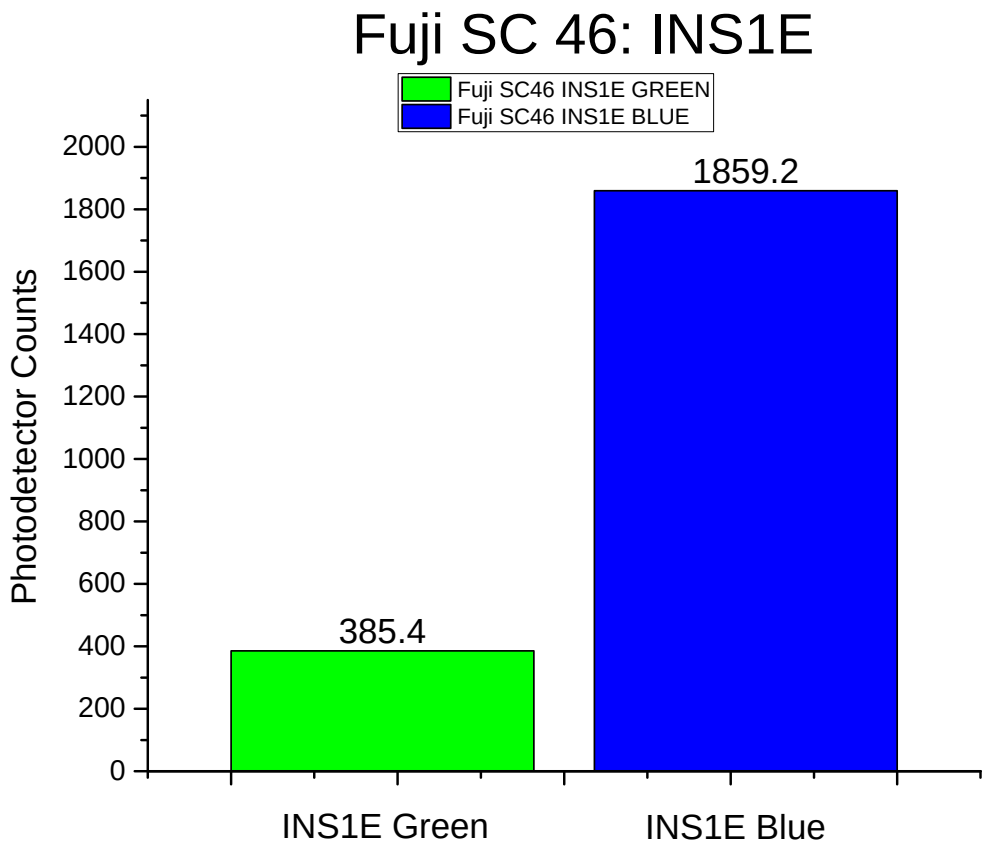

Figure 3.19 – Fuji SC 46 INS 1E Cells Blue and Green. The standard deviation for the Blue count was 3.34 counts or 0.18 %. The standard deviation for the Green count was 1.34 counts or 0.35%.

It can be seen from Figure 3.19 that the INS1E green counts over a sample of five data points were 385.4 and the blue counts were 1859.2. The standard deviation was negligible in both cases. The key insights here are that the filter is firstly even at 100 mA LED bias current and 22.4 ms integration time able to keep the absolute value of the counts well within the dynamic range of the 16 bit photo-detector. Thus giving us room to add more cell aggregates and most importantly not saturating the photodetector.

The counts are very well marked with two distinct levels and these separate non overlapping signatures add a degree of clarity into the distinguishing these cells. The values also clearly demonstrate that the blue counts are higher than the green ones, hence, verifying that the probe is non-existent. These distinct count levels enable offset calibration when used in relation to the F10 cells. From the first impression it looks obvious that this filter probably is not so effective in filtering the blue light.

Fuji SC 46 F10 Cells

It can be seen from Figure 3.20 that the F10 green counts, over a sample of five data points, were 1447.2 and the blue counts were 2263.4. The standard deviation was negligible in both cases. The counts are very well marked with two distinct levels and these separate non overlapping

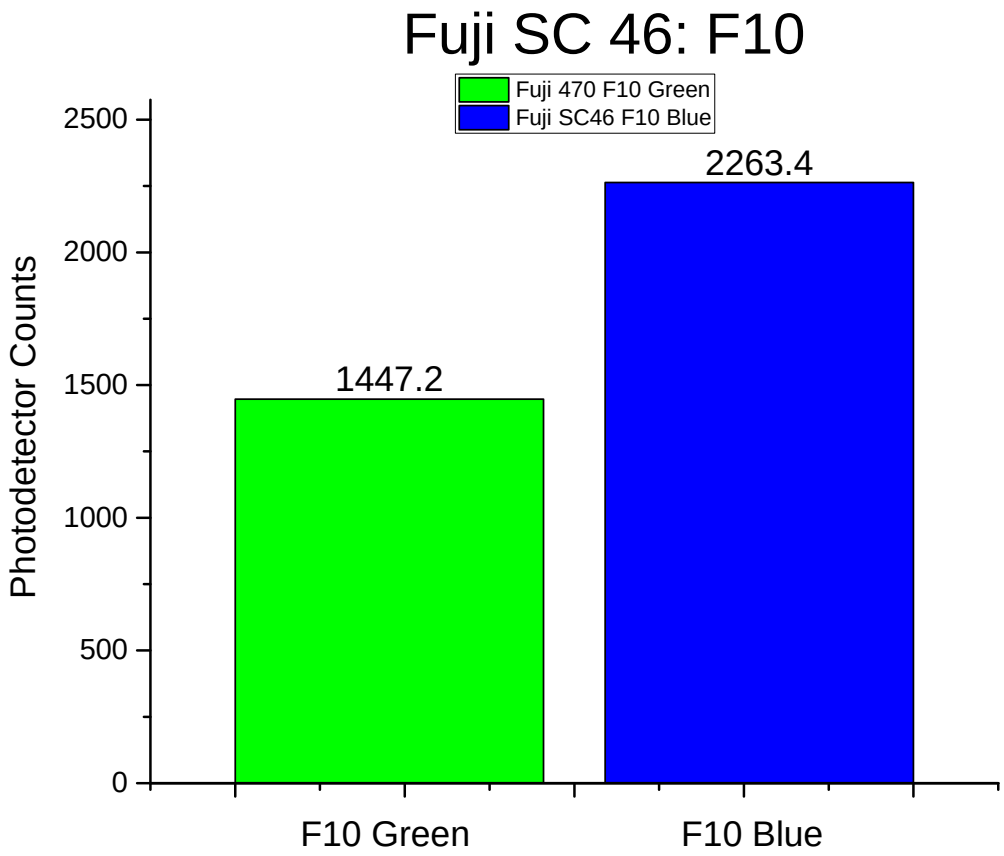

Figure 3.20 – Fuji SC 46 F10 Cells Blue and Green.The standard deviation for the Blue count was 1.51 counts or 0.06%. The standard deviation for the Green count was 2.16 counts or 0.15%.

signatures add a degree of clarity into the distinguishing these cells. The values also clearly demonstrate that the green counts are higher than the green counts of the INS1E cells, hence, verifying that the probe is existent in the F10 cells but the effect of the fluorescence is over shadowed by the noise of the blue counts. The same number of cells were used for both INS1E and F10 cells.

Fuji SC46 (F10 - INS1E) Cells for Green Fluorescence and Blue Fluorescence Components

Figure 3.21 shows the result after removing the INS1E component of the Green and Blue counts from the F10 cell counts. The green fluorescence component is 1061.8 counts while the blue fluorescence component is 404.2 counts.

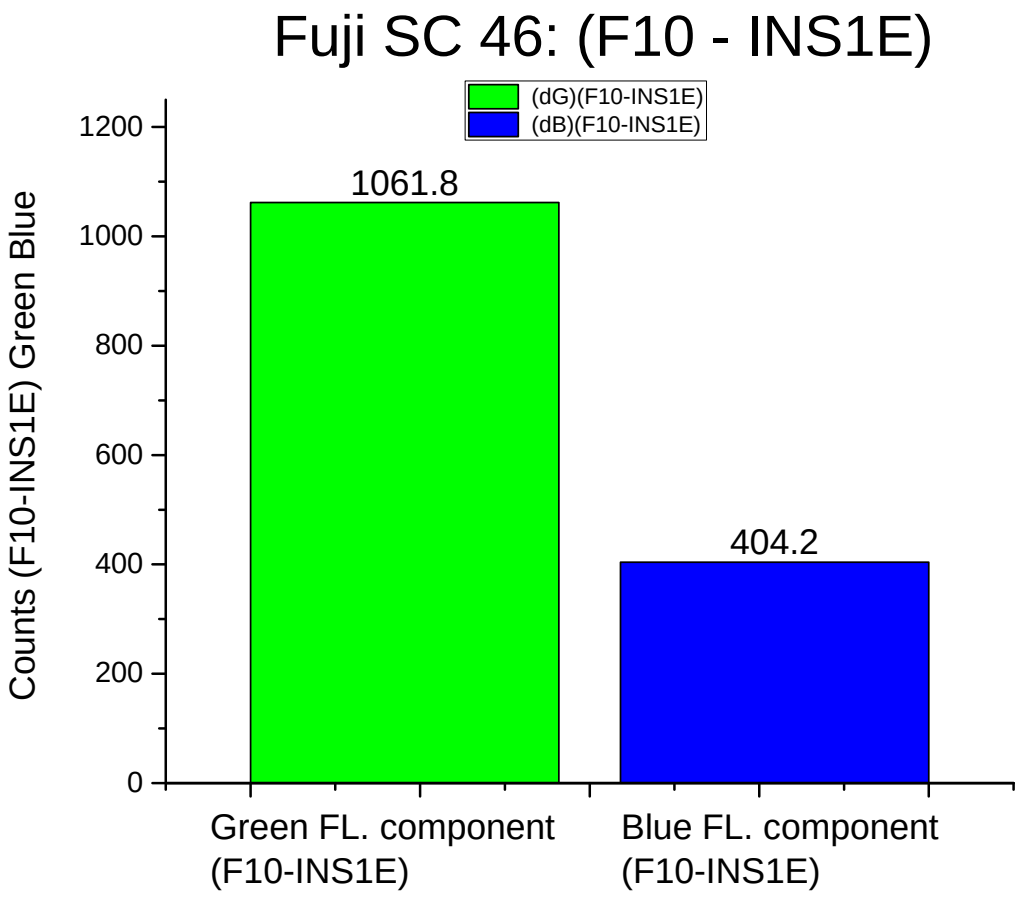

Figure 3.21 – Fuji SC 46 (F10 - INS1E) Counts for Blue and Green. The Gaussian error of propagation for the Blue count is 3.66 counts and Green Count is 2.54 counts.

Fuji SC46 (Green - Blue) for INS1E and F10 Cells.

Figure 3.22 shows the result of subtracting the Green and Blue components of light to observe the efficacy of the filter for both INS1E and F10 cell counts. It is clear that in both cases there is a higher component of the Blue counts on both the photo-detector pixels indicating a higher amount noise and artifacts.

The Green-Blue for the INS1E cells was -1473.8 while that for the F10 cells was -816.2. The

lower difference of -816.2 in the F10 cells is indicative of the FRET probe and the fluorescence effect. However, the magnitude of this difference is bigger than the MIDOPT filters, indicating once again that this filter is not so effective.

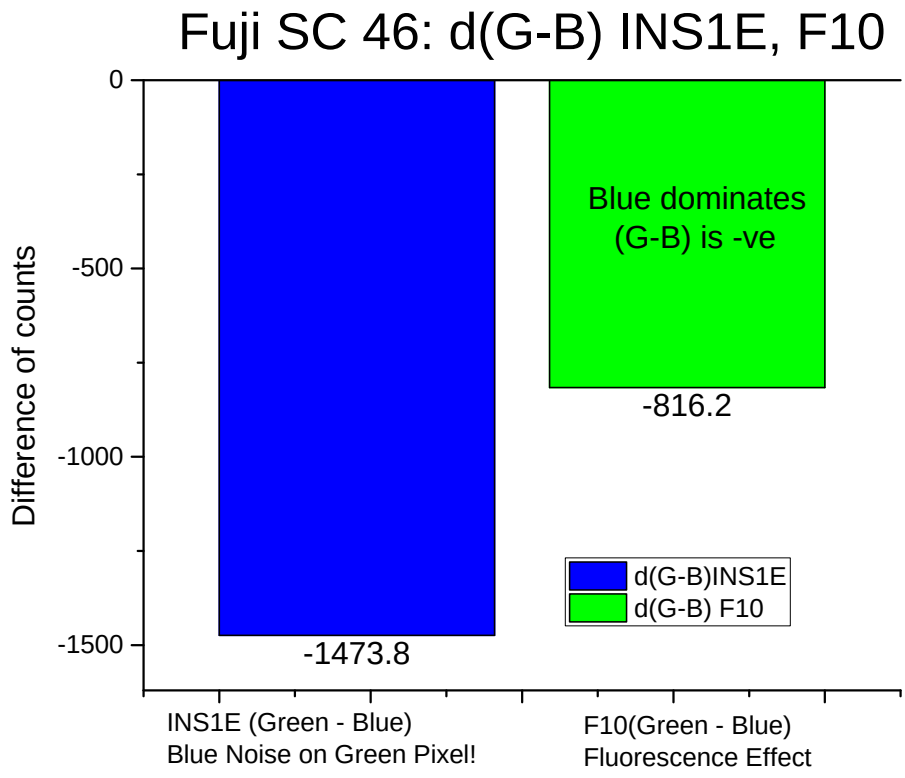

Figure 3.22 – Fuji SC 46 (Green - Blue) for both INS1E and F10 Cells. This graph shows if strength of the Green vs Blue components of the light as a function of the filtering efficacy of the filter and also elucidates the effect of the overlapping wavelength range among the Green and Blue pixels of the PD and the leakage from spectrum of the excitation LED's FWHM range. Clearly this filter does not have a very strong effect in discriminating the Blue and the Green counts.

Fuji SC46 (green/blue) ratio for INS1E and F10 Cells.

Figure 3.23 shows the ratio of the green/blue counts for both INS1E and F10 cells. Since we use a Ca^{2+} signaling FRET probe that works on a ratio metric principle, this is one of the most important measurements to be analyzed.

The ratio for the INS1E cells was 0.207 while that for the F10 cells was 0.639. This clearly shows the signature of the FRET probe producing the florescence in the cell culture medium when excited with the 435 nm light was the YFP and CFP molecules come closer than 10 nm in

distance and thus create a sub-conduction band tunneling and emit a light at a lower energy or a higher wavelength of 535 nm.

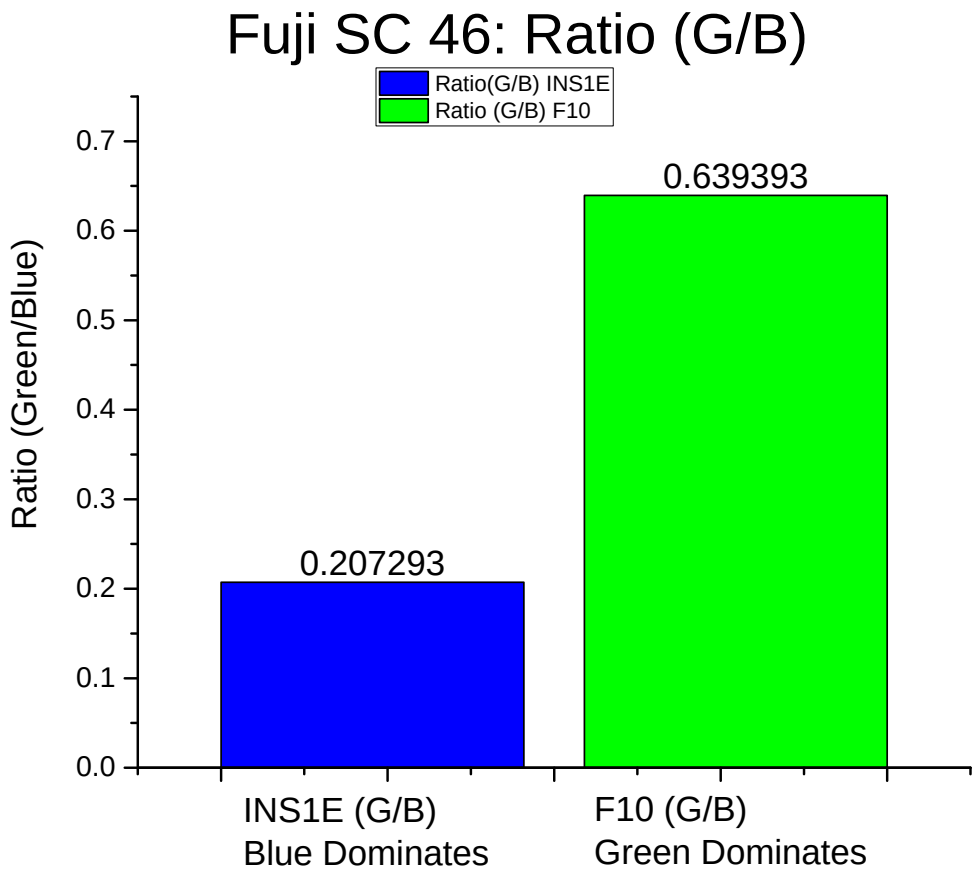

Figure 3.23 – Fuji SC 46 (Green/Blue) Ratio for both INS1E and F10 Cells. The standard deviation of the ratio for the INS1E cells was 0.0004 or 0.21%. The standard deviation of the ratio for the F10 cells was 0.0013 or 0.21%.

Fuji SC46 efficacy on the overall change Signal to Noise (SNR) ratios

Figure 3.24 shows the ratio of the green/blue counts for both INS1E and F10 cells.

There is a 208% improvement in the ratio between the F10 and INS1E cells. Measurements were made without the filter, with just the bare photodiode in the electronic system and the relative change was measured w.r.t the case when the optical absorption filter was used. We see a 2.98% improvement in the ratio for the INS1E cells and a significant 201.79% change in the ratio in the case of the F10 cells.

The reason for this small change with the INS1E is probably due to the surface imperfections of

the filter that make it hard to align atop the photodetector and this leads to a direct leaking of the blue light through those crevices. Moreover, dicing the filter sheet into smaller pieces the material expands on the edges leading to a very non-linear surface contour and also affects the filtering capacity.

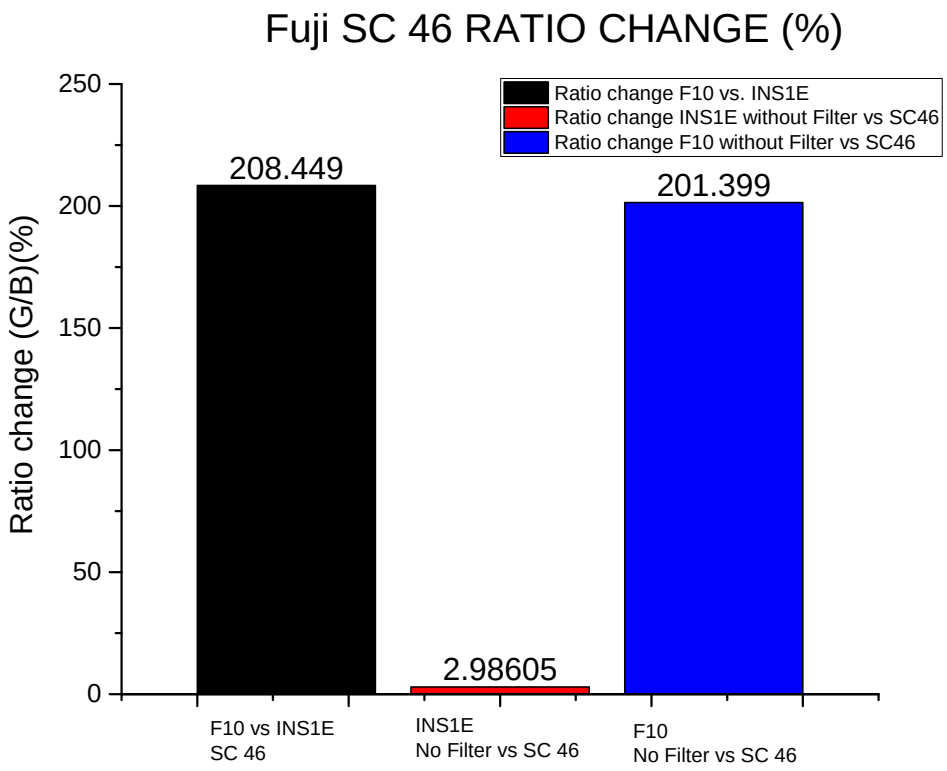

Figure 3.24 – Fuji SC 46 change in ratio with the filter for both INS1E and F10 cells. This graph shows a high level picture of the impact of the optical filter. It can be seen here that indeed the filter helps improve the SNR significantly only for the F10 cells and has almost no effect for the INS1E cells.

As shown in Figure 3.25 the Fiji SC 46 and SC 48 (next section) can have a lot of surface imperfections when cut from a filter film leading to uneven landscapes on the surface and sides of the filter. This is because of the mechanical stress that leads to a totally non-linear and random material expansion around the edges where the blade cutter passes through.

This leads not only to air gaps but also changes the native filter characteristics as absorption based filters, filter components of light based on their thickness, higher the thickness greater the filtering and vice-versa.

This is also one of the reasons adding to the lackluster performance of these filters for this application.

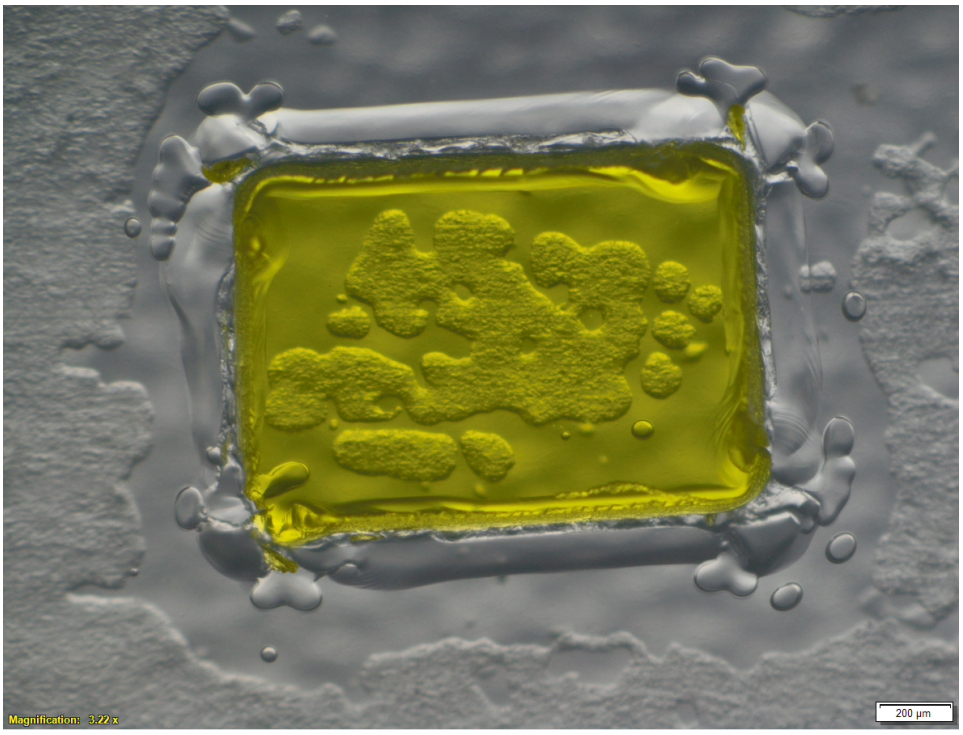

(a) Fuji Tri Acetyl Cellulose Filter SC 46 Surface imperfections

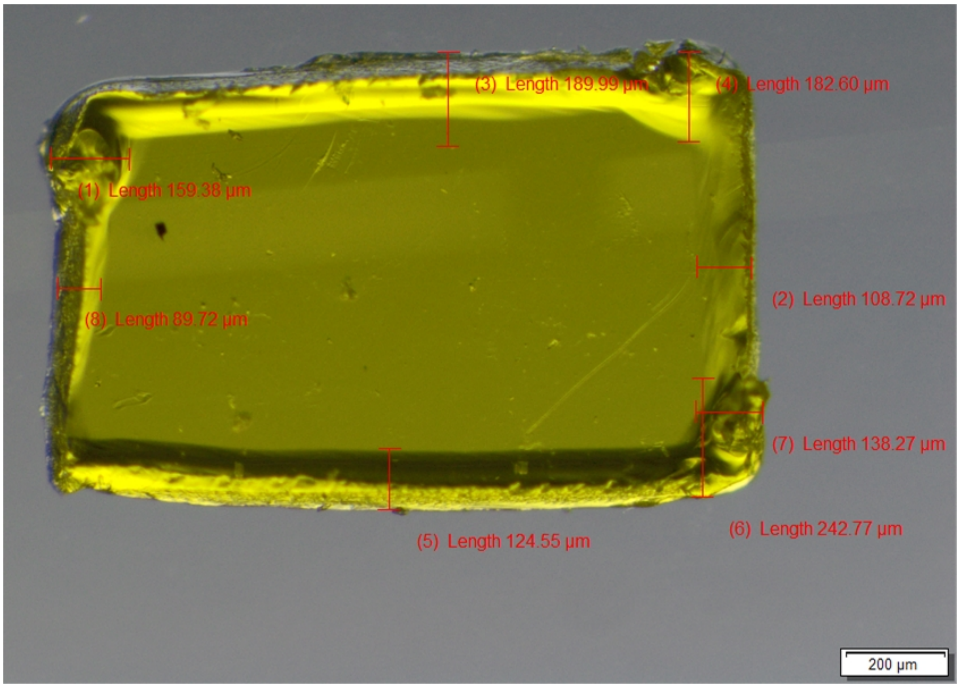

(b) Fuji SC 46 Filter Surface imperfections

Figure 3.25 – Surface imperfections and measured, mechanical stress causing non-linear material expansion around the edges of the filter. Source [15]

3.3.4 Fuji Angle Independent Tri Acetyl Cellulose Filter: SC 48

Figure 3.26 shows the picture of the Fiji sharp cut (SC) Tri Acetyl Cellulose Filter and its transmission characteristic.

As seen this is a thin sheet of filter that looks yellowish in color and is very pertinent based on its transmission characteristics.

(a) Fuji Tri Acetyl Cellulose Filter SC 48

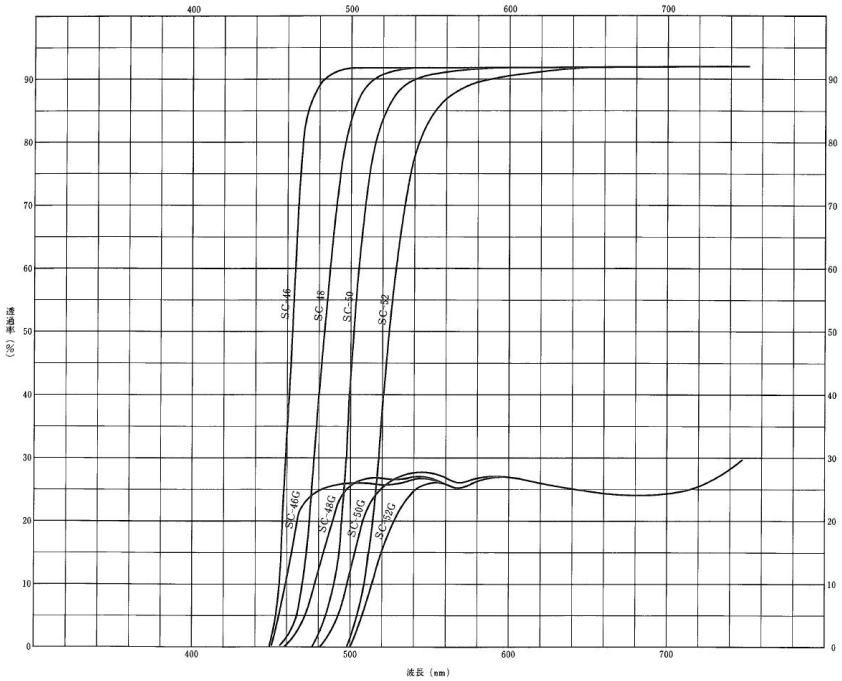

(b) Fuji SC 48 Transmission Data (Typical) X axis-Wavelength, Y-axis: Transmission Percentage

Figure 3.26 – Fuji Angle Independent Tri Acetyl Cellulose Filter: Sharp Cut SC 48. SC 48 transmission data. Source [15]

Fuji SC 48 INS1E Cells

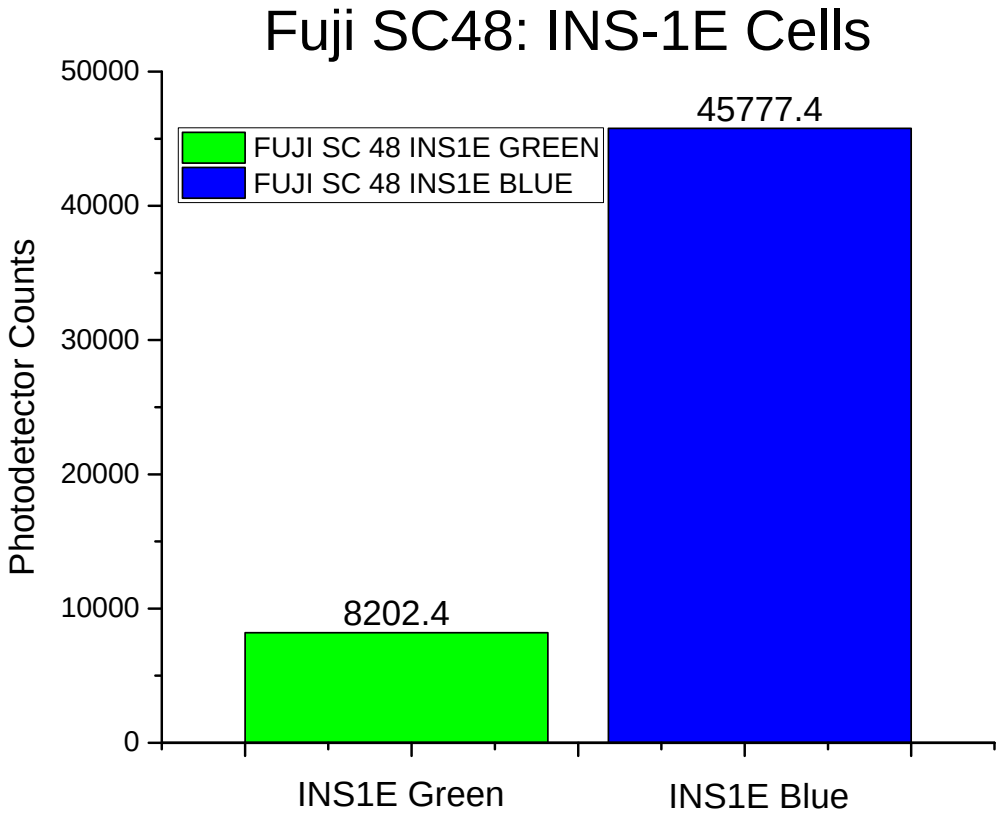

Figure 3.27 – Fuji SC 48 INS 1E Cells Blue and Green. The standard deviation for the Blue count was 108.67 counts or 0.23 %. The standard deviation for the Green count was 21.01 counts or 0.25%.

It can be seen from Figure 3.27 that the INS1E green counts, over a sample of five data points, were 8202.4 and the blue counts were 45777.4. The standard deviation was negligible in both cases. The key insights here are that the filter is firstly even at 100 mA LED bias current and 22.4 ms integration time able to keep the absolute value of the counts well within the dynamic range of the 16 bit photo-detector, thus giving us room to add more cell aggregates and most importantly not saturating the photodetector. The counts are very well marked with two distinct levels and these separate non overlapping signatures add a degree of clarity into the distinguishing these cells. The values also clearly demonstrate that the blue counts are higher than the green ones, hence, verifying that the probe is non-existent. These distinct count levels enable offset calibration when used in relation to the F10 cells that have the probe. The offset correction is necessary as the reflections arise from various sources including the petri dish, the mechanical 3D printed part creating auto-fluorescence and the cell culture medium that reflects off right owing to its light red color.

The blue count of 45777.4 indicative that the filtering capacity of this filter is very poor and it is also close to the upper limit of the dynamic range for this power. This issue can be even more significant at lower intensities of light.

Fuji SC 48 F10 Cells

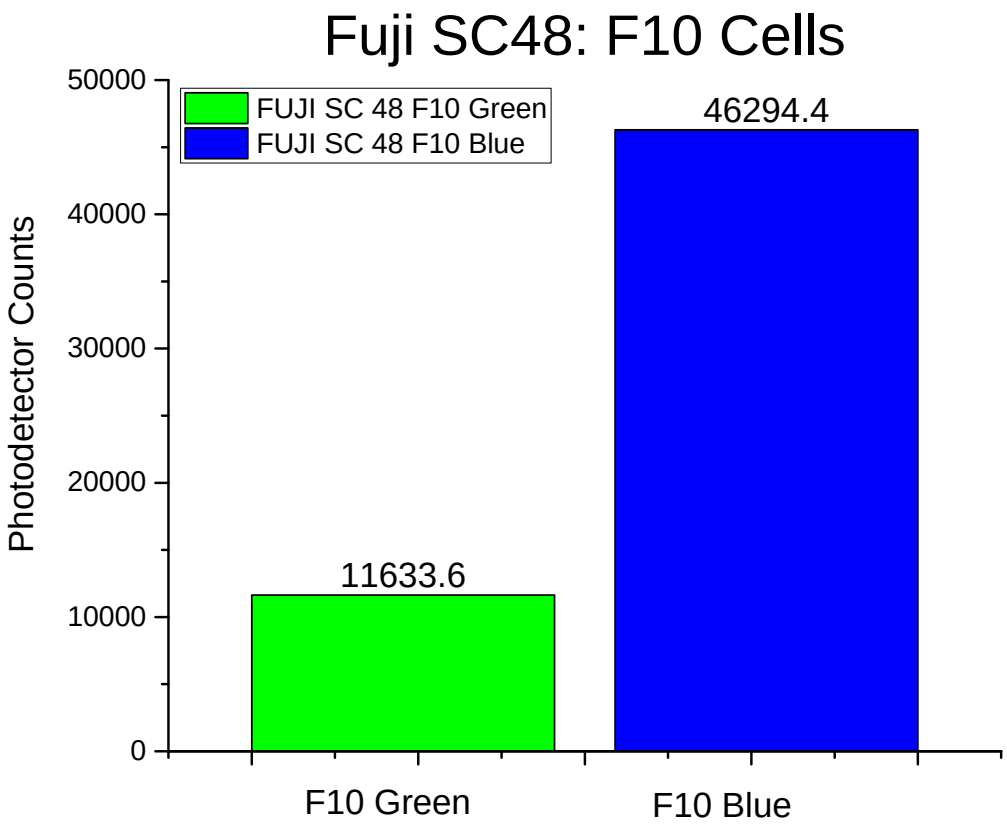

Figure 3.28 – Fuji SC 48 F10 Cells Blue and Green.The standard deviation for the Blue count was 111.72 counts or 0.24%. The standard deviation for the Green count was 44.42 counts or 0.38%.

It can be seen from Figure 3.28 that the F10 green counts, over a sample of five data points, were 11633.6 and the blue counts were 46294.4. The standard deviation was negligible in both cases. Even though the green counts are higher than in the case of the INS1E cells, the absolute value of the blue counts indicates the excessive blue count noise in the photo-detector pixels and the inability of the filter to block this component of light.

The key insights here are that the filter is firstly, even with a LED bias current of 100 mA and 22.4 ms integration time, able to keep the absolute value of the counts well within the dynamic

range of the 16 bit photo-detector, thus giving us room to add more cell aggregates and most importantly not saturating the photodetector. The counts are very well marked with two distinct levels and these separate non overlapping signatures add a degree of clarity into the distinguishing these cells. The values also clearly demonstrate that the green counts are higher than the green counts for the INS1E cells. Hence, verifying that the probe is existent in the F10 cells.

The effect of the fluorescence of the cells depends on the number, size and health of the 3D cell aggregates that were cultured. It should be noted that the same number of cells were used for both INS1E and F10 cells.

Fuji SC48 (F10 - INS1E) Cells for Green Fluorescence and Blue Fluorescence Components

Figure 3.29 shows the result after removing the INS1E component of the Green and Blue counts from the F10 cell counts.

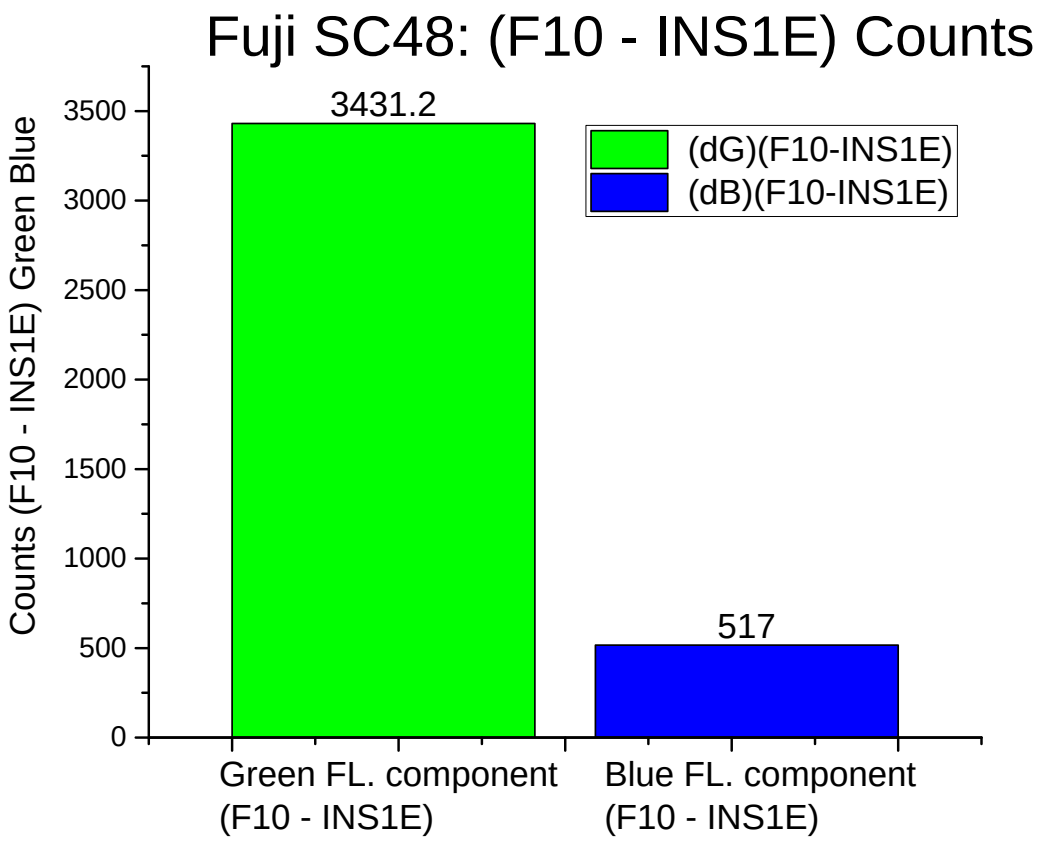

Figure 3.29 – Fuji SC 48 (F10 - INS1E) Counts for Blue and Green. The Gaussian error of propagation for the Blue count is 155.85 counts and Green Count is 49.57.

Fuji SC48 (Green - Blue) for INS1E and F10 Cells.

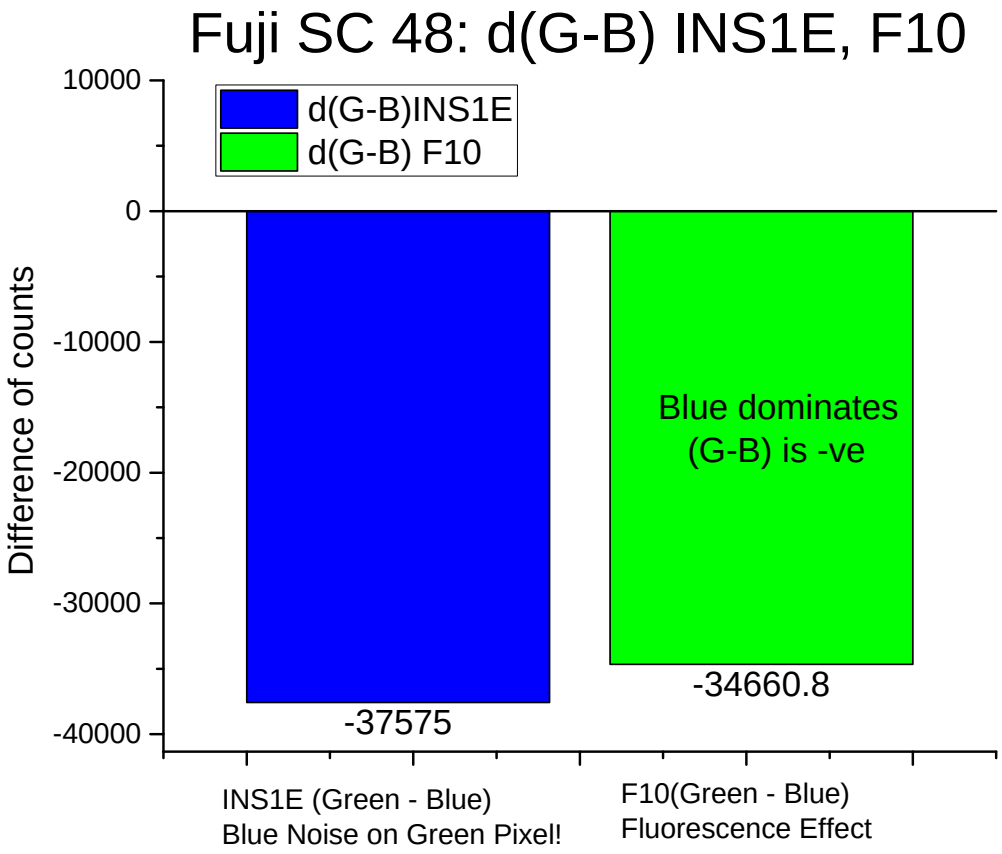

Figure 3.30 – Fuji SC 48 (Green - Blue) for both INS1E and F10 Cells. This graph shows if strength of the Green vs Blue components of the light as a function of the filtering efficacy of the filter and also elucidates the effect of the overlapping wavelength range among the Green and Blue pixels of the PD and the leakage from spectrum of the excitation LED's FWHM range.

Figure 3.30 shows the result of subtracting the Green and Blue components of light to observe the efficacy of the filter for both INS1E and F10 cell counts. It is clear that in both cases there is a higher component of Blue counts on both the photo-detector pixels indicating a higher amount noise and artifacts. The (Green-Blue) for the INS1E cells was -37575 counts while that for the F10 cells was -34660.8 counts.

Fuji SC48 (green/blue) ratio for INS1E and F10 Cells.

Figure 3.31 shows the ratio of the green/blue counts for both INS1E and F10 cells. Since we use a Ca^{2+} signalling FRET probe that works on a ratio metric principle, this is one of the most important measurements to be analyzed.

The ratio for the INS1E cells was 0.179 while that for the F10 cells was 0.251. This clearly shows the signature of the FRET probe producing the florescence in the cell culture medium when excited with the 435 nm light was the YFP and CFP molecules come closer than 10 nm in distance and thus create a sub-conduction band tunneling and emit a light at a lower energy or a higher wavelength of 535 nm. The change in the ratio, even though is at two distinct levels, is not significant with the F10 cells.

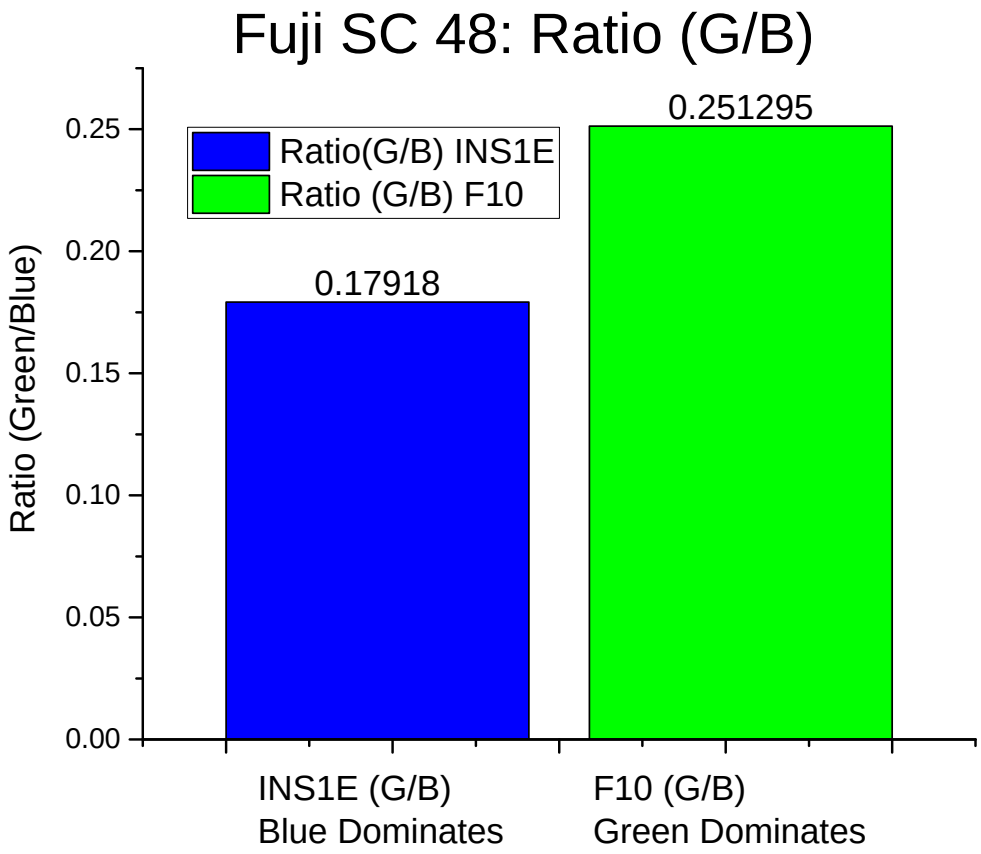

Figure 3.31 – Fuji SC 48 (Green/Blue) Ratio for both INS1E and F10 Cells. The standard deviation of the ratio for the INS1E cells was 0.00025 or 0.14%. The standard deviation of the ratio for the F10 cells was 0.00035 or 0.14%.

Fuji SC48 efficacy on the overall change Signal to Noise (SNR) ratios

Figure 3.32 shows the ratio of the green/blue counts for both INS1E and F10 cells.

There is 28.69% improvement in the ratio between the F10 and INS1E cells. Measurements were made without the filter, with just the bare photodiode in the electronic system and the relative change was measured w.r.t the case when the optical absorption filter was used. We see 0.388%

improvement in the ratio for the INS1E cells, which is close to nothing and a small 28.97% change in the ratio in the case of the F10 cells. Overall, the performance with this this filter was definitely poor and the FC 46 seems a better choice, while the MIDOPT filters outperform this filter clearly.

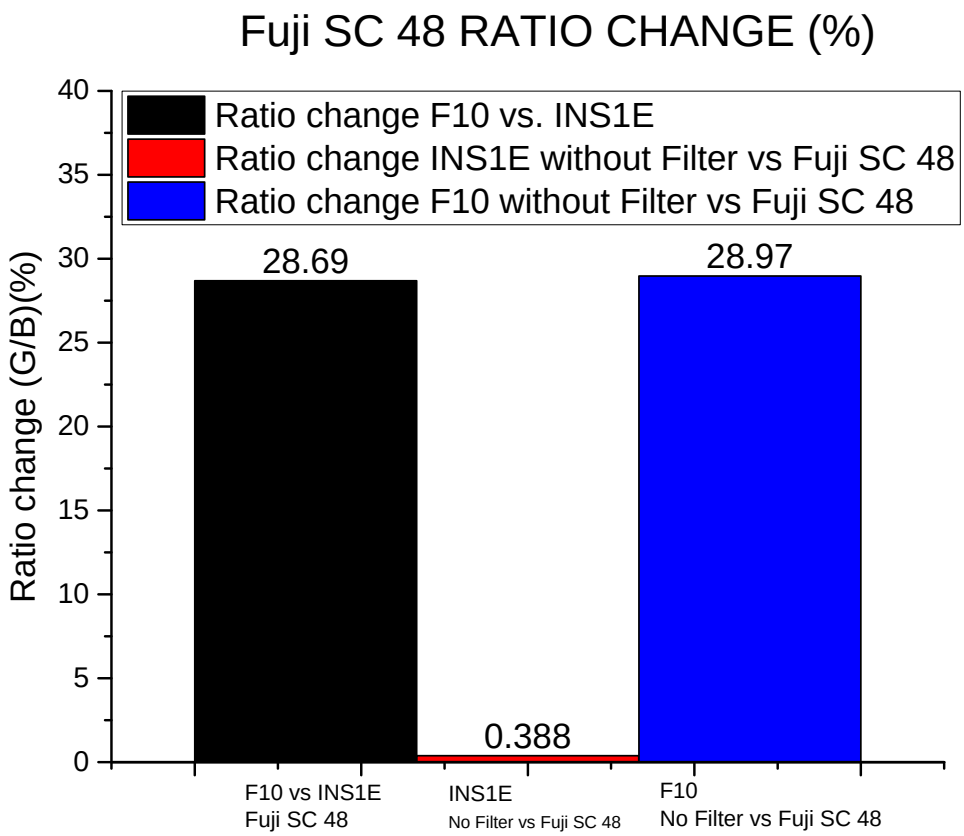

Figure 3.32 – Fuji SC 48 change in ratio with the filter for both INS1E and F10 cells. This graph shows a high level picture of the impact of the optical filter. It can be seen here that indeed the filter helps improve the SNR only for the F10 cells. Though the effect is not significant it is still a viable candidate.

3.3.5 Kodak gelatin based filters: Wratten 2 Filter 3

Figure 3.33 shows the Kodak Wratten 2 Filter 3, which is based on a gelatin material. It is called Filter 3 because it blocks lights below the 440 nm range in the spectrum.

This filter met the technical specifications for this project and was therefore considered a viable candidate. This filter was characterized as it was at the time of study for academic use and its supply was surplus and easily accessible in Europe.

Figure 3.33 – Kodak Gelatin based Wratten 2 Filter Number 3. This is light yellow Longpass filter blocking wavelengths below 440 nm.

Kodak Wratten 2 Filter 3: INS1E Cells

It can be seen from Figure 3.34 that the INS1E green counts, over a sample of five data points, were 2681 counts and the blue counts were 15463. The standard deviation was negligible in both cases. The key insights here are that the filter is first even at 100 mA LED bias current and 22.4 ms integration time able to keep the absolute value of the counts well within the dynamic range of the 16 bit photo-detector, thus giving us room to add more cell aggregates and most importantly not saturating the photodetector.

The counts are very well marked with two distinct levels and these separate non overlapping signatures add a degree of clarity into the distinguishing these cells.

These distinct count levels enable offset calibration when used in relation to the F10 cells that

have the probe.

The offset correction is necessary as the reflections arise from various sources including the petri dish, the mechanical 3D printed part creating auto-fluorescence and the cell culture medium that reflects off right owing to its light red color.

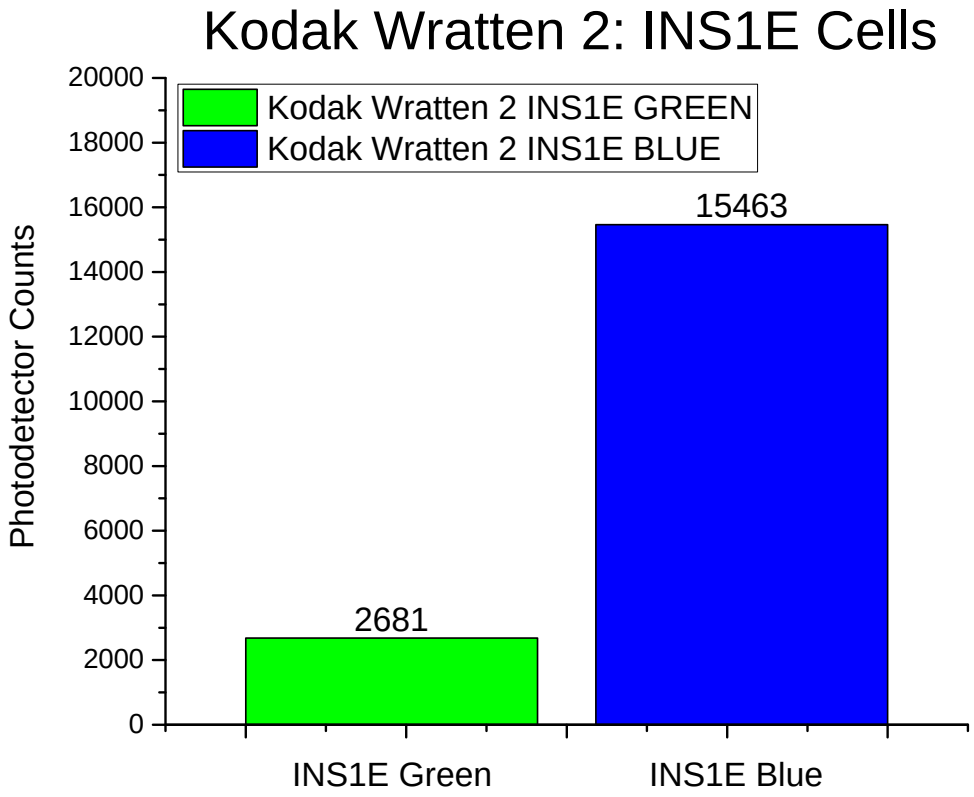

Figure 3.34 – Kodak Wratten 2 Filter: INS 1E Cells Blue and Green. The standard deviation for the Blue count was 23.39 counts or 0.15 %. The standard deviation for the Green count was 9.30 counts or 0.34%.

Kodak Wratten 2 Filter 3: F10 Cells

It can be seen from Figure 3.35 that the F10 green counts, were 7911.4 and the blue counts were 17566.6. Even though the F10 counts for the green pixel are higher than in the case of the INS1E cells for the same filter, the blue counts also significantly increase, indicating the green photons adding noise on the blue pixels. The standard deviation was negligible in both cases.

The key insights here are that the filter is firstly, even with a LED bias current of 100 mA and 22.4 ms integration time, able to keep the absolute value of the counts well within the dynamic range of the 16 bit photo-detector, thus giving us room to add more cell aggregates and most

importantly not saturating the photodetector.

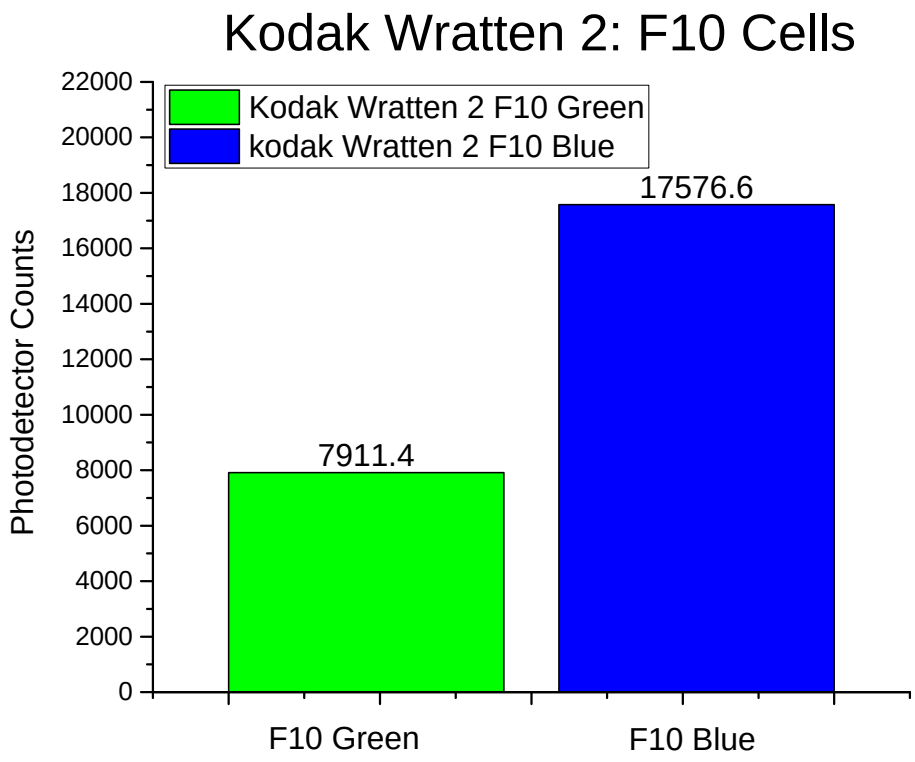

Figure 3.35 – Kodak Wratten 2 Filter: F10 Cells Blue and Green.The standard deviation for the Blue count was 19.47 counts or 0.11%. The standard deviation for the Green count was 21.11 counts or 0.26%.

The counts are very well marked with two distinct levels and these separate non overlapping signatures add a degree of clarity into the distinguishing these cells. The values also clearly demonstrate that the green counts are higher than the green counts of the INS1E cells, hence, verifying that the probe is existent in the F10 cells.

The effect of the fluorescence of the cells depends on the number, size and health of the 3D cell aggregates that were cultured. It should be noted that the same number of cells were used for both INS1E and F10 cells.

Kodak Wratten 2 Filter 3 (F10 - INS1E) Cells for Green Fluorescence and Blue Fluorescence Components

Figure 3.36 shows the result after removing the INS1E component of the Green and Blue counts from the F10 cell counts.

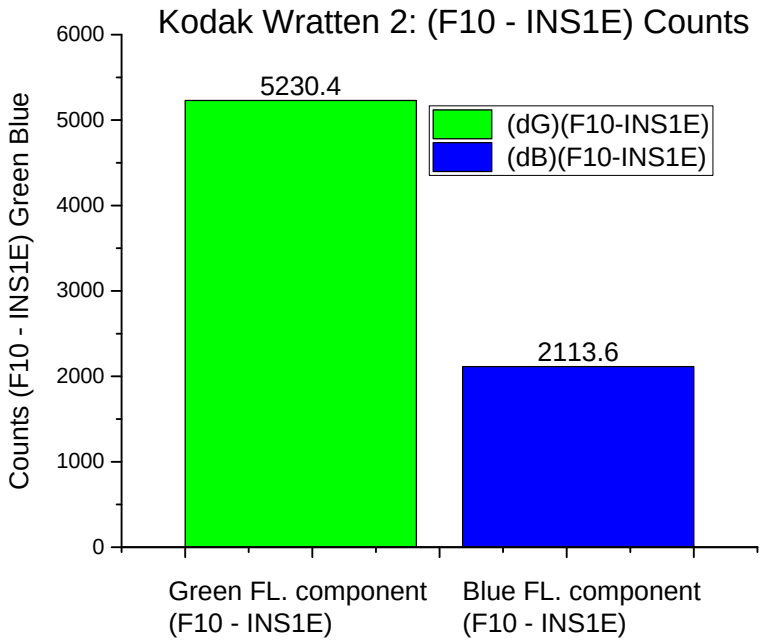

Figure 3.36 – Kodak Wratten 2 Filter: (F10 - INS1E) Counts for Blue and Green. The Gaussian error of propagation for the Blue count is 30.43 and Green Count is 23.06.

Kodak Wratten 2 Filter 3 (Green - Blue) for INS1E and F10 Cells.

Figure 3.37 shows the result of subtracting the Green and Blue components of light to observe the efficacy of the filter for both INS1E and F10 cell counts.

It is clear that in both cases there is a higher component of the Blue counts on both the photo-detector pixels indicating a higher amount noise and artifacts. The Green-Blue for the INS1E cells was -12782 while that for the F10 cells was -9665.2.

Kodak Wratten 2 Filter 3 (green/blue) ratio for INS1E and F10 Cells.

Figure 3.38 shows the ratio of the green/blue counts for both INS1E and F10 cells. Since we use a Ca^{2+} signalling FRET probe that works on a ratio metric principle, this is one of the most important measurements to be analyzed.

The ratio for the INS1E cells was 0.17 while that for the F10 cells was 0.45. This clearly shows the signature of the FRET probe producing the florescence in the cell culture medium when excited with the 435 nm light was the YFP and CFP molecules come closer than 10 nm in distance and thus create a sub-conduction band tunneling and emit a light at a lower energy or a higher wavelength of 535 nm.

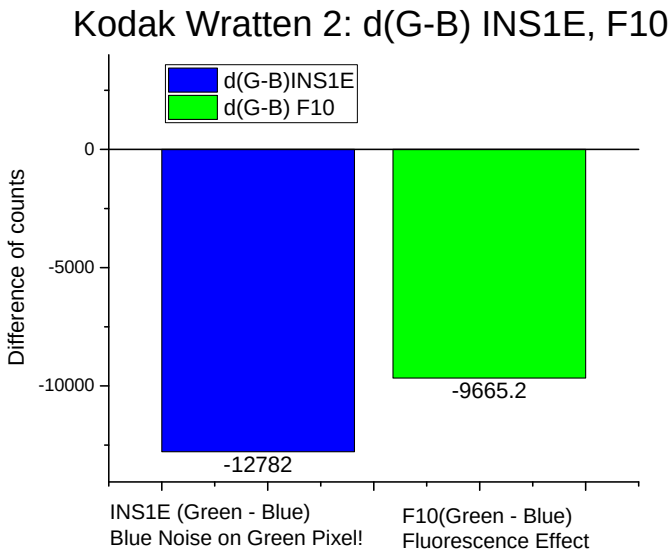

Figure 3.37 – Kodak Wratten 2 Filter: (Green - Blue) for both INS1E and F10 Cells. This graph shows if strength of the Green vs Blue components of the light as a function of the filtering efficacy of the filter and also elucidates the effect of the overlapping wavelength range among the Green and Blue pixels of the PD and the leakage from spectrum of the excitation LED's FWHM range. Clearly there is a lot of noise on the Green pixel from the Blue component of light.

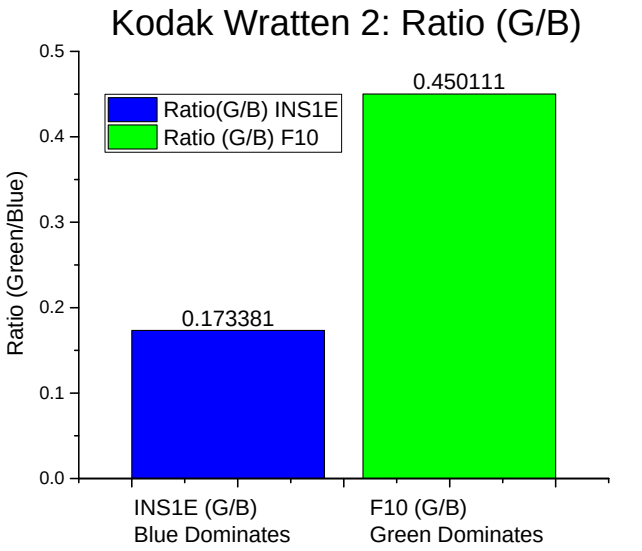

Figure 3.38 – Kodak Wratten 2 Filter: (Green/Blue) Ratio for both INS1E and F10 Cells. The standard deviation of the ratio for the INS1E cells was 0.00035 or 0.2%. The standard deviation of the ratio for the F10 cells was 0.0016 or 0.35%.

Kodak Wratten 2 Filter 3 - efficacy on the overall change Signal to Noise (SNR) ratios

Figure 3.39 shows the ratio of the green/blue counts for both INS1E and F10 cells.

There is 61.48% improvement in the ratio between the F10 and INS1E cells. Measurements were made without the filter, with just the bare photodiode in the electronic system and the relative change was measured w.r.t the case when the optical absorption filter was used. We see -4.2% degradation in the ratio for the INS1E cells and a significant 59.8% change in the ratio in the case of the F10 cells. This does not make it a viable filter as opposed to the Fuji filters.

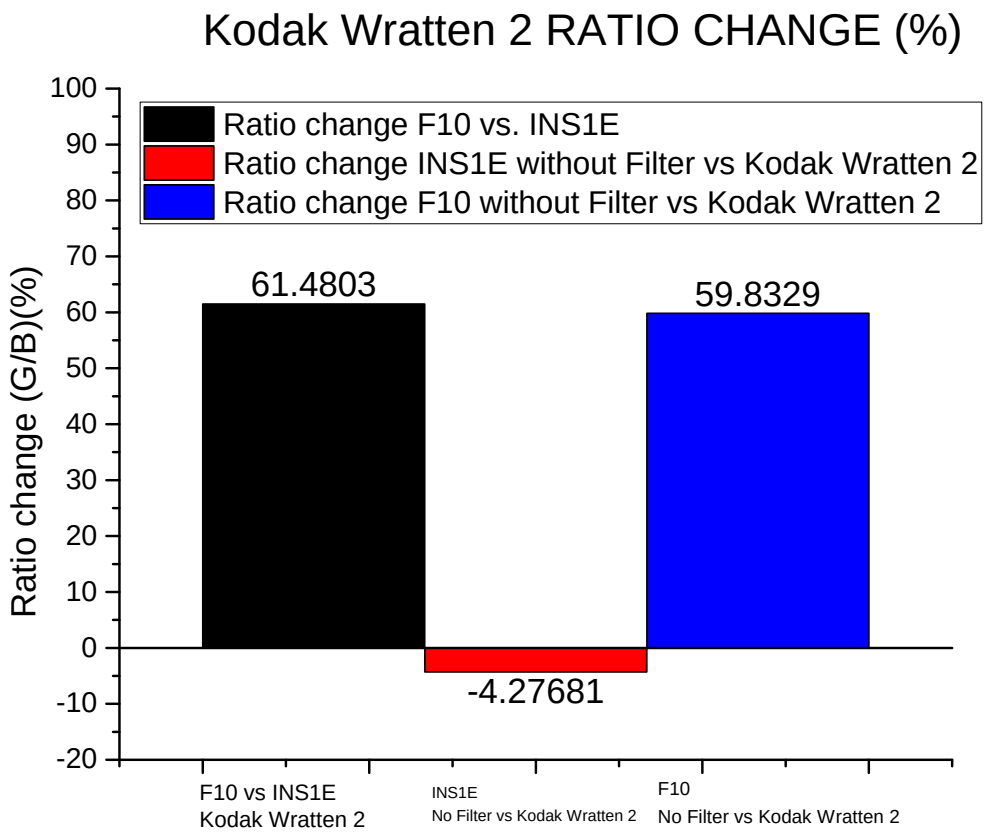

Figure 3.39 – Kodak Wratten 2 Filter: change in ratio with the filter for both INS1E and F10 cells. This graph shows a high level picture of the impact of the optical filter. It can be seen here that indeed the filter helps improve the SNR only for the F10 cells. For the INS1E its even worse than no filter, we believe this is due to the reflections from the Blue wavelength of light.

3.4 Dichroic principle angle dependent glass filters

Dichroic filters work on the principle of very precisely transmitting only the wavelength of interest through a thin film material. They block the unwanted or out-of-band wavelengths by reflecting the light away with the aid of the reflective surface of the filter as shown in Figure 3.2.

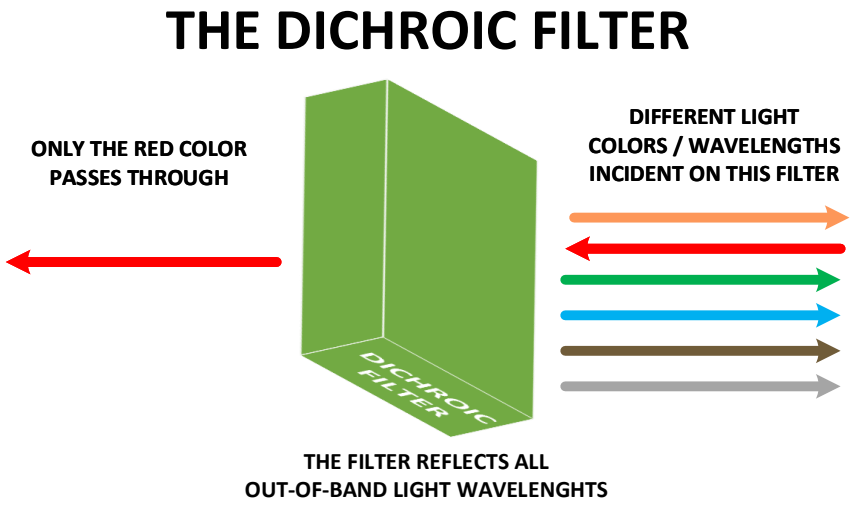

Figure 3.40 – The Dichoric Filter - Working Principle

An illustrative example the dichroic filter is displayed in Figure 3.41

The angle of incidence is very important for these filters and it is usually recommended to operate them with a 0° angle of incidence. Any deviation from this leads to all the unwanted light being transmitted as the thin film material would not be able to reflect these components of light away. This is a major challenge in handling this filter. We assume that the incident light would mostly be incident perpendicular to the filter for our characterization as we try to confine the cells in a small volume just atop the photo-detector and the filter.

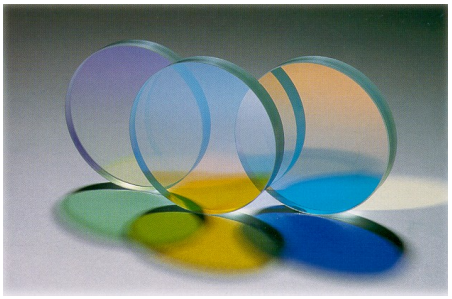

Figure 3.41 – Illustrative picture of Dichoric Filters. Source [61] . Laser Components Triband Dichoric Filter chosen passed 3 wavelengths, the two relevant ones were 490 nm (14 nm bandwidth) and 535 nm (12 nm bandwidth).

3.4.1 Laser Components (LC) dichroic glass based filter: LC-HBP40 10-586 Dual Band

Laser Components TriBand Dichoric Filter - INS1E Cells

It can be seen from Figure 3.42 that the INS1E green counts, over a sample of five data points, were 1394.6 and the blue counts were 9483.4. The standard deviation was negligible in both cases. The key insights here are that the filter is firstly even at 100 mA LED bias current and 22.4 ms integration time able to keep the absolute value of the counts well within the dynamic range of the 16 bit photo-detector, thus giving us room to add more cell aggregates and most importantly not saturating the photodetector. The counts are very well marked with two distinct levels and these separate non overlapping signatures add a degree of clarity into the distinguishing these cells.

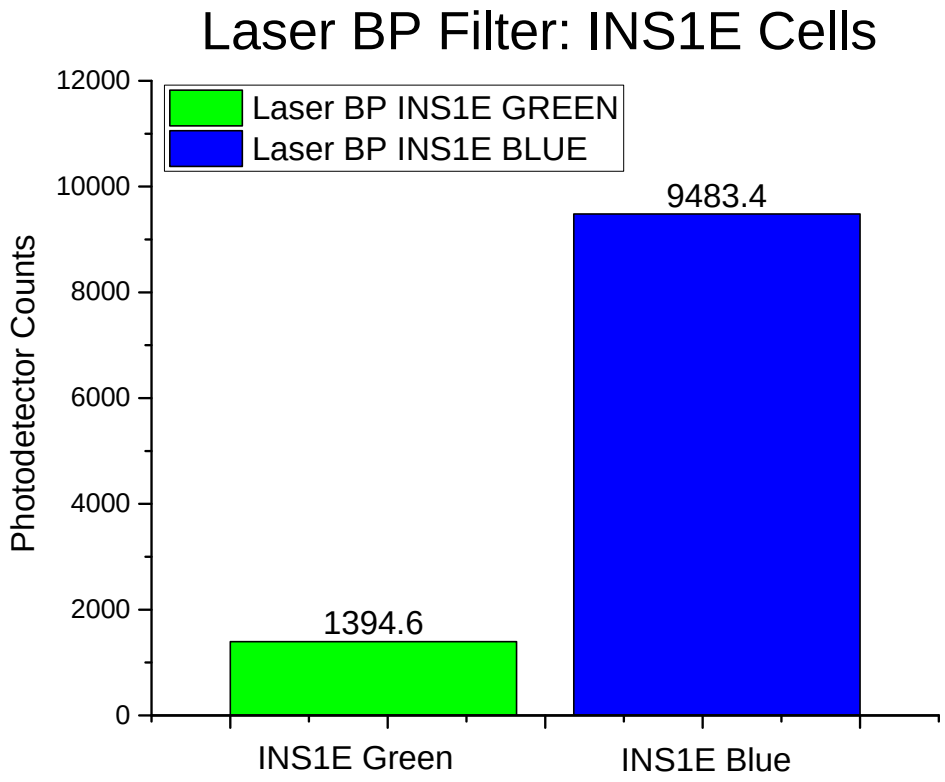

Figure 3.42 – Laser BP Filter: INS 1E Cells Blue and Green. The standard deviation for the Blue count was 17.41 counts or 0.18 %. The standard deviation for the Green count was 5.17 counts or 0.37%.

Laser Components TriBand Dichoric Filter - F10 Cells

It can be seen from Figure 3.43 that the F10 green counts, over a sample of five data points, were 1537.2 and the blue counts were 9597.6. The standard deviation was negligible in both cases. The key insights here are that the filter is, even with a LED bias current of 100 mA and 22.4 ms integration time, able to keep the absolute value of the counts well within the dynamic range of the 16 bit photo-detector, thus giving us room to add more cell aggregates and most importantly not saturating the photodetector. The counts are very well marked with two distinct levels and these separate non overlapping signatures add a degree of clarity into the distinguishing these cells. The values also clearly demonstrate that the green counts are higher than the green counts of the INS1E cells, hence, verifying that the probe is existent in the F10 cells. The effect of the fluorescence of the cells depends on the number, size and health of the 3D cell aggregates that were cultured. It should be noted that the same number of cells were used for both INS1E and F10 cells.

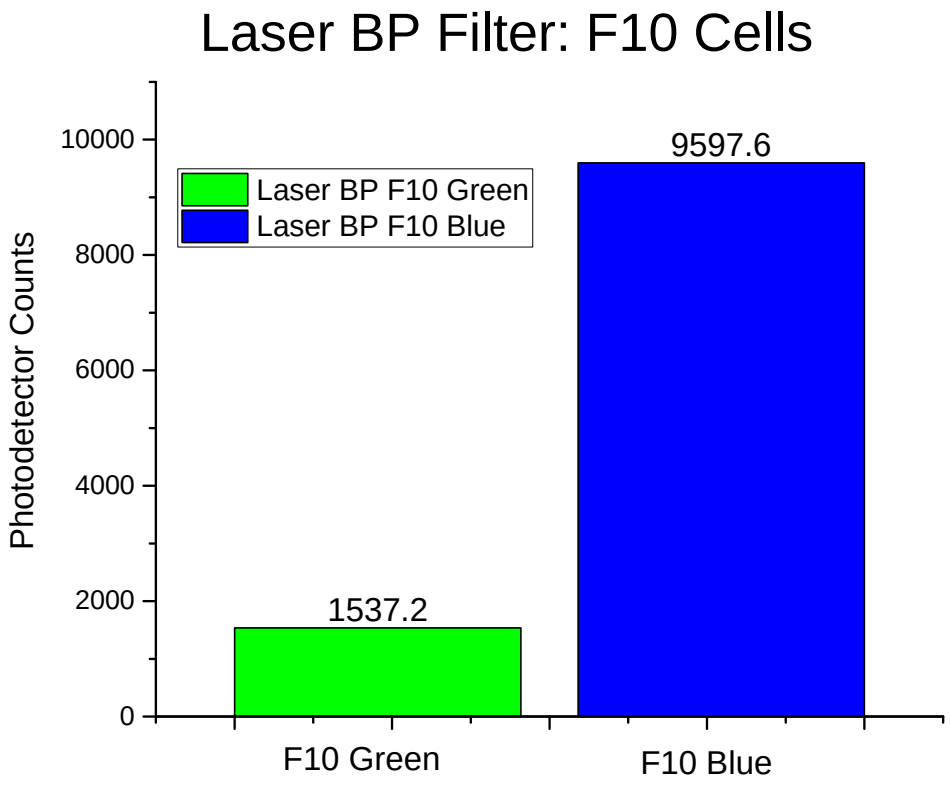

Figure 3.43 – Laser BP Filter: F10 Cells Blue and Green.The standard deviation for the Blue count was 24.32 counts or 0.25 %. The standard deviation for the Green count was 4.20 counts or 0.27%.

LC TriBand Dichoric Filter (F10 - INS1E) Cells for Green and Blue Fluorescence

Figure 3.44 shows the result after removing the INS1E component of the Green and Blue counts from the F10 cell counts. The Green fluorescent component was 142.6 counts, while the Blue fluorescent component was 114.2.

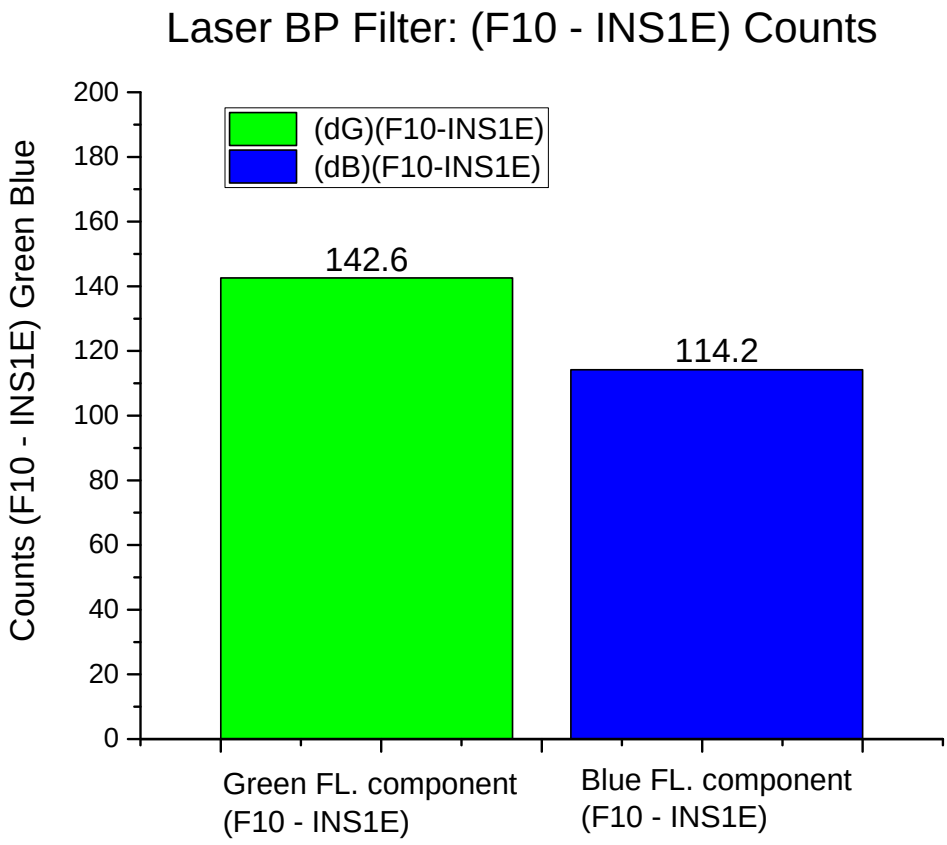

Figure 3.44 – Laser BP Filter: (F10 - INS1E) Counts for Blue and Green. The Gaussian error of propagation for the Blue count is 29.90 counts and Green Count is 6.66 counts.

LC TriBand Dichroic Filter (Green - Blue) for INS1E and F10 Cells.

Figure 3.45 shows the result of subtracting the Green and Blue components of light to observe the efficacy of the filter for both INS1E and F10 cell counts.

It is clear that in both cases there is a higher component of the Blue counts on both the photo-detector pixels indicating a higher amount noise and artifacts. The Green-Blue for the INS1E cells was -8068 while that for the F10 cells was -8060.

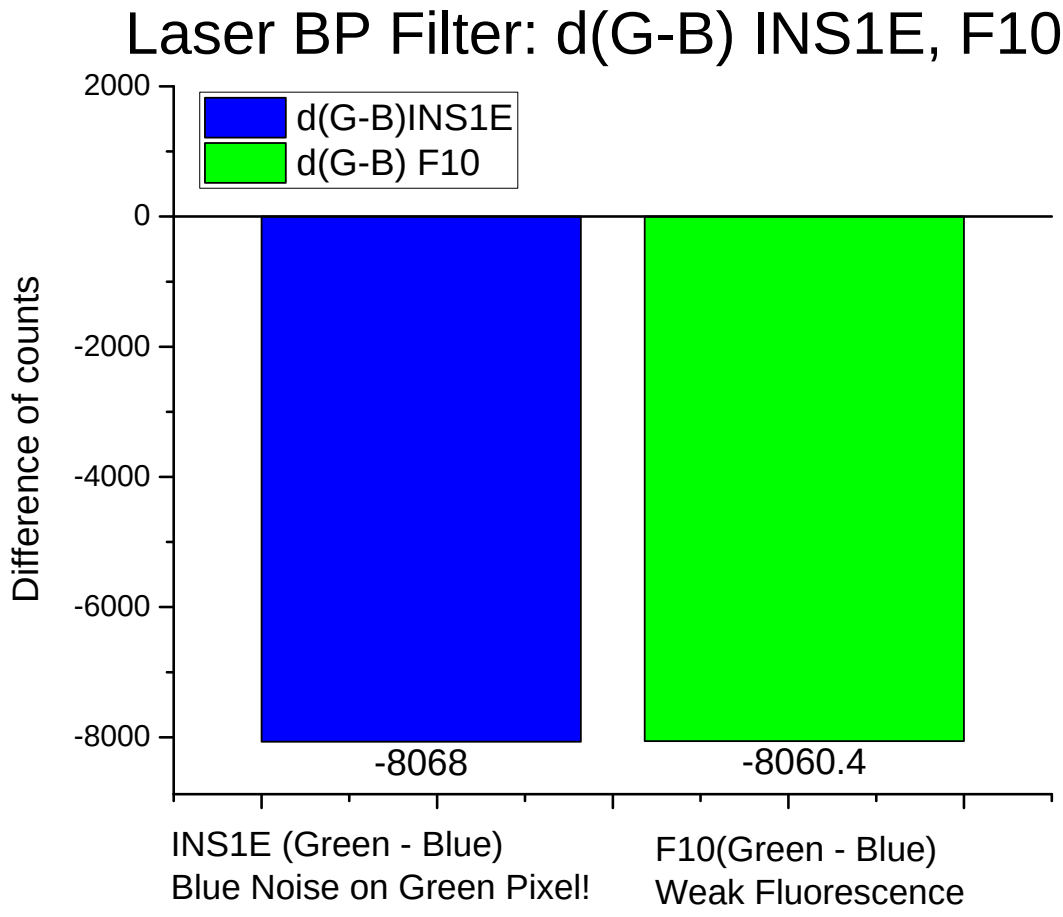

Figure 3.45 – Laser BP Filter: (Green - Blue) for both INS1E and F10 Cells. This graph shows if strength of the Green vs Blue components of the light as a function of the filtering efficacy of the filter and also elucidates the effect of the overlapping wavelength range among the Green and Blue pixels of the PD and the leakage from spectrum of the excitation LED's FWHM range.

LC TriBand Dichoric Filter (green/blue) ratio for INS1E and F10 Cells.

Figure 3.46 shows the ratio of the green/blue counts for both INS1E and F10 cells. Since we use a Ca^{2+} signalling FRET probe that works on a ratio metric principle, this is one of the most important measurements to be analyzed.

The ratio for the INS1E cells was 0.147 while that for the F10 cells was 0.16. This clearly shows the signature of the FRET probe producing the florescence in the cell culture medium when excited with the 435 nm light was the YFP and CFP molecules come closer than 10 nm in distance and thus create a sub-conduction band tunneling and emit a light at a lower energy or a higher wavelength of 535 nm.

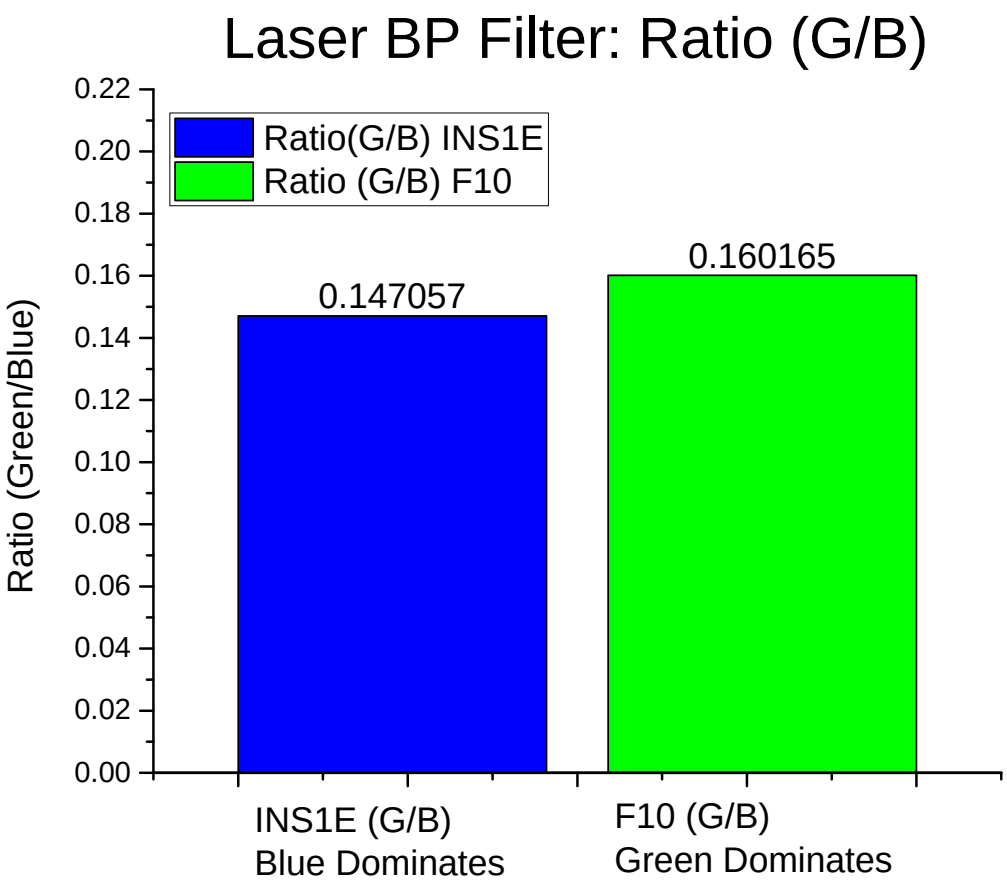

Figure 3.46 – Laser BP Filter: (Green/Blue) Ratio for both INS1E and F10 Cells. The standard deviation of the ratio for the INS1E cells was 0.00027 or 0.20%. The standard deviation of the ratio for the F10 cells was 0.00012 or 0.075%.

Laser Components TriBand Dichoric Filter efficacy on the change in SNR

Figure 3.47 shows the ratio of the green/blue counts for both INS1E and F10 cells.

There is a 8.18% improvement in the ratio between the F10 and INS1E cells. Measurements were made without the filter, with just the bare photodiode in the electronic system and the relative change was measured w.r.t the case when the optical absorption filter was used.

We observed a 1.2% improvement in the ratio for the INS1E cells and a significant 9.3% change in the ratio in the case of the F10 cells. Overall, this is among the worst filters from the six characterized for this application because of its angle dependence.

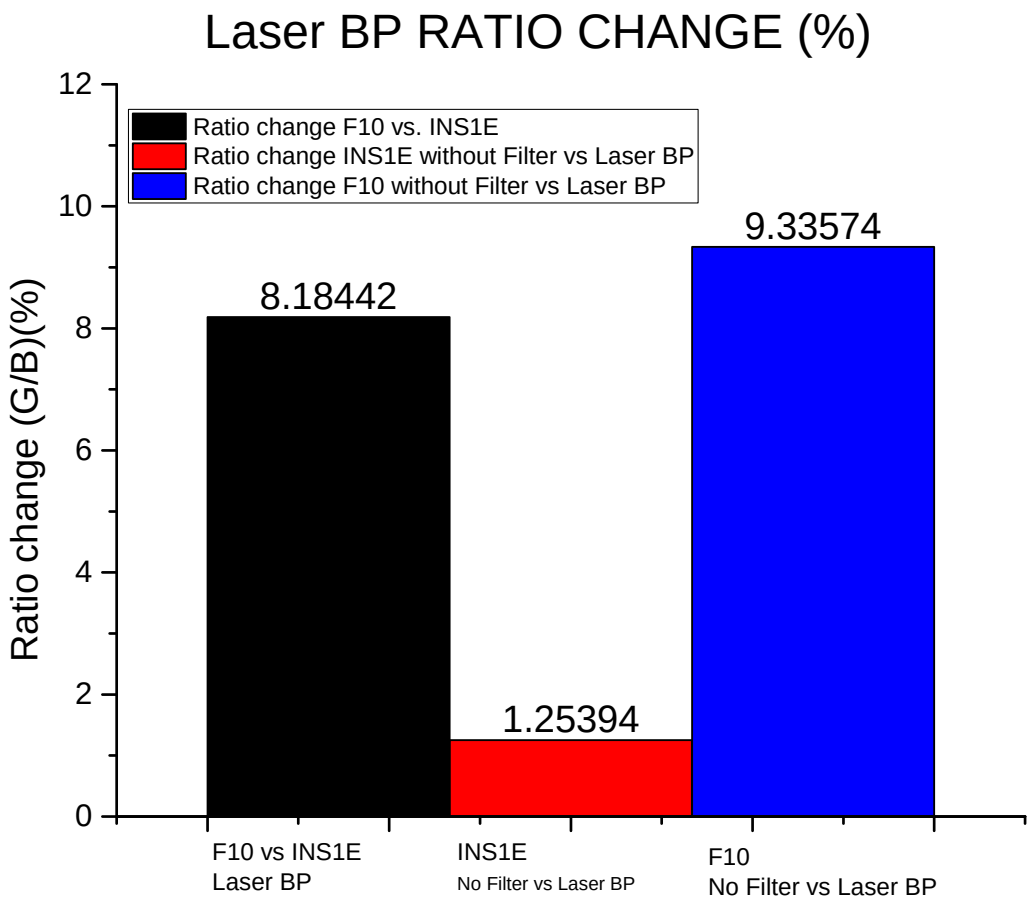

Figure 3.47 – Laser BP Filter: change in ratio with the filter for both INS1E and F10 cells. This graph shows a high level picture of the impact of the optical filter. It can be seen here that indeed the filter is one of the lowest performing among the 6 filters. This filter almost has no effect in filtering the light at all. This is owing to its dichroic effect.

3.5 Filter of choice

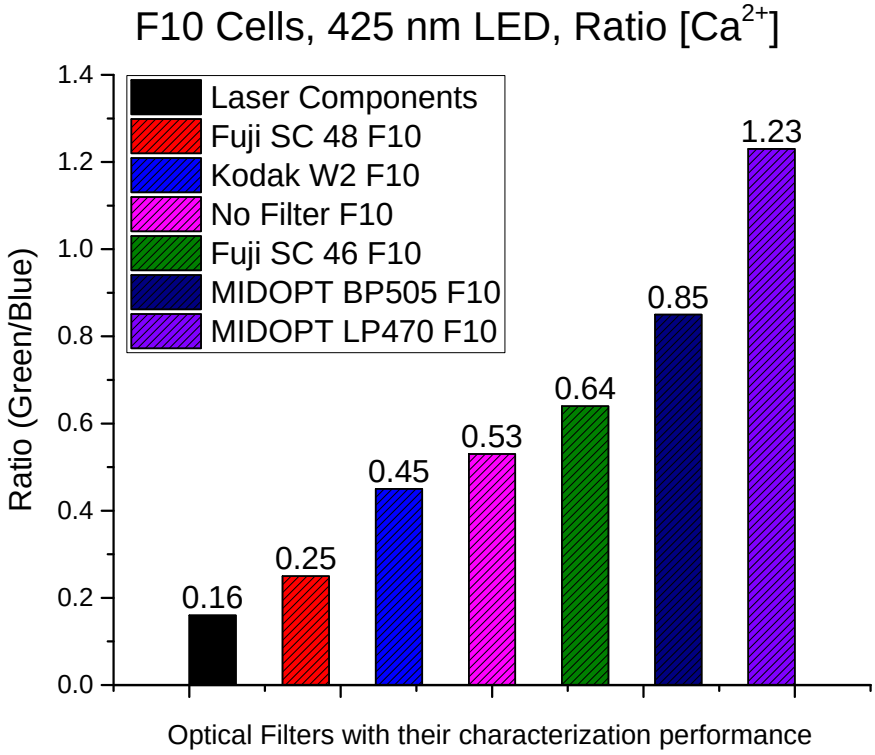

Figure 3.48 – Comparison results of the optical filter characterization for the F10 cells having the genetically engineered FRET probe.

Figure 3.48 shows the ratio of the green/blue counts for the F10 cells for all the filters that were characterized. There is also the measurement point which shows the ratio when no filter was used and the F10 cells fluorescence was measured directly. As it can be seen on the column graph the Laser Components, Fuji SC 48 and Kodak Wratten 2 Filter 3 performed worse than if no filter was used. Clearly the Fuji SC 46, MIDOPT BP505 and MIDOPT LP470 filters performed the best. The best filter among them to carry out the biological measurements was the MIDOPT LP 470 which provides the highest ratio of 1.23 for the same measurements conditions. This filter is also easy to handle as it is glass based and can be diced in house, plus can be mounted atop the photo detector directly and its smooth planar face ensures it seals any leaky light paths to the PD.

3.6 Filter of choice with offset correction

Figure 3.49 shows the offset-corrected ratio of the MIDOPT LP 470 filter for the F10 cells. It seen that there is already a 82% improvement in the ratio with the filter when the F10 cells are measured keeping the INS1E cells as a reference. There is 234% improvement in the INS1E cells ratio and

a 480% improvement in the F10 cells ratio with the filter as opposed to a case when no filter was used. When the offset of the INS1E is incorporated in the F10 cells measurements then we see a 1163% improvement in the F10 cells ratio with respect to using no filter at all. A significant improvement in the ratio and demonstrates the efficiency of the filter. This corrected offset can be used in all biological measurement results to get a better insight into the interpretation of the measurement results.

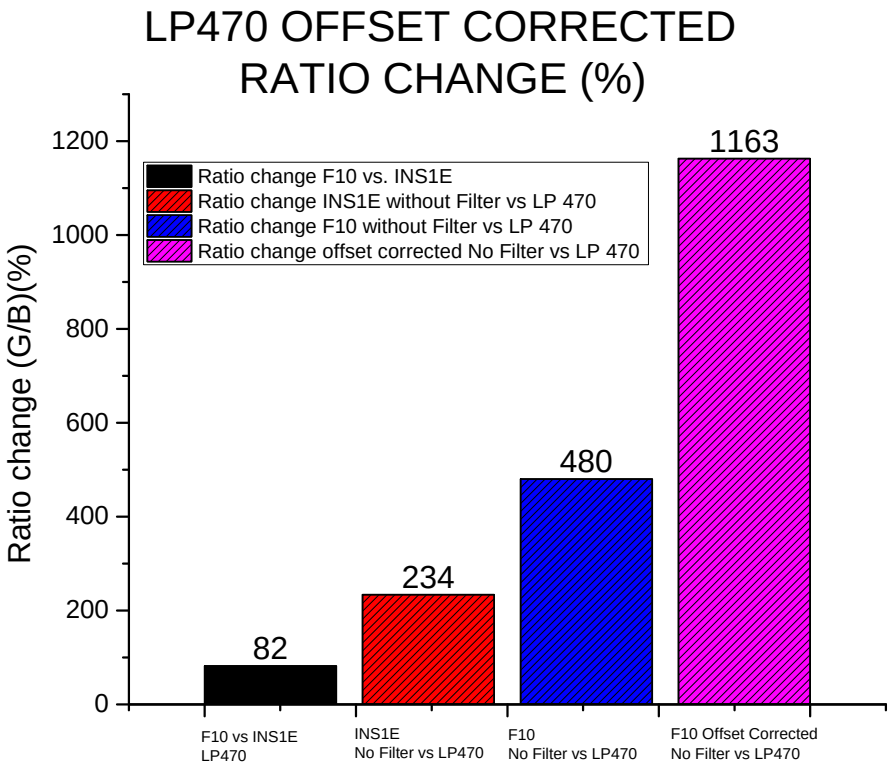

Figure 3.49 – Final selected filter LP 470 with the offset correction.

3.7 LED bias current and integration time: design point

The excitation LUXEON Philips LED emits optical power that is directly proportional to the bias current of the LED. More bias current therefore means more irradiated optical power and stronger excitation of the cells, which increases the absolute value of the emission counts from the F10 cells. On the other hand the photo-detector collects the emitted photons to give an indication of the green and blue fluorescent components. If the photo-detector is exposed to the light of the F10 cells for a very short amount of time for a weak LED bias current then it might either not collect any photons or might collect a scanty number of photons insufficient for getting a suitable SNR. On the contrary, if the photo-detector is exposed for a longer duration, it would integrate more photons, leading, to higher absolute values of both green and blue counts. After a certain

cut-off point the ratio remains the same as both the green and blue counts scale proportionately keeping the ratio the same. The ratio of the green/blue counts settles in this context at around 1.29 which is the guiding factor to choose the optimal operating point in this design. These are two parameters that are considered as degrees of freedom. Figure 3.50 shows the plot of the ratio on the y-axis for different LED bias current and changing the integration time of the photo-detector on the x-axis. It can be seen that there are 3 distinct zones, namely, noise, design point and saturation zones. The values in the noise zone are to be discarded and its an over design to operate in the saturation zone. In pertinence to an in vivo system a design point of 2.4 mA LED bias current and 5.5 ms integration time seems the best option for optimal power. The other alternative if the number of cells is scanty, is at the 5 mA LED bias current with the 5.6 ms integration time. As it can be seen going higher in both LED bias current and integration time has no affect on the ratio and this leads to a higher power consumption. In the context of an externally powered *in vitro* system this power constraint is relaxed and enables us to be do measurements at design points such as 5 mA LED bias current with a 5.6 ms integration time or 10 mA LED bias current with a 5.6 ms integration time.

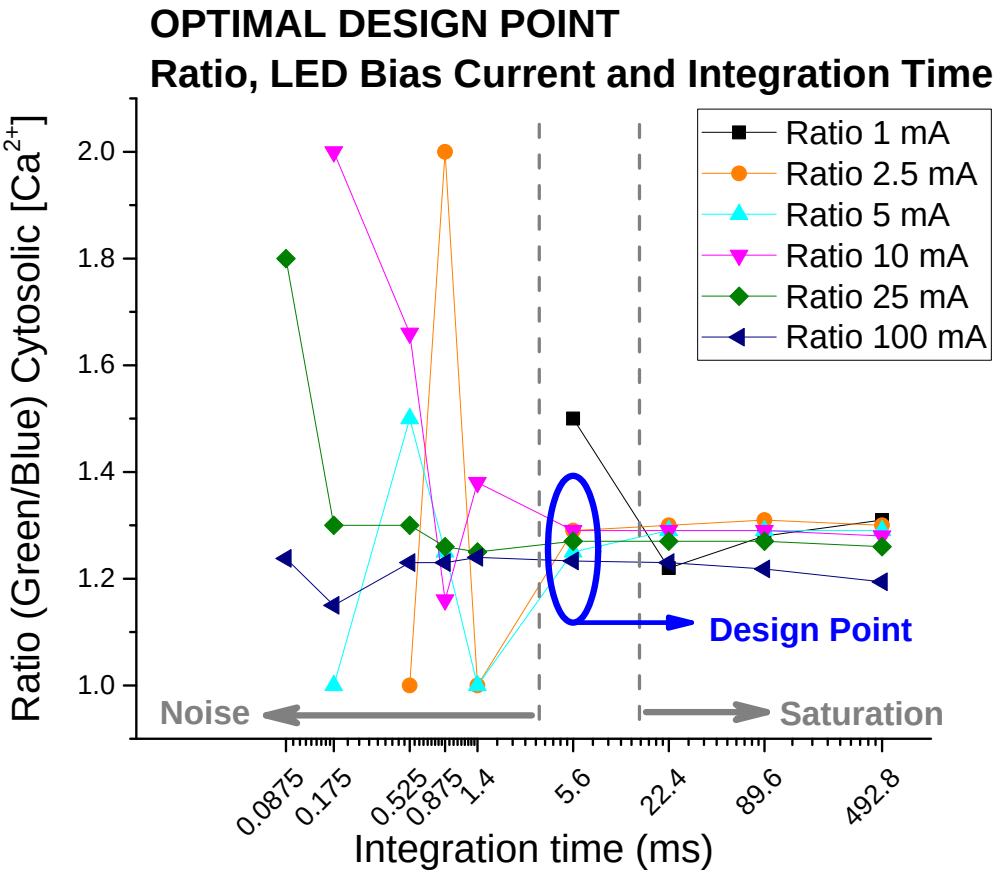

Figure 3.50 – Optimal operating point for the design.

3.8 Excitation LED center wavelength: effect on the SNR

An interesting aspect of selecting the center wavelength of the excitation LED is that it automatically limits the cutoff wavelength at which the excitation blue photons are emitted, reflected and collected by the photodetector. When the FRET probe is excited with different wavelengths, the change in the ratio is between 14% for the 400 nm and 425 nm excitation sources and about 5 to 8% for the 410 and 420 nm wavelengths as shown in Figure 3.51.

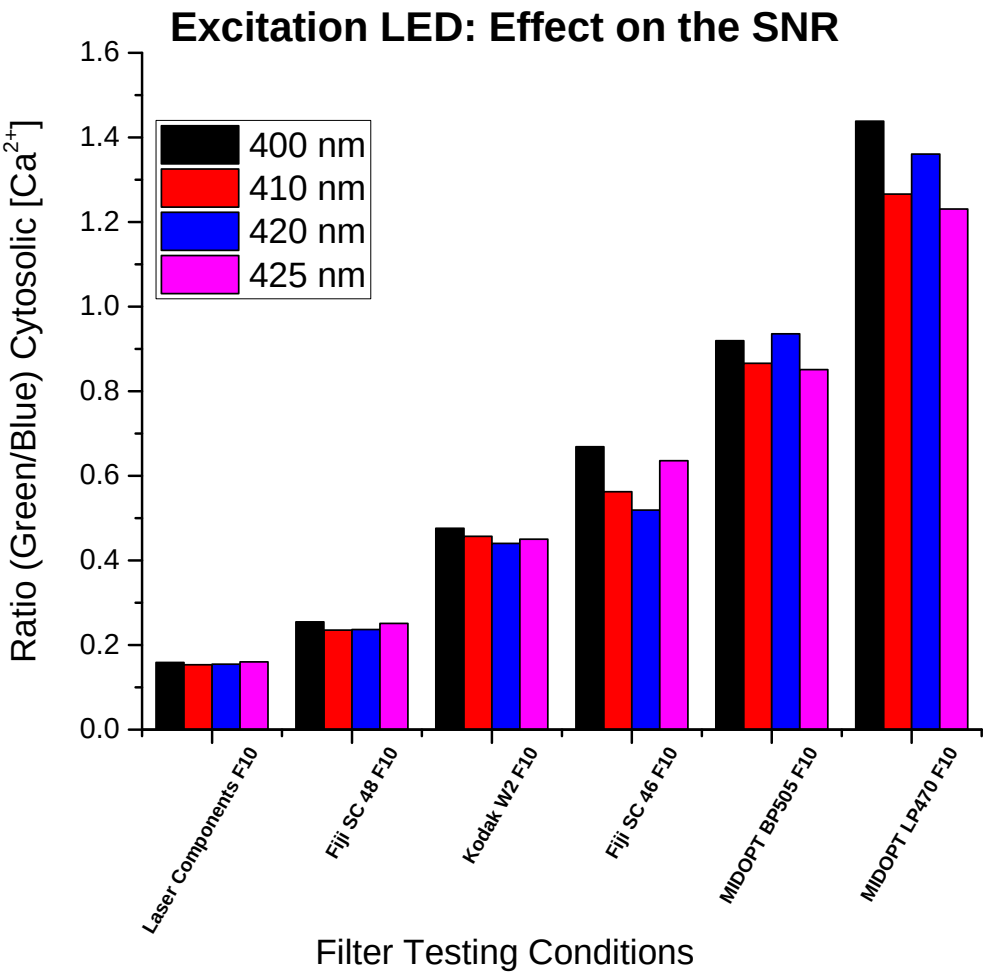

Figure 3.51 – Excitation LED Effect on the SNR of the G/B ratio.

The lower the wavelength of the upper end of the excitation LED band width, easier its noise could be reduced by the cut-off wavelength of the filter. This is clearly demonstrated by the conspicuous contrast in the results of the 400 nm excitation LED vs the 420 nm excitation LED. For the 410 nm and 420 nm LEDs, the results are consistent and in the same trend with an extremely small aberration due to measurement conditions. The important point to note here is

that the power in the 425 nm excitation at its 435 nm component is the maximum among the four excitation LED's. This is the most conducive LED from the biosensor point of view. The fact that the ratios are almost the same also confirms the FRET principle, which states that the emission wavelengths are not directly affected when the excitation center wavelength is shifted.

3.9 Conclusion on filter characterization

After extensive characterization of both absorption and dichoric filters the MIDOPT LP 470 was chosen for subsequent designs for both *in vitro* and in vivo demonstrator development. Various offset and noise sources were canceled out by subtracting the F10 cell components from the INS-1E cells, aiding further with the ratiometric probe. The operating point for the LED bias current and the photo-detector integration time (and hence the time for keeping the excitation LED signal alive) was determined. This serves as an input for a low power system, as the ratio is unaffected for powers and integration times beyond the ideal design point. The FRET principle was confirmed by using excitation LEDs with different center wavelengths, yet having an excitation energy component at the 435 nm wavelength. The ratio improved a bit for all filters whist using the 400 nm excitation LED versus the 425 nm LED, owing to the decrease in the reflected excitation noise, the change in the ratio itself was within 14% among them.

4 *In vitro* measurements with INS-1E pancreatic β-cell based biosensor

The fully automated electronic demonstrator with the selected filter for best SNR was used to carry out several *in vitro* biological experiments. These experiments elucidate the gamut of possible applications with the *in vitro* demonstrator. The experiments carried are for cell counting, cell growth and death, oxygenation of cells, response of the cells to temperature changes. Glucose stimulation was done for continuous glucose monitoring for periodic glucose stimulation and binary stimulation with cell culture medium containing glucose vs KRBH solution containing no glucose at all. The experiments are described below, starting with the method for cell culturing the INS-1E cells in which the probe was expressed to produce the F10 cells.

4.1 INS-1E YC3.6$_{cyto}$ cell line generation and cell culturing

Poly-ornithine, which is a synthetically produced amino acid sequence, with a positive charge, consisting of a single hydrobromide per unit was used to plate the INS-1E cells. This is because Poly-ornithine facilitates cell growth and adhesion of cells in the Petri dish. The diameter of the Petri dish used was 10 cm. The transaction was carried out using a plasmid having the gene sequence for the YC3.6$_{cyto}$ FRET sensor [52]. This transfection was carried out with the DharmaFECT reagent from Thermo Scientific. In order to decipher the cells that were successfully transfected a 2-step procedure using 300 µg mL^{-1} of G418, the most suitable plate with cells was selected and sorted using the fluorescence activated cell sorting (FACS) technique using a 488 nm wavelength for emission. These cells were then cultured in cell culture selection media. Subsequently, these cells were sorted again using FACS and cultured on a 96 well plate. The signals from these colony of YC3.6$_{cyto}$ cells were detected using fluorescence.

The selected cells were then stored in vials in the freezer for using them to perform different experiments. The passage number for each cell vial was recorded. After a certain number of passages the cells were no longer seeded and cultured from a particular vial and cells from a new vial had to be loaded to ensure that the characteristics of the cells were not aberrant with respect to the first cell passage.

4.2 Number of Cells

This application of the *in vitro* system was to check its capacity for quantifying the total number of F10 cells upon culturing them over several days. The cell were cultured and grown in 3D aggregates as described in the previous section. The cells were characterized for 2 million, 4 million, 6 million and 8 million cells as shown in Figure 4.1. The reference cell count was obtained with a cell counting machine. A 425 nm LED with a bias current of 5 mA and photo-detector integration time of 89.6 ms was used to measure the fluorescence of the F10 cells.

The green counts were 227 for 4 million cells and 175 for 2 million cells. This was a significant 29.7% increase in counts. The ratio increased to 1.0509 for 4 million cells from the 0.906 for the 2 million cells which was an increase in 13% of fluorescence. The rising counts and ratio trend is depicted in Figure 4.1. However, the trend although upward, does not increase with the same scaling factor for the 4 million and 8 million cells. A plausible explanation for this plateauing effect is the meager change in the number of photons collected per unit square given the optical and mechanical dimensions of the system. An interesting observation is the increase in the (Green-Blue) counts significantly from 2 million to 4 million cells and another jump between 6 million and 8 million cells.

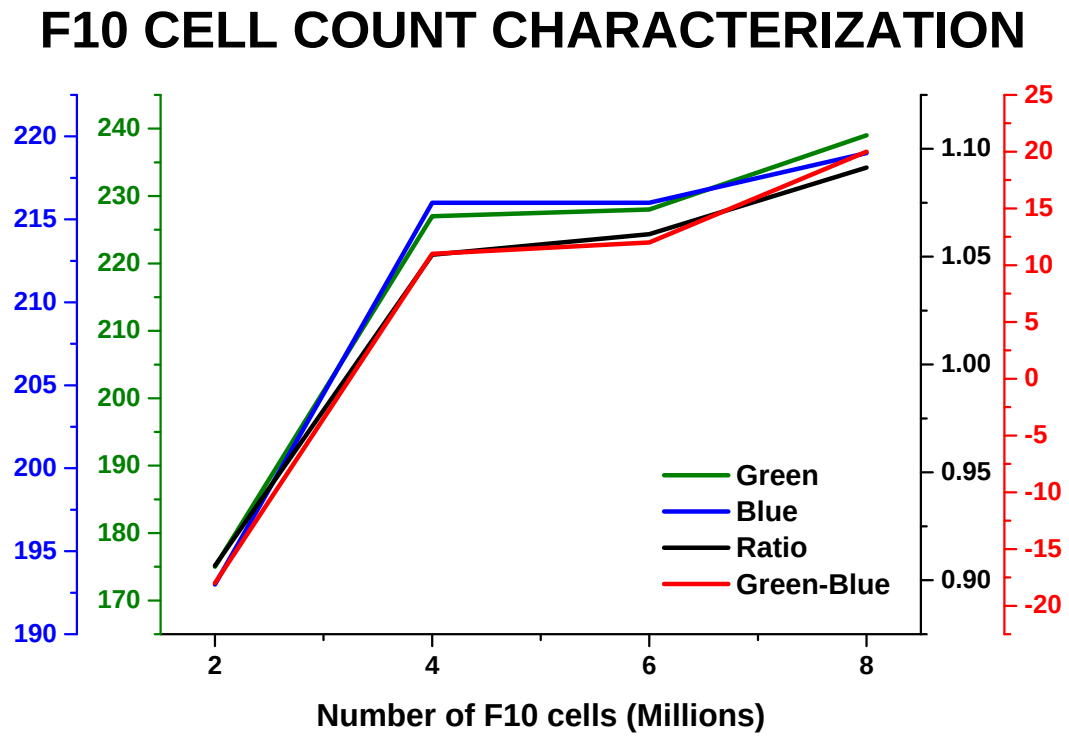

Figure 4.1 – F10 Cell Count Characterization.

4.3 Cell growth death trend characterization

This section explains the experimental results for characterizing the cell growth / death trend of a cell culture over a span of five days. The cells were seeded on day zero and kept in the incubator inside the clean room at 35.6 °C with controlled 0.9% 16.3 CO_2 levels. The cells were incubated in the TED Pella Inc black Petri dish in order to reduce the noise components from a transparent Petri dish. The 425 nm LED with 50 mA LED bias current and 89.6 ms integration time of the photodiode were used for these measurements.

The green counts on day zero were 1372 while the blue counts were 1896 with the ratio being 0.724. After incubating the cells for three days and cultivating the 3D aggregated on a stirrer the counts were measured again to obtain 1295 counts for the green and 1928 counts for the blue with a decreasing ratio of 0.671. The cells were subsequently measured again on day 4 and we obtained even lower counts of 1203 for the green, 1966 for the blue and a decreased ratio of 0.612. We observe the trend was a decreasing green counts, indicating a lack of fluorescing cells and as a result also increase in the blue as they both go anti-parallel in the scope of this system. This experiment therefore indicates a downward trend and a negative cell growth indication. In the context of both *in vitro* and *in-vivo* this is an example of measuring lower fluorescence upon several days of cell culturing, and is an application for measuring cell death.

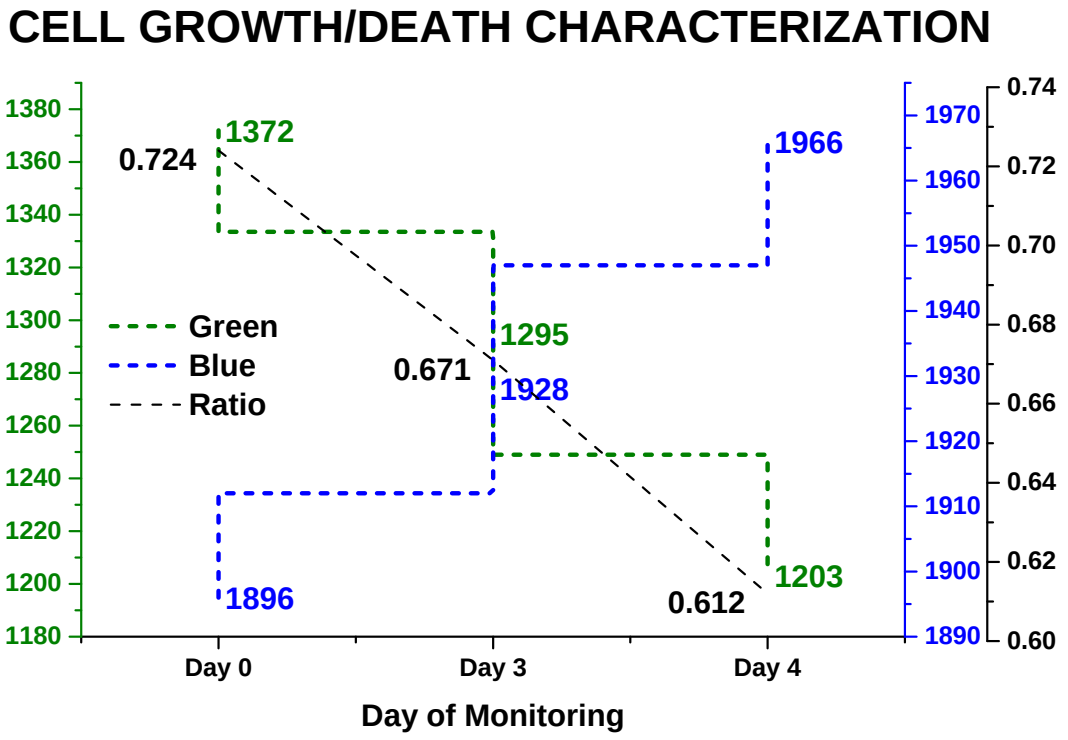

Figure 4.2 – F10 Cell Growth/Death Characterization.

4.4 Temperature response of the FRET cell line

This section explains the effect of change in temperature on the fluorescence response of the F10 cells. The cells were seeded with 10 mM of glucose concentration in the cell culture medium. The cells were initially transferred in a KRBH solution after medium exchange and kept in the incubator before transferring them to the *in vitro* experimental setup. A pre-heated temperature chamber at 40 °C, completely dark and optically sealed, hosting the 3D printed setup and the electronic system with the Petri dish on top was used to load the cells in. The cells were loaded into a mesh that was sealed to the bottom with a bio-compatible glue. This mesh was used to ensure the cells stayed localized within a certain space whilst the media circulated owing to a small magnet in the Petri dish that was spun in order to enable oxygenation and promote media circulation. The cells were stimulated with a 10 mM of glucose and the ratio-metric fluorescence recordings were made. The measurements were taken with a LED excitation bias current of 20 mA and a photo-detector integration time of 492.8 ms. The temperature was changed from 40 °C to 26 °C with around 7 minutes 30 seconds for change in temperature every time. The profile of the decreasing temperature and the evolution of the green, blue counts and the ratio is shown in Figure 4.3. It is seen that there is inverse relationship between the change in the temperature. A fall in the temperature leads to a rise in the counts and the ratio.

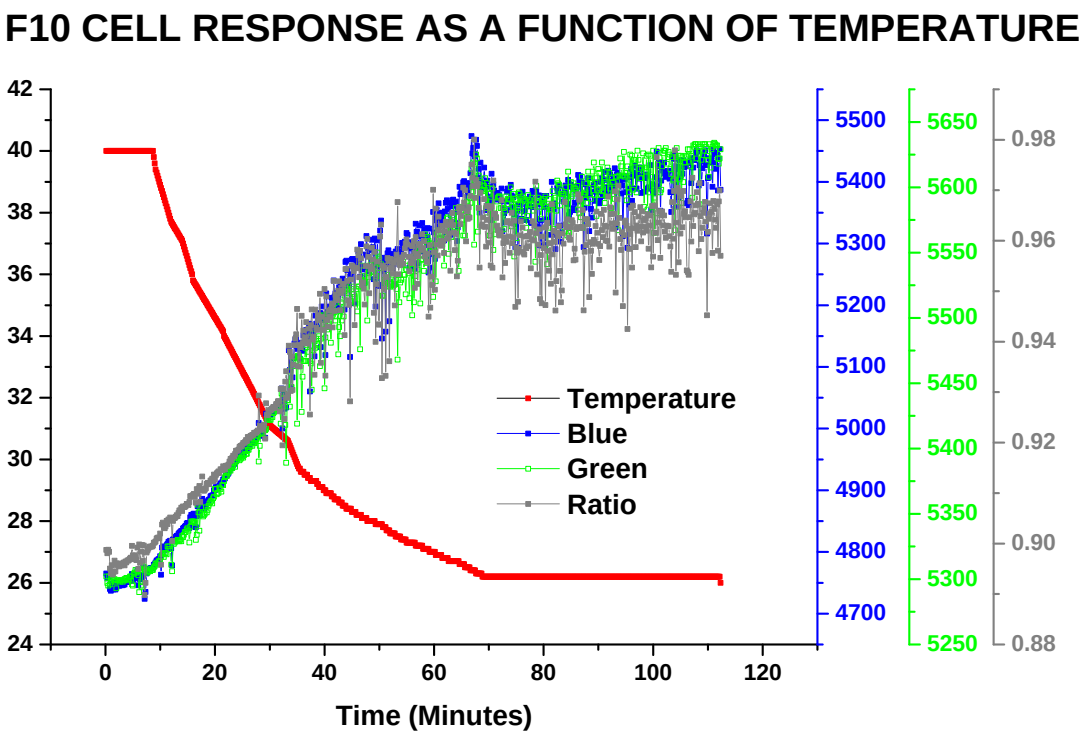

Figure 4.3 – Cell counts as a function of time with change in temperature.

4.4.1 Polynomial fit of the evolution of temperature, blue, green counts and the ratio with respect to time

Figure 4.4 shows the polynomial fit of ratio, green, blue counts and temperature with respect to time. The temperature is held constant for the first 7.5 minutes at 40 °C in a pre-heated temperature chamber. It is then decreased down to 26 °C at rate of change in temperature once every 7.5 minutes. There is an opposite effect on the green, blue counts and the ratio with this change in temperature. This is predictable and reproducible with similar results over several experiments. As its seen in Figures 4.4b 4.4c and 4.4d the locus of these plots traces a opposite direction with respect to the locus of the temperature plot. There is a plateauing effect towards the end, owing to the settling of the temperature. Interestingly, there is a lot of firing of the FRET signals from the cells indicating a strong response of the cells between 26 °C to 28 °C.

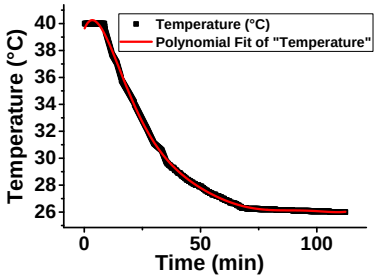

(a) Temperature profile with a polynomial fit.

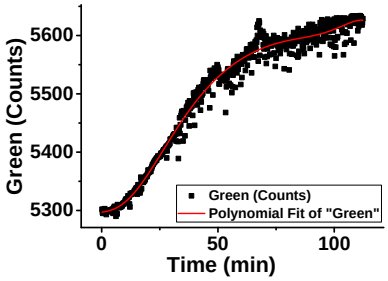

(b) Green counts profile with a polynomial fit.

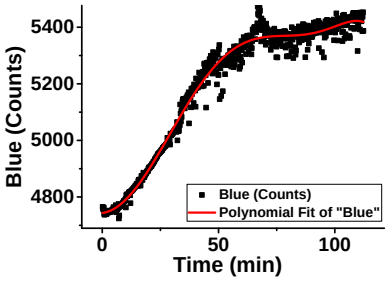

(c) Blue counts profile with a polynomial fit.

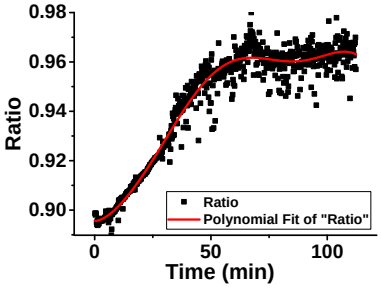

(d) Ratio profile with a polynomial fit.

Figure 4.4 – Polynomial fit (red) of the temperature, blue, green counts and ratio. It can be seen the model fairy accurately traces the locus of the evolution of the counts,ratio and temperature with the change in the time.

The most accurate fit was found as given by Equation 4.1. The tables 4.1 and 4.2 give the coefficients for each of these fitted curves.

$$Y = Intercept + B1 * x^1 + B2 * x^2 + B3 * x^3 + B4 * x^4 + \mathrm{B5*x^5} + B6 * x^6 + B7 * x^7 + B8 * x^8 \quad (4.1)$$

Temp.	Value	Std. Error	RATIO	Value	Std. Error
Intercept	39.5738	0.0465547	**Intercept**	0.895565	0.00173242
B1	0.42931	0.0189838	**B1**	6.1592E-5	7.06437E-4
B2	-0.0779477	0.00250333	**B2**	7.09403E-5	9.31556E-5
B3	0.00336672	1.50026E-4	**B3**	-2.65042E-6	5.58287E-6
B4	-7.52804E-5	4.77026E-6	**B4**	8.78786E-8	1.77514E-7
B5	9.74055E-7	8.58362E-8	**B5**	-1.90944E-9	3.19419E-9
B6	-7.30448E-9	8.76893E-10	**B6**	2.19345E-11	3.26315E-11
B7	2.9352E-11	4.73796E-12	**B7**	-1.22726E-13	1.76312E-13
B8	-4.86904E-14	1.05083E-14	**B8**	2.6469E-16	3.9104E-16

Table 4.1 – Coefficients for the polynomial fit of the temperature and ratio.

GREEN	Value	Std. Error	BLUE	Value	Std. Error
Intercept	5297.05	4.78907	**Intercept**	4743.74	10.2682
B1	0.609552	1.95286	**B1**	0.957308	4.18709
B2	0.0160789	0.257518	**B2**	0.375643	0.552139
B3	0.0150497	0.0154332	**B3**	3.76874E-4	0.03309
B4	-6.72785E-4	4.90716E-4	**B4**	-1.51713E-4	0.00105213
B5	1.31362E-5	8.82995E-6	**B5**	1.69513E-6	1.89321E-5
B6	-1.36559E-7	9.02059E-8	**B6**	-5.56617E-9	1.93409E-7
B7	7.38592E-10	4.87393E-10	**B7**	8.39164E-12	1.04501E-9
B8	-1.63412E-12	1.08098E-12	**B8**	-6.23226E-14	2.31771E-12

Table 4.2 – Coefficients for the polynomial fit of the green and blue counts with respect to change in temperature over time.

Figures 4.5, 4.6, 4.7, 4.8 shows the residue profiles and histograms with a non-linear polynomial fit, as it can be seen the model fairy accurately traces the ratio locus of the evolution of the temperature. Figure 4.5 shows the regular residue of the temperature with respect to an independent variable and it is seen that the data points are fairly largely scattered.We do see a lot of fluctuations in the regular residue with respect to the independent variable towards the beginning of the data plot. This explains the fact that the temperature was held constant at 40 °C as the starting point keeping the initial condition stable. After about 7.5 minutes the slope of the graph was only downward and this difference is captured by this graph. It can be seen that towards the end of plot the regular residue of temperature is almost close to zero as the fall in the temperature is fairly smooth. On the contrary the graph on the bottom left in Figure 4.5 has a slightly flipped effect owing to the nature of the fit.

In the upper right graph of Figure 4.5 is the histogram of the regular residual counts of the temperature. The symmetrical Gaussian profile of the histogram indicates that the predicted fit is a good fit for the experimental data. This is because this histogram distribution signals if the variance is distributed normally. The symmetrical nature of the spread in the histogram signifies that the assumption of the fit and its normalcy is highly likely to be true. The two highest distributions of the counts are around the regular residue of 0 ±0.1.

The percentiles plotted versus the regular residue of the temperature gives us insight that the variance is fairly well distributed as the resulting graph is almost linear from -0.5 to +0.28, the deviation towards the +0.5 is is biologically due to the tremendous activity of the F10 cells with a lot of cells emitting the FRET signals almost incessantly. We can overall therefore decipher from the contour of the histogram spread and the percentile regular residual plots that this is indeed a good approximation.

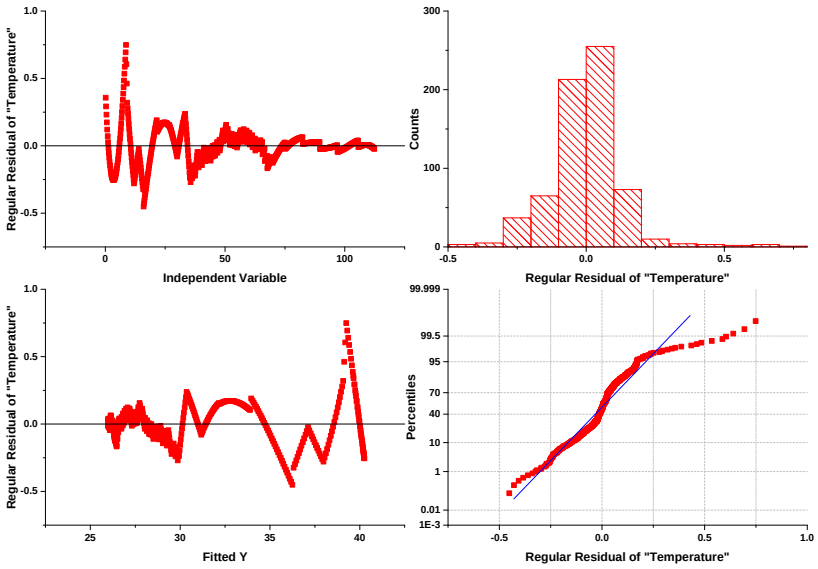

Figure 4.5 – Temperature profile - Residual Plot.

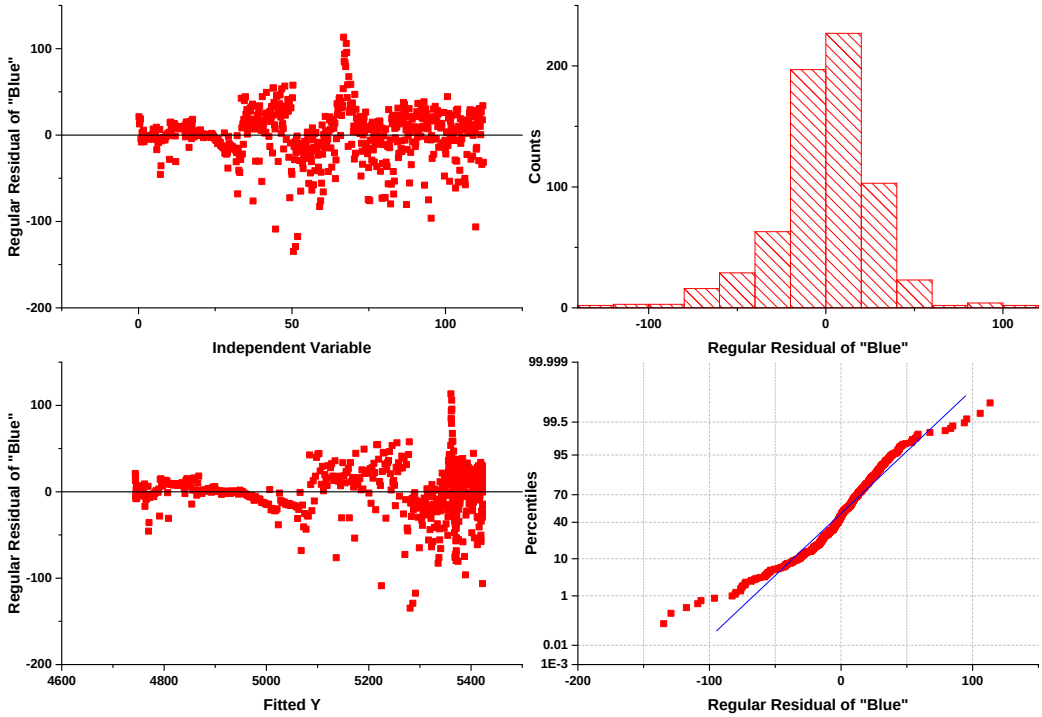

Figure 4.6 – Blue Counts F10 cells - Residual Plot.

The histogram values of the residuals of the blue counts are as shown in Figure 4.6 on the top right. This histogram also has a fairly symmetrical Gaussian spread of the counts. The regular residue of the blue counts were fairy randomly scattered in both the cases of the independent and fitted Y variables. The percentile when plotted versus the regular residue of the Blue shows that this is an excellent fit as most of the points lie on the line.

The histograms values of the residuals of the green counts are as shown in Figure 4.7 on the top right. This histogram also has a fairly symmetrical Gaussian spread of the counts. The regular residue of the blue counts and the ratio were fairy randomly scattered in both cases of the independent and fitted Y variables. The percentile when plotted versus the regular residue of the green and the ratio shows that this is an excellent fit as most of the points lie on the line.

The histogram of the ratio shows pronounced Gaussian symmetry and the percentile plot versus the regular residue of the ratio shows an extremely close match indicating the efficacy of the model. The regular residual plot of the ratio versus the independent variable for the ratio shows a really random and even spread of points.

While the regular residue of the ratio versus the fitted Y show a profoundly random scatter except towards the end where there is slight spread symmetrically around zero owing to the fluctuations in the counts.

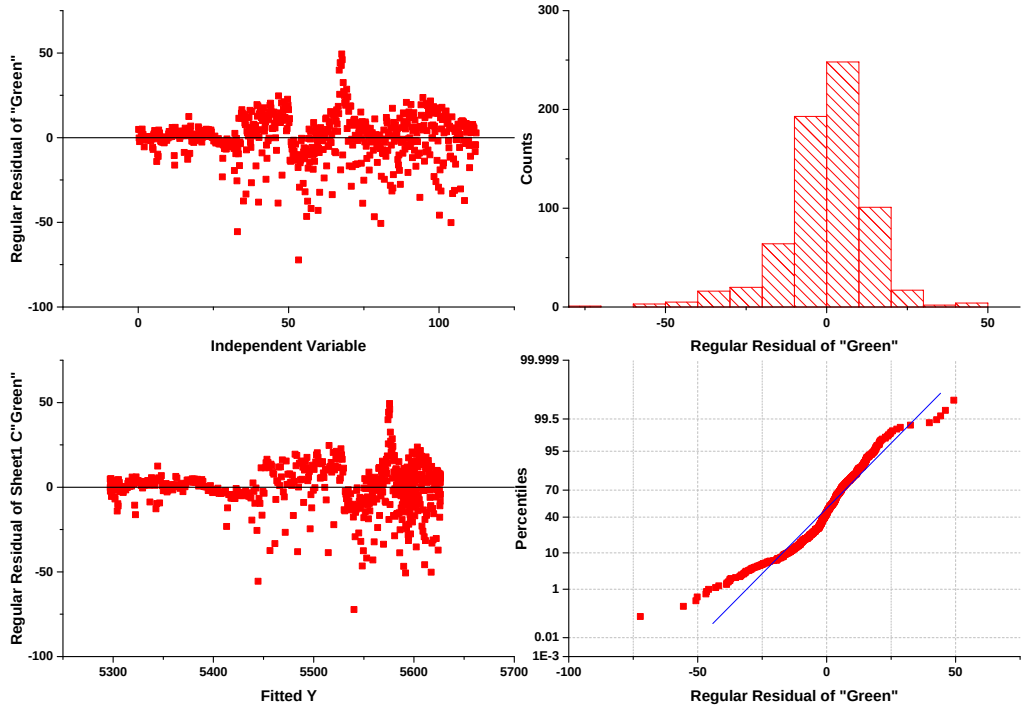

Figure 4.7 – Green Counts F10 cells - Residual Plot.

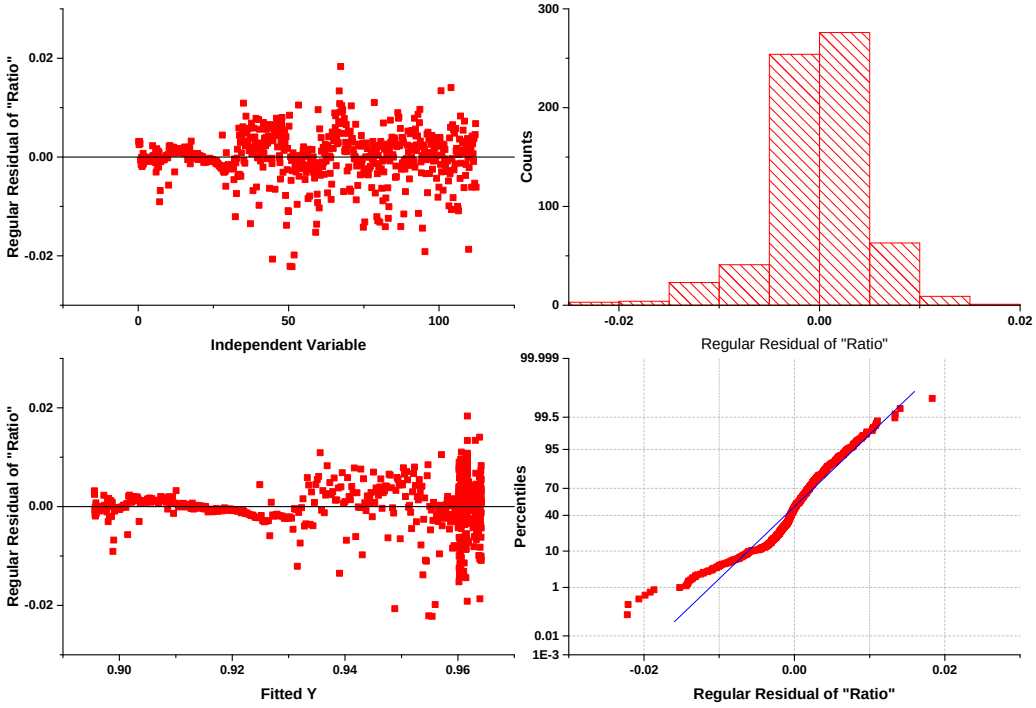

Figure 4.8 – Ratio Green/Blue Counts - Residual Plot.

4.5 Fluorescence as function of light intensity and exposure time

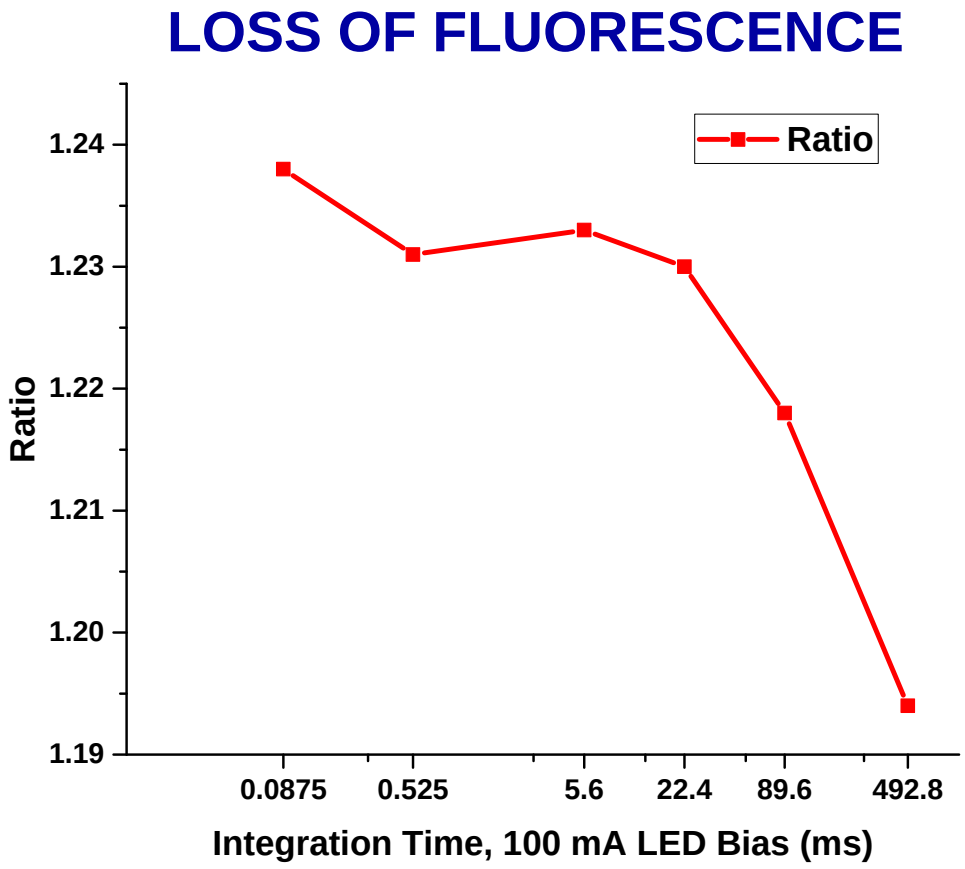

Figure 4.9 – Loss of fluorescence at high light intensities and exposure times.

Figure 4.9 shows the effect of using higher integration times (or higher exposure times) to high intensity excitation light on the F10 cells. The F10 cells were exposed to the 425 nm centered excitation LED with a bias current of 100 mA for varying integration times. The time between measurements was 10 ms.

It can be seen from Figure 4.9 that the ratio was approximately 1.24 for an integration time of 87.5 us, which hovered around the 1.23 mark for integration times of 525 us, 5.6 ms and 22.4 ms showing a tendency to fall. At 89.6 ms the ratio fell to about 1.215 and even further to 1.193 at 492.8 ms. This was about 3.8% loss in fluorescence within the scope of the dynamic range of the LED excitation power. A trend was consistently observed across several experiments.

This seems to prove the point that there is a saturation limit for the amount of excitation light power that can be used to stimulate the cells. There is a trade off, after crossing the noise floor, leading to the choice of the excitation light power that is most conducive for the F10 cells. The next experiment shows the outcome of aggrandizing this effect.

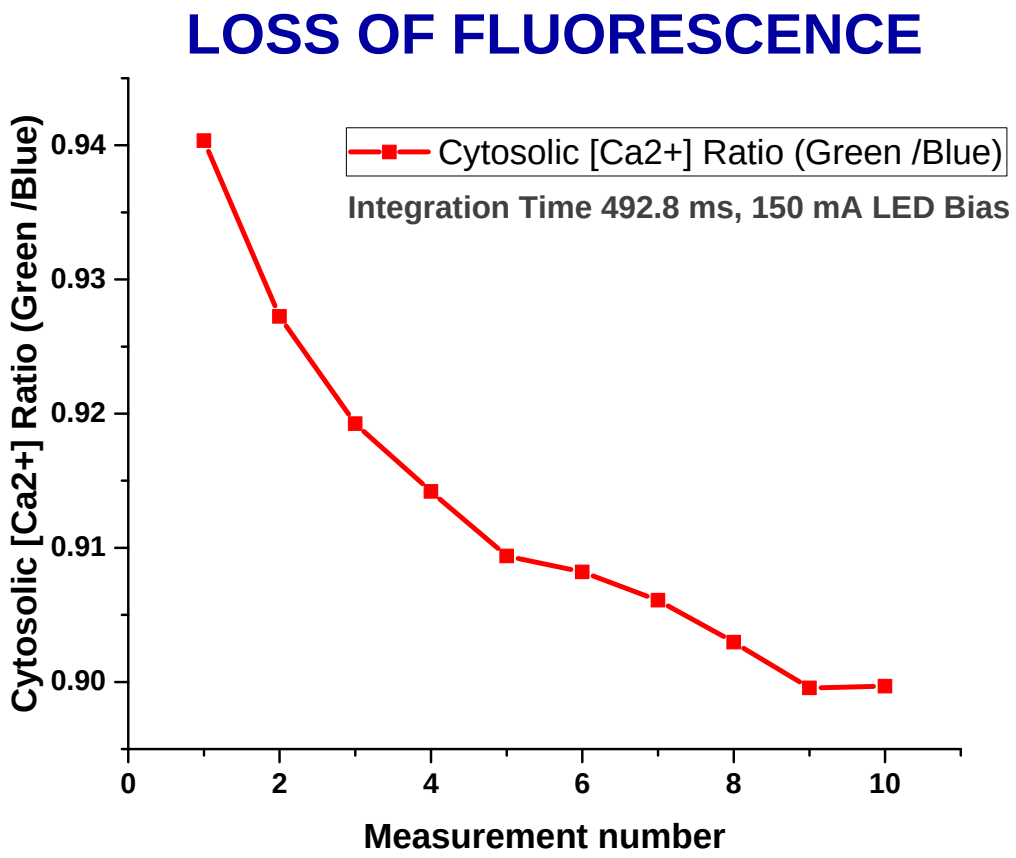

Figure 4.10 – Loss of fluorescence at high light intensities and long exposure times.

Figure 4.10 shows the effect of exciting the cells with an even higher flux of light with an irradiated power for 150 mA of excitation LED bias and an integration time of 492.8 ms. This integration time actually amounts to about 2 seconds of light exposure as this is the amount of time per channel and the PD has four channels and therefore takes four times the amount of time for the same. The time between the measurements was once again 10 ms. In this case 10 measurements points were made for the same testing conditions. It is observed from Figure 4.10 that the cytosolic Ca^{2+} ratio was 0.94 for the first measurement and decreased to about 0.89 for the tenth measurement point. This was about 5.3% drop in fluorescence, which is about 1.5% more than the previous experimental condition.

A plausible explanation for this drop in fluorescence is that the excess energy disrupts the covalent bonds in the florescence molecules and the electrons move from the valence to the conduction band. It maybe possible that the electrons go back to the valence band again, taking the molecule back to its low energy confirmation. If the energy however was too high, the electrons could actually escape as free electrons into the medium. In this scenario we loose fluorescence permanently. This is explored further in the next experiment.

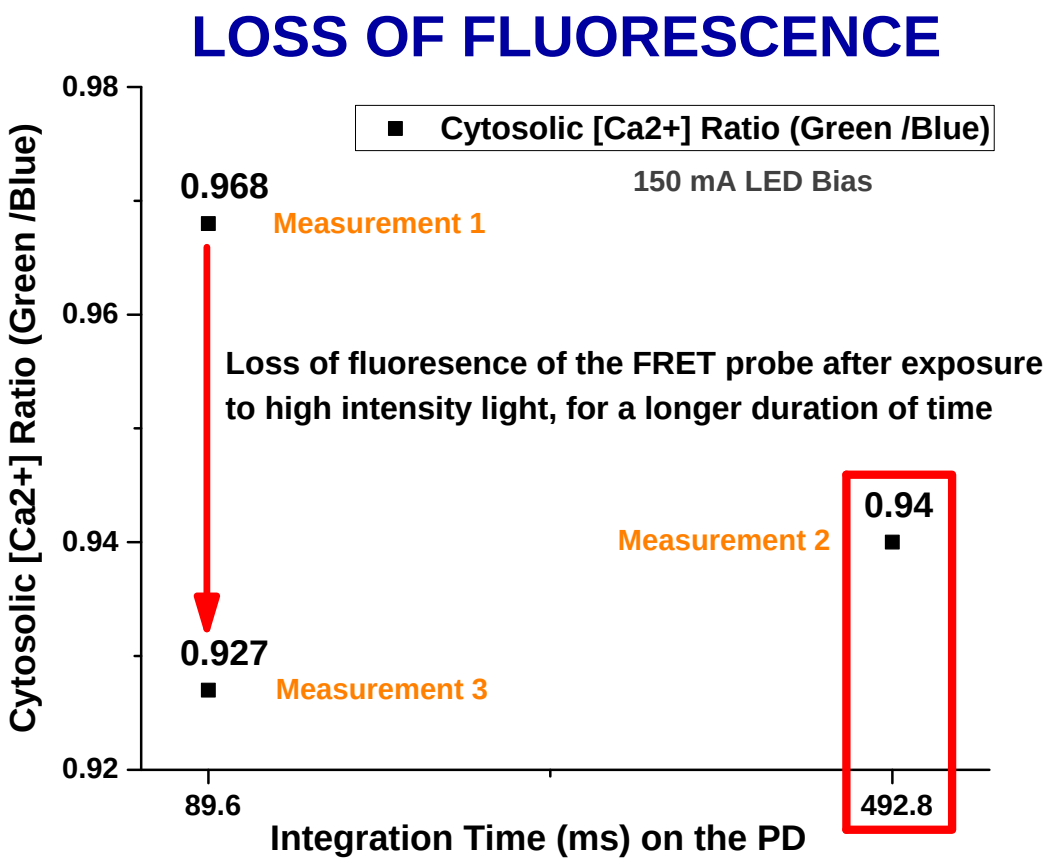

Figure 4.11 – Loss of fluorescence for the same measurement conditions after exposure to high intensity light for long duration.

Figure 4.11 displays the cytosolic Ca^{2+} ratio of the F10 cells with the same experimental conditions with a longer duration of excitation with the same intensity of light. Measurement 1 was performed with an excitation LED bias current of 150 mA and integration time of 89.8 ms (359.6 ms totally). The cytosolic Ca^{2+} ratio was 0.968. The same cell culture was then excited for 492.8 ms integration time (1.97 seconds totally) and the cytosolic Ca^{2+} ratio dropped to 0.94 in measurement 2.

After this the cells were re-exposed to the original excitation LED bias current of 150 mA and integration time of 89.8 ms (359.6 ms totally). The ratio for measurement 3 dropped to 0.927 from 0.968 of the measurement 1. This was a 4.2% loss in fluorescence.

This indicates the inability of some of the FRET producing cells to function with the same efficacy after exposure to high intensities of excitation light for longer time periods. These measurements shed light on the upper end of the dynamic range of the excitation light and can be used a guiding tool for both *in-vivo* and *in vitro* measurements.

4.6 Response of the cells in KRBH solution and cell culture medium

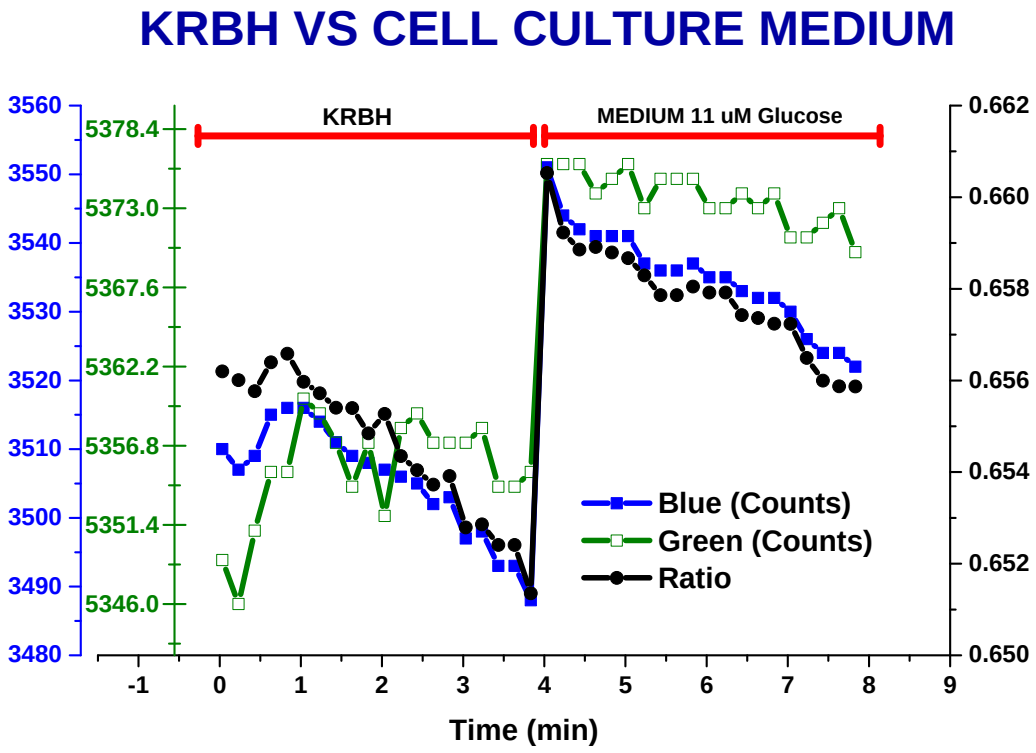

Figure 4.12 – Distinguishing cell response for KRBH solution vs Cell Culture Medium.

Figure 4.12 shows the cytosolic Ca^{2+} ratio (green/blue) of the F10 cells when exposed to KRBH buffer solution vs cell culture medium having 11 mM glucose concentration. The excitation LED bias current of 20 mA was used with a photo-detector integration time per channel of 492.8 ms. Each measurement was taken 40 times and the averaged result is used in the graph, the standard deviation less than 0.2% being neglected. The time interval between measurements was 10 seconds. The first 20 counts were used to measure the cells in the KRBH solution and the next 20 counts the medium was exchanged with the cell culture media.

As seen in Figure 4.12 there is a transition in the ratio from 0.651 to 0.661 and particularly in the green counts. This is because, when the cells are subjected to a glucose medium, this triggers the influx of the cytosolic Ca^{2+} ions though the cell membrane and these Ca^{2+} ions ions enable the FRET molecular complex to come in close conformation thus emitting the light at 535 nm when excited with the blue light having energy component at the 435 nm. As a result we also see a decrease in the blue counts of the PD.

During these experiments we realized ensure good oxygenation and glucose circulation were needed to have a healthy response from the cells and we solved this using a small spinning magnet inside the Petri dish hosting the cells that are discussed in the next experiment.

4.7 Oxygenation of the cells: stimulation using glucose and KCL

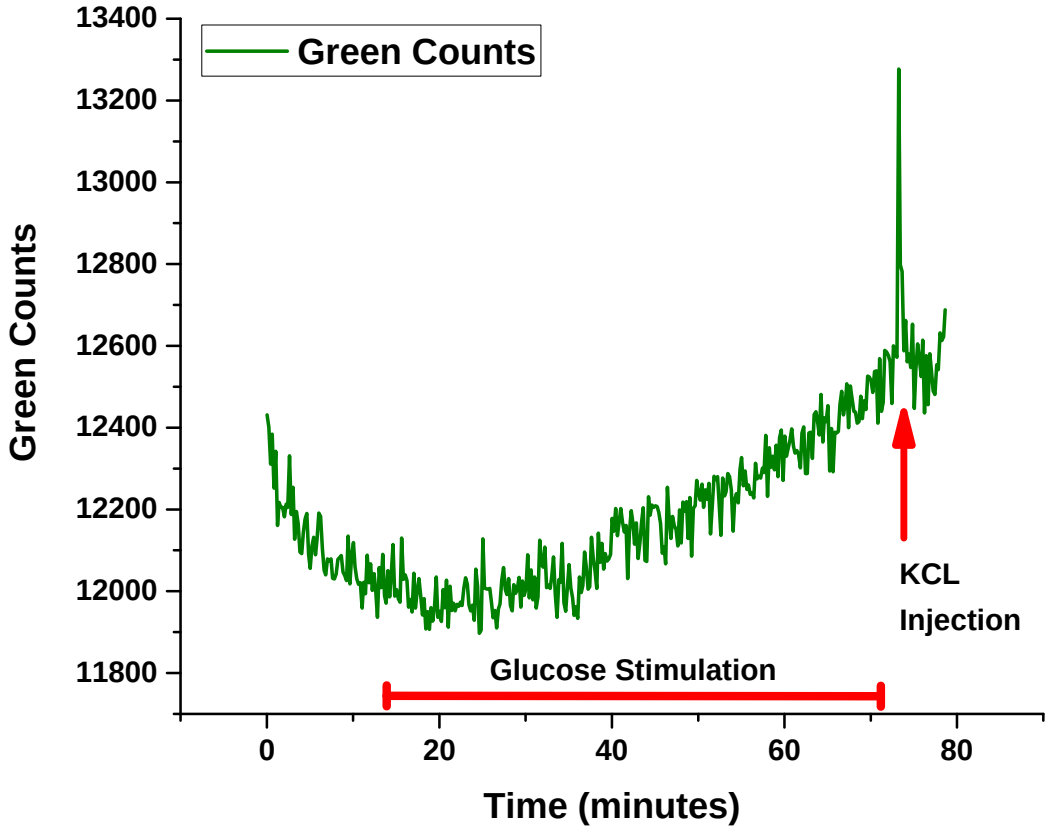

Figure 4.13 – Green Counts: Oxygenation with a stirring magnet for Glucose and KCL stimulation. 20 mA LED bias and 492.8 ms PD integration time were used.

In order for the cells to stay alive and respond when stimulated with glucose and KCL is was necessary that the media in which the cells were immersed circulate. This was achieved in our case with a simple stirring magnet. A 10 mM glucose concentration was used in the culture medium. A mesh was glued with a bio compatible glue on the bottom surface of the Petri dish to host the cell in-order to confine them to a spot while they're in the Petri dish with the stirring magnet. A 2.5 mM of glucose was injected a few minutes after loading. It can be seen in Figure 4.13 the stirring effect of the magnet causes a lot of spikes on the graph and a green counts graph that is rising in locus indicating the effect of glucose.

Towards the 72^{nd} minute we injected KCL in the medium causing depolarization of the cell membrane channels leading to a huge influx of Ca^{2+} ions in the cell, thus creating a huge fluorescence green spike on the graph. The blue counts graph and the cytosolic Ca^{2+} ratio (green/blue) are explained next.

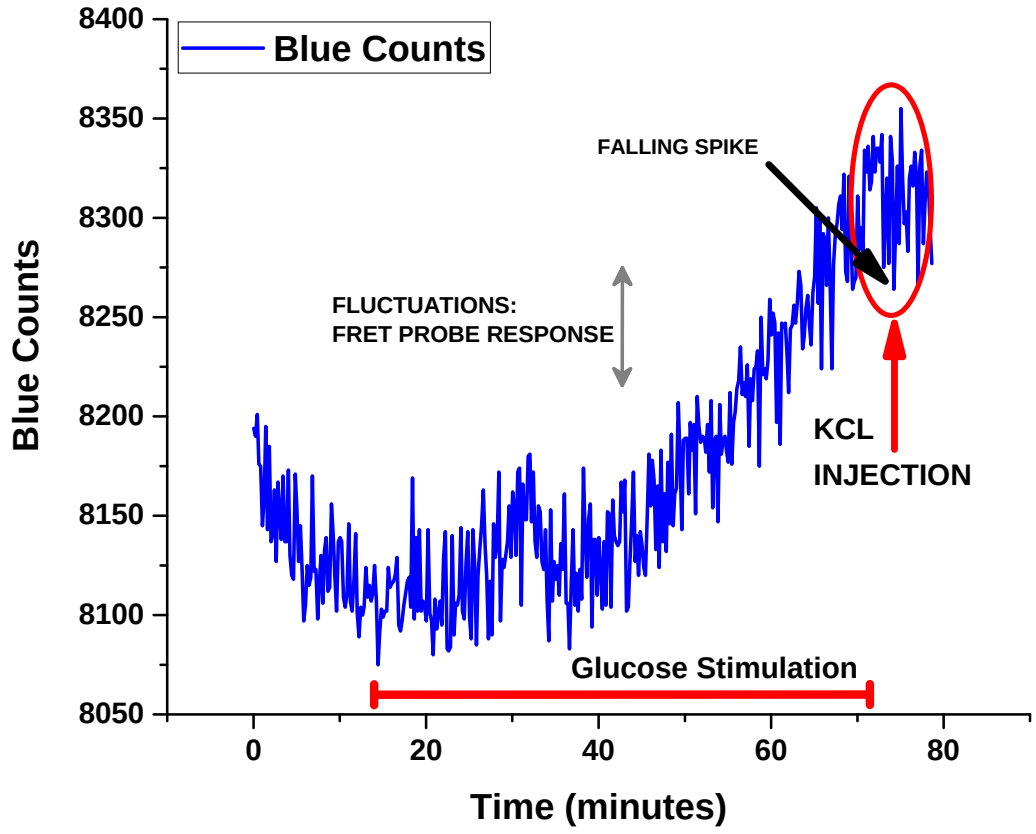

Figure 4.14 – Blue Counts: Oxygenation with a stirring magnet for Glucose and KCL stimulation. 20 mA LED bias and 492.8 ms PD integration time were used.

The FRET probe has two emissions, namely one at 485 nm (blue) and the second one at 535 nm (green). The blue counts also show this upward and downward firing trend upon stimulation with glucose as shown in Figure 4.14. We use 3D cell aggregates from the cell culture, are stimulated with glucose and then excited with light. Since there is a range of periods in which the 3D aggregates are excited, not all of them emit the green wavelength at the same time and gives rise to an averaging effect. As a result, two effects can be observed. Firstly, when a group of aggregates that access glucose is stimulated the blue counts are emitted in an anti-parallel fashion (downward trend) with respect to the green counts. This is seen in many of the downward spikes. Secondly, when a cluster of cell aggregates that do not receive the glucose exceeds the ones that receives the glucose emits a higher blue counts and this is seen in the upward spikes. However, a part of the upward component is also due to the overlap in the bandwidths and the blue and green pixels. Most interestingly when the cells are stimulated with KCL around the 72^{nd} minute we see a sharp falling signal, is opposite to that observed in the Green counts. These panoply of effects are elucidated conspicuously in the cytosolic Ca^{2+} ratio (green/blue) graph explained next.

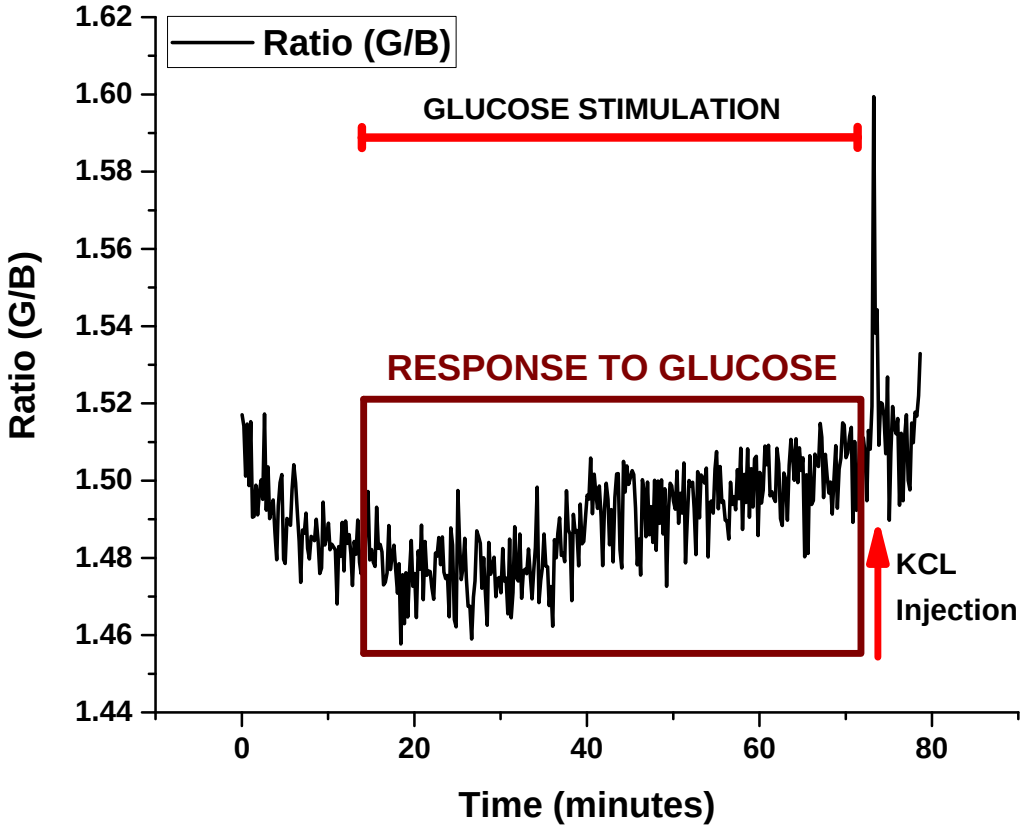

Figure 4.15 – Ratio (Green/Blue): Oxygenation with a stirring magnet for Glucose and KCL stimulation. 20 mA LED bias and 492.8 ms PD integration time were used.

The cytosolic Ca^{2+} ratio (green/blue) is shown in Figure 4.15. The boxed brown region on the graph shows the emission of the FRET signals from the F10 cells and it is seen that there is a fairly consistent, in range response of the cells to the glucose stimulation. This ratio varies between 1.46 to 1.51 for about 60 minutes approximately, with a range of about between 0.02 to 0.024 per excursion. This is approximately 3.42% dynamic range for the given number of cell aggregates and about 1.37% per excursion. Upon stimulation with KCL around the 72^{nd} minute the ratio jumps from 1.5 to 1.6, which is around 6.7% relative change. KCL depolarizes the cell membrane of all the aggregates, over a short period of time after stimulation with KCL, this is seen by the peak in the fluorescence. When this relative difference for KCL is compared to the change in glucose stimulation, we can extrapolate that around 20% of the cells aggregates are actively fluorescing at any given time when stimulated with glucose. Having got a response from glucose stimulation, we carried out several experiments to observe the effects of glucose stimulation, running in duration from 2-24 hours. One such experiment with 18 hours continuous glucose monitoring is described next.

4.8 Continuous automated glucose monitoring for 18 hours

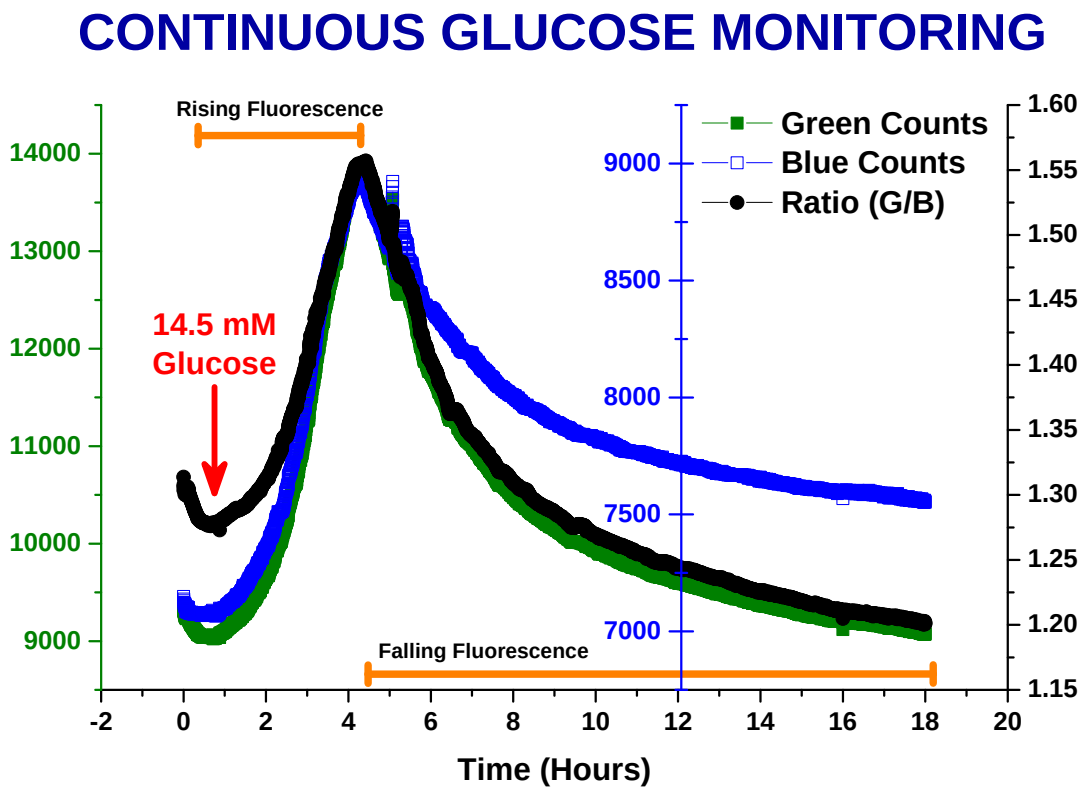

Figure 4.16 – Continuous Glucose Monitoring for 18 hours.

The aim if this experiment was to gauge the response of the F10 cells to glucose with a magnetic stirrer in the cell culture medium. The cells were loaded from the cell culture room at 37.2°C into the dish with the mesh at room temperature and transported to the bench top in the lab inside the temperature chamber which was about 37 °C. A total of 5400 automated measurements were made with the excitation LED bias current of 20 mA and a photo-detector integration time of 492.8 ms with 10 seconds between measurements. A dose of 14.5 mM of glucose was injected in the Petri dish after about 20 minutes. As shown in Figure 4.16 the ratio increased consistently by about 22.8% for 5 hours after glucose stimulation, owing to the green fluorescence (increasing green counts) from the 535 nm component of the FRET probe. We see a drop in the ratio and the fluorescence after 5 hours, and a non-symmetrical locus of the blue counts in this falling cycle as opposed to its ditto trend in the rising locus after stimulation. This is plausibly because the amount of glucose in the medium actually started to decrease as the cells consume glucose for normal functioning. This lack of glucose means there would be a lesser influx of the Ca^{2+} ions and therefore the FRET probe would take its open molecular confirmation state, thereby emitting light at 485 nm when excited with a light of 435 nm. We delve into a step-wise glucose stimulation in the next experiment to study the effects and response of the cells for this scenario.

4.9 Periodic glucose stimulation

The goal of this experiment was to study the effect of step-wise glucose stimulation on F10 cells. In the beginning the cells were loaded from the incubator and allowed to settle to a steady state for 20 minutes. The F10 cells were then stimulated with 2.5 mM of glucose roughly every 20 minutes as shown by the cytosolic Ca^{2+} ratio (green/blue) in Figure 4.17. There is a conspicuously sharp, though small, change of 0.9% to 1% in ratio upon each stimulation as seen in the ratio and the green counts in Figures 4.17 and 4.18a. A clear signature of the glucose stimulation is observed in the blue counts graph in Figure 4.18b as these counts do not rise as much, due to the decrease in the emission at 485 nm. It is seen in Figure 4.17 that the ratio tends to settle down back to a relatively quasi stable state after every stimulation due to the insulin secretion of the F10 cells. This can be interpreted as an average fluorescence signal from the cell aggregates. The sixth glucose stimulation was followed up with a diazoxide injection leading to both a rise and fall of the counts sequentially. The cells were stimulated with KCL at 110 minutes, leading to a huge depolarization effect on the cells with a 7.3% spike in fluorescence. Based on this we can infer that only 14% of the cell aggregates on an average responded to glucose stimulation.

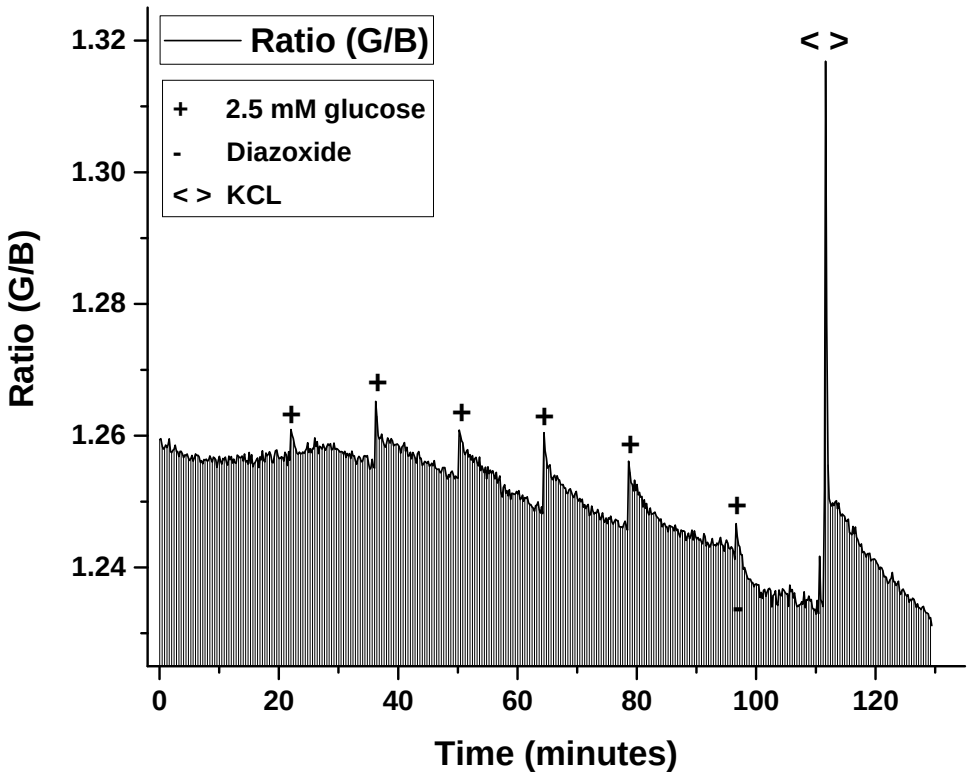

Figure 4.17 – Continuous Glucose Monitoring - Ratio, observe the average response of the F10 cells for every glucose stimulation.

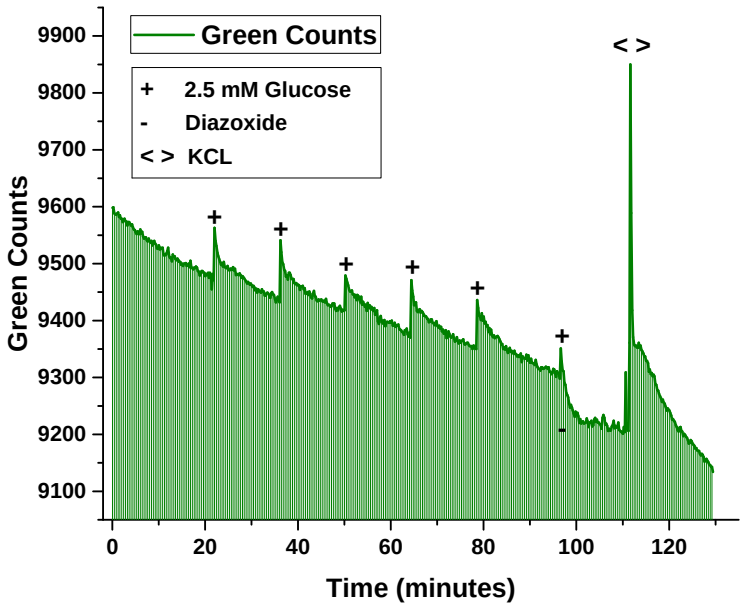

(a) Continuous Glucose Monitoring - Green Counts, observe the average response of the F10 cells for every glucose stimulation.

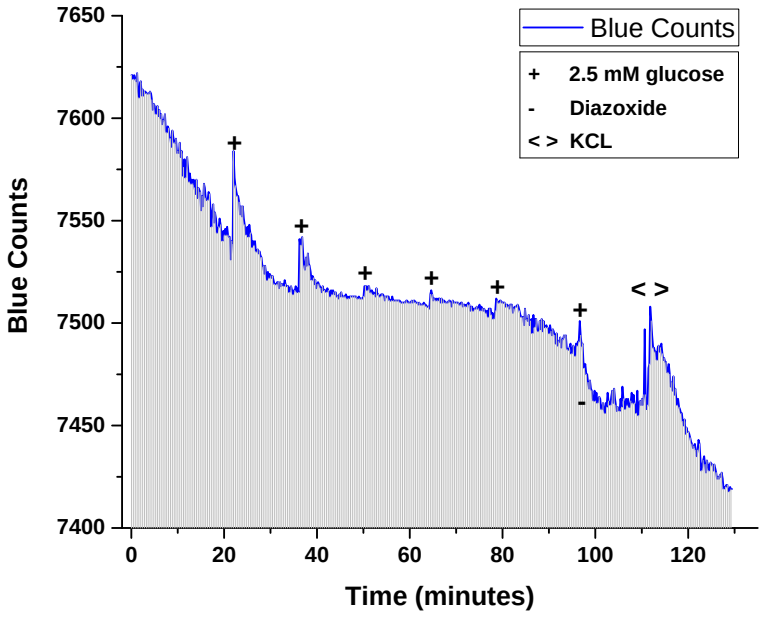

(b) Continuous Glucose Monitoring - Blue Counts, observe the average response of the F10 cells for every glucose stimulation.

Figure 4.18 – Continuous Glucose Monitoring: Observe the average response of the F10 cells for every glucose stimulation.

4.10 Glucose binary pulse stimulation

This experiment was performed to access the response of the cells to binary glucose stimulation with 11 mM of glucose and 0 mM of glucose.

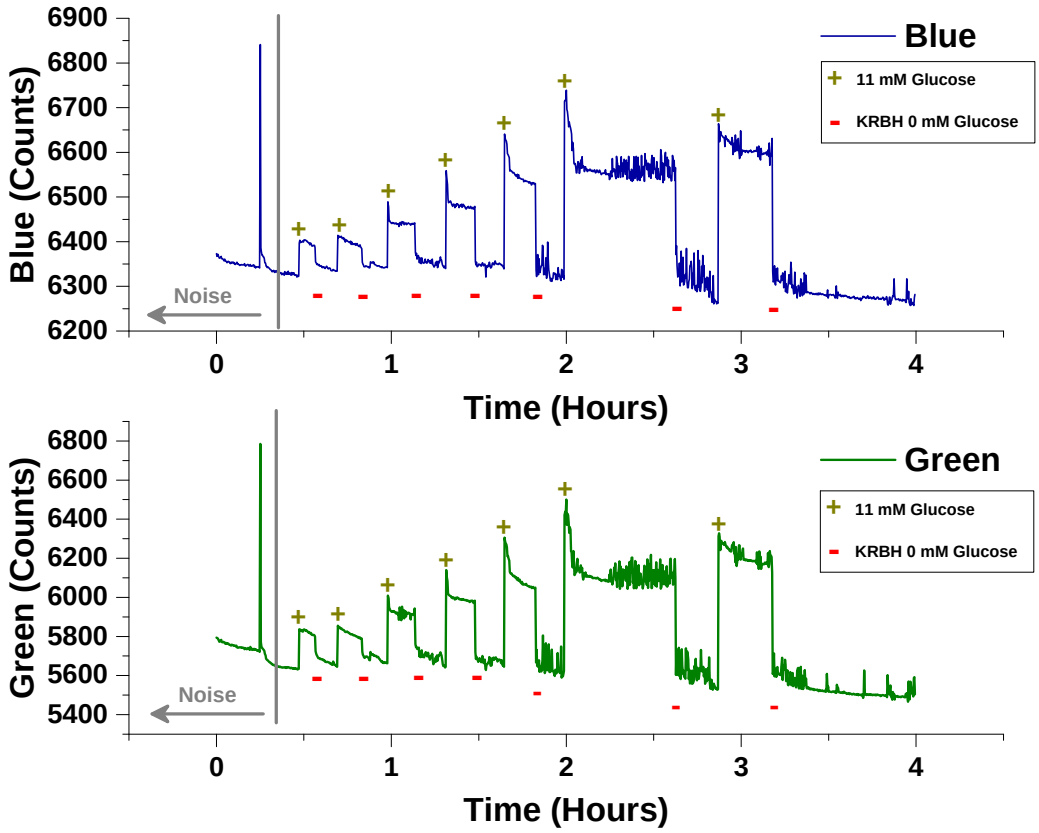

Figure 4.19 – Glucose Pulse Stimulation alternating between 11 mM Glucose of the cell culture medium and KRBH with 0 mM Glucose. Green and Blue Counts.

To do this, cells were taken out of the incubator and brought under the hood where they were loaded under the mesh at the bottom of the Petri dish. The UV Glue based gel was used to seal the mesh with the cells inside. The cells were transported to the temperature chamber in the other lab. A stirrer was a magnetic shaker was used for promoting media circulation and oxygenation. The excitation LED bias current for this measurement was 20 mA and the integration Time (ms) per channel (R/G/B/IR) was 492.800 ms. A total of 2000 points were measured in an automated fashion with a 10 second gap between measurements.

As shown in Figures 4.19 and 4.20 the initial 20 minutes were neglected as noise. After this the F10 cells were stimulated with 11 mM of glucose, leading to a rise in the fluorescence, a pause time and then depletion of glucose by cell medium exchange with KRBH solution having 0 mM

glucose. This was done seven times for each of the stimulants as shown in Figures 4.19 and 4.20.

It is seen that the ratio for the KRBH always settled closely around the 0.89 level. The glucose stimulation led to very sharp spike in the florescence peaks, followed by sharp falling peaks and a plateauing level. The sharp peaks are attributed to the effect of insulin secretion upon a sudden glucose stimulus. It is seen that during the plateauing phase there are manifold instances of anti-parallel responses of the FRET probe, its blue and green emissions leading to a pulsating spiking ratio around the plateau average as seen between 2 to 2.5 hours or 2.5 to 3.5 hours. We also observe an overall ascending trend in the locus of the peaks of the ratio for every instance of glucose stimulation, even for changing periods of glucose stimulation.

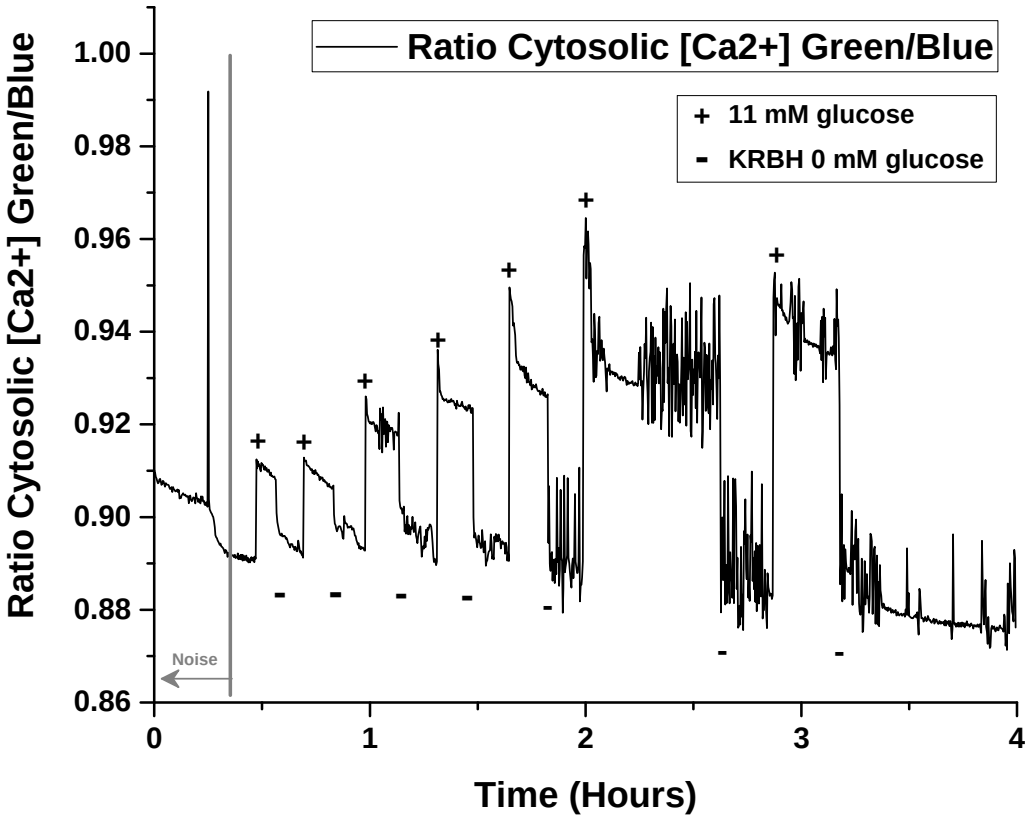

Figure 4.20 – Glucose Pulse Stimulation alternating between 11 mM Glucose of the cell culture medium and KRBH with 0 mM Glucose. Cytosolic Ca^{2+} Ratio Green/Blue.

4.11 Conclusion of *in vitro* biological experiments and glucose monitoring

This chapter therefore provides working proof of the panoply of *in vitro* experimental possibilities and applications with this system. We have successfully demonstrated that we can characterize the total number of cells, cell growth and death, effects on fluorescence after exposure to excess light intensity for long periods of time, all in a quantitative fashion. The proof-of-concept for one time glucose stimulation along with stirring for promoting oxygenation and media circulation was successful as we observed a clear response from the F10 cells. Continuous glucose stimulation and monitoring for several hours, step-wise glucose stimulation and monitoring and binary glucose stimulation (glucose, no glucose) was monitored successfully. This proves the potential of this system for *in vitro* glucose stimulation and monitoring.

5 Analog Front End Circuit in 0.18 µm CMOS for optical glucose detection

5.1 Metrics for classifying accuracy and precision of sensors used for glucose monitoring

The two fundamental attributes of glucose sensors are their accuracy and reliability. Accuracy in this context means how close in real value is the measured value to the real glucose value. Reproducibility on the other hand adds another dimension to the measurement, in this context it means the ability of the sensor to produce the same result for a given input for any number of measurements. Reproducibility is a dimension that relates to how precise is the output of such a sensor over an extended duration of time.

When we refer to a sensor pertinent to glucose measurements the two widely cited figures of merits are the Mean Absolute Relative Difference, abbreviated as MARD, and Clarke error graph which is grid analyzed [62].

MARD with a value below 10% is indicative of a sensor that is of a acceptable accuracy for continuous glucose monitoring (CGM). For this MARD can be used to make critical decisions of delivery of insulin boluses to the patient [63]. It is crucial to know that MARD is not a totally fool proof number objectively defined rooting from thresholds apposite to a patient with an imminent hypoglycemia event [64].

The onus of using the MARD is also that it does not give an insight on the absolute direction (rising or falling) trend of the error. This can be dangerous at the boundaries of normal glucose level ranges.

The second fable aspect of using MARD as a metric is that it is not a constant error for different levels of glucose. But, the error in itself is a dynamic variable as a function of glucose and that's not very well defined. The precipice of the MARD metric is that its computation method is not standardized and it is affected by the method of designing the study concomitant with a motley of reference standards being used in various studies.

Clarke Error Grid Analysis (EGA) is a graphical method for gauging a CGM devices performance versus risk w.r.t sensor error. As shown in Figure 5.1, the y-axis represents the performance of the device to be tested and the x-axis represents a reference glucose measuring device output. The Clarke's error grid therefore highlights any associated clinical risk in the measurement of glucose. There are five regions of the grid which are labeled A through E.

- Values in zone A fall 20% within the range of the reference sensor and are considered clinically accurate,
- Values in the zone B fall outside the 20% range of the reference sensor and are attributed benign with the leverage that they would not result in an inappropriate treatment,
- Values in zone C would result in a treatment a bit unnecessary for the patient,
- Values in zone D indicate a failure to detect both hypoglycemia and hyperglycemia, and
- Values in zone E are the most erroneous and dangerous one as they confound treatment for hyperglycemia with hypoglycemia and vice-versa.

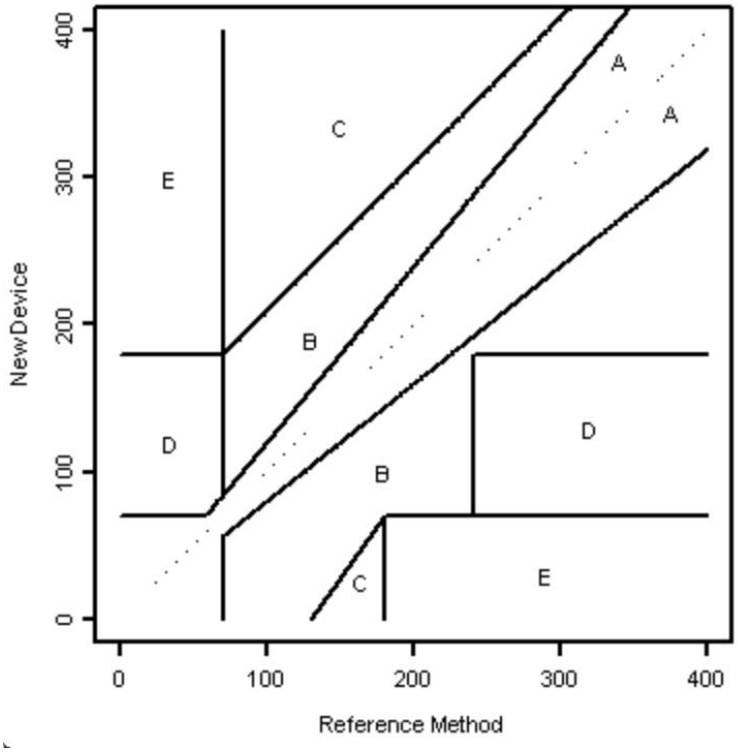

Figure 5.1 – The Clarke Error Grid. Source [16]

5.2 CMOS Analog Front-End (AFE) amplifiers for optical biosensor applications with pertinence to glucose sensing.

A lot of scientific research is being carried out to build front-end circuits and systems for sensing and measuring glucose using CMOS technology [65] [66]. Nanotechnology us used on the biosensor side widely [67], however, their reproducibility and cyto-toxic effects remain a concern for long term implants. Some of the CMOS systems for sensing glucose are wireless and fully implantable [68] making it easier for long term monitoring. There are systems using artificial intelligence for gauging blood glucose levels and taking corrective actions [69]. The most common type of CMOS architecture used for optical bio-sensing is the trans-impedance amplifier (TIA) topology. A light based optical system usually consists of three parts, namely an excitation source (typically an LED), the sample or sensor that is excited, and a photo readout sensor to read the emitted light from the analyte. The photo diode usually emits a current which is read by the analog front end readout circuit. The noise sensitivity and the offset created along the path of this read-out circuit directly limit the current that is readout.

The architectures can be classified into shunt-feedback [70, 71, 72] and current-mode circuits [73, 74, 75]. These architectures have very often been designed and well analyzed for high speed wide-band applications. They are optimized to mitigate the effect of the input capacitance of the sensor reading element, which is the photo-diode, and are usually designed to enhance to input swing of the circuit.

As shown in Figure 5.2a, a current mode circuit has the photo-diode interfaced to the diode connected transistor M1 with input impedance approximated to $1/g_{m1}$, corresponding to a very low impedance path for the current at its input. The current that is readout can be translated into a voltage with the aid of a resistive load.

The second commonly designed silicon architecture is the shunt-feedback system as shown in Figure 5.2b. In a shunt-feedback system the feedback arrives back at the input of the circuit. The effect of the feedback circuit is that it reduces the input impedance by the gain of the amplifier in the feedback loop. The input impedance is therefore R_f/A_0. This is the advantage of this topology, as the input impedance is low, which facilitates the flow of charge, the current, that flows through the feedback resistor. The OTA (Operational Trans-conductance Amplifier) in the shunt-feedback architecture can be implemented with a three-stage Miller compensated amplifier [76] [77].

The trade-off for the topology is between the current mode readout circuit though it gives a low input impedance and higher bandwidth, and the noise. The TIA architecture, however, can easily handle electrical stimuli for both curved and abrupt transitions. It can also reduce the voltage gain at relatively low frequencies at the price of a delayed bandwidth response.

The TIA clearly outperforms the current readout circuit and is a very useful system architecture for low and medium frequency biomedical applications such as glucose sensing using light.

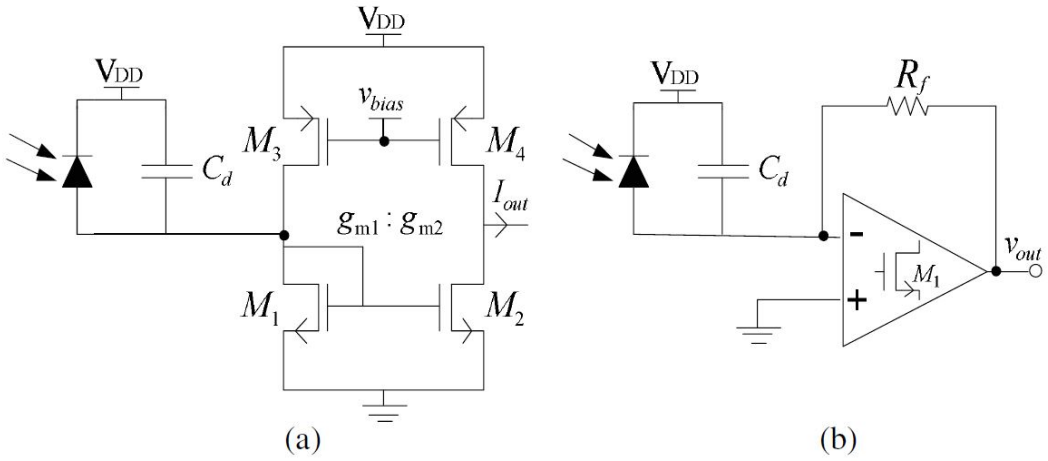

Figure 5.2 – Transimpedance Amplifiers (TIAs) Architectures. Source [17]

5.3 Multimodal spectroscopy for non-invasive highly accurate estimation of blood glucose levels non-invasively

In this work optical and electrical sensing devices are combined to achieve an accurate reading of the blood glucose level. This combined approach is referred to as Multi-Modal Spectroscopy. The optical method used is the multi-wavelength near-infrared spectroscopy (mNIRS), whilst the electrical method used is the impedance spectroscopy (IMPS). The two measurements are combined using an Artificial Neural Network (ANN) to achieve a high precision estimation of blood glucose levels non-invasively.

5.3.1 Principle of Blood Glucose Estimation

The principles of IMPS and mNIRS are as depicted in Figure 5.3.

In the context of IMPS, the influence of glucose on the erythrocyte membrane is shown in Figure 5.3a. An increase in the concentration of glucose in blood leads to the admission of the glucose molecule in the cell via the glucose transporter located in the cell membrane. Through the process of cellular respiration the glucose molecule is converted into ATP. The energy generated by the ATP is used to regulate the ion pump channel of the cell, which changes the ion permeability of the cell membrane [78]. As a consequence, the electrical properties of the tissues in the vicinity are changed. This changed impedance can be measured electrically with an RLC resonating circuit having a resonant frequency F_{min} and a resonant impedance Z_{min}.

The NIRS method on the contrary uses the optical scattering properties of the glucose molecule directly as shown in Figure 5.3b . As a result, when the blood glucose level increases, so does the reflected light in the near infrared region of light and vice-versa. Each of these techniques have

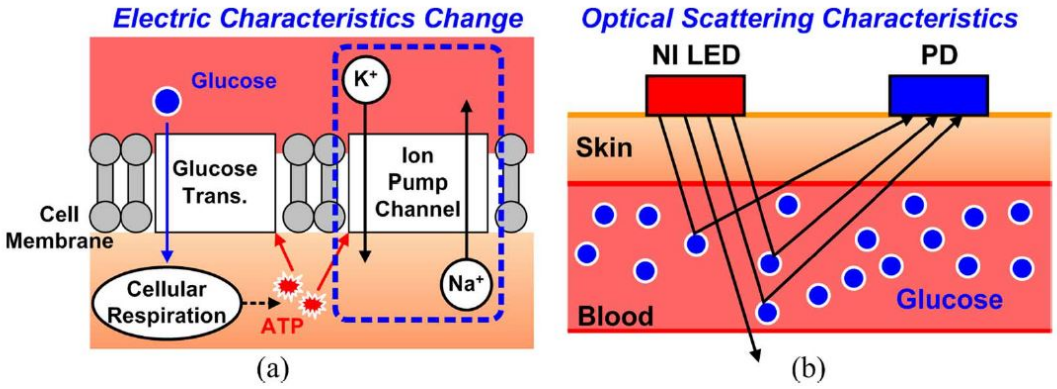

Figure 5.3 – Cartoon Illustration of non-invasive glucose detection and monitoring (a) Image depicts the electrical impedance change that is used for the sensing principle for impedance spectroscopy (IMPS), (b) Image graphically shows the excitation of the glucose molecules inside the body and the reflected light being collected by the photo-detector. Source [18]

their advantages and limitations.

The IMPS measures glucose indirectly, has a shallow penetration depth, works based on a contact electrode and is subject to systematic perturbations such as temperature and disease.

The NIRS on the other hand is intrinsically a direct method of blood glucose estimation, has a deep penetration depth, is a optical non-contact electrode-based method and is subject to systematic perturbations such as mechanical motion and heterogeneity of tissue. These two techniques, when fused together compensate each other and lead to much reduced error, which is the advantage of this method [18].

5.3.2 CMOS System Architecture for blood glucose measurement

The architecture of the multi-modal spectroscopy IC is shown in Figure 5.4. The blocks contain the circuits for both IMPS and NIRS high efficiency glucose measurements. For the IMPS an off-chip sinusoidal signal is swept through an inductor for a specific model of the RC resonant circuit. Circuits are built within to find the resonance frequency parameters F_{min} and Z_{min}. In context of the MIRS, LED driver circuits for driving 3 LED of wavelengths 850 nm, 950 nm and 1300 nm are implemented.

Within the same system an TIA is implemented to convert the received light, that accumulates as charge on a capacitor from the reverse biased diode of the photo-detectors. These independent signals are digitized using a 10-bit ADC and the result from the confluence of these two techniques is then mixed in a DSP running an ANN algorithm.

The measurements were done simultaneously on a subject as shown in the Figure 5.5 with IMPS data collected from the left hand wrist and the NIRS data collected from the right hand wrist. For

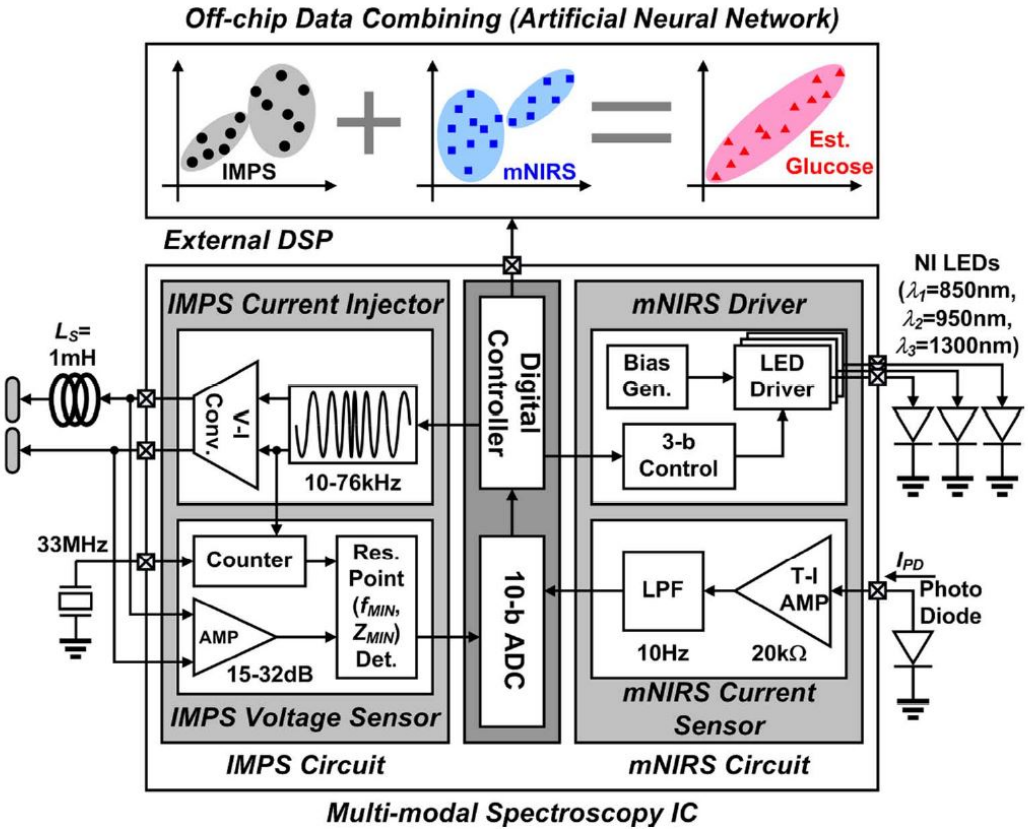

Figure 5.4 – System Architecture with the Impedance and Multi-Wavelength NIRS detection blocks. Source [18]

IMPS they used Ag/AgCl bipolar electrodes and fixed wired connections were used to minimize the effects of the perturbations. For NIRS three LED wavelengths namely 850 nm, 950 nm and 1300 nm were used. For the purposes of accuracy the dark current of the photo diode was measured before the NIRS measurements.

The magnitude of the light reflected for each wavelength of light was measured in a sequential fashion, for a duration of one second each.

The results of the two methods were combined using the ANN algorithm in a DSP. Very interestingly the architecture of the amplifier used here in the front end circuit was a pole split Miller amplifier which is used as one of the references in the scope of this thesis along with the NIRS method.

An Artificial Neural Network (ANN) method was used in this work as it is a based on non-linear statistics that depict neural systems representing complex biological entities. The ANN is capable of simulating advanced mathematical formulations exhibiting complicated input-output relationships. Hence, the non-linear nature of the ANN is better suited for assessing the accuracy of the blood glucose concentration in humans [79]. In the ANN used by this work four inputs were

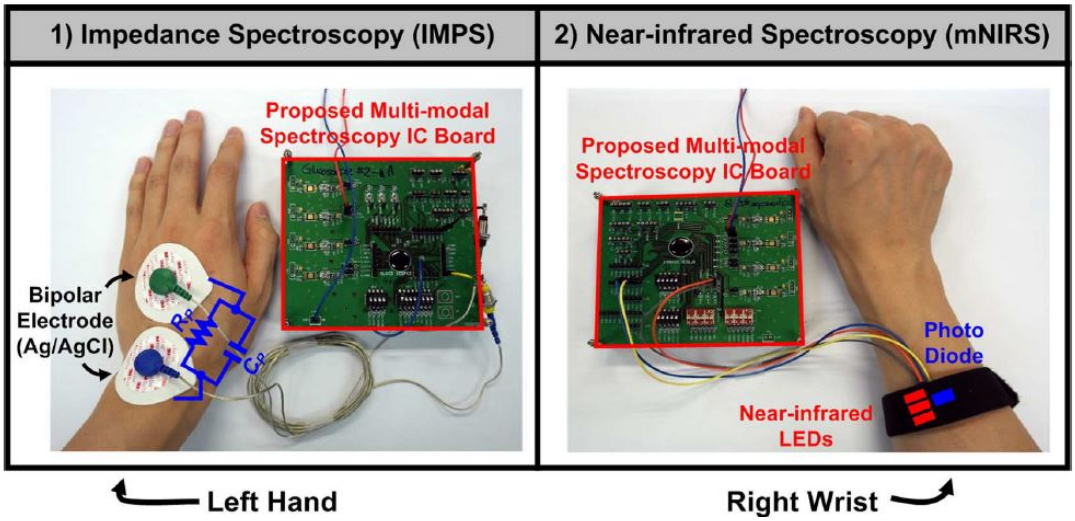

Figure 5.5 – Measurement setup and scenario for Glucose estimation using both IMPS and mNIRS. Source [18]

combined, namely C_p arising form the IMPS method and the three I_{pds}'s arising from the mNRIS method, as depicted in Figure 5.6. There were four nodes in the hidden layer and to achieve an estimation of the blood glucose level using this method and 20 MAC (multiply-accumulate) operation in conjunction with five sigmoid operation was used. An external DSP was used for achieving this goal.

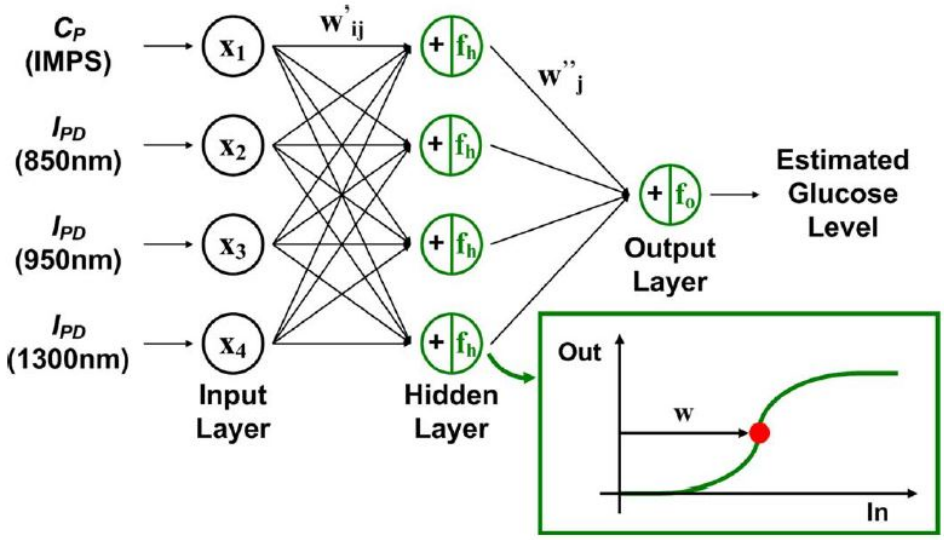

Figure 5.6 – Artificial Neural Network (ANN) Data Combing Method. Source [18]

The overall results of the two methods combined with the ANN method are shown in the graphs on Figure 5.7. As seen in Figure 5.7a the raw MARD of the NIRS method was between 15.0–20.0% and that of the IMPS method was around 15.0%. Subsequently, the results of the IMPS and

wavelengths of the NIRS were combined using the 2-input ANN technique as illustrated in Figure 5.7b. There was an improvement observed in the performance of the three wavelengths of light namely 850 nm, 950 nm and 1300 nm, as the MARDs were curtailed to 16.0%, 12.0%, and 15.0%, respectively. It can ben seen in Figure 5.7c that when the ANN technique was used to combine the results of both IMPS and mNIRS the overall mARD reduce further to 8.3%. With respect to the figures of merit we have defined before, the CGE from fifty samples depicts the efficacy of the 4 input ANN method as the zone A data increases from 66% to 90%.

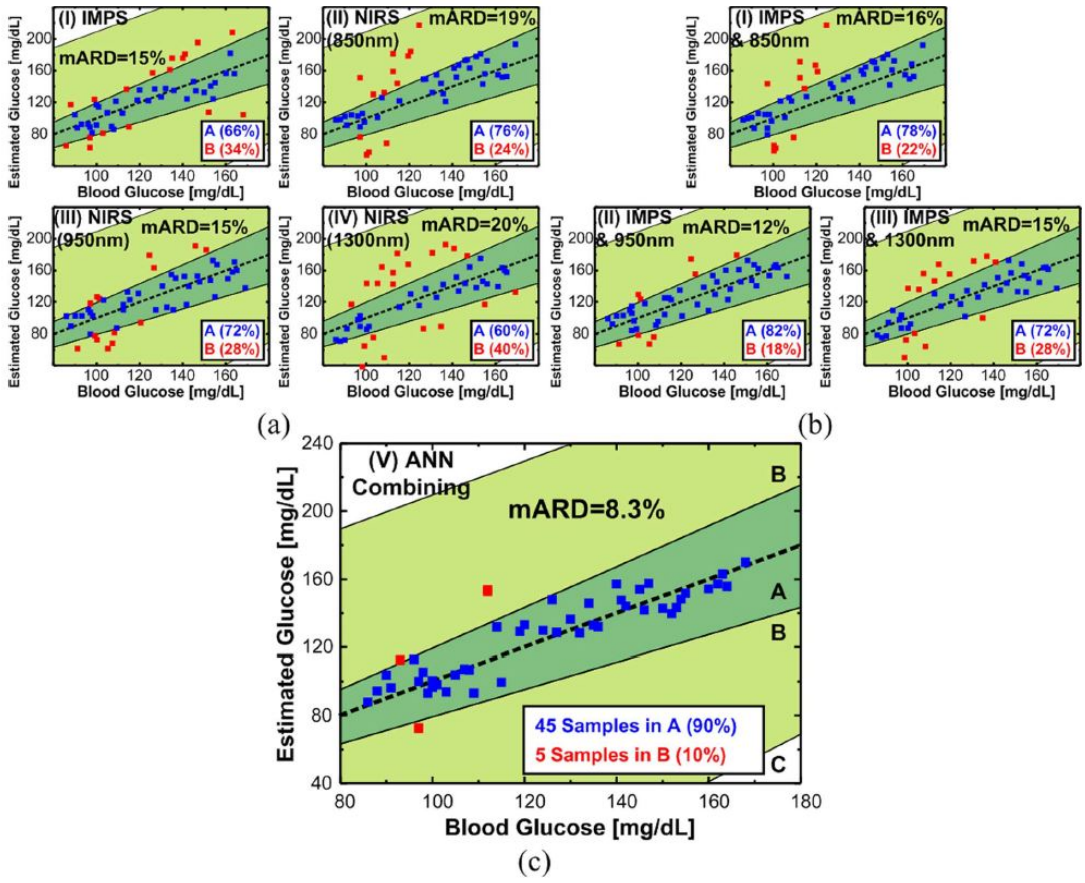

Figure 5.7 – Results of the Glucose Estimation with the proposed system with 50 samples from one human volunteer (a) Prior to the ANN method (b) Results after 2 input ANN combination (c) Results after 4 input ANN combination. Source [18]

5.4 An innovative 3-stage Miller compensated, cross-coupled load, based photo-diode front end readout is designed for glucose monitoring

An innovative 3-stage Miller compensated, cross-coupled load, based photo-diode front end readout was designed for glucose monitoring. The Near Infrared Spectroscopy (NIRS) technique

was used for the optical sensing of glucose non-invasively. The stable 3-stage open loop amplifier was designed for a gain of 68.3 dB, phase margin of 65°, GBW of 12.6 MHz and had a power consumption of 0.26 mW. The trans-impedance amplifier achieved a gain of 84.46 dB Ω, phase margin of 65°, has an input referred noise of 20.4 pA/$\sqrt{Hz}$ and consumed 0.55 mW of power from a 3.3 V supply using a 0.18 um CMOS technology node [80].

5.4.1 Introduction

In a healthy human, the amount of glucose in the blood should constantly stay at around 100 mg/dl. If this value drops below 70 mg/dl it is called hypoglycemia which means that the cells do not get enough energy. This is especially harmful to the nervous system because it is very sensitive to energy shortage. A glucose level over 125 mg/dl, on the other hand, is called hyperglycemia and is the characteristic of diabetes.

In diabetes care, it is important to measure the amount of glucose in the blood. Fasting Plasma Glucose (FPG) Level, 2-h glucose and the hemoglobin A1c test are important test, whose relevant values are summarized below in Table 5.1 [81, 82].

Table 5.1 – Relevant values for the different glucose tests [5] [8]

Test	Normal	Pre-Diabetic	Diabetic
FPG	70 - 99 mg/dl	100 - 125 mg/dl	$\geq$ 126 mg/dl
2-h Glucose	140 mg/dl	140 - 199 mg/dl	$\geq$ 200 mg/dl
A1c	5.7	5.8 - 6.5	$\geq$ 6.5

There are several optical techniques for measuring relative glucose concentration using light based on mechanisms such as fluorescence resonance energy transfer (FRET). However, these techniques are indirect co-related measurements [57]. We propose to use NIRS to measure the concentration of glucose directly. The NIRS is based on the optical scattering of the glucose molecules. An Infrared light source, for example, an LED, illuminates the tissue and a photo-diode is used to measure the amount of reflected light, which depends directly on the blood glucose level enabling non-invasive blood glucose monitoring. The relevant ranges of blood glucose levels are mapped to the device ranges of several commercial devices on the market as shown in Figure 5.8.

5.4.2 Glucose Readout System Architecture and system specifications

This sections deals with the entire architecture of the CMOS front-end system with the sensor, circuit and specification parameters [80].

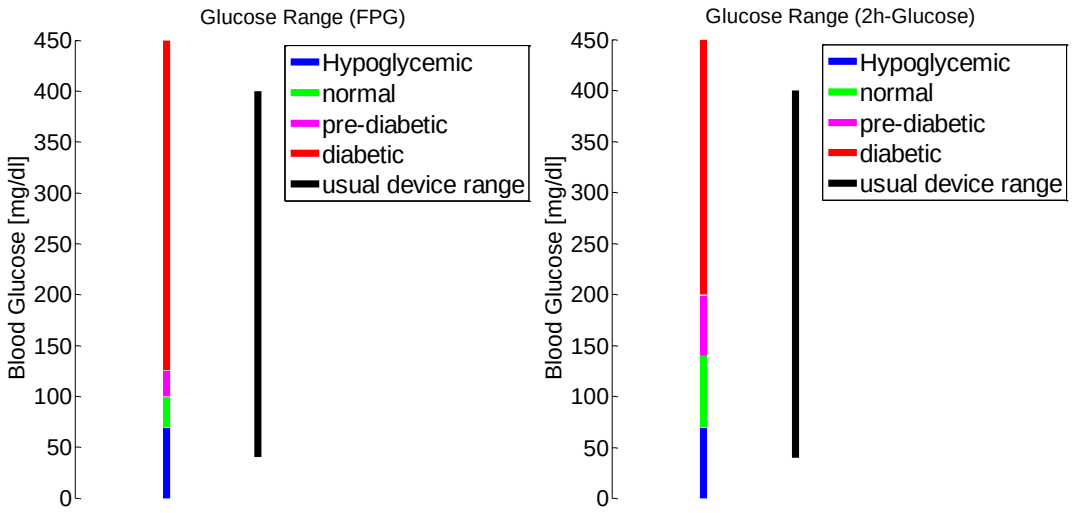

Figure 5.8 – FPG and 2h-Glucose Range of modern CGM (Continuous Glucose Monitoring) devices with clinical interpretation

5.4.3 Light Penetration Depth

Human skin is characterized by three different layers: the epidermis, the dermis and the subcutaneous tissue. The epidermis is the layer on the outside, which contains barely any blood vessels but the layer below, the dermis, contains a well-developed system of blood vessels making it well suited for NIRS. If NIRS measurement should be performed in the dermis a penetration depth between 0.3-1.3 mm is required. ([83] p208)

5.4.4 Wavelength and its specifications

For wavelengths below 800 nm the absorption from deoxyhemoglobin, oxyhemoglobin and melanin become high and the measurements become difficult since the reflected light is strongly attenuated. For wavelengths above 1.4 µm the water absorption becomes strong.

The penetration depth in the window between 0.8-1.4 µm, is around 1-100 mm. This window lies in the near infrared range (NIR: 0.75 µm -2.5 µm). Thus NIRS is conducive for optical glucose detection [84].

5.4.5 Sensor System Architecture

The topology used in this project is a non-inverting operational amplifier (OPAMP) together with an additional resistor R_f to convert the photo-diode current to a voltage [18] as shown in Figure 5.9.

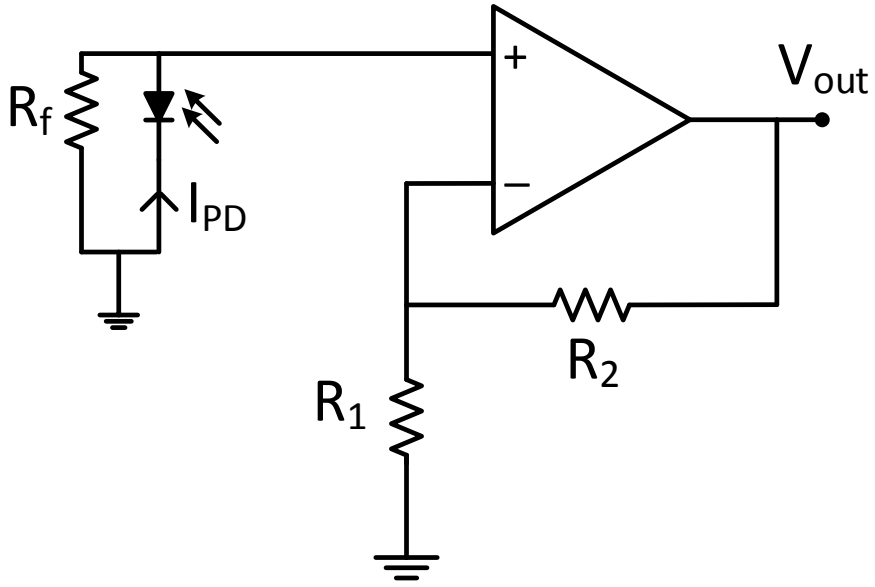

Figure 5.9 – Architecture of the Trans-impedance Amplifier Based Glucose Readout System

The advantage of this design is that the gain as described in Equation 5.1 is determined by the ratio of the feedback resistors, allowing higher resistances which in turn relaxes the requirements on the driving strength of the OPAMP.

$$V_{out} = (1+\frac{R_2}{R_1}) * R_f * I_{PD} \tag{5.1}$$

5.4.6 Photodiode Sensor Model and and its specifications

A photo-diode can be modeled as an ideal diode in parallel with a current source, for the light-induced current, the junction capacitor C_j and a resistor $R_{sh,}$ modeling the dark current, as shown in Figure 5.10. An additional resistor is added in series for modeling the resistance of the metal connection which can usually be neglected. The junction capacitance depends on the diode voltage but can be considered constant if the bias voltage does not change much as is the case for our design.

For the evaluation of the amplifier designed during this project, the photo-diode S1087-01 from Hamamatsu was chosen as reference. It has a rather large active area which would result in a bigger current for a given amount of reflected light. The characteristics of the photo-diode are:

I_{dark} = 10 pA,

R_{sh} = 10 GΩ,

C_j = 200 pF,

I_L = 0.56 $\frac{A}{W}$@λ= 960 nm, and

A_{sens}= 1.3 x 1.3 mm^2.

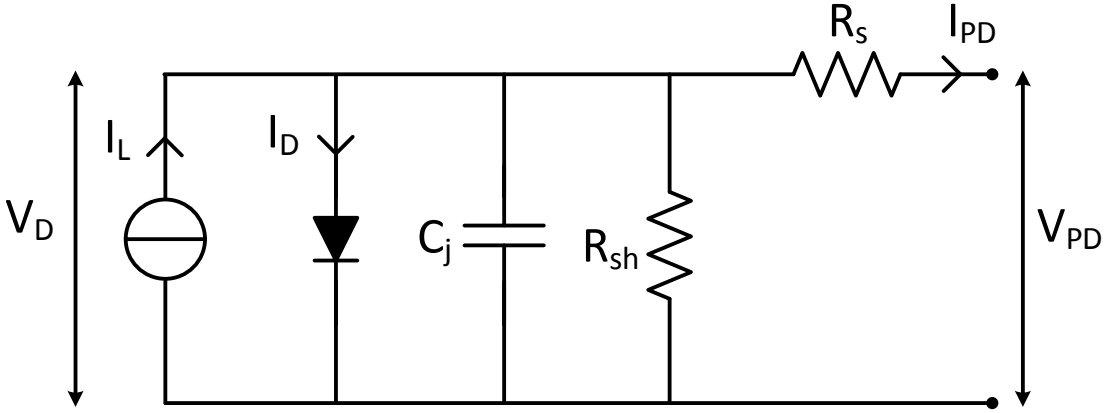

Figure 5.10 – Equivalent Circuit for a Photodiode

5.4.7 Circuit Architecture, Analysis and Design

The circuit diagrams, along with the small signal equivalent for the building blocks for deriving the transfer functions and corresponding simulation results are presented in the sections below.

5.4.8 Amplifier Circuit

The innovative circuit which is used in this project is displayed in Figure 5.11. It consists of a differential pair with a cross-coupled load which is integrated into a symmetrical OTA [18]. A Miller Compensation ensures stability and a common drain output stage protects the gain if a resistive load is connected.

The circuit is designed in 180 um technology in which 3.3 V transistors are used. In the following section, transistor sizing is explained in a bottom-up approach starting with the differential pair. The analysis and calculations are based on the EKV model for MOS transistors [85]. The sizing of the transistors is explained in a methodical manner with simulations results at different points.

5.4.9 Differential Pair with Cross-Coupled Load

The differential pair with the cross-coupled load as shown in Figure 5.12 is the first stage of our amplifier. The idea behind using a cross-coupled pair as load is that this induces a negative conductance which reduces the total conductance of the active load and increases the

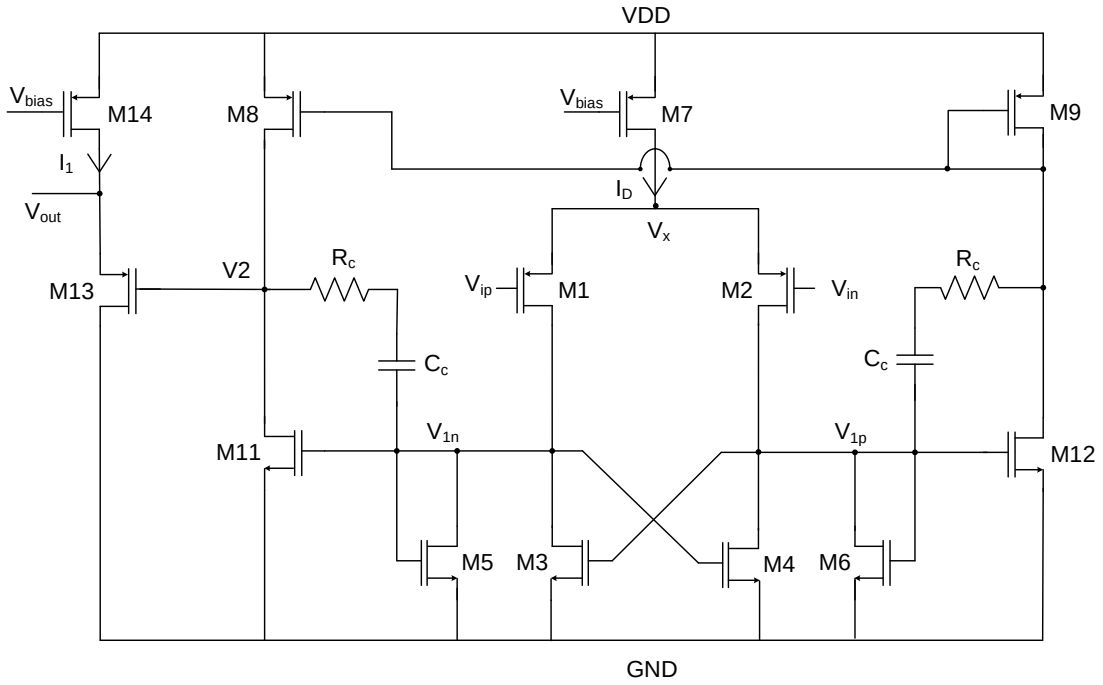

Figure 5.11 – Complete OTA Circuit with the Output Stage

gain [86] [87].

From the small signal equivalence circuit shown in Figure 5.13, it is possible to derive the formula for the gain.

$$A_1 = \frac{V_{1p} - V_{1n}}{V_{ip} - V_{in}}$$

$$A_1 = \frac{g_{m1,2}}{g_{m5,6} - g_{m3,4} + g_{ds1,2} + g_{ds3,4} + g_{ds5,6}} \tag{5.2}$$

Since the g_{ds}in Eqn. 5.2 are much smaller than the gm this formula can be simplified to Eqn. 5.3.

$$A_1 = \frac{g_{m1,2}}{g_{m5,6} - g_{m3,4}} = \frac{g_{m1,2}}{g_{m5,6}} * \frac{1}{1-\alpha} \tag{5.3}$$

with,

$$\alpha = \frac{g_{m3,4}}{g_{m5,6}} \tag{5.4}$$

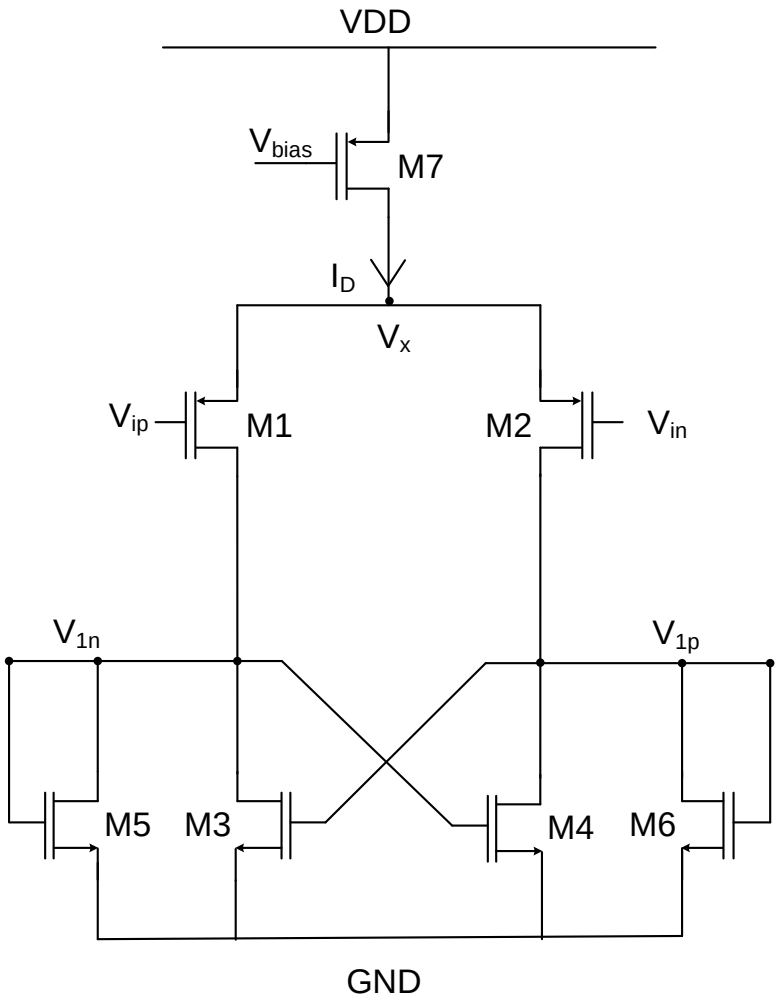

Figure 5.12 – Differential Pair with Cross-Coupled Load

The second stage of the amplifier consists of a symmetrical OTA which also performs the differential-to-single-ended conversion. Figure 5.11 depicts the symmetrical OTA together with the first stage while the small signal equivalence signal for the second stage is shown in Figure 5.14.

From the circuit in Figure 5.14 it is possible to deduce the gain of the second amplifier stage as described below:

$$A_2' = \frac{V_2}{V_{1p} - V_{1n}} = \frac{g_{m11,12}}{g_{ds8,9} + g_{ds11,12}} \tag{5.5}$$

$$A_2 = \frac{V_2}{V_{ip} - V_{in}} = A_1 * A_2'$$

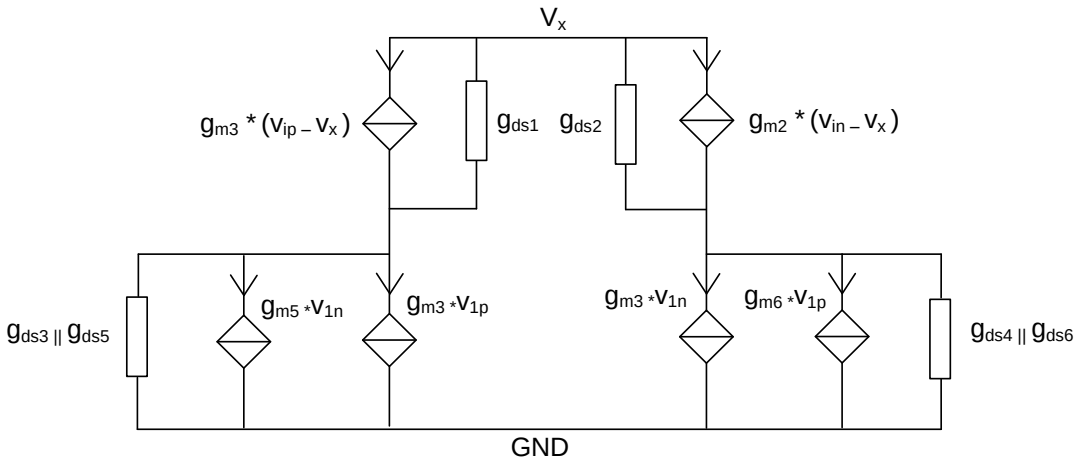

Figure 5.13 – Small Signal Equivalence Circuit for the Differential Pair with Load

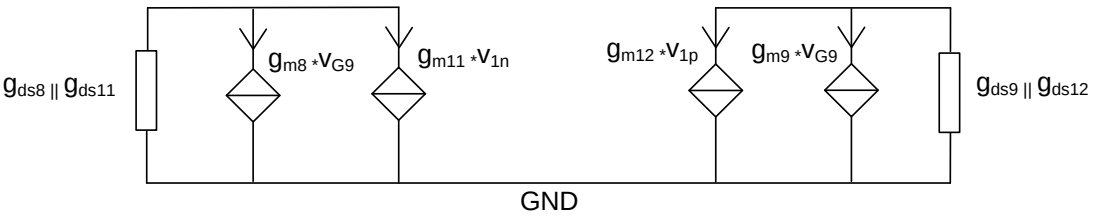

Figure 5.14 – Small Signal Equivalence Circuit for the second stage of the Amplifier

$$A_2 = \frac{g_{m11,12}}{g_{ds8,9} + g_{ds11,12}} * \frac{\beta}{1-\alpha} \tag{5.6}$$

with

$$\beta = \frac{g_{m11,12}}{g_{m5,6}}$$

The resistor of the compensation network is determined by $g_{m11,12}$.

Usually, it is advised to keep R_c smaller than $(3*g_{m1,2})^{-1}$ [88]. However, since this value is smaller than the lower bound given by $g_{m11,12}$ this is not possible in our case.

$$g_{m11,12} = 35\,\mu S$$

$$R_c = \frac{1}{g_{m11,12}} = 29\,k\Omega$$

It is important to keep C_c as small as possible to not reduce the bandwidth unnecessarily. For this reason, a parametric sweep was performed for the capacitance to obtain the desired phase margin of 65° (Figure 5.16) and C_c was chosen 1.1 pF. The last stage of the amplifier is a common drain stage (M13 and M14 in Figure 5.11) which provides a low output resistance and protects the amplifier gain if a resistive load is connected. The small signal model of this stage is shown in Figure 5.15 below.

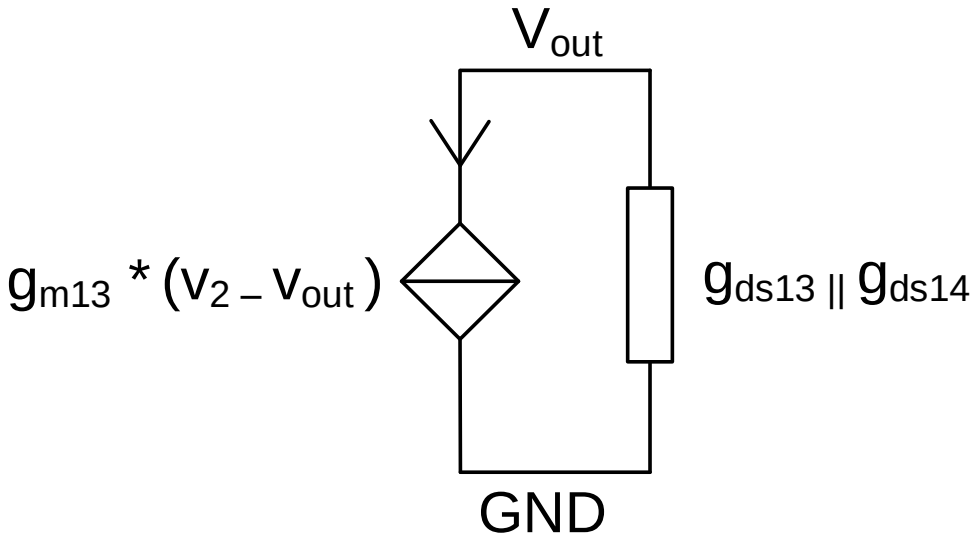

Figure 5.15 – Small Signal Equivalent Circuit for the output stage

From the small signal circuit in Figure 5.15 it is then possible to deduce the gain, as we did for the previous sub-circuits. Again, it is possible to neglect the g_{ds} with respect to the bigger g_m in Eqn. 5.7.

$$V_{out} = \frac{g_{m13}}{g_{m13}+g_{ds13}+g_{ds14}} * V_2 \approx V_2$$

The Bode diagram with the gain margins are shown in Figure 5.16. A DC gain of 68.3 dB is obtained with a phase margin of 65°,with a GBW of 12.6 MHz.

5.4.10 Circuit Architecture for the Glucose Sensor Front End Readout

The trans-impedance amplifier circuit has been adapted for our purpose. An additional resistor R'_f was added to set the input common mode to 1 volt, which is required by our amplifier. To

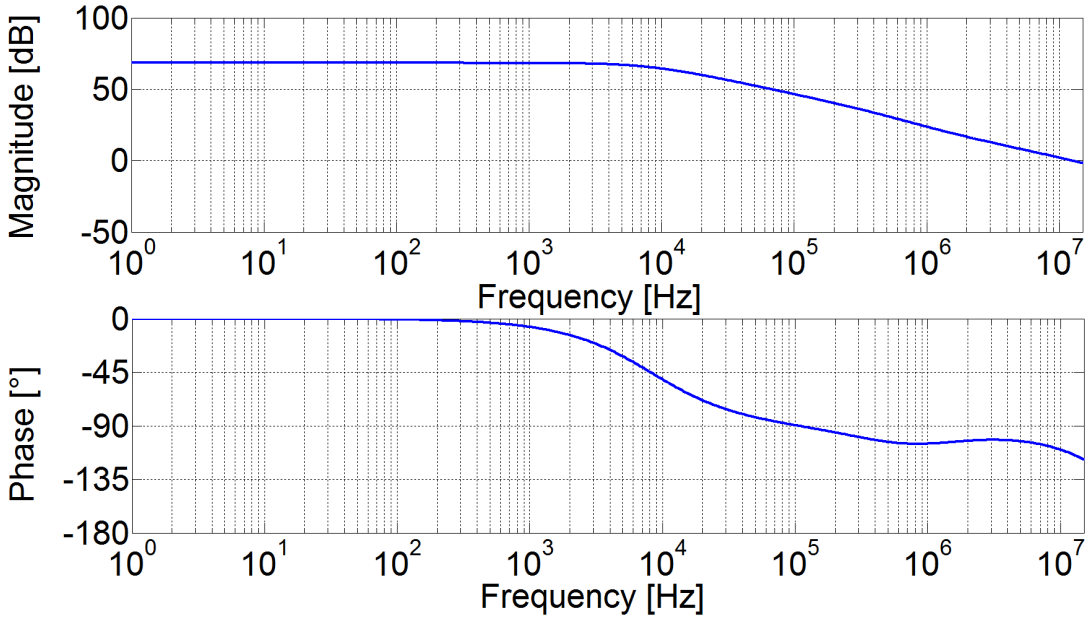

Figure 5.16 – Bode plot of the designed amplifier in open loop

reduce the noise of the reversed biased photo-diode an additional capacitor C_2 is added in parallel to R_2. For the photo-diode model, the values of the S1087-01 from Hamamatsu are used.

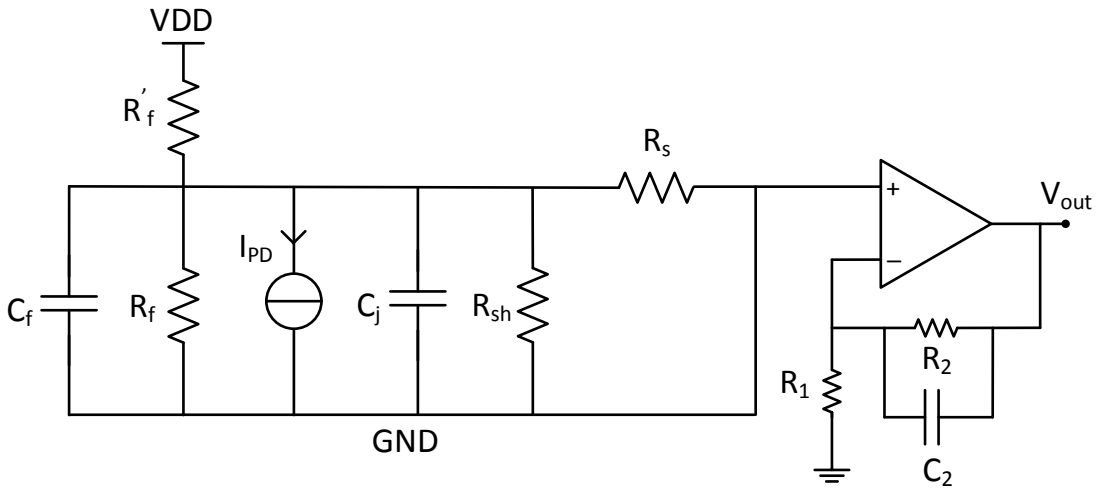

Figure 5.17 – Schematic of the photo-diode Amplifier with additional C_f for stability

Adding R_f' decreases the gain a bit, as described in Eqn. 5.7. Since it is in parallel to R_f for small signals. R_{sh} is big enough so that it can be neglected.

$$V_{out} = -\left(1+\frac{R_2}{R_1}\right) * R_f || R'_f * I_{light} \tag{5.7}$$

For the values given in Table 2, this results in the following DC-gain A_0, which matches the one obtained by simulation is displayed in Fig. 5.18.

$$A_o = \frac{V_{out}}{I_{light}} = 84.46\,dB\Omega$$

The Bode Plot can be seen in Fig. 5.18.

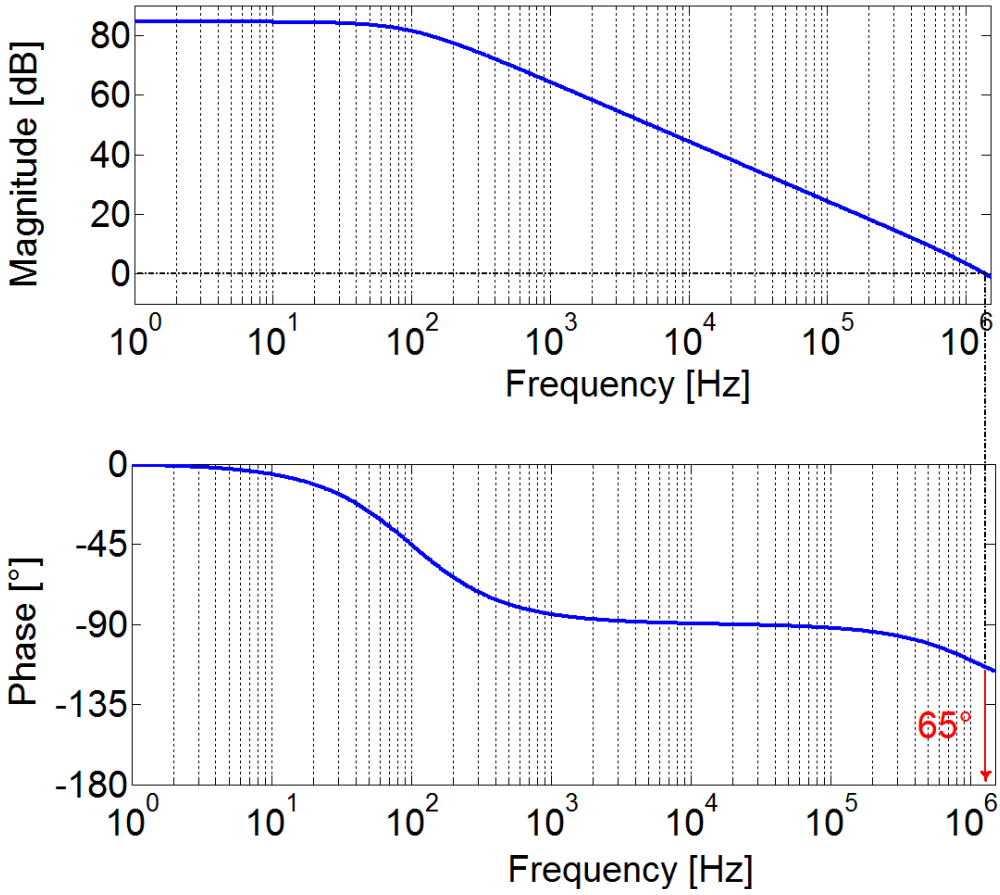

Figure 5.18 – Bode Plot for the closed loop Photodiode Amplifier

Noise analysis of the circuit in Figure 5.11 shows that the main noise contribution comes from the active load and the cross-coupled pair and consists of 1/f noise which is around 70% of the total noise. Because we are operating at low frequencies the 1/f noise dominates as can be seen from the noise functions in Figure 5.19.

The second big noise source is the resistive feedback R_1 and R_2 which makes around 22 % of the input referred noise.

There are other advanced techniques for noise reduction such as co-related double sampling and

chopping [89], that can be used to further reduce the effect of the 1/f noise and the offset of the amplifiers.

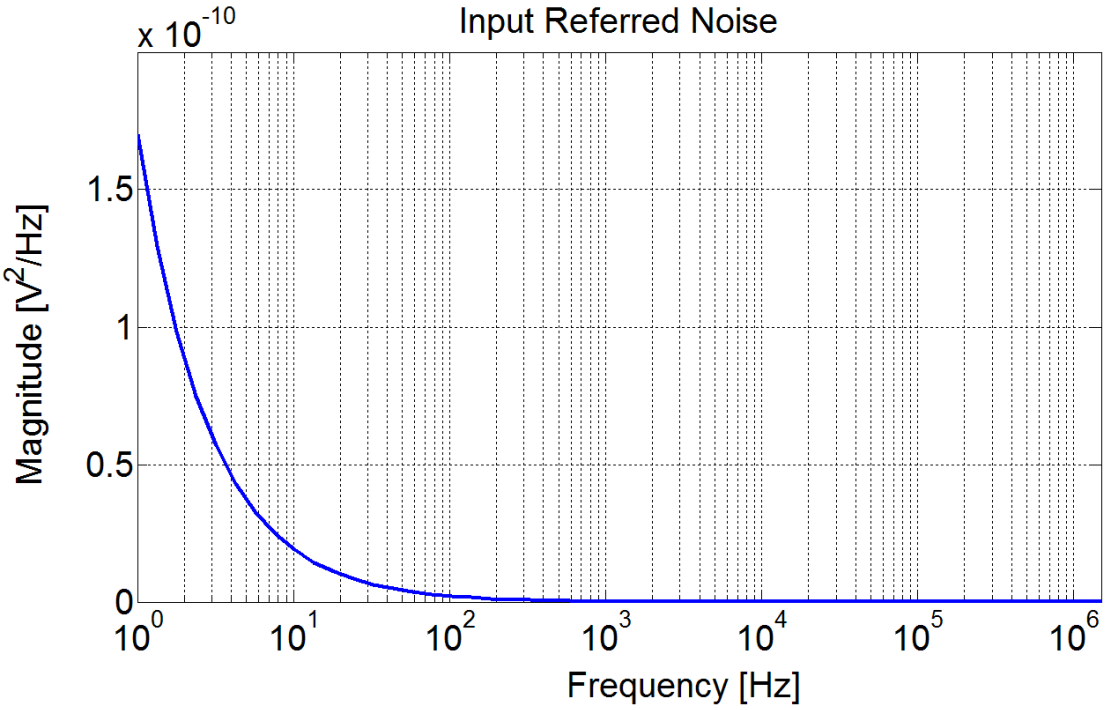

Figure 5.19 – Noise Function of the closed loop Photo-diode Amplifier

The performance is given in Table 5.2.

Table 5.2 – Performance of the Photodiode Amplifier

Supply Voltage	3.3 V
Power Consumption	0.55 mW
Phase Margin	65°
DC-Gain	84.46 dBΩ
Input Current Noise	20.4 pA/$\sqrt{Hz}$ @ 10 kHz
GBW	1.8 MHz

5.4.11 Results and Conclusion

A 3-stage Miller compensated CMOS photo-diode readout circuit has been designed and simulated using a standard 0.18 µm CMOS technology. An innovative technique to use a cross-coupled load to creating negative resistance in a 3-stage miller compensated operational amplifier to boost the gain is presented in this design. For lower supply voltages this topology with the cross-coupled -ve resistance load is even more suitable as it saves power.

The output stage drives the resistive feedback load of the trans-impedance amplifier readout circuit used to interface the photo-diode that reads the current, non-invasively, from the light that is reflected from the glucose molecules inside the body. A DC gain of 68.3 dB is obtained with a phase margin of 65°, having a gain bandwidth (GBW) product of 12.6 MHz consuming 0.25 mW of power from a 3.3 V supply within the scope of the system.

5.5 Short term outlook and long term vision for wearable glucose monitoring devices

5.5.1 Apple iWatch4

Given the acceleration in the adoption of wearable technologies such as the Apple watch 4 as shown in Figure 5.20, the short term outlook for a non-invasive glucose monitoring device seems high. The important feature of the iWatch4 is that it has two electrodes to measure the electrical activity of the heart and a green LED with photo-detectors all around in a circular periphery to measure the reflected light from the arm giving the number of heart beats per minute of the person.

Looking into the short term future it is possible that by changing the wavelengths of the LED to the NIRS range the same device design could be used to multiplex two different measurements namely the BPM and glucose levels while the electrodes could be used to measure the impedance.

Figure 5.20 – Apple iWatch 4 with its optical based sensor for heart BPM monitoring. Source [19]

A search into the patent database for some of the latest approvals for Apple reveals this interesting trend [20]. Published by the United States patent office on the 23rd August 2018 "Reference switch architectures for non-contact sensing of substances" elucidates techniques though which an electronic device can be calibrated and used to measure contact-less concentration of a particular substance. As shown in Figure 5.21 the system has a light source which provides the excitation light that passes through the monochromator and then a beamsplitter.

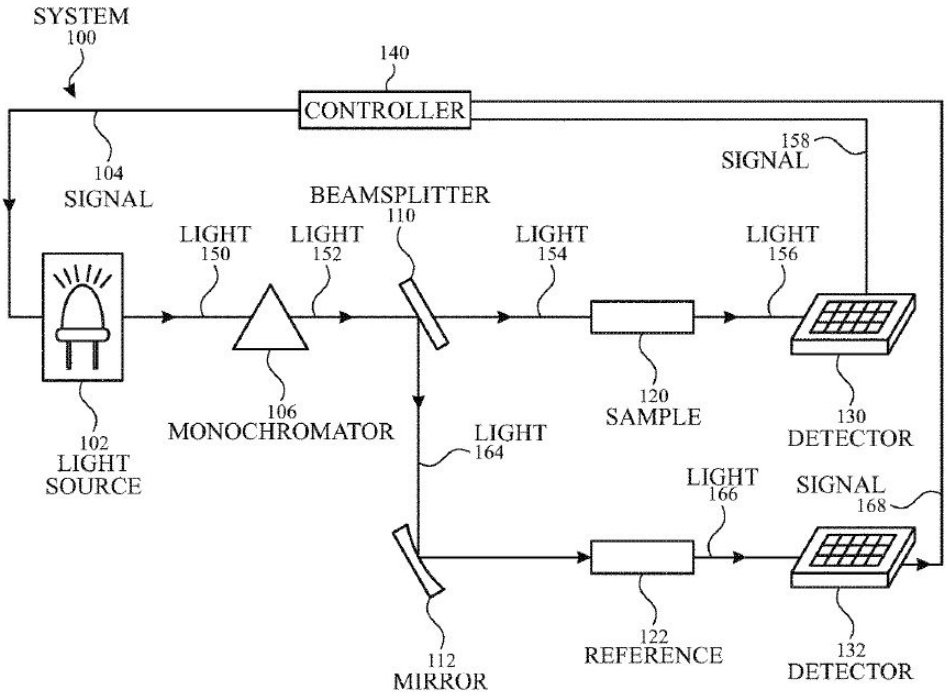

Figure 5.21 – Apple Patent System Diagram. Source [20]

The two components of the light are created by the beamsplitter are used to excite the sample and a reference. The reflected light from both these sources is collected by two identical detectors and compared with a controller, the results of which guide the light source output.

The principle is that, as light traverses through the sample, each molecule in the target absorbs energy at a signature wavelength. This absorption of energy causes a modulation in the properties of the light that is emitted when it exits the sample and hits the detector. The logical sequence of these operations are explained in the flowchart shown in Figure 5.22.

The monochromator separates the light into two discrete wavelengths and the beamsplitter splits the light into two different paths. Crucially, a mirror is used to redirect the path of the second beam of light that hits the reference.

The electrically converted signals from the two detectors are passed sequentially to the controller that divided the sample and reference absorbance to determine the concentration of the substance in the sample, which could plausibly be glucose molecules. The reason for having a reference built into the system for calibration is that the inventors realize the systematic and local adjustments they need to make for each person individually.

The measurement principle is broken down into two phases namely the calibration phrase and the measurement phase with times that can vary as shown in Figure 5.23.

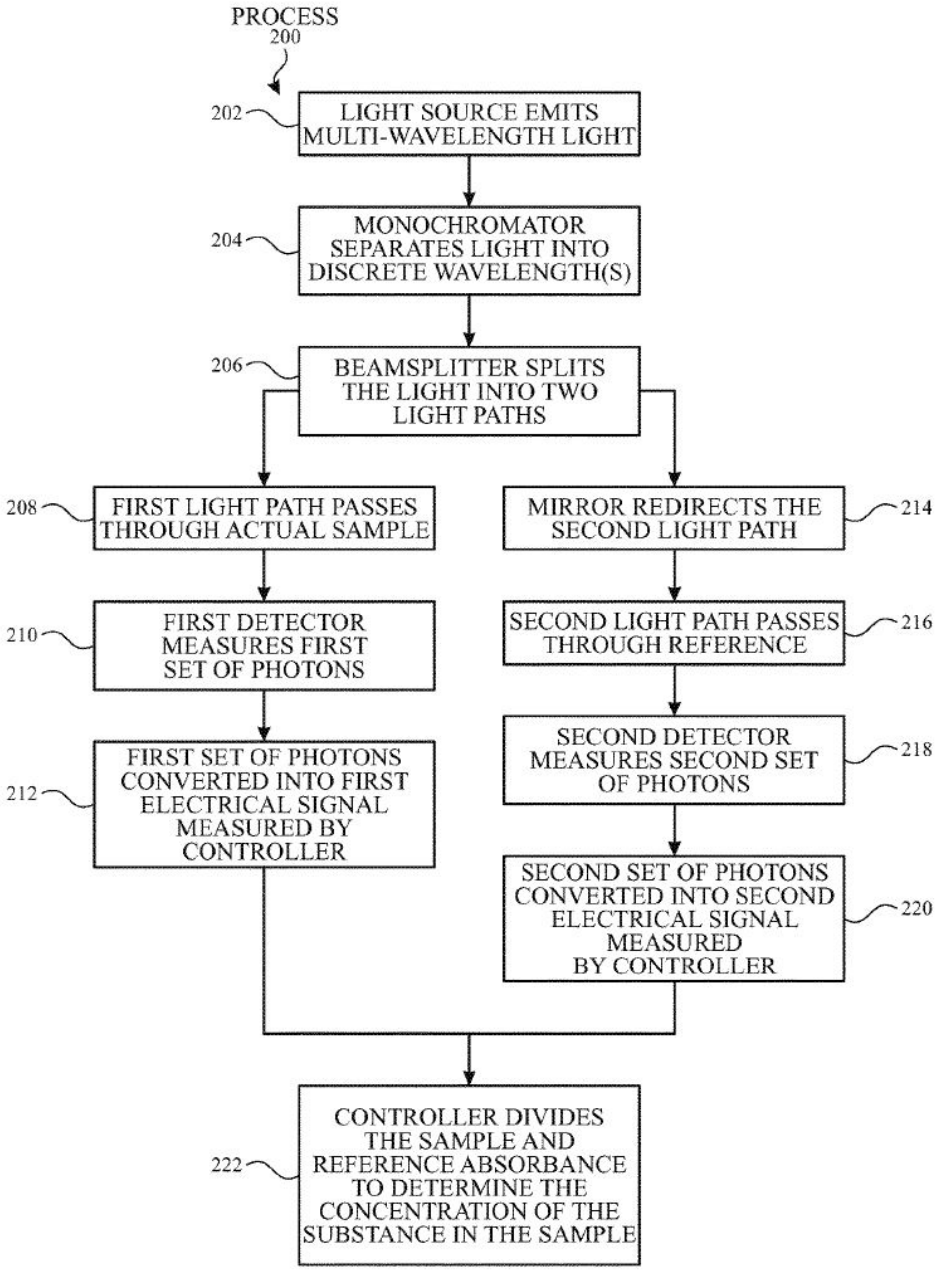

Figure 5.22 – Logical sequence of operations. Source [20]

Since different substances have different behaviors for absorbing light these leads to different results in absorption spectroscopy. Apple also emphasizes on the fluctuations, systematic and random variations, and drifts that have the power to impact the accuracy of the overall results. There are therefore two phases of measurement as shown in the Figure 5.24, the calibration phase and the measurement phase. The measurement point is referred to as sampled point, as shown in Figure 5.24 referred as 574.

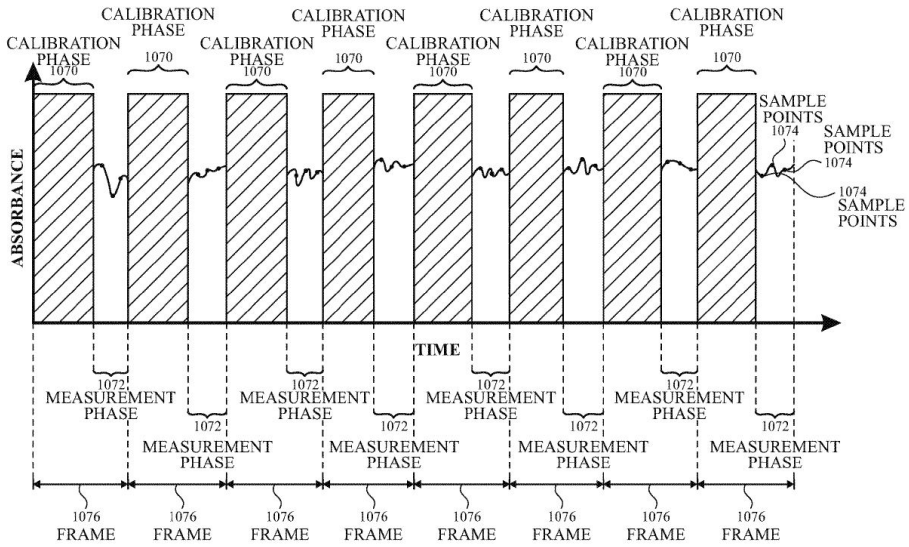

Figure 5.23 – Measurement phases: calibration phrase and the measurement phase. Source [20]

In some systems hundreds of these points were measured, whilst in others only a few values were sampled that were averaged with the controller to get a mean value. It is crucial to see in Figure 5.24 that, long measurement times lead to long times between consecutive calibration phases. This results in the drifting of the zero level that is set at actual zero level. This leads to gain drift, that is seen by the conspicuous shift of the value of two adjacent measurements.

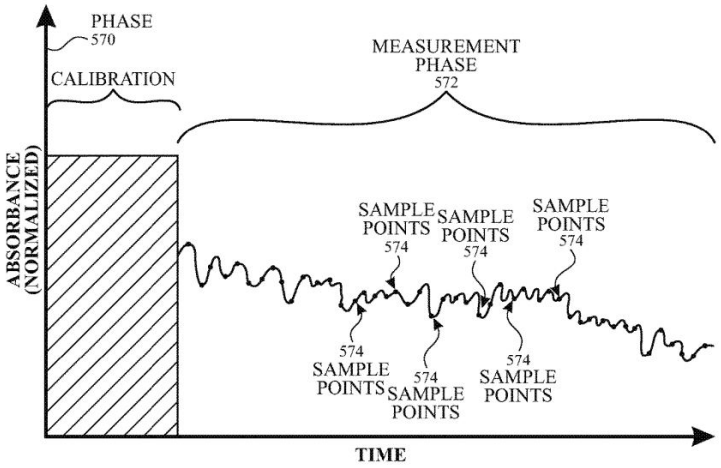

Figure 5.24 – Drifting of the zero level due to long measurement phases. Source [20]

The system diagram in the Figure 5.25 shows the different components such as light emitters, filters, beamsplitters, short-wavelength infrared (SWIR) detectors that are incorporated in the system. The shown diagram fits in the scheme of the non-invasive glucose monitoring in humans.

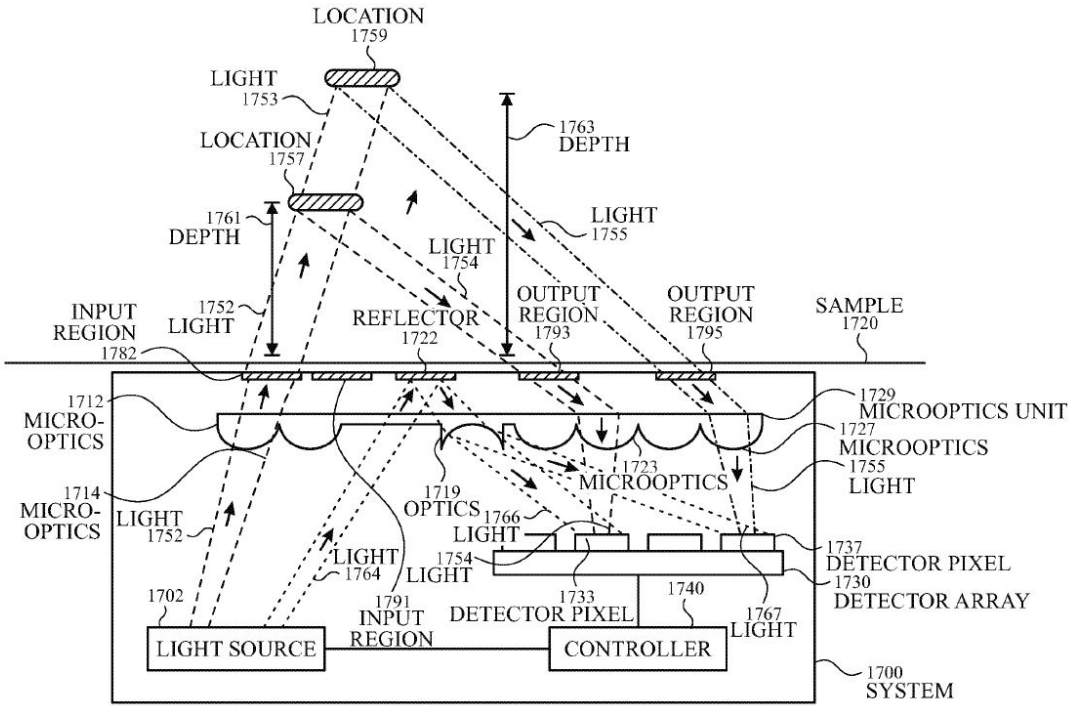

Figure 5.25 – System diagram with the different components. Source [20]

In the long term, glucose monitoring along with heart rate and BPM monitoring would probably be a common, preventive method available on a large scale to people, thus reducing the impact of serious health problems.

6 Conclusion and future scope

Diabetes is a global pandemic causing millions of deaths every year. There has been a huge spike in the number of FDA-approved devices for both diabetes monitoring and treatment in the last three years. Most of the approved devices are based on electrical methods for the detection of glucose, with one product being an outlier using light to detect glucose. The proof-of-concept of using pancreatic beta cells as FRET cell based biosensor was successful. Stable cell lines with consistent fluorescence were cloned during the project. The advantage of using this mechanism was that the probe worked on a ratio metric principle, meaning that we detected relative changes in the cytosolic [Ca^{2+}] ratio, and that common effects were averaged out in the ratio. It was shown that the signals from 3D cell cultures produced more fluorescence that normal 2D cell cultures that are commonly used in biology labs. Various photo-diodes and LEDs were evaluated in order to choose the ones that were most suitable for SNR requirements of this application. The Lumileds LUXEON LED was chosen for excitation as it has a narrow excitation bandwidth obviating the need for an additional excitation filter. The Hamamatsu RGB photo-detector was used, as it has three components readily built in namely the image pixel, front end readout circuits with signal processing blocks and a direct digital output. The linearity of the system was characterized with fluorosphere micro beads and subsequently tested with the INS-1E F10 cells. It was noted that the SNR of the dichoric filter used in the first demonstrator had a poor performance, as it was highly angle dependent. This drove the project to look for filters that could give better SNR values.

Several optical filters were tested and characterized for the achieving the best SNR. The two main categories of filters validated were absorption-based filters and dichoric-based filters with transmission and bandwidths within the specification of the system. Two categories of absorption based filters were tested based on their material composition, namely glass-based and polymer-based. Both long pass and band pass filters were tested. Through rigorous testing we identified that the absorption based filters out performed the polymer based filters. The MIDOPT long pass filter LP 470 was the best filter and it was subsequently used in all the other experiments.

Several biological experiments were carried out with a completely automated hardware-software

system. We could successfully monitor cell growth, cell counts, effect of temperature and loss of fluorescence in the cells upon exposure to high intensity light for long duration. We were able to distinguish between a KRBH solution and the cell culture medium. It was identified that cell oxygenation and media circulation were needed, and a small spinning magnet was used in the setup inside the petri dish to promote oxygenation and media circulation. We have then observed a better result for continuous glucose monitoring for times up to 18 hours. Successful experiments were performed to stimulate the cells with continuous glucose, step-wise glucose stimulation and binary glucose stimulation.

In-lieu of a complete system on a chip, an analog front end with cross coupled load having a negative resistance load was designed. Extensive small signal analysis of the proposed amplifier was conducted and simulation results closely matched the hand calculations.

In the scope of the future work, a fully implantable in vivo system with bio-compatible packaging and autonomous powering is envisaged.

Bibliography

[1] I. D. F. IDF, "International diabetes federation atlas 8th edition," https://diabetesatlas.org/across-the-globe.html.

[2] M. Medtronic, "Fda approved medtronic minimed 630g system with smartguard - p150001/s021," https://www.fda.gov/MedicalDevices/ProductsandMedicalProcedures/DeviceApprovalsandClearances/Recently-ApprovedDevices/ucm600601.htm.

[3] A. D. C. Inc, "Freestyle libre," https://freestylediabetes.co.uk/freestyle-thinking/post/FreeStyle-Libre-system-measure.

[4] F. USA, "Freestyle libre fda approval notice," https://www.fda.gov/MedicalDevices/ProductsandMedicalProcedures/DeviceApprovalsandClearances/Recently-ApprovedDevices/ucm614903.htm.

[5] A. D. C. Inc, "Freestyle libre," https://www.freestylelibre.co.uk/libre/products/starter-pack.html.

[6] T. T. Diabetes, "t:slim x2™ insulin pump," https://www.tandemdiabetes.com/products/t-slim-x2-insulin-pump.

[7] . M. Inc, "Minimed™ 670g insulin pump system," https://www.medtronicdiabetes.com/products/minimed-670g-insulin-pump-system.

[8] U. F. 2018 and D. A. (FDA), "Eversense continuous glucose montioring system - p160048," https://www.fda.gov/MedicalDevices/ProductsandMedicalProcedures/DeviceApprovalsandClearances/Recently-ApprovedDevices/ucm614564.htm.

[9] U. F. FDA and D. A. (FDA), "Eversense: The only long-term continuous glucose monitoring (cgm) system," https://www.eversensediabetes.com/products/.

[10] A. Atala, R. Lanza, T. Mikos, and R. Nerem, *Principles of regenerative medicine*. Academic Press, 2018.

[11] D. Forecast, "Encapsulated cells for diabetes treatment," http://www.diabetesforecast.org/2015/may-jun/beta-cell-breakthroughs.html.

[12] U. of Illinois, "Principle and formula of the fret mechanism," http://bio.physics.illinois.edu/techniques.asp.

[13] M. B. F. MIDOPT INC, "Filter transmission data and transmission wavelengths," https://midopt.com/filters/bp505/.

[14] M. L. F. MIDOPT INC, "Filter transmission data and transmission wavelengths," https://midopt.com/filters/lp470/.

[15] F. J. Fuji, "Fujifilm filter optical tri acetyl cellulose," https://fujifilm.jp/support/filmandcamera/download/pack/pdf/ff_opticalfilter_001.pdf.

[16] C. C. U. W. Wikipedia, "Clarkerrorgrid," https://en.wikipedia.org/wiki/Clarke_Error_Grid.

[17] A. Trabelsi and M. Boukadoum, "Comparison of two cmos front-end transimpedance amplifiers for optical biosensors," *IEEE Sensors Journal*, vol. 13, no. 2, pp. 657–663, 2013.

[18] K. Song, U. Ha, S. Park, J. Bae, and H.-J. Yoo, "An impedance and multi-wavelength near-infrared spectroscopy ic for non-invasive blood glucose estimation," *IEEE Journal of Solid-State Circuits*, vol. 50, no. 4, pp. 1025–1037, 2015.

[19] A. Inc., "Apple iwatch 4," https://www.apple.com/lae/apple-watch-series-4/design/.

[20] Apple, "Apple glucose monitoring patent," https://patentimages.storage.googleapis.com/54/dd/91/ad9c31315d584a/US20180238794A1.pdf.

[21] U. F. FDA and D. Administration, "Medical devices section of the fda usa," https://www.fda.gov/MedicalDevices/default.htm.

[22] Medtronic, "Guardian connect system – p160007," https://www.fda.gov/MedicalDevices/ProductsandMedicalProcedures/DeviceApprovalsandClearances/Recently-ApprovedDevices/ucm604253.htm.

[23] M. Inc, "Guardian connect system – p160007 app," https://hcp.medtronic-diabetes.com.au/guardian-connect.

[24] T. Diabetes, "t slim x2 insulin pump with basal-iq," https://www.tandemdiabetes.com/.

[25] U. F. 2018 and D. A. (FDA), "Minimed™ 670g insulin pump system fda approval," https://www.fda.gov/MedicalDevices/ProductsandMedicalProcedures/DeviceApprovalsandClearances/Recently-ApprovedDevices/ucm614616.htm.

[26] G. Orive, R. M. Hernández, A. R. Gascon, R. Calafiore, T. M. Chang, P. De Vos, G. Hortelano, D. Hunkeler, I. Lacik, A. J. Shapiro *et al.*, "Cell encapsulation: promise and progress," *Nature medicine*, vol. 9, no. 1, p. 104, 2003.

[27] G. D. Nicodemus and S. J. Bryant, "Cell encapsulation in biodegradable hydrogels for tissue engineering applications," *Tissue Engineering Part B: Reviews*, vol. 14, no. 2, pp. 149–165, 2008.

[28] D. An, A. Chiu, J. A. Flanders, W. Song, D. Shou, Y.-C. Lu, L. G. Grunnet, L. Winkel, C. Ingvorsen, N. S. Christophersen *et al.*, "Designing a retrievable and scalable cell encapsulation device for potential treatment of type 1 diabetes," *Proceedings of the National Academy of Sciences*, vol. 115, no. 2, pp. E263–E272, 2018.

[29] A. J. Vegas, O. Veiseh, M. Gürtler, J. R. Millman, F. W. Pagliuca, A. R. Bader, J. C. Doloff, J. Li, M. Chen, K. Olejnik *et al.*, "Long-term glycemic control using polymer-encapsulated human stem cell–derived beta cells in immune-competent mice," *Nature medicine*, vol. 22, no. 3, p. 306, 2016.

[30] N. C. Hunt and L. M. Grover, "Cell encapsulation using biopolymer gels for regenerative medicine," *Biotechnology letters*, vol. 32, no. 6, pp. 733–742, 2010.

[31] H. Zhan, H. de Jong, and D. W. Lowik, "Comparison of bioorthogonally cross-linked hydrogels for in situ cell encapsulation," *ACS Applied Bio Materials*, 2019.

[32] S. Utech, R. Prodanovic, A. S. Mao, R. Ostafe, D. J. Mooney, and D. A. Weitz, "Microfluidic generation of monodisperse, structurally homogeneous alginate microgels for cell encapsulation and 3d cell culture," *Advanced healthcare materials*, vol. 4, no. 11, pp. 1628–1633, 2015.

[33] T. A. DESAI, C. Nyitray, and R. Chang, "Thin film cell encapsulation devices," Oct. 2 2018, uS Patent App. 10/087,413.

[34] Y. Ye, J. Yu, C. Wang, N.-Y. Nguyen, G. M. Walker, J. B. Buse, and Z. Gu, "Microneedles integrated with pancreatic cells and synthetic glucose-signal amplifiers for smart insulin delivery," *Advanced Materials*, vol. 28, no. 16, pp. 3115–3121, 2016.

[35] M. Farina, J. F. Alexander, U. Thekkedath, M. Ferrari, and A. Grattoni, "Cell encapsulation: Overcoming barriers in cell transplantation in diabetes and beyond," *Advanced drug delivery reviews*, 2018.

[36] V. Sourjik and H. C. Berg, "Binding of the escherichia coli response regulator chey to its target measured in vivo by fluorescence resonance energy transfer," *Proceedings of the National Academy of Sciences*, vol. 99, no. 20, pp. 12 669–12 674, 2002.

[37] B. Bajar, E. Wang, S. Zhang, M. Lin, and J. Chu, "A guide to fluorescent protein fret pairs," *Sensors*, vol. 16, no. 9, p. 1488, 2016.

[38] J. Shi, C. Chan, Y. Pang, W. Ye, F. Tian, J. Lyu, Y. Zhang, and M. Yang, "A fluorescence resonance energy transfer (fret) biosensor based on graphene quantum dots (gqds) and gold nanoparticles (aunps) for the detection of meca gene sequence of staphylococcus aureus," *Biosensors and Bioelectronics*, vol. 67, pp. 595–600, 2015.

[39] T. Yoshida, S. Alfaqaan, N. Sasaoka, and H. Imamura, "Application of fret-based biosensor "ateam" for visualization of atp levels in the mitochondrial matrix of living mammalian cells," in *Mitochondria*. Springer, 2017, pp. 231–243.

[40] M. Zaccolo, "Fret biosensor to uncover camp nano-domains," *Journal of Molecular and Cellular Cardiology*, vol. 120, p. 17, 2018.

[41] S. G. Lee, J. S. Ha, and J. J. Song, "Method for detecting ligand using fret biosensor," Mar. 20 2018, uS Patent 9,921,215.

[42] J. Shi, F. Tian, J. Lyu, and M. Yang, "Nanoparticle based fluorescence resonance energy transfer (fret) for biosensing applications," *Journal of materials chemistry B*, vol. 3, no. 35, pp. 6989–7005, 2015.

[43] H. H. Chang and J. V. Rocheleau, "Simultaneous imaging of apollo-nadp+ and fucci to correlate beta-cell nadph/nadp+ redox state to the cell cycle," *Biophysical Journal*, vol. 114, no. 3, p. 359a, 2018.

[44] H.-C. Wang and A.-R. Lee, "Recent developments in blood glucose sensors," *Journal of food and drug analysis*, vol. 23, no. 2, pp. 191–200, 2015.

[45] M. Schifferer, D. A. Yushchenko, F. Stein, A. Bolbat, and C. Schultz, "A ratiometric sensor for imaging insulin secretion in single β cells," *Cell chemical biology*, vol. 24, no. 4, pp. 525–531, 2017.

[46] C. V. Bui, C. W. Boswell, B. Ciruna, and J. V. Rocheleau, "Apollo-nadp+ expressed in the pancreatic beta-cells of living zebrafish responds to glucose and diamide to reveal nadph dynamics," *Biophysical Journal*, vol. 114, no. 3, p. 359a, 2018.

[47] K. M. Seckinger, "Regulation of glucokinase in pancreatic beta cells," *Biophysical Journal*, vol. 112, no. 3, p. 461a, 2017.

[48] A. D. Elliott, N. Bedard, A. Ustione, M. A. Baird, M. W. Davidson, T. Tkaczyk, and D. W. Piston, "Hyperspectral imaging for simultaneous measurements of two fret biosensors in pancreatic β-cells," *PloS one*, vol. 12, no. 12, p. e0188789, 2017.

[49] A. Volkenhoff, J. Hirrlinger, J. M. Kappel, C. Klämbt, and S. Schirmeier, "Live imaging using a fret glucose sensor reveals glucose delivery to all cell types in the drosophila brain," *Journal of insect physiology*, vol. 106, pp. 55–64, 2018.

[50] C. Boss, E. Meurville, J.-M. Sallese, and P. Ryser, "A viscosity-dependent affinity sensor for continuous monitoring of glucose in biological fluids," *Biosensors and Bioelectronics*, vol. 30, no. 1, pp. 223–228, 2011.

[51] U. De Marchi, J. Thevenet, A. Hermant, E. Dioum, and A. Wiederkehr, "Calcium co-regulates oxidative metabolism and atp synthase-dependent respiration in pancreatic beta cells," *Journal of Biological Chemistry*, vol. 289, no. 13, pp. 9182–9194, 2014.

[52] T. Nagai, S. Yamada, T. Tominaga, M. Ichikawa, and A. Miyawaki, "Expanded dynamic range of fluorescent indicators for ca2+ by circularly permuted yellow fluorescent proteins," *Proceedings of the National Academy of Sciences*, vol. 101, no. 29, pp. 10 554–10 559, 2004.

[53] A. Miyawaki, J. Llopis, R. Heim, J. M. McCaffery, J. A. Adams, M. Ikura, and R. Y. Tsien, "Fluorescent indicators for ca 2+ based on green fluorescent proteins and calmodulin," *Nature*, vol. 388, no. 6645, p. 882, 1997.

[54] H. J. Hamamatsu, "Hamamatsu photonics rgb ics," //www.hamamatsu.com/jp/en/index.html.

[55] L. LUMILEDS, "Lumileds luxeon z uv," //https://www.lumileds.com/.

[56] Y. Sunaga, M. Haruta, T. Yamaguchi, M. Motoyama, Y. Ohta, H. Takehara, T. Noda, K. Sasagawa, T. Tokuda, and J. Ohta, "An implantable green fluorescence imaging device using absorption filters with high excitation light rejection ratio," in *2014 IEEE Biomedical Circuits and Systems Conference (BioCAS) Proceedings*. IEEE, 2014, pp. 248–251.

[57] B. Vinchhi, C. Boss, M. Conrad, A. Hermant, U. De Marchi, A. Wiederkehr, E. Meurville, N. Bouche, and C. Dehollain, "Electronic system for fret based in vitro sensing of cytosolic ca2+ in ins-1e pancreatic β-cells," in *2015 IEEE Biomedical Circuits and Systems Conference (BioCAS)*. IEEE, 2015, pp. 1–4.

[58] P. Petrocchi, S. Quaresima, P. M. Mongiardi, C. Severini, and R. Possenti, "Activation of kinase phosphorylation by heat-shift and mild heat-shock," *Cell biology international reports*, vol. 17, no. 1, pp. 9–12, 2010.

[59] S. Friant, K. D. Meier, and H. Riezman, "Increased ubiquitin-dependent degradation can replace the essential requirement for heat shock protein induction," *The EMBO journal*, vol. 22, no. 15, pp. 3783–3791, 2003.

[60] R. Possenti, A. M. Rinaldi, G.-L. Ferri, P. Borboni, E. Trani, and A. Levi, "Expression, processing, and secretion of the neuroendocrine vgf peptides by ins-1 cells," *Endocrinology*, vol. 140, no. 8, pp. 3727–3735, 1999.

[61] W. D. F. Wikipedia, "Dichoric filters," https://en.wikipedia.org/wiki/Dichroic_filter.

[62] P. Avari, M. Reddy, and N. Oliver, "Is it possible to constantly and accurately monitor blood sugar levels, in people with type 1 diabetes, with a discrete device (non-invasive or invasive)?" *Diabetic Medicine*, 2019.

[63] B. P. Kovatchev, S. D. Patek, E. A. Ortiz, and M. D. Breton, "Assessing sensor accuracy for non-adjunct use of continuous glucose monitoring," *Diabetes technology & therapeutics*, vol. 17, no. 3, pp. 177–186, 2015.

[64] T. S. Bailey, "Clinical implications of accuracy measurements of continuous glucose sensors," *Diabetes technology & therapeutics*, vol. 19, no. S2, pp. S–51, 2017.

[65] A. F. Yeknami, X. Wang, I. Jeerapan, S. Imani, A. Nikoofard, J. Wang, and P. P. Mercier, "A 0.3-v cmos biofuel-cell-powered wireless glucose/lactate biosensing system," *IEEE Journal of Solid-State Circuits*, vol. 53, no. 11, pp. 3126–3139, 2018.

[66] T. Tokuda, T. Kawamura, K. Masuda, T. Hirai, H. Takehara, Y. Ohta, M. Motoyama, H. Takehara, T. Noda, K. Sasagawa *et al.*, "In vitro long-term performance evaluation and improvement in the response time of cmos-based implantable glucose sensors," *IEEE Design & Test*, vol. 33, no. 4, pp. 37–48, 2016.

[67] K. A. Al Mamun, S. K. Islam, D. K. Hensley, and N. McFarlane, "A glucose biosensor using cmos potentiostat and vertically aligned carbon nanofibers," *IEEE transactions on biomedical circuits and systems*, vol. 10, no. 4, pp. 807–816, 2016.

[68] A. DeHennis, S. Getzlaff, D. Grice, and M. Mailand, "An nfc-enabled cmos ic for a wireless fully implantable glucose sensor," *IEEE journal of biomedical and health informatics*, vol. 20, no. 1, pp. 18–28, 2015.

[69] T. M. Quan, T. Doike, D. C. Bui, S. Arata, A. Kobayashi, M. Z. Islam, K. Niitsu *et al.*, "Ai-based edge-intelligent hypoglycemia prediction system using alternate learning and inference method for blood glucose level data with low-periodicity," in *2019 IEEE International Conference on Artificial Intelligence Circuits and Systems (AICAS)*. IEEE, 2019, pp. 201–206.

[70] E. Sackinger, "The transimpedance limit," *IEEE transactions on circuits and systems I: regular papers*, vol. 57, no. 8, pp. 1848–1856, 2010.

[71] P. Wright, K. B. Ozanyan, S. J. Carey, and H. McCann, "Design of high-performance photodiode receivers for optical tomography," *IEEE Sensors Journal*, vol. 5, no. 2, pp. 281–288, 2005.

[72] J. G. Graeme and J. G. Graeme, *Photodiode amplifiers: op amp solutions*. McGraw-Hill New York, 1996.

[73] W.-Z. Chen, Y.-L. Cheng, and D.-S. Lin, "A 1.8-v 10-gb/s fully integrated cmos optical receiver analog front-end," *IEEE journal of solid-state circuits*, vol. 40, no. 6, pp. 1388–1396, 2005.

[74] H. M. Lavasani, W. Pan, B. Harrington, R. Abdolvand, and F. Ayazi, "A 76 db 1.7 ghz 0.18um cmos tunable tia using broadband current pre-amplifier for high frequency lateral mems oscillators," *IEEE journal of solid-state circuits*, vol. 46, no. 1, pp. 224–235, 2011.

[75] R. Y. Chen and Z.-Y. Yang, "Cmos transimpedance amplifier for gigabit-per-second optical wireless communications," *IEEE Transactions on Circuits and Systems II: Express Briefs*, vol. 63, no. 5, pp. 418–422, 2016.

[76] Z. Qin, A. Tanaka, N. Takaya, and H. Yoshizawa, "0.5-v 70-nw rail-to-rail operational amplifier using a cross-coupled output stage," *IEEE Transactions on Circuits and Systems II: Express Briefs*, vol. 63, no. 11, pp. 1009–1013, 2016.

[77] M. Taghavi, L. Belostotski, and J. Haslett, "A cmos low-power cross-coupled immittance-converter transimpedance amplifier," *IEEE Microwave and Wireless Components Letters*, vol. 25, no. 6, pp. 403–405, 2015.

[78] Y. Hayashi, L. Livshits, A. Caduff, and Y. Feldman, "Dielectric spectroscopy study of specific glucose influence on human erythrocyte membranes," *Journal of Physics D: Applied Physics*, vol. 36, no. 4, p. 369, 2003.

[79] C. Z. Ming, P. Raveendran, and P. S. Chew, "A comparison analysis between partial least squares and neural network in non-invasive blood glucose concentration monitoring system," in *2009 International Conference on Biomedical and Pharmaceutical Engineering*. IEEE, 2009, pp. 1–4.

[80] B. Vinchhi, D. Berger, and C. Dehollain, "3-stage miller cross-coupled load based photodiode readout for glucose monitoring," in *2018 40th Annual International Conference of the IEEE Engineering in Medicine and Biology Society (EMBC)*. IEEE, 2018, pp. 3918–3921.

[81] A. T. Kharroubi and H. M. Darwish, "Diabetes mellitus: The epidemic of the century," *World journal of diabetes*, vol. 6, no. 6, p. 850, 2015.

[82] A. D. Association *et al.*, "Diagnosis and classification of diabetes mellitus," *Diabetes care*, vol. 37, no. Supplement 1, pp. S81–S90, 2014.

[83] V. V. Tuchin, *Handbook of optical sensing of glucose in biological fluids and tissues*. CRC press, 2008.

[84] A. Tura, A. Maran, and G. Pacini, "Non-invasive glucose monitoring: assessment of technologies and devices according to quantitative criteria," *Diabetes research and clinical practice*, vol. 77, no. 1, pp. 16–40, 2007.

[85] C. C. Enz, F. Krummenacher, and E. A. Vittoz, "An analytical mos transistor model valid in all regions of operation and dedicated to low-voltage and low-current applications," *Analog integrated circuits and signal processing*, vol. 8, no. 1, pp. 83–114, 1995.

[86] M. Ho, J. Guo, T. W. Mui, K. H. Mak, W. L. Goh, H. C. Poon, S. Bu, M. W. Lau, and K. N. Leung, "A two-stage large-capacitive-load amplifier with multiple cross-coupled small-gain stages," *IEEE Transactions on Very Large Scale Integration (VLSI) Systems*, vol. 24, no. 7, pp. 2580–2592, 2016.

[87] M. Gal-Katziri and A. Hajimiri, "Analysis and design of coupled inductive bridges for magnetic sensing applications," *IEEE Journal of Solid-State Circuits*, 2019.

[88] W. M. Sansen, *Analog design essentials*. Springer Science & Business Media, 2007, vol. 859.

[89] J. Kim and H. Ko, "A 1.2 v low-power cmos chopper-stabilized analog front-end ic for glucose monitoring," *IEEE Sensors Journal*, vol. 16, no. 17, pp. 6517–6518, 2016.

Bakul Vinchhi, Ph.D.

Rue du Crêt 10, 1006 Lausanne, Switzerland. +41 (0)78 838 79 96
bakul.vinchhi@epfl.ch, vinchhibakul@gmail.com, in/bakul-vinchhi

Strengths

- Strong scientific experience in research projects from conception, design, implementation and testing.
- 11 years of industry experience in medical devices, pharma, food-nutrition, and semiconductors.
- Ability to function in a multicultural, interdisciplinary team set up, build strong and prolific collaborations.
- Core strengths: Medical Devices, Microelectronics, Optics, IC Design, and Translation Engineering

Education

2014 – 2019 Ph.D. in Microsystems and Microelectronics / EPFL, Switzerland
Optical Microsystems for Genetically Engineered Biosensors. Case Study: Glucose Monitoring.

2009 - 2012 Master of Science M.S. / KU Leuven, Belgium
Nanoscience and Nanotechnology, major engineering, cum laude
ATHENS Exchange Program: TU Delft, Netherlands, 2010 and MINES ParisTech, France, 2011

2011 - 2012 Master Thesis / ETH Zurich, Switzerland
Low Noise Current Readout Circuit for Neurotransmitter Detection

2005 Bachelor of Engineering / Visvesvaraya Technological University, India
Electronics and Communication Engineering. First class with distinction.

Executive Management Education

2017 – 2018 CAS Management of Biotech, Medtech & Pharma Ventures / EPFL, Switzerland
Strategic Alliances, Partnership, and Outsourcing - Clinical Trial Management & Regulatory Affairs

2015 HBS HBX CORe Program / Harvard Business School, USA
Business Analytics, Economics for Managers, Financial Accounting

Honors and Awards

- Winner 1st Place, Startup Weekend Lausanne 2016
- Winner 1st Place, Startup Weekend Zurich 2016
- Winner Public Award, Medical Device for Breast Cancer Detection, Startup Weekend Bern 2016
- Swissnex - Nominated for the FinTech Startup Tour India 2017
- Nominated for the highly selective Venture Challenge 2014 program at EPFL
- ISSCC 2016, IEEE Solid-State Circuits Society, Student Travel Grant Award (STGA)
- ETH Zürich - Merit Scholarship of CHF 7200 during the Masters 2011
- iGEM KU Leuven - World Championship Qualifier and Gold Medal Winner
  Massachusetts Institute of Technology, MIT Boston, 2011
- Infineon Star Team of the Quarter (Q4) 2008 MIPI PHY Development Team
- Infineon YiP (Your Idea Pays) Award for IC Manufacturing Line Process Optimization

Industry Experience

2014 – 2019 Industrial Ph.D. / Nestlé, EPFL, Lausanne, Switzerland

- Led a CHF 500k project with Nestlé - signed under NDA agreement.
- Interdisciplinary industrial Ph.D. involving microelectronics, optics, and genetics.
- Successfully executed the proof of concept for a novel glucose detection diagnostic tool.
- Planned the project milestones, design strategy and delivered a tested product.
- Established collaboration with scientists, academics and senior management executives.
- Negotiated contracts leading to deal closure with suppliers from the United States, Japan, and Europe.
- Supervised master students for semester and thesis projects.

2016 – 2017 Co-Founder & CTO / ValUBot, Zurich, Switzerland

- MVP development, Go-to-market strategy, Swissnex - Customer & market outreach.
- Interaction with VCs, Business Angels & C-Level exec, Pitch in the Bombay Stock Exchange.

2012 – 2014 Team Leader / Fraunhofer IIS, Erlangen, Germany

- Led a project with a budget of over 2.5 Million Euros for Vestibular Implants.
- Industrial partners in Austria, France, Germany and scientific partners in the USA and Italy.
- Project management, customer interaction, setting timelines and reporting into a matrix organization.
- Achieved 10x reduction in power consumption with the designed and taped-out CMOS Analog Circuit.
- Screening, interviewing job applications and on-boarding of new employees.
- Build external recruitment networks with the HR department.

2010 DESIGN & TEST / imec, Leuven, Belgium

- UV Imagers for Space Applications. Ultra-low power and cryogenic electronics.

2005 – 2009 Project Leader / Infineon, Bangalore, India

- Planning, coordination, and execution of complex analog mixed-signal SOCs across cross-geographical teams in EU, Asia Pacific and North America. Worked successfully with team sizes from 10-80 engineers and concept designers.
- 10+ full custom ASIC designs from Specifications to Schematic to GDSII Tape-Outs in CMOS from 40 nm to 350 nm.
- Wireline, Wireless, Medical, Chip Card, Automotive and Industrial segments with Competitive Market Intelligence.
- Introduced Agile Management practices with visibility and recognition from the global headquarters in Germany.
- Responsible for the MIPI camera interface SoC design deployed in the Apple iPhone3 camera interface.

Additional Experience

2005 CTI TELEPHONY / SIEMENS, Bangalore, India

Skills

Hardware: CMOS Analog Circuit Design, Layout, Cadence Virtuoso, Specter, Altium PCB design, Xilinx ISE
Systems: Biomedical system design, TI MSP430, TI CCS Studio, Microchip PIC, Oscilloscopes, Network Analyzer
Optics: Filter Design, Spectrometer, Absorption and Dichroic Filters
Microscopy: Confocal Microscopy, Fluorescence Microscopy, Wide Angle Microscopy, Image Processing
Biology: Cell Culture, cell sorting, cell encapsulation, experiment setups, clean room handling
Programming Languages: C, C++, Python, LabVIEW, Matlab, Origin
Computer Skills: Microsoft and Mac OS Platform, Full Adobe Platform and 3D printing

Publications

Conferences

- **Electronic system for FRET based in vitro sensing of cytosolic Ca^{2+} in INS-1E pancreatic β-cells**
  Bakul Vinchhi et. Al. IEEE Biomedical Circuits and Systems Conference, BioCAS 2015, Atlanta, Georgia, USA
- **In-Vitro Platform for Continuous Monitoring of Cytosolic Ca^{2+} Upon Glucose Stimulation in a Genetically Engineered INS-1E Pancreatic β-Cell Line**
  Bakul Vinchhi, C Boss, et al. IEEE EMBS Conference on Micro and Nanotechnology in Medicine 2016, Hawaii, USA
- **3-Stage Miller Cross-Coupled Load based Photodiode Readout for Glucose Monitoring**
  Bakul Vinchhi, Daniel Berger, Catherine Dehollain. IEEE EMBC 2018, Honolulu, Hawaii, USA
- **Pancreatic cell based optical biosensor and system for continuous glucose monitoring**
  Bakul Vinchhi, Christophe Boss, Ninad Agashe, Catherine Dehollain. IEEE BioCAS 2019, Nara, Japan
- **Optical pancreatic β-cell based biosensor, applications and glucose monitoring**
  Bakul Vinchhi, Christophe Boss, Catherine Dehollain. IEEE Sensors 2019, Montreal, Canada
- **A 83dB SNDR low power readout ASIC for piezoresistive nanogauge based gyroscopes**
  A Nikas, O Leman, H Zhou, JL Lagos, BJ Vinchhi, J Hauer. IEEE ISCAS 2016, Montreal, Canada
- **A versatile analog front-end for sensors based on piezoresistive silicon nanowire detection**
  O Leman, A Nikas, H Zhou, JL Lagos, BJ Vinchhi, J Hauer, G Jourdan et. Al. IEEE ISCAS 2015, Lisbon, Portugal

Journals

- **Optical filter characterization for an pancreatic β-cell based biosensor based in vitro system**
  Biosensors and Bioelectronics, Journal, Elsevier (in preparation)

Languages

- English - C2 Fluent, Native language
- French - Intermediate level B1 (5 years of immersion in the French-speaking part of Switzerland)
- German - Advanced Intermediate Level B2 (2 years of industry work in Erlangen, Germany)
- Hindi, Kannada, Gujarathi - Fluent C2, Native Language
- Flemish - Spoken A2 (2 years of stay in Flanders, Belgium)

Extracurricular Activities

- **President** - Lindy Hop Association 2018-2019, Promotion of Jazz Era Dancing on the EPFL UNIL campuses
- **Head of Fundraising** - Model United Nations, MUN 2016, debating and negotiation society at EPFL
- **Rowing** - Active since 2+ years, competition and training, 500+ KMs/year
- **Clarinet** - 3 semesters at the Ecole de Jazz et de Musique Actuelle (EJMA) Lausanne, Switzerland
- **Biking** - Team leader for the Bike2Work project aimed at reducing CO_2 footprint on the planet